DOPING OF EPITAXIAL III-V SEMICONDUCTORS FOR OPTOELECTRONIC AND MAGNETOELECTRONIC APPLICATIONS

By

MARK E. OVERBERG

A DISSERTATION PRESENTED TO THE GRADUATE SCHOOL
OF THE UNIVERSITY OF FLORIDA IN PARTIAL FULFILLMENT
OF THE REQUIREMENTS FOR THE DEGREE OF
DOCTOR OF PHILOSOPHY

UNIVERSITY OF FLORIDA

2001

And the sea shall grant each man new hope, as sleep brings dreams of home.

—Christopher Columbus, 1493

ACKNOWLEDGMENTS

The most important person for me to thank is Dr. Cammy Abernathy, who saved me from certain academic doom when I first came to UF, and to whom I am completely indebted to for making me a better thinker and a better person. A few words are not nearly enough to accurately describe how great she is as a mentor and a friend. When I think of our interaction over the last three and a half years, I immediately think of those words by St. Augustine: “Patience is the companion of wisdom.” I thank Dr. Stephen Pearton, for serving on my committee and for his support of my professional development. I thank my committee member Dr. Arthur Hebard, for allowing me to make use of his equipment to complete this study. Finally, I also thank Dr. Paul Holloway and Dr. Rajiv Singh for serving on my committee.

I especially thank everyone in the Overberg clan for their love, support, and encouragement. My parents and my brother deserve special thanks for hanging in there through four more years of education. By graduating, I hope that I can provide for my parents the retirement plans that my father believes a Ph.D. son enables him to afford. Most of my contemporaries deserve thanks: particularly Neil and Libby, Kurt and Bev, Heidi and Keith, Julie, Brian, Elizabeth and Jim, Sue, and Steven, for their love and support, without asking too many questions. One of the few regrets I have is that my paternal grandfather did not live long enough to see me graduate from college, or even from high school. I miss him every day.

I credit much of any of the success I've had during my "formative" years to several people I've known personally and professionally. I thank Mrs. Renee Zimmerman and Brother Phil DiMarchi for their early guidance. I acknowledge Dr. Sam Nablo, Dr. Stuart Denholm, and Mr. Jack Weisman, the founders of Energy Sciences, Inc. for their support, direct and indirect, over the years. I also thank Patrick Splinter and Phil Ring of the Axcelis (formerly Eaton) Corporation, for the internship opportunities. Finally, I thank Dr. Marcel Gaudreau of Diversified Technologies, Inc., for his support and encouragement.

I acknowledge Prof. Toh-Ming Lu of the Physics Department at Rensselaer. He was the first person to recommend the Materials Department at UF when I approached him for advice on graduate programs.

Many people at UF deserve a lot of credit. From Dr. Abernathy's group, I thank Dr. Devin MacKenzie, Dr. Sean Donovan, Dr. K.N. Lee, Keiko Harris, Jerry Thaler, and Karen Waldrip. I thank Eric Lambers and Wish Krishnamoorthy of the MAIC for their help with characterization and discussion. From Prof. Hebard's group, I thank Dr. Steve Arnason, Nikoleta Theodoropoulou, and Kevin McCarthy for their help with magnetic data acquisition and interpretation. I thank Dr. Jeff Childress and Dr. Fred Sharifi for their early support. Other good friends include Billie Abrams, Loren Rieth, Caroline Kondoleon, Josh Howard, Wayne Johnson, Kyu-Pil Lee, Don Kent, Charley Malpass, Eric Fodran, and Dr. Dan Park.

Three very important people to me deserve a special acknowledgement. I thank Dr. Chris Werner of Los Alamos National Lab for our friendship, all the frustrating RPI hockey games we went to, and making sure that everything fell into place after I left New

York for good. Melissa Norman deserves a large “thank you” for being a very special friend for the last three years. She can always be counted on as a source of enthusiasm, support, and encouragement, especially when it is needed most. Finally, I acknowledge Brent Gila. I thank him for being a source of support and guidance, for the TEM, for the constant qualifier harassment, for the softball, all the nights we spent fixing the MBE, for being an excellent friend, and for the two trips to the emergency room.

TABLE OF CONTENTS

page
ACKNOWLEDGMENTS.......iii

ABSTRACT.......ix

CHAPTER
1 INTRODUCTION.......1
1.1 Photonics.......1
    1.1.1 Development of Telecommunication.......1
    1.1.2 Laser Diodes and Rare Earth Doping.......3
1.2 Electronics.......7
    1.2.1 Qubits and Quantum Information Technology.......7
    1.2.2 Spintronic Devices.......10
1.3 Motivation.......13

2 REVIEW OF RARE EARTH DOPING IN GaN.......20
2.1 Rare Earth Doping in Si and Non-Nitride III-V Semiconductors.......20
2.2 Rare Earth Doping in III-Nitrides.......21
2.3 Codoping Effects in Rare Earth Doped Semiconductors.......25

3 REVIEW OF DILUTE MAGNETIC SEMICONDUCTOR MATERIALS.......30
3.1 Theories of Dilute Magnetic Semiconductor Ferromagnetism.......30
3.2 Review of Transition Metal Doping in Semiconductor Host Materials.......33
    3.2.1 Manganese in Group IV Materials.......34
    3.2.2 Manganese in Group III-Arsenide Materials.......35
    3.2.3 Manganese in Group III-Antimonide Materials.......38
    3.2.4 Manganese in Group III-Nitride Materials.......40
    3.2.5 Manganese in Group III-Phosphide Materials.......42
    3.2.6 Manganese in II-VI Semiconductors.......42
    3.2.7 Other DMS Semiconductors.......44

4 EPITAXIAL GROWTH WITH THE MOMBE TECHNIQUE.......51
4.1 System Geometry.......51
4.2 Group III Sources.......52
4.3 Group V Sources.......54
4.4 Dopant Sources.......55
4.5 System Control.......55

4.6 System Safety……56
4.7 Sample Loading and Preparation……57

5 SAMPLE CHARACTERIZATION……65
5.1 Atomic Force Microscopy……65
5.2 Scanning Electron Microscopy……66
5.3 X-ray Diffraction……66
5.4 Reflection High Energy Electron Diffraction……67
5.5 Auger Electron Spectroscopy……68
5.6 Secondary Ion Mass Spectrometry……69
5.7 Photoluminescence……69
5.8 Hall Effect……70
5.9 SQUID Magnetometry……71

6 RESULTS AND DISCUSSION: RARE EARTH DOPING OF GaN……78
6.1 Gallium Nitride Doped with Er Grown Using Triethylgallium……78
  6.1.1 Material Growth by MOMBE……78
  6.1.2 Sample Morphology……79
  6.1.3 Photoluminescence Analysis……80
6.2 Gallium Nitride Doped with Er Grown Using Elemental Ga and Codoped with C...81
  6.2.1 Material Growth by GSMBE……82
  6.2.2 Effect of Carbon Doping on Film Morphology……82
  6.2.3 Effect of Carbon Doping on Film Luminescence……84
  6.2.4 Annealing of GaN:Er and GaN:Er:C……87
6.3 Gallium Nitride Doped with Eu Grown Using Elemental Ga……88
  6.3.1 Material Growth by GSMBE……88
  6.3.2 Photoluminescence Analysis……88

7 RESULTS AND DISCUSSION: GaMnN……107
7.1 Incorporation of Mn into GaN……107
  7.1.1 Starting GaN Growth Recipe……107
  7.1.2 Doping with Mn……108
  7.1.3 Structural Characteristics of the GaMnN……110
7.2 Effect of Substrate Type and C Doping on GaMnN Magnetic Properties……111
  7.2.1 Gallium Manganese Nitride Growth Recipe……111
  7.2.2 Structural Characteristics of the GaMnN and GaMnN:C……112
  7.2.3 Magnetic Properties of GaMnN and GaMnN:C……114
7.3 Gallium Manganese Nitride Growth at Elevated Temperature……115
  7.3.1 Material Growth……116
  7.3.2 Structural Properties……116
  7.3.3 Electrical and Magnetic Properties……117

8 RESULTS AND DISCUSSION: GaMnP……139
8.1 Growth of P-Type GaP:C……139
  8.1.1 Starting Recipe……139
  8.1.2 Structural and Electrical Characterization……141

8.2 Production of GaMnP:C by Ion Implantation...142
  8.2.1 Implantation Procedure...143
  8.2.2 Magnetic Characterization...143
8.3 Epitaxial Growth of GaMnP:C by MBE...145
  8.3.1 Doping with Mn...145
  8.3.2 Electrical Properties and Phase Diagram of GaMnP:C...147
  8.3.3 Growth Dynamics and Structural Characterization of GaMnP:C...149
  8.3.4 Microstructural Properties...153
  8.3.5 Magnetic Characterization...154

9 SUMMARY AND CONCLUSIONS...175

APPENDIX: LABVIEW™ CONTROL OF THE VARIAN INTEVAC MOD GEN II MBE...179

REFERENCES...187

BIOGRAPHICAL SKETCH...199

Abstract of Dissertation Presented to the Graduate School
of the University of Florida in Partial Fulfillment of the
Requirements for the Degree of Doctor of Philosophy

DOPING OF EPITAXIAL III-V SEMICONDUCTORS FOR OPTOELECTRONIC AND MAGNETOELECTRONIC APPLICATIONS

By

Mark E. Overberg

August, 2001

Chairperson: Dr. Cammy Abernathy
Major Department: Materials Science and Engineering

Doped III-V semiconducting materials were studied in this dissertation for use in optoelectronic and magnetoelectronic applications. The specific areas of use are emitters for fiber optic communication and room temperature ferromagnetic layers for spintronic devices. The general requirement for both application areas is the ability to heavily dope (or alloy) the III-Vs with the intended active element, while still maintaining good crystallinity and semiconducting properties. Four dopant/semiconductor systems were investigated: erbium in gallium nitride (GaN:Er), europium in gallium nitride (GaN:Eu), manganese in gallium nitride (GaMnN), and manganese in gallium phosphide (GaMnP).

These materials were fabricated using variants of the molecular beam epitaxy (MBE) technique, where beams of the constituent elements are produced in a high vacuum environment. The technique allows for a wide variety of parameters to be adjusted during the material preparation. The materials were deposited on sapphire, gallium nitride, and gallium phosphide surfaces; with particular emphasis on the correlation between growth conditions and the final chemical, structural, morphological, electronic, optical, and magnetic properties. The materials were characterized using a variety of techniques.

Results with the GaN:Er material indicated that several percent of Er could be successfully incorporated into the material, and that the optical emission could be increased by incorporating C impurities into the film. These impurities were found to increase the overall emission and decrease the quenching of the emission with temperature. Optical emission results for GaN:Eu indicated that this material produced a visible red emission that was brighter under optical excitation than the AlGaAs used in commercial red emitting devices. The dilute magnetic semiconductors n-GaMnN and p-GaMnP were produced for the first time by the MBE technique. The SQUID magnetometry and magnetotransport results for n-GaMnN indicated the presence of ferromagnetic ordering with a Curie temperature between 20 K and 25 K. Magnetic measurements of the p-GaMnP indicated the presence of ferromagnetic ordering to 250 K, far above the theoretically predicted value of 100 K. Similar results were also produced by the direct implantation of Mn into GaP.

CHAPTER 1
INTRODUCTION

Beginning with the invention of the written alphabet in ancient Phoenicia, and continuing with the spread of this knowledge by seaborne trade, the art of communication has always been evolving. Advances in communication serve to make our planet a smaller and smaller place, whether they are in the form of improved roads or other transmission routes; or in the form of the basic technique used to communicate, such as the Morse Code. The current quest to communicate quickly and securely is referred to as the Information Age, using light and electricity as the means of sharing ideas, thought, and commerce.

1.1 Photonics

1.1.1 Development of Telecommunication

The beginnings of the Information Age can be traced to Alexander Graham Bell's invention of the telephone in 1876 in Boston, Massachusetts. For roughly the next 100 years, telephone transmission relied on signals being sent via copper wires. However, Bell hypothesized early on that optical radiation (as opposed to electronic) would be more advantageous for the telephone signal [1]. In 1881, Bell invented and demonstrated his photophone, which used a high-purity selenium crystal as part of its electrical circuit (Figure 1-1). His assistant transmitted the first message by means of light ("Mr. Bell, if you hear what I say, come to the window and wave your hat.") over a distance of 213 meters. This invention was impractical and crude as it relied on non-coherent light for operation. The fundamental advantage of using coherent light was not realized until 80 years later: first with the ruby laser developed in 1960, and then with the double heterojunction laser diode developed in 1970. However, a feasible transmission medium for this laser light was not yet available. It was recognized in the 1930's that glass fibers could be used for transmitting optical signals, and that a fiber loss of approximately 20 dB/km was the threshold for an optical transmission system. Due to technological constraints, it was not until 1970 that a clad glass fiber was developed with a 20 dB/km loss. Further advances in materials development and fiber drawing reduced the loss to 1.1 dB/km in 1974, and then to 0.47 dB/km by 1979, allowing fiber optics to be used on a permanent commercial basis starting in 1980.

Although fiber optic cable development progressed rapidly, the 0.47 dB/km cable that began to be used extensively in 1980 still had a finite loss. As such, it was clear from the outset that the light signal, like the electronic signal in a copper wire, would eventually require regeneration. The development of optical amplifiers paralleled the development of silica fiber optic cable. The first demonstration of optical regeneration was made in 1962 with a ruby optical amplifier, producing a gain of 6 dB. These initial electrically regenerative repeaters, in use for the next 25 years, converted an optical signal to an electronic one, which was then regenerated with a recovery circuit, and then transformed back into an optical signal with a laser. Unfortunately, these systems were extremely complex, problematic, large, and expensive for devices that could handle more than several gigabits per second of data transfer. The real breakthrough in amplification technology was made in 1987. By this time, it was well known that a fiber optic cable, like an electrical one, possessed resistance. However, the resistance (or loss) of the fiber optic cable depends on the wavelength of light that is being passed through it (Figure 1-2). The two observed minima peaks correspond to wavelengths of 1.3 μm and 1.54 μm, respectively the dispersion minima and the attenuation minima. Therefore, the fiber optic light source and detector should operate at one of these two wavelengths. In 1987, a 20 dB high gain fiber amplifier operating in the 1.54 μm region was developed using erbium doped silica fibers, the so-called erbium doped fiber amplifier (EDFA). This first device used excitation from an argon laser, but by 1988 the technology had commercialized into practical, compact EDFA's using laser diodes. The EDFA's in use today do not experience changes in gain with changes in bit rate, eliminating the need for high speed electronics compared to older amplifiers. It was therefore possible to produce high gain, high power, low noise, broadband, and high reliability devices, though no amplifier can simultaneously meet all of these requirements. EDFA's also have large optical interaction lengths (meters) to produce the desired (20 dB) amplification, which although reducible with planar waveguide structures, is still considerable. Today's state-of-the-art technology fiber amplifiers are therefore still complex and expensive.

1.1.2 Laser Diodes and Rare Earth Doping

In the previous section it was mentionned that a modern silica fiber has loss minima at approximately 1.3 μm and 1.54 μm. It was also noted that a modern optical communication system makes use of a laser diode and a photodetector tuned to operate at one of these "magic wavelengths." Currently, these lasers and photodetectors are based on the InGaAsP/InP semiconductor system. The machanism of operation for the InGaAsP device is a conduction band to valence band, electron to hole recombination to produce the 1.3 μm or 1.54 μm photons. The emission wavelength and thus the bandgap of the material is controlled by the epitaxy of the quaternary alloy. However, this material has several disadvantages [2]. As it is a four-component alloy, this semiconductor is difficult to produce, requiring highly specialized crystal growth. Second, devices made from this material rely on a band-to-band recombination (constant bandgap) for proper operation. But, the bandgap of a semiconductor, in general, is dependent on temperature, which will lead to poor wavelength stability and reliability in an InGaAsP device. This places a limit on the operating environment of such a device. Finally, the direct integration of InGaAsP with Si (for a potential combined electronic and photonic circuit) is limited by lattice mismatch. InGaAsP was found to be particularly susceptible to mismatch defects, which can kill the operation of a diode-type device. Therefore, any device that could avoid any or all of these issues could potentially be an ideal replacement.

The EDFA discussed in Section 1.1 avoids band recombination effects to produce 1.54 μm radiation via erbium ions (Er^{+3}) incorporated into the silica glass of the device. The electronic configuration of the lanthanide rare earth elements (such as erbium) is very similar and is based on the gradual filling of the 4f subshell along the series. Table 1 shows the electronic configuration of the elements in the lanthanide series, from cerium to ytterbium.

For most of the lanthanide rare earth elements, the +3 state is prefered for ionization. When ionization occurs, the two 6s electrons and one 4f electron are removed, leaving the ion with the xenon structure plus a certain number of 4f electrons. As these remaining 4f electrons determine the electronic configuration, the observed

Table 1-1: Electronic structure of the lanthanide rare earth elements.

Element	Atomic Number (Z)	Configuration
Cerium	58	$[Kr]4d^{10}4f^{2}5s^{2}5p^{6}6s^{2}$
Praseodymium	59	$[Kr]4d^{10}4f^{3}5s^{2}5p^{6}6s^{2}$
Neodymium	60	$[Kr]4d^{10}4f^{4}5s^{2}5p^{6}6s^{2}$
Promethium	61	$[Kr]4d^{10}4f^{5}5s^{2}5p^{6}6s^{2}$
Samarium	62	$[Kr]4d^{10}4f^{6}5s^{2}5p^{6}6s^{2}$
Europium	63	$[Kr]4d^{10}4f^{7}5s^{2}5p^{6}6s^{2}$
Gadolinium	64	$[Kr]4d^{10}4f^{7}5s^{2}5p^{6}5d^{1}6s^{2}$
Terbium	65	$[Kr]4d^{10}4f^{9}5s^{2}5p^{6}6s^{2}$
Dysprosium	66	$[Kr]4d^{10}4f^{10}5s^{2}5p^{6}6s^{2}$
Holmium	67	$[Kr]4d^{10}4f^{11}5s^{2}5p^{6}6s^{2}$
Erbium	68	$[Kr]4d^{10}4f^{12}5s^{2}5p^{6}6s^{2}$
Thulium	69	$[Kr]4d^{10}4f^{13}5s^{2}5p^{6}6s^{2}$
Ytterbium	70	$[Kr]4d^{10}4f^{14}5s^{2}5p^{6}6s^{2}$

emission spectra (IR and visible) of trivalent rare earth are due to transitions between 4f states, producing a rich optical structure unique to each ion. In addition, as the $5s^2$ and $5p^6$ outer shells are the shells involved in atomic bonding, the 4f shells are shielded. Therefore, the rare earth elements will have similar chemical properties. This also allows the rare earth emission to be host-material insensitive, because the influence of the external host (silica glass in an EDFA) is very weak [3]. By the quantum mechanical selection rules ($\Delta\ell = \pm1$), 4f-4f transitions are parity forbidden, while 4f-5d transitions are allowed electric dipoles. Because of coulombic interaction between 4f electrons and spin orbit coupling, the 4f energy levels split in each rare earth ion. Figure 1-3 details the rare earth ion energy levels and laser transitions reported for Er^{+3} [4]. The numbers in the figure are the approximate photon wavelengths for each transition. From Figure 1-3, the $^4I_{13/2}\rightarrow{}^4I_{15/2}$ transition produces a 1.6 μm photon. This appears to be contrary to the fact that the same transition produces a 1.54 μm photon in an EDFA, matching the attenuation loss minima for a silica glass fiber. Several other mechanisms produce this wavelength shift that are not shown in the figure; this figure is constructed for transitions between Er^{+3} ions isolated in space. In additon to the electron-electron and spin-orbit interactions, a third interaction causes a further split in the energy levels (of all the rare earth elements). This is due to the ions being in a condensed matter environment. When the ion is placed in the electric field of a single crystal solid (or even in the field of an amorphous solid such as silica glass), the energy levels split by the spin-orbit interaction undergo further hyperfine splitting. This further splitting is called the Stark effect and is comparable to the Zeeman effect (hyperfine splitting due to an applied magnetic field). The other mechanism at work producing the wavelength shift allows the $^4I_{13/2} \rightarrow {}^4I_{15/2}$ transition to occur, even though it seems to violate the 4f-4f selection rule. When the ion sits in a lattice site with local tetragonal or hexagonal symmetry (or in an amorphous material exhibiting local short range order), the noncentrosymmetric crystal field that produces the Stark effect also allows intermixing of states with different parity, resulting in a finite radiative decay lifetime for a 4f-4f transition [5]. These transitions, shielded by the 5s and 5p shells, are typically characterized by long decay times (~ms), and narrow emission peak widths (~5-20 cm^{-1}) [6]. Examples of ions that exhibit this behavior are Tb^{+3}, Pr^{+3}, Tm^{+3}, Eu^{+3}, and Er^{+3}. However, transitions that normally would be allowed by the dipole selection rule ($4f^{n-1}5d^1$-$4f^n$) are not shielded strongly (involvement of the 5d electron), so the ionic spectral properties are strongly affected by the host material. Transitions such as these are characterized by wide spectral widths (1000 cm^{-1}) and short decay times (ns-μs). The Ce^{+3} ion exhibits this type of behavior. Because of the abundance of available emission wavelengths, semiconductors doped with rare earth elements could potentially be patterned and processed into active emitting device structures that would be simpler and more robust than current devices that rely on band edge emission.

1.2 Electronics

1.2.1 Qubits and Quantum Information Technology

The preceding sections show that the fields of information technology and information transfer are in a constant state of refinement. The maturity of photonic and electronic technology to this point in time, pushed by the desire to make devices smaller and faster, was aided by a greater understanding of the quantum behavior of electrons in materials. However, all current device architecture continues to view the electron as a particle, obeying the classical laws of physics. It was forseen that as dimensions continue to shrink, the wavelike properties of the electron will come into play.

The manifestation of the quantum properties of the electron in technology have been hypothesized to exist in many forms, such as electrons confined in quantum dots, atoms in a beam interacting with photons, or electrons engaged in a superconducting system [7]. However, the most popular application regards the exploitation of the electron's spin in addition to its charge within a device structure. Devices and architecture that use spin are catergorized as part of the field of spintronics. The realization of spintronic devices will enable the development of the new field of Quantum Information Technology (QIT). Although these devices will not replace current silicon-based information technology, they will enable advances in several specific areas, such as quantum cryptography and the development of a quantum computer.

If the electron spin can be used as a basic logic element, several simple aspects fundamental to quantum mechanics will in theory allow it to be superior for certain specific computing applications. Classically, bits of data are represented as either a "1" or a "0." This can be represented on the atomic scale as the spin being either up or down for the comparable "quantum bit" or "qubit." In this case, the up or down nature of the spin is reflected mathematically with the spin wavefunction. A wavefunction, Ψ_0, can represent a spin down, while another wavefunction, Ψ_1, can represent a spin up. The first mechanical property to come into play is the principle of superposition. Superposition allows a single qubit wavefunction to exist in a linear combination of the spin up and spin down states, such as:

$$\Psi = a\Psi_0 + b\Psi_1 \qquad (1.1).$$

The only requirement is that the sum of the squares of Coefficients a and b equals one (meaning the spin has to exist in some state). Conceivably, this means that the spin system can exist in all of its observable states simultaneously [8]. In a classic computer, the memory register is used as space to hold data and record the intermediate results of a computation. The size of the register (the number of separate configurations it can be in) goes as 2^n, n being the number of data bits. Therefore, a 4 bit classical register can be in one of 16 possible states. The size of the register also determines the size and complexity of the problem it can effectively "crunch." This is shown schematically in Figure 1-4a. In a quantum register, a single 4-qubit quantum state (Figure 1-4b) can also exist in 16 possible states, but in an almost infinite number of superpositions because of the complex coefficients (Figure 1-4c). Thus superposition allows a quantum computer to be massively parallel. Recent estimates have calculated that a system of 61 spins would be comparable to 10^{18} gigabytes of current memory [9]. However, this quantum superposition is very fragile. Although other quantum principles come into play during superposition, the most important is decoherence. Decoherence is an action that will cause the superposition state to collapse irreversibly. Decoherence can be imparted through making a measurement of the system at any time, the interaction of the environment of the quantum computer with the quantum superposition, or simply the quantum computer finishing its computation. When this occurs, the qubit will always give either a “1” or a “0.” For a 4-qubit string, decoherence will produce one of the sixteen possible strings given in Figure 1-4c. Alternatively, the system of 61 spins, while corresponding to 10^{18} gigabytes of memory, will produce an answer only 61 characters long. So, although a quantum computer can be asked a very difficult question, it can only give a very simple answer. This specifically is the limitation of a quantum machine that will prevent it from replacing traditional silicon-based machines. However, it is seen as being immediately applicable in the areas of factoring (to break RSA encryption), simulations, searching, and estimation.

It is the principle of decoherence that makes QIT also very desirable for data encryption. Mathematically, the most secure encryption system is the one-time pad (Vernam) cypher, where the key changes with every use. It is generally difficult to use in practice. A system of data encryption based on the superposition of the spin wavefunction is also ultimately secure, as eavesdroppers cannot read the system without disturbing it. As an example, if Eve intercepts a message from Alice to Bob, Bob will know immediately that the superposition state of their message was corrupted. The quantum mechanics of the superposition of spin states also posesses the property of non-clonability. Non-clonability states that it is physically impossible to copy states or infer the prior states of the system from a single measurement. So, Eve cannot copy the message, send the copy to Bob, and read the original version. The property of non-clonability is a direct consequence of the Heisenberg Uncertainty Principle, which states that it is impossible to make an observation of both observable quantities in a pair with infinte precision simultaneously. Therefore, eavesdroppers cannot beat the encryption system either [8].

1.2.2 Spintronic Devices

Conceptually, the prospect of QIT is very appealing. In order to realize the potential of the spin property of electrons, active device structures must therefore be fabricated to exploit it. To date, commercial devices that use the spin-induced effect of magnetoresistance are readily available or in advanced stages of development [10]. These devices use either anisotropic magnetoresistance (AMR) of roughly 2% or giant magnetoresistance (GMR) of roughly 10 to 100% in a variety of applications. These include magnetic field sensors and sensor arrays for nondestructive evaluation, currency detection, vehicle identification, land mine identification, and biomedical assay applications. GMR materials are also used in read heads, isolators, and magnetic random access memory (MRAM).

The logical extension of the use of electron spin from the metallic stacks used in magnetoresistance devices is to incorporate the spin with semiconductors. The spin property could then be used in combination with logic elements that form the basis of modern CMOS and bipolar integrated circuit technology. For many years, spin-induced ferromagnetism and semiconducting properties have been known to exist in magnetic semiconductors such as the chalcogenides and semiconducting spinels [11]. In 1990, a device structure was proposed that uses polarized electrons as the majority carriers between two ferromagnetic contacts, the spin-FET [12,13]. The configuration of this device is given in Figure 1-5a. In this device, the Fe or Permalloy ($Ni_{80}Fe_{20}$) contacts act as the polarizer (source) and the analyzer (drain) to preferentially inject and detect a particular spin state. The polarized electrons are carried through the channel via a 2DEG established in a narrow gap (InGaAs) semiconductor, where a slight Zeeman effect exists. The Zeeman-split 2DEG will only transport electrons of a certain polarization. Modulation of the spin current arises by an application of a gate voltage causing the spins to precess. Experimentally, it was found that the degree of spin polarization in this kind of device is on the order of 20%, making it inefficient for practical use [14]. The low efficiency arises from spin scattering at the ferromagnet/semiconductor interface. Such low efficiencies are to be expected in structures that incorporate metallic ferromagnets and semiconductors, due to the dissimilar nature of the two classes of materials in regard to crystal structure, bonding, and physical and chemical properties [15]. Therefore, it was further proposed that if a semiconductor can be made ferromagnetic, it can serve as a more efficient material for spin injection into devices [16]. Collective ferromagnetic behavior was proposed to occur if a semiconductor host is alloyed with a suitable transition or rare earth magnetic ion. In such a dilute magnetic semiconductor (DMS), magnetism results from an exchange interaction between the magnetic ions.

Light emitting diode structures incorporating DMS materials, the spin-LED, have been proposed and fabricated using the DMS as a spin injection layer [17,18]. This device consists of an n-$Zn_{0.94}Mn_{0.06}Se$ DMS contact layer on an AlGaAs clad GaAs quantum well (Figure 1-5b). For this device, the ZnMnSe layer is not ferromagnetic but is paramagnetic, so a magnetic field (3 T) must be applied during its cryogenic operation (4.2 K). Under these conditions, it is found that the conduction band of the ZnMnSe splits into spin-up and spin-down states by way of the giant Zeeman effect, producing a population of spin-down electrons. When the device is placed under forward bias, these spin-polarized electrons are injected into the GaAs quantum well via the n-AlGaAs clad layer, while unpolarized holes from the p-AlGaAs layer are injected into the quantum well as normal. When the polarized electrons and the unpolarized holes recombine, polarized photons will be produced. The degree of optical polarization will be proportional to the spin polarization of the electrons, and provides a qualitative measure of the spin injection efficiency. High efficiency is essential for spintronic devices. For the device shown in Figure 1-5b, a lower bound of the injection efficiency was measured to be 65%. Injection efficiencies as high as 90% have been measured in similar structures using an n-BeMnZnSe paramagnetic contact layer [19]. Finally, spin-LEDs using the injection of spin polarized holes from GaMnAs layers into InGaAs quantum wells have also been fabricated [20].

Other traditional electronic device structures have been proposed and modified for spintronic applications. These include resonant tunneling diodes (RTD), unipolar spin diodes, and unipolar spin transistors [21,22]. The unipolar devices would consist of either 2 spin layer devices (diode) or 3 spin layer devices (transistor) with each spin layer oriented antiparallel to each other. In this regard, these devices would be analogous to a pn junction or a pnp or npn bipolar transistor. However, as p/n devices have charge depletion regions, such a spin device will have a spin depletion region in the form of a

Neél wall. The wall thickness is set by the ratio between the magnetic anisotropy energy and the magnetic stiffness. In a device, this thickness should be thin to avoid precession of the spins across the interface. If the spins precess, the layers will act as a single conductor, limiting the overall usefulness of the device.

1.3 Motivation

From the preceeding sections of this chapter, it is clear that semiconductor host materials doped with either rare earth elements (for optoelectronics) or transition metal elements (for magnetoelectronics) could be very useful in many practical applications. Therefore, wide bandgap III-V semiconductors could be ideal candidates. The III-N binary semiconductors are characterized by large bandgaps (Table 1-2), permitting a range of energies between 1.9 eV and 6.2 eV in ternary alloys [24,25]. These large bandgaps permit III-N based devices to be used in high power and high temperature environments with a long service life. Conversely, they are able to emit and detect short wavelength light, enabling ultraviolet application. The III-N semiconductors are also characterized by the strong ionic component of their bonding, compared to other III-Vs

Table 1-2: Properties of III-V compound semiconductor materials.

Semiconductor	Bandgap (eV)	ΔElectronegativity (eV)	Lattice Constant (Å)
GaAs	1.4	-0.4	5.65 (a)
InAs	0.4	-0.4	6.06 (a)
AlAs	2.2	-0.6	5.66 (a)
GaP	2.3	-0.4	5.45 (a)
InP	1.3	-0.4	5.87 (a)
AlP	2.5	-0.6	5.45 (a)
GaN	3.4	-1.2	5.19 (c)
InN	1.9	-1.2	5.76 (c)
AlN	6.2	-1.4	4.98 (c)
Si	1.1	-	5.43 (a)

(Table 1-2). This is important as it was suggested that the electronic environment provided by ionic semiconductors enhances the interband transitions in rare earth ions [26]. Finally, research with LEDs and laser diodes has shown that the III-N system has a high tolerance to growth defects without degrading device performance, showing that high concentrations of dopants could be possible. Gallium phosphide is also a promising host semiconductor, for in addition to its large bandgap, it is also closely lattice-matched to Si (Table 1-2). A doped GaP layer may then be directly integrated into current Si-based device and processing technology,

In this dissertation, the doping of rare earth elements into GaN for optical activity and transition metal elements into GaN and GaP for magnetic activity were investigated. The objective of the overall work was to tailor the epitaxial growth of the individual materials to produce the maximum optical or magnetic effect. Particular emphasis was placed on the role of impurities and structure in relation to the incorporated dopant atoms. By influencing the microscopic environment surrounding the dopants, a significant effect on the overall macroscopically observed material properties can result.

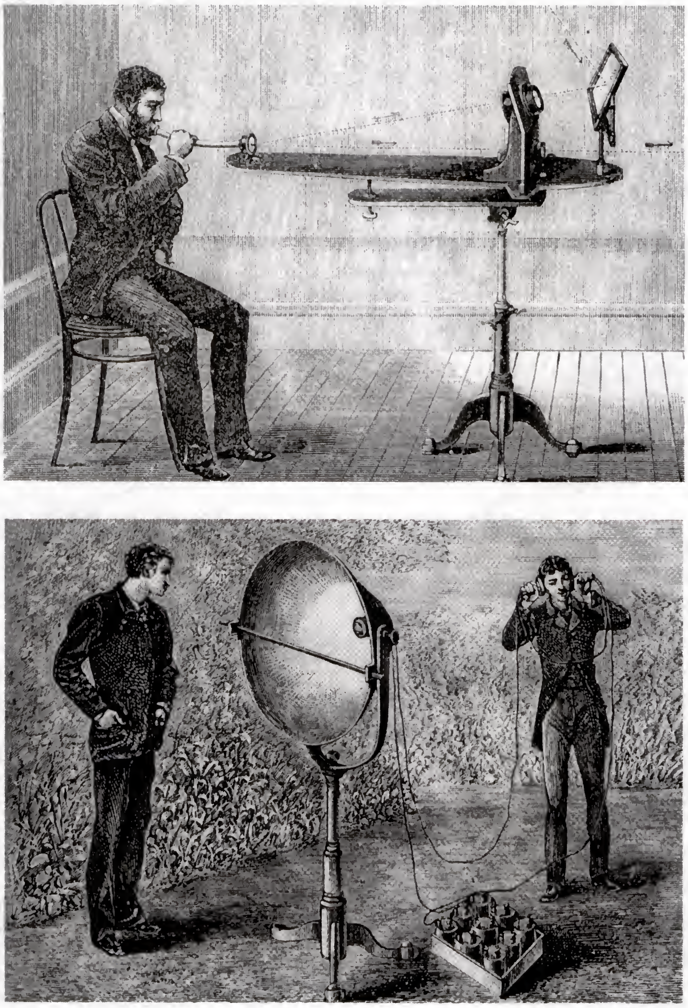

Figure 1-1: The photophone devised by Alexander Graham Bell [1]. The voice signal is modulated by a flexible mirror (top, at end of mouthpiece), and picked up by the dish (bottom) containing the selenium crystal.

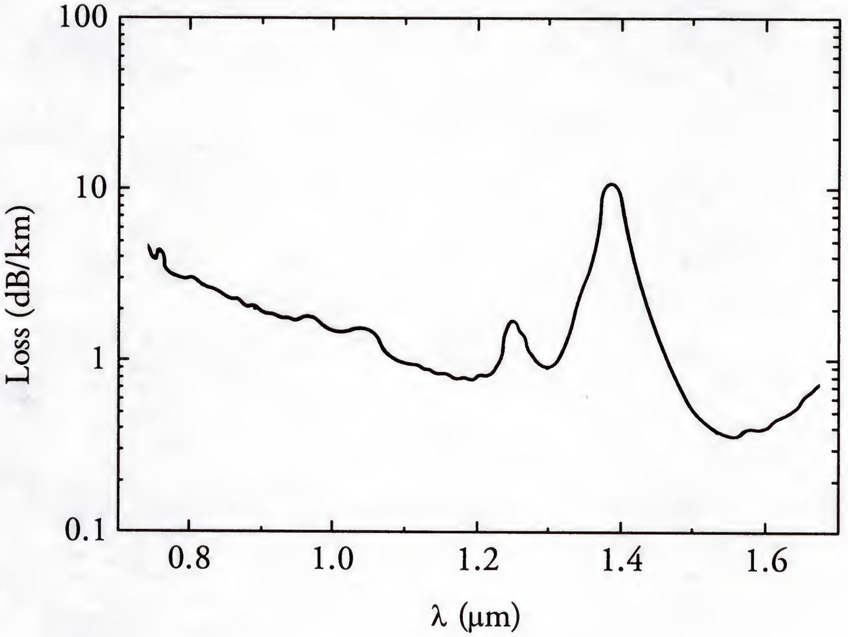

Figure 1-2: Loss of a silica fiber in the near infrared region.

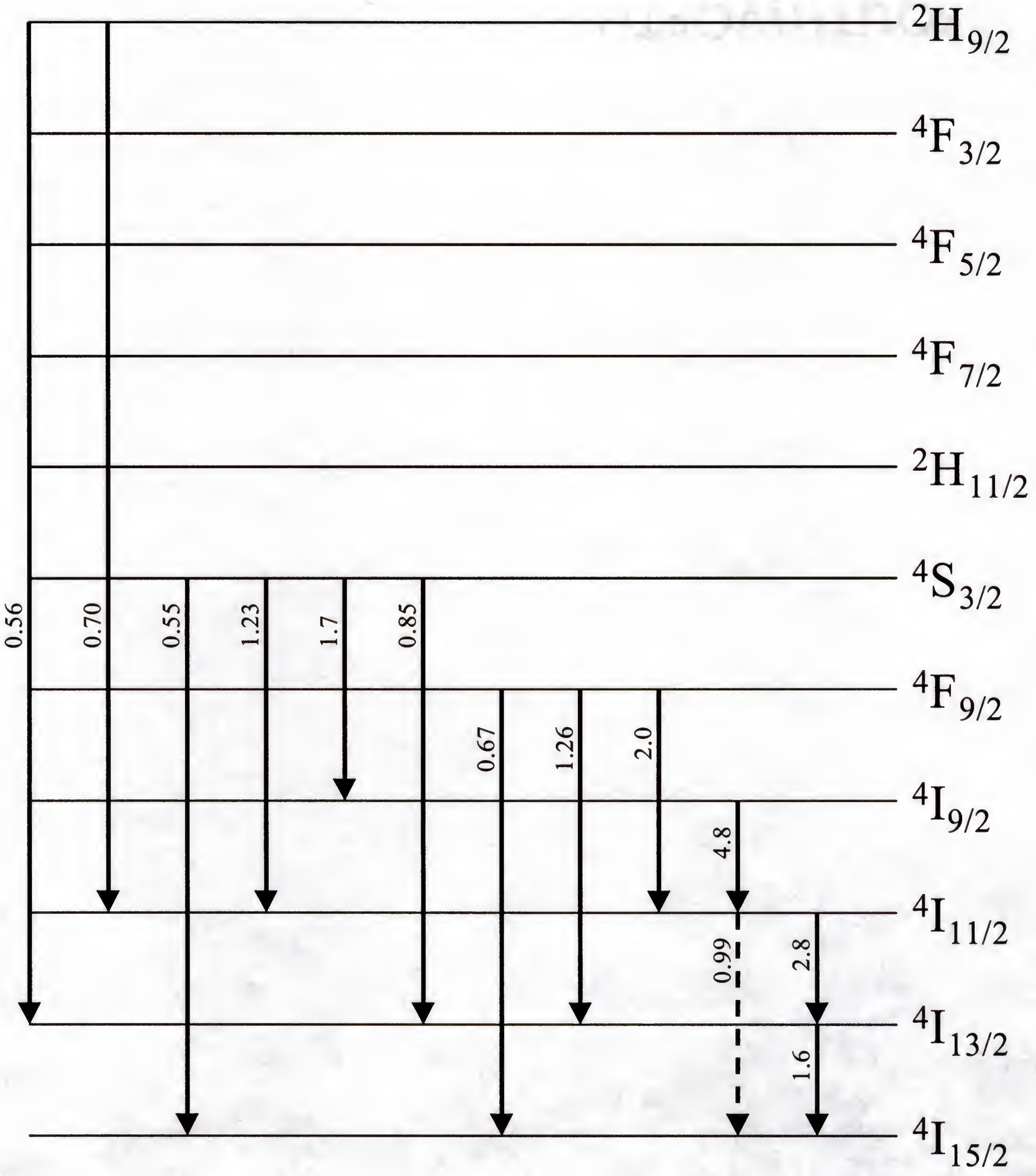

Figure 1-3: Er^{+3} energy levels and transition wavelengths (μm).

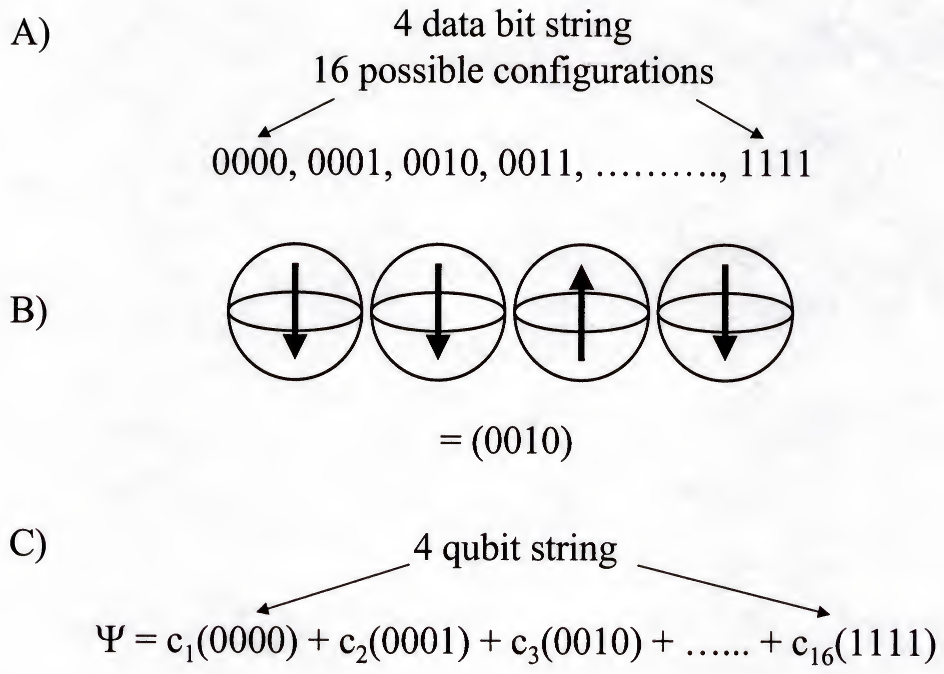
A)
4 data bit string
16 possible configurations
0000, 0001, 0010, 0011, ..., 1111
B)
= (0010)
C)
4 qubit string
$\Psi = c_1(0000) + c_2(0001) + c_3(0010) + \ldots\ldots + c_{16}(1111)$

Figure 1-4: Computer memory registers (A) Classical memory register (B) A possible state of 4 qubits (C) 4 qubit superposition state.

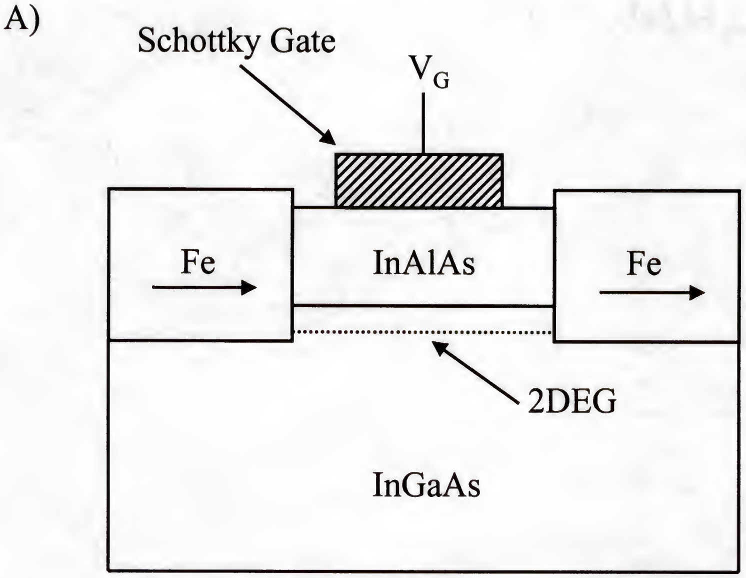

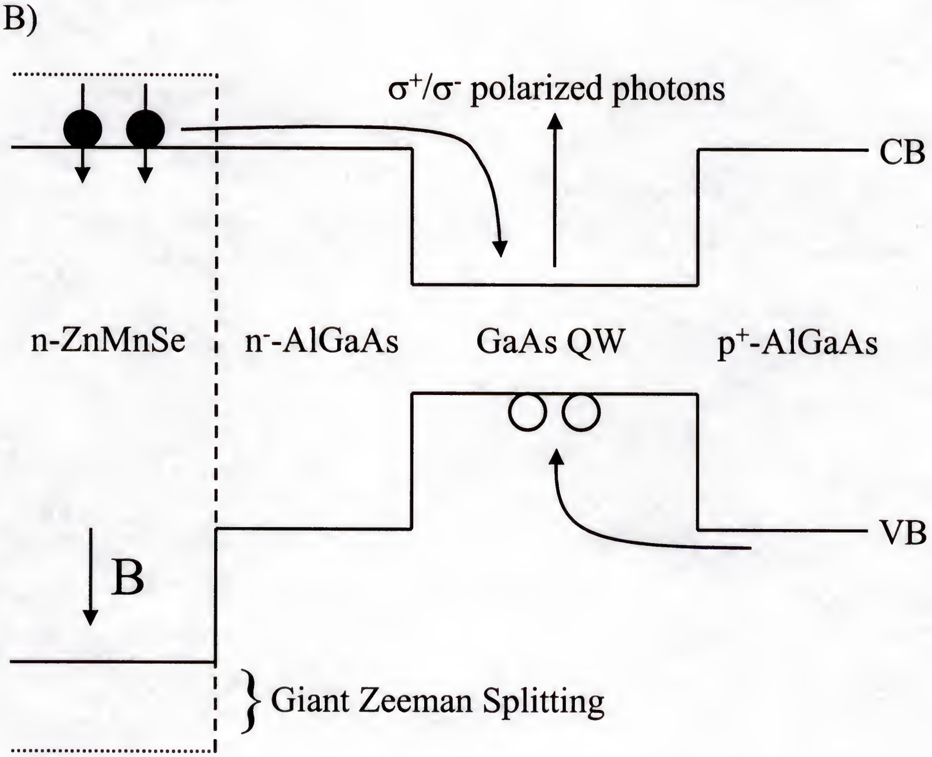

Figure 1-5: Spintronic device structures (A) spin-FET [12] (B) spin-LED [17,18].

CHAPTER 2
REVIEW OF RARE EARTH DOPING IN GaN

Because of their potential use in devices as an emitting material, research into rare earth doped semiconductors actively started after the development of EDFAs. It was recognized early that rare earth doped materials emitting in the visible to IR regions could be useful for a variety of photonic applications [6]. These include solid state UV and visible lasers, visible and IR emitters in semiconductors, optical data storage, and for use in visible displays with a variety of host materials.

2.1 Rare Earth Doping in Si and Non-Nitride III-V Semiconductors

An extensive amount of work has been performed on the rare earth doping of semiconductors, with particular emphasis on erbium doping due to the 1.54 μm emission. Erbium was incorporated into Si [27-47], GaAs [48-54], GaP [55-58], InP [59], InGaP [60-62], and AlGaAs [63]. Although the 1.54 μm Er^{+3} is detected in each case by photoluminescence spectroscopy (PL), typically the measurements must be performed at cryogenic temperatures via a cold finger. Measurements are typically reported at 77K, and in some cases at liquid helium temperatures. The integrated PL spectra at ever lower temperatures increases significantly over the room temperature value. The integrated and normalized PL at 1.54 μm versus temperature is plotted in Figure 2-1 for Er^{+3} in several of the aforementionned semiconductors [64]. Especially note from Figure 2-1 the large degree of thermal quenching that occurs between 0K and room temperature. This thermal quenching phenomena (> 500X for Si and GaAs) is the principal reason why these Er (or other rare earth) doped materials would not be applicable for use in commercial devices, and is why rare earth doping research in semiconductors such as Si and GaAs is not as active as it once was. It is also interesting to note from Figure 2-1 how the degree of thermal quenching at room temperature seems to decrease as the bandgap of the semiconductor increases. This is possibly due to the fact that the electronic environment provided by the more ionic semiconductor (which would tend to have a higher E_g) enhances the 4f transitions of the Er^{+3} ion. A direct result of this would be an enlarged intensity output.

2.2 Rare Earth Doping in III-Nitrides

Based on the data presented in Figure 2-1, it is apparent that wide bandgap semiconductors such as the group III-nitrides would be more advantageous to minimize the thermal quenching effect. The group III-nitrides also possess strong ionic bonding ($\Delta EN \cong 1.3$), so conceivably thermal quenching will not be as great. As with the non-nitride compound semiconductors, group III-nitrides doped with erbium have also received attention due to their possible application in telecommunications. The 1.54 μm luminescence was first reported by Wilson et al. in Er implanted GaN and AlN grown by metalorganic molecular beam epitaxy (MOMBE) in 1994 [2]. The gallium and aluminum fluxes were provided by triethylgallium (TEG) and dimethylethylamine alane (DMEAA), while an ECR plasma source provided the reactive nitrogen. It was found that the hexagonal GaN grown on sapphire had 25X larger Er^{+3} signal that GaN or AlN grown on GaAs, which was of a mixed cubic/hexagonal structure. The Er atom density was roughly $8x10^{18}/cm^3$. It was found from the below bandgap PL measurement, that the

GaN:Er on sapphire spectra decreased roughly by a factor of 2 between 6K and 300K. This would place the GaN measurement with the bandgap/quenching prediction based on Figure 2-1. Luminescence from AlN:Er was only seen at low temperatures. The GaN:Er on sapphire sample only luminesced when implanted with an equal profile of oxygen. This suggests that the internal quantum efficiency is increased when the Er atoms are surrounded by a strongly electronegative ligand field, shorter and more ionic Er-ligand bonds increasingly enhancing the Er^{+3} luminescence [27], hence the greater effect of O over N in the GaN. In addition, although the samples were annealed after implantation, the effects of implant induced damage would quench the Er^{+3} luminescence over a sample with equal Er content but with lower numbers of lattice defects. To remove the effects of ion damage, AlN and GaN samples grown via MOMBE by MacKenzie et al. on GaAs and sapphire were doped for the first time during growth with solid Er [64-67]. Doping the nitrides during growth allows more flexibility over implantation due to the absence of damage, unlimited layer thickness, and better control of the doping profile. In addition to TEG and DMEAA, a solid Ga source was also used. It was found that the PL from below bandgap excitation was two orders of magnitude higher for the samples doped during growth over the implanted samples. The mixed structure samples grown on GaAs had considerably weaker PL than the single crystal samples grown on sapphire, showing the significant effect of structural quality on optical activity. The thermal quenching measurements of the GaN and AlN placed them in line with the implanted samples on the quenching versus temperature plot, based on their respective bandgaps. It was found that in the case of AlN:Er on sapphire, the PL saturated at doping levels of $2x10^{19}/cm^3$. Also, rounded AlN:Er surface features began to form on the AlN:Er surface, gradually increasing in size from ~1-2 μm to ~3-5 μm. This suggests that at an Er concentration of approximately $3 \times 10^{17}/cm^3$, the AlN reached its solubility limit, with solubility effects limiting the incorporation efficiency. No such behavior was observed in GaN:Er grown on sapphire. Oxygen backgrounds of $\sim 10^{20}/cm^3$ as determined by SIMS were observed in all samples.

Further investigation into the 1.54 μm emission of GaN:Er thin films [68-70] and patterned devices [71-73] was carried out by Steckl et al. The GaN:Er films were grown by molecular beam epitaxy (MBE) on Si substrates using solid sources for Ga and Er, with the reactive nitrogen provided via an RF plasma source. While Steckl et al. have observed 1.54 μm emission from their GaN:Er material, the primary research focus is centered on the demonstration of strong green emission at 537 nm and 558 nm. These emissions have been attributed to the $^2H_{11/2} \rightarrow {}^4I_{15/2}$ and $^4S_{3/2} \rightarrow {}^4I_{15/2}$ transitions, respectively, the FWHM of the peaks being roughly 3 nm. This is the first demonstration of visible emission from an erbium doped semiconductor. The atomic Er doping level for the films was approximately $2 \times 10^{20}/cm^3$. The luminescence was investigated with above (λ=325 nm) and below (λ=488 nm) bandgap photoluminescence (PL). No green Er^{+3} transitions were observed using the 488 nm excitation, while the 325 nm produced a less intense band edge emission at 370 nm compared to the green emission. The 1.54 μm emission was observed using both excitation sources. The effect of growth condition and sample morphology on the intensity of the green emission was also investigated. It was found that the integrated PL increased as the GaN:Er growth temperature was increased from 750 °C up to a cutoff point at 950 °C, where the growth rate and emission decreased. As the temperature increased, the film surface roughness increased with no change in the green emission. From atomic force microscopy (AFM) and scanning electron microscopy (SEM), the general trend of increased surface roughness with increasing Er content is observed. It is believed the roughening is due to a non-optimized AlN buffer layer between the substrate and the GaN. From secondary ion mass spectrometry (SIMS) analysis, it was found that these samples had high levels of O ($\sim 10^{18}/\mathrm{cm}^3$) and C ($\sim 5\times10^{17}/\mathrm{cm}^3 - 5\times10^{18}/\mathrm{cm}^3$). From this work, it is not clear as to the effect of the donor nature of the O and C on the emission and morphology of these films, although they undoubtably would increase the luminescence, as seen previously [2]. The GaN:Er films were also patterned into reverse bias Schottky barrier diodes to investigate electroluminescence (EL), using indium tin oxide (ITO) as the electrode material. The major peaks at 537 nm, 558 nm, and 1.54 μm were investigated. The IR device (FWHM = 25 nm) conditions were 75 V at 19 mA, while the green device (FWHM – 6 nm) conditions were 155 V at 3.85 mA. The external quantum efficiency for the 537 nm peak was found to be 0.012 % for GaN:Er grown on Si, but 0.1 % for GaN:Er grown on sapphire. Generally, as the applied electrical power increased, the number of observable Er peaks also increased. It was found that a linear relation is maintained between the optical output and the reverse bias current (150 nW at 10 mA).

In addition to doping GaN with Er, Steckl et al. have doped with Pr to get red emission [74,75], with Eu to get red emission [76], and with Tm to get blue emission [77]. For GaN:Pr, doped to roughly $10^{20}/\mathrm{cm}^3$, red emission (FWHM = 1.2 nm) was obtained at 650 nm from the ${}^3P_0 \rightarrow {}^3F_2$ transition in Pr^{+3} with PL measurements at 325 nm and 488 nm. The PL result using the above gap 325 nm source was more intense than the below gap source. The ${}^1G_4 \rightarrow {}^3H_5$ transition at 1.3 μm was also observed, but again the research focus is on the visible emission. The 650 nm peak was also observed in an EL Scottky diode (FWHM = 7 nm) operating at 144 V at 17.3 mA. Similar results were found with GaN:Eu for the 621 nm emission due to the $^5D_0 \rightarrow {}^7F_2$ transition, with doping levels between $10^{18}/cm^3$ and $10^{21}/cm^3$. The FWHM for the 325 nm PL emission was 6 nm, and also was much more intense than the below gap measurement. Reverse bias Scottky diodes operated at 46 V at 12.5 mA producing 623 nm emission with a FWHM of 7 nm. Finally, blue emission was obtained for GaN:Tm doped between $10^{19}/cm^3$ to $10^{20}/cm^3$. Patterned EL devices operating at 116V at 1.03 mA produced 477 nm emission with a FWHM of 7.5 nm due to the $^1G_4 \rightarrow {}^3H_6$ transition in Tm^{+3}. In all three additional doping cases (Pr, Eu, Tm), each was the first application of that particular rare earth as a GaN dopant, and the first observed case of visible emission for Pr and Tm.

2.3 Codoping Effects in Rare Earth Doped Semiconductors

In Section 2.2 it was mentioned that the addition of O to the implanted GaN:Er enhanced the 1.54 μm luminescence due to the ligand producing more ionic Er-ligand bonds. Research efforts towards understanding the effects of codoping on Er^{+3} have paralleled the investigation of rare earth doping in general in semiconductors, particularly in Si and GaN.

The work of Markmann et al. [78] on the effects of codopants (C, O, F) on the 1.54 μm emission in Si:Er has found that codoping allows Er incorporation in to the Si host up to high concentrations ($\sim 10^{20}/cm^3$) without segregation or precipitation effects, and enhances the luminescence. More amorphous layers were found to have lower luminescence intensity due to the high density of defects causing shorter carrier lifetimes, and therefore less effective Er^{+3} excitation. Finally, it was found by Markmann et al. that for Er and C levels of ~$4x10^{19}/cm^3$, the improved optical activation over Si:Er is due to the increased number of C atoms surrounding Er atoms, or by higher lattice strain caused by substitutional C. It was found that for C levels above $4x10^{19}/cm^3$, the 1.54 µm PL decreases strongly. This could be caused by C-C clusters, SiC precipitates, or other C related defects enhancing nonradiative band to band recombination. The Si:Er:C was found to have larger thermal quenching compared to Si:Er:O with the same codopant level.

The research of Coffa et al. [43,79-83] has resulted in similar conclusions for the codoping of Si:Er. It was also found that codoping reduces thermal quenching, the degree of quenching being more pronounced when the codopant concentration is increased. The O was found to increase the Er solubility in Si and to prevent Er segregation during epitaxy, the Er concentration being well above the threshold for Er precipitation in non-codoped Si. Increasing the O concentration from $10^{16}/cm^3$ to $10^{18}/cm^3$ for an Er level of $10^{18}/cm^3$ produced an order of magnitude increase in the 1.54 µm emission. Further increases in the O level initially increased the luminescence, but then decreased it. As before, this decrease is attributed to defects and precipitates caused by over codoping that enhance the number of nonradiative recombination sites. It is believed there exists an optimum O concentration for a given Er concentration in order to reach the maximum PL emission intensity. Such an effect was also observed by Favennec et al. for the Si:Er system [84]. Coffa et al. observed from DLTS the formation of new Er^{+3} sites and the reduction in the number of deep level states with increased codoping levels. Decreased numbers of deep levels cause a reduction in the magnitude of competitive recombination routes for the electron/hole recombination that is believed to be a mechanism for Er^{+3} excitation. Impact excitation caused by hot carriers is also believed to contribute. The result of lower numbers of less desirable recombination sites produces an enhancement of the pumping efficiency and a reduction of thermal quenching. In regard to thermal quenching measurements, for a constant Er level of $10^{18}/cm^3$, a 30X reduction in PL was observed when going from 77K to 300K for a O level of $10^{20}/cm^3$. The reduction increased to 90X for $3x10^{19}/cm^3$ of O, 300X for $10^{18}/cm^3$ of O, and finally >300X for $10^{16}/cm^3$ of O. At this point, the 1.54 µm signal fell below the detection limit of the system being used by Coffa and his coworkers. The strong Er-O interaction (or alternatively the Er-C or Er-F interactions) allows the formation of well defined luminescent Er-O complexes, some of which introduce a level in the Si bandgap (as determined by DLTS) at 0.15 eV from the conduction band. This level was recognized as a possible pathway for energy transfer from the electronic system of the Si to the Er 4f shell. It is believed that for Si:Er, O codoping is the most efficient for producing this level, followed by C and F. The intensity enhancement may also be due to the Er-codopant complex causing promotion of Er from the +2 to the active +3 state. Coffa et al. also produced Si:Er diodes to test the effects of codoping on electroluminescence. Using a p-i-n type device, it was found that the 1.54 µm emission under reverse bias was 16X the emission for the device under forward bias. The performance of the diodes in thermal quenching measurements was also different. Between 77K and 300K, the integrated emission decreased by 4X under reverse bias, but decreased 30X under forward bias (similar to PL measurements done with above bandgap excitation). This result suggests that the above bandgap PL and the forward biased diode have the same excitation mechanism (e/h recombination), while the reverse bias data supports excitation by impact excitation. Work by Reittinger et al. confirms this result [39].

Comparable codopant effects have also been observed in III-V semiconductors. Rutter et al. observed enhanced Er incorporation and 1.54 μm luminescence from Er-O complexes in MOCVD derived GaAs:Er [85]. MacKenzie et al. observed an increase in 1.54 μm emission from GaN of two orders of magnitude over a non-codoped sample [67]. This codoped sample had C and O backgrounds of $10^{21}/cm^3$ and $10^{20}/cm^3$, respectively, compared to the non-codoped sample where C and O concentrations were less than $10^{19}/cm^3$. The Er level in both instances was $\sim 3x10^{18}/cm^3$. Effects were also observed by MacKenzie et al. in regards to 1.54 μm thermal quenching behavior. The codoped sample quenched by 40% between 15 K and 300 K, while the non-codoped sample quenched by 85%. Finally, Torvik et al. have observed codopant effects under electroluminescence and cathodoluminescence. [86-88]. The GaN films coimplanted with Er ($10^{14}/cm^3$) and O ($10^{16}/cm^3$) was found to thermally quench under CL by only 5% from 6K to room temperature. Under below bandgap excitation at 983 nm from an InGaAs diode laser, it was found that there was a 20X increase in integrated PL intensity with the presence of a 10:1 O to Er ratio, over non-codoped GaN:Er. Torvik et al. also produced Er and O coimplanted m-i-n diodes to test codopant effects under electroluminescence. The devices were implanted with $10^{16}/cm^3$ O and $10^{15}/cm^3$ Er. The O codoping also increased the Er^{+3} luminescence by 20X over the non-codoped device when the diode was operated under reverse bias. No 1.54 μm emission was observed when operated under forward bias.

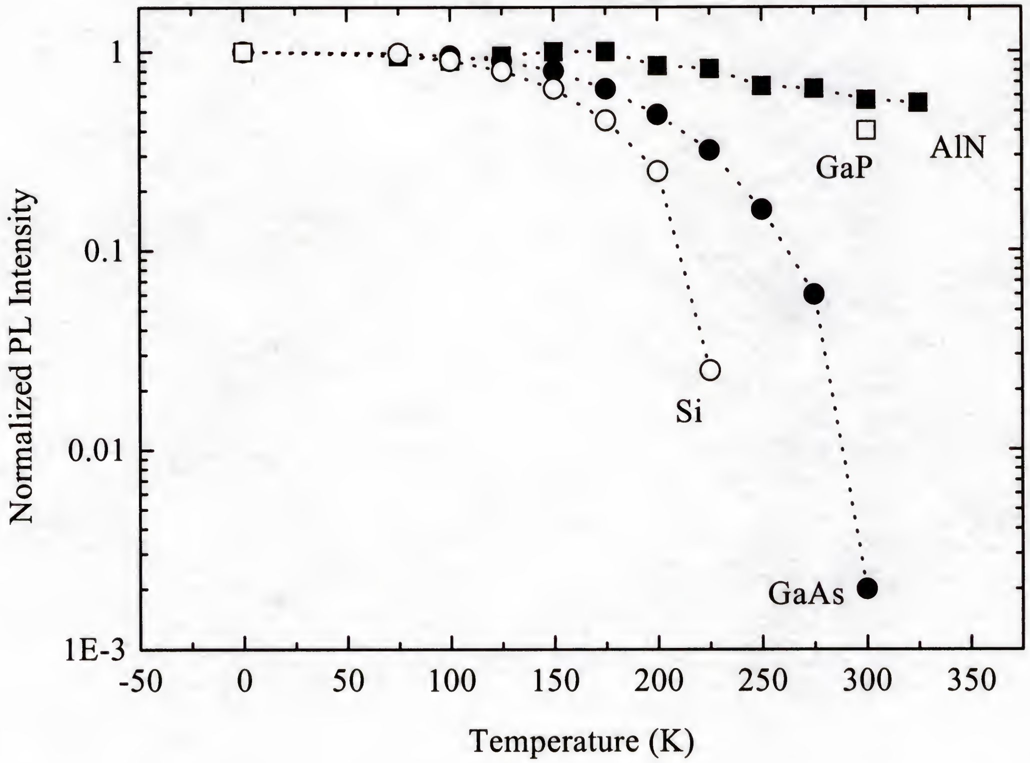

Figure 2-1: Normalized photoluminescence versus measurement temperature in degrees Kelvin for Er in various semiconductor matrices.

CHAPTER 3
REVIEW OF DILUTE MAGNETIC SEMICONDUCTOR MATERIALS

3.1 Theories of Dilute Magnetic Semiconductor Ferromagnetism

In Chapter 1, the use of dilute magnetic semiconductors (DMS), semiconductors alloyed with magnetic ions, were discussed in regard to the suitability of such a material in a spintronic device. If such a material could be spontaneously magnetic, i.e. ferromagnetic, the application of an external magnetic field would not be required for spin injection, as in the spin-LED. Recently, several theories have been advanced that serve to explain the origin and predict the properties of DMS materials. The highlights of these models will be discussed qualitatively in this Section.

The principal theory that explains the origin of DMS ferromagnetism, as well as the one that has received the most attention, was advanced by Tomasz Dietl and his coworkers [89-91]. This theory revolves around the action of a cluster of Mn ions within the semiconductor called a bound magnetic polaron (BMP). A drawing of a BMP is given in Figure 3-1. A BMP is initially formed by a few Mn ions in close proximity with randomly aligned magnetic moments, as well as a charge carrier (electron or hole) that is local to this cluster. The charge carrier's own moment is also randomly oriented (Figure 3-1, left). However, if the charge carrier becomes ferromagnetically coupled to a Mn ion, i.e. there is an interaction between them that favors a parallel alignment of their moments, then it will become energetically favorable for all the Mn ions in this cluster to also align parallel with each other. When this occurs, there will be a "sphere" or "cloud" of polarized Mn ions about the charge carrier (Figure 3-1, right). This "sphere" is the BMP. Due to the parallel alignment, the charge carrier becomes localized to the polaron, effectively becoming trapped inside. Dietl's theory then postulates that the ferromagnetism is due to an exchange interaction or communication between these BMPs based on the RKKY mechanism [92]. The RKKY mechanism infers that the exchange between the magnetic polarons is mediated by free carriers within the material. In RKKY, the free carriers closest to the BMP have their spins polarized in the same direction. However, after a short distance, the magnetic energy due to the aligned free carrier moments will become large, so the next few free carrier spins will align antiparallel, to lower the system energy. But then these spins will overcompensate slightly, so the next few will again align antiparallel, etc. This alternation of the carrier spins is shown in Figure 3-2 about a BMP. As the distance increases from the BMP, the numbers of spins that align parallel/antiparallel to the BMP decay quickly. The collective ferromagnetism results if two BMPs come close together. If two polarons with separated moments approach each other so that their respective parallel regions of aligned free carriers overlap, then an exchange interaction will develop between the two BMPs, locking their moments together in parallel. If this occurs over the scale of a whole layer, then collective ferromagnetism will result (Figure 3-2, top). However, a similar effect can result in antiferromagnetism amongst the BMPs (Figure 3-2, bottom). This effect can be looked at in a similar way using Figure 3-3, which is a curve showing the RKKY induced magnetization versus distance. This plot describes a situation where the first polaron is at $2k_Fr = 0$, k_F being the wavevector on the Fermi sphere. Regions on the curve where M is positive correspond to spins parallel to the polaron, so if a second polaron is located at a distance away from the first corresponding to positive M, ferromagnetism will result (Figure 3-2, top). If the second polaron is located at a distance away corresponding to negative M, antiferromagnetism will result (Figure 3-2, bottom). Therefore, if the second polaron is located where $0 \leq 2k_Fr \leq 2$ or $4 \leq 2k_Fr \leq 5$, the material will be ferromagnetic. The first region is physically very short, on the order of an atomic radius. If calculated on a concentration basis, the semiconductor must be doped with roughly 5 % Mn, for the second polaron to sit between 4 and 5

Based on this model, Dietl and his coworkers have developed an equation to predict the Curie temperature of DMS materials:

$$T_{Curie} = \frac{x_{eff} N_0 S(S+1) \beta^2 A_F \rho_S \left|\Psi\right|^2}{12 k_B} - T_{AF} \qquad (3.1).$$

In this equation, $x_{eff}N_0$ represents the concentration of Mn, S represents the Mn spin, β represents the strength of the Mn-carrier interaction, ρ is proportional to the effective mass of the exchange carriers, Ψ represents the physical confinement of the BMP-charge carrier system, T_{AF} takes into account possible antiferromagnetic effects, and k_B and A_F are constants. From this equation, the Curie temperatures of many of the III-V semiconductors have been calculated for 5 % Mn and a hole concentration of $3.5 \times 10^{20}/\text{cm}^3$. These are given in Figure 3-4. Note that the T_{Curie} for GaN is predicted to be well above room temperature. In this model, the presence of holes serving as the charge carriers is an important factor, as the effective mass and β for holes is much larger than for electrons. Although an electron-mediated BMP exchange will produce ferromagnetism, the value for T_{Curie} is extremely small, approximately 0.6 K compared to

10 K for the case of CdMnTe [91]. The Dietl theory also discriminates between II-VI and III-V semiconductors. It was calculated that in a II-VI host, the BMP is much larger than in a II-V. The larger size increases the probability of antiferromagnetic interactions at the periphery of the polaron. As a result, $(x_{eff}N_0)_{II\text{-}VI} < (x_{eff}N_0)_{III\text{-}V}$, and $(T_{AF})_{II\text{-}VI}$ is finite whereas $(T_{AF})_{III\text{-}V} \approx 0$, so the Curie temperatures expected in II-VI semiconductors should be smaller than in III-Vs. Through the parameter Ψ, it is also expected that as dimensions shrink (as in a quantum well or dot), T_{Curie} will increase. Further refinements to particular aspects of this theory have been reviewed in the literature [93,94].

The second major theory of DMS ferromagnetism calculates the expected Curie temperatures in a variety of quantum well geometries [95]. This much more complex model performs a series of more refined calculations by incorporating more sophisticated spin and charge interactions. Although based on a different approximation than the Dietl theory, it produces comparable results. The final theory examines the predicted Curie temperatures for electron and hole mediated exchange in a variety of semiconductor hosts with a variety of transition metal dopants [96].

3.2 Review of Transition Metal Doping in Semiconductor Host Materials

Research in the area of transition metal doped semiconductor materials has been investigated for many years. However, much of this work predates the concept of dilute magnetism, especially in regard to the use of Mn as the magnetic dopant. As such, much of the material doped with Mn in the literature was not measured magnetically. The primary goal at the time was to use Mn as a p-type dopant for III-V semiconductors, due to its position in the group II column of the periodic table. The following subsections review the transition metal doping of semiconductors. The information in Table 3-1 summarizes this review, giving the predicted Curie temperature (T_{Curie}) that was calculated to date (as per Section 3.1), the highest T_{Curie} measured to date, the Mn range investigated to date, the hole concentration measured to date, and the bandgap energy, for the majority of the semiconducting materials. In addition, the information in Table 3-2 outlines the Curie temperatures for many of the alternate phases found in Mn-doped III-V materials. This information will become more relevant later in this Section.

3.2.1 Manganese in Group IV Materials

The growth of Ge doped with Mn to date has yet to produce what could be classified purely as dilute magnetic behavior. Epitaxy of Ge with Mn, or the solid state reaction of thin Mn/Ge multilayers is dominated by the formation of intermediate Mn_xGe_y compounds. By multilayer reaction, hexagonal Mn_5Ge_3 was formed, having a ferrimagnetic T_{Curie} of approximately 304 K [97,98]. The amorphous spin glasses Mn_3Ge_2 and MnGe have been formed with spin transition temperatures of 53 K and 48 K respectively [99]. The $Mn_{11}Ge_8$ phase has also been produced using MBE, and was found to have a T_{Curie} of 300 K [100]. However, it has also been found that by adding C during growth, producing $Mn_5Ge_3C_x$, Curie temperatures as high as 445 K can result.

Due to their chemical similarity, Si doped with Mn produces magnetic behavior comparable to Ge:Mn. The crystalline MnSi phase has a T_{Curie} of 30 K, close to that of MnGe [101]. Heavily doped Si:Mn films prepared by laser ablation have resulted in Mn concentrations as high as 18 %. The 5 % required by theory is then perfectly feasible [102]. As with $Mn_5Ge_3C_x$, doping Mn_5Si_3 with C to produce $Mn_5Si_3C_x$ can result in significantly elevated Curie temperatures. For $x_C = 0.22$, a T_{Curie} of 152 K was demonstrated, while raising x_C to 0.75 increases T_{Curie} to 350 K [103,104]. However, no experimental evidence exists thus far for 5 % Mn in Si, thus no conclusions can yet be drawn regarding the accuracy of current DMS theories for Group IV materials..

3.2.2 Manganese in Group III-Arsenide Materials

The first III-V material to be specifically investigated for DMS-based ferromagnetism was $In_{1-x}Mn_xAs$, which has also been the most heavily investigated DMS material [105-117]. Normally, InAs grown by MBE is performed at a substrate temperature of approximately 430 °C. In the first investigation of InMnAs, it was found that at these temperatures only Mn levels between 10^{18}-$10^{19}/cm^3$ could be incorporated without surface segregation or phase separation of the Mn species [108]. This is considerably less than the 5 % (x = 0.05) required by theory. MBE at lower growth temperatures was then employed as a way to incorporate more of the Mn into the InAs. However, the temperature should not be dropped below the point where single crystal InMnAs (as evidenced by a streaky 2D RHEED pattern) will result. The majority of the InMnAs films have been grown on either (100) InAs or GaAs substrates, on which either an InAs or GaAs buffer layer was grown by MBE at normal growth temperatures. The upper and lower bounds for the successful growth of InMnAs layers were quickly determined [108,116]. If the growth temperature is higher than 375 °C, it was found that all of the Mn incorporates as the metallic phase MnAs, regardless of the Mn level. As the MnAs is magnetic (Table 3-2), this phase readily appears in magnetometry measurements of the InMnAs with its characteristically high T_{Curie}. Below 175 °C, InAs cannot be grown as a single crystal. Therefore, in order to grow InMnAs that is a single crystal and is free of MnAs particles, T_{growth} must be between 175 °C and 375 °C. In this temperature region, Mn levels between 0.4 % and 18 % have been incorporated while maintaining a good (1 X 2) reconstruction on the InMnAs surface which is indicative of good crystal quality [105-116]. Once incorporated into the semiconductor lattice, the Mn ions are also supposed to act as electrical dopants, providing free holes to mediate the ferromagnetism. If the growth temperature is between 175 °C and 275 °C, the InMnAs produced is n-type regardless of Mn level, and only displays paramagnetic properties when measured magnetically [108,116]. This suggests that the majority of the Mn is not becoming electrically active. When the growth temperature is increased to between 275 °C and 375 °C, the Mn becomes electrically active, producing p-InMnAs, with typical hole concentrations between of 2-3.8x10^{19}/cm^3 [105,106,109]. In this region, ferromagnetic behavior was observed in $In_{0.987}Mn_{0.013}As$, as manifested by hysteresis in the Hall resistance and in magnetization (M) versus temperature (T) data [105]. From the M vs. T data, a T_{Curie} of 7.5 K was determined. In other material, large values of the anomalous Hall effect have been measured, also indicating ferromagnetism [106,115]. The anomalous Hall effect was not observed in n-type material with an identical concentration of Mn, indicating the importance of holes in the overall magnetic process [115]. In the InMnAs, it was found that the easy direction for magnetic measurements is perpendicular to the sample plane [111]. For $In_{0.93}Mn_{0.07}As$ grown at a temperature of 275 °C, ferromagnetism resulted with a measured T_{Curie} between 30-35 K, which is the highest recorded temperature to date in this semiconductor [111]. Further work has indicated that although InMnAs grown between 275 °C and 375 °C is p-type, it contains particles of the MnAs phase if the Mn level is greater than 2.6 % [116]. Therefore, the actual DMS material will be produced only if the Mn level is less than 2.6 %. The 5 % required by theory to produce the T_{Curie} in Table 3-1 appears to be out of reach. No work has been done to date with Mn levels in this range with hole concentrations higher than $3.8 \times 10^{19}/\text{cm}^3$, so it remains to be seen if the T_{Curie} can approach that which is theoretically predicted.

The DMS $Ga_{1-x}Mn_xAs$ is the second main III-V based material to be investigated, and has shown the highest measured III-V T_{Curie} to date [118-129]. As with InMnAs, it was found that low temperature MBE of GaMnAs is required to incorporate the necessary amounts of Mn while avoiding the formation of MnAs second phases. GaAs is typically grown at a temperature of 600 °C. It was found experimentally that GaMnAs grown with a Mn concentration greater than 8 % or at temperatures higher than 300 °C will produce MnAs phases [120]. In terms of a lower limit for growth, it was found that polycrystalline material will result for T_{growth} lower than 140 °C and 3D growth, as determined by spotty RHEED patterns, will result for temperatures less than 160 °C, regardless of the Mn level [129]. Between 160 °C and 300 °C, single crystal GaMnAs layers will be grown with (1 X 2) reconstruction [119]. The GaMnAs is typically grown on semi-insulating (001) GaAs substrates, with a buffer layer of GaAs grown at $T_{\text{growth}} =$ 580 °C preceding the GaMnAs layer. GaMnAs layers grown at a temperature of 250 °C have been shown to have hole concentrations between 10^{18}-$10^{20}/\text{cm}^3$, with Mn levels up to 8 % [119]. In this material, T_{Curie} as high as 110 K was observed, close to what is predicted theoretically. SQUID magnetometry measurements of these materials have shown hysteresis in M vs. H with saturation magnetizations (M_s) as high as 33 emu/cm^3, and large negative magnetoresistance [124,125]. The easy direction is found to be parallel to the sample plane. For a given concentration of Mn, it was found that the GaMnAs will undergo a paramagnetic to ferromagnetic transition with increasing T_{Curie} as the growth temperature is increased [119]. This indicates an increase in the concentration of free holes within the material, and the overall importance of the holes in the carrier mediated Mn-Mn exchange interaction.

AlMnAs was grown epitaxially using vapor phase epitaxy (VPE) and liquid phase epitaxy (LPE) [130,131]. Due to its low growth temperature, Mn was incorporated into the AlAs up to its solubility limit with the LPE approach. Due to the high growth temperatures used during the VPE approach (1000 °C – 1100 °C), no Mn was found to incorporate into the AlMnAs substitutionally. Instead, it was found that at these temperatures all the Mn was incorporated by forming the Mn_2As phase, a similar effect as to what was observed when growing InMnAs and GaMnAs at too high a growth temperature.

3.2.3 Manganese in Group III-Antimonide Materials

The synthesis of InMnSb initially was driven by its potential use in thermoresistors at ultra low temperatures (mK). In all known cases, InMnSb was exclusively produced using the Czochralski (CZ) bulk growth technique. Mn levels between $10^{12}/cm^3$ and $10^{18}/cm^3$ have been reported, with hole concentrations ranging from $3x10^{17}/cm^3$ to $3x10^{18}/cm^3$ [132-138]. An InMnSb sample grown with a Mn concentration of $1x10^{17}/cm^3$ and the same hole concentration (as determined via Hall measurements) was shown to have negative magnetoresistance at a temperature of 80 mK [132]. Independent experiments producing a hole concentration between $3x10^{17}/cm^3$ and $1.3x10^{18}/cm^3$ showing negative magnetoresistance produced calculated Curie temperatures of approximately 0 K, as extrapolated from magnetic susceptibility data

[134]. Early in the course of this work, it was believed that the RKKY mechanism was at play as the exchange mechanism between the Mn atoms [135-139].

Development of GaMnSb constitutes the third main semiconductor to appear in the literature chronologically and in regard to the amount of published material. Early work with this semiconductor centered on its production using the bulk Bridgman and CZ techniques [140-146]. Due to the nature of the method used, Mn could only be incorporated up to the solubility limit of ~$10^{18}/cm^3$. GaMnSb is seen as being advantageous in regard to its electrical properties; undoped GaSb is nominally p-type on the order of $10^{17}/cm^3$. This allows Mn to be incorporated and immediately raise the concentration of holes, without having to first compensate donor sites, as is common with many III-V semiconductors. Interest in GaMnSb was renewed in light of its predicted ferromagnetism, and has recently been grown epitaxially using MBE [147-149]. The normal T_{growth} for epitaxial GaSb is approximately 560 °C. As with InMnAs and GaMnAs, low temperature MBE growth is used to overcome the solubility limit of Mn in GaSb and to prevent surface segregation or second phases. It was observed that GaMnSb layers grown between 550 °C and 570 °C produce a complete phase separation of GaSb and MnSb, the MnSb clusters being observed by Atomic Force Microscopy (AFM) measurements of the surface. Magnetic measurements on this material indicate ferromagnetic order with a measured moment of 3.5 μ_B per Mn atom, and a T_{Curie} of 585 K, which matches that of pure MnSb, as given in Table 3-2. By lowering the T_{growth} to 250 °C, GaMnSb was produced with $x = 0.023$ and a hole concentration of $1.3x10^{20}/cm^3$. A (1 X 3) reconstruction was maintained throughout the growth, indicating the lack of obvious second phases within the material. When measured magnetically, this material showed negative magnetoresistance below 50 K, anomalous Hall behavior, and hysteresis in M vs. H, believed to be originating from the GaMnSb. Evaluations from Arrott plots (M^2 vs. B/M) indicate a $T_{Curie} = 25$ K for the GaMnSb [147-149]. However, magnetic hysteresis was still observed at 300 K, indicating the presence of MnSb particles within the GaMnSb [147].

Work on Mn doping of AlSb was limited to the growth of AlMnSb with the vacuum enclosed CZ technique [150]. The equilibrium growth of AlMnSb produced a Mn concentration of $5x10^{18}/cm^3$ within the material, while Hall measurements indicate a concentration of $6x10^{17}/cm^3$. The sample was p-type with a hole concentration of $2.7x10^{16}/cm^3$. Undoped AlSb grown utilizing the same method was p-type with a hole concentration of $1.8x10^{17}/cm^3$. The increase in hole concentration with Mn doping verifies the empirical observation that Mn should act as an acceptor within a III-V semiconductor.

3.2.4 Manganese in Group III-Nitride Materials

Work on AlMnN has centered entirely on material preparation and optical characterization. AlMnN was prepared in a powder form by the pyrolysis of hexafluoaluminate in an ammonia atmosphere utilizing $MnCl_2$ as the Mn source [151]. AlMnN was also prepared by diffusing Mn into AlN powders, by RF sputtering, or by MOCVD growth [152,153]. The MOCVD process used ammonia and trimethylaluminum reacting on Si substrates with manganese decacarbonyl ($[Mn(CO)_5]_2$) as the Mn source. The powder samples were found to contain 0.01 – 1.0 at % Mn, the MOCVD samples < 0.01 % Mn, and the sputtered samples 0.5 % to 4.0 % Mn.

Luminescence measurements of the powder samples show an orange band at 600 nm and a green band at 515 nm, attributed to Mn^{+4} and Mn^{+2} centers respectively.

Due to the projected T_{Curie} of 414 K for the ideally prepared GaMnN material, research in this area has increased significantly in recent years. As with AlMnN, GaMnN to date was prepared in a powder form. The crystal growth technique involves the nitridation of pure metallic Ga in highly chemically active supercritical ammonia, in a special autoclave at a low growth temperature (550 °C) and a high pressure (5 kbar) [154]. The GaMnN crystals come out in the form of microcrystalline, regular grains with a pink color, the range of Mn levels being between 0.01 and 0.2 %. X-ray diffraction of the powder samples show peaks attributable to the GaN and the Mn_3N_2 phases. Micro-Raman spectroscopy also shows peaks over that found normally in GaN [155]. These peaks are assigned to disorder states caused by the high concentration of Mn, and are believed to be a characteristic property of GaMnN crystals. Magnetization data shows a combination of paramagnetism and ferromagnetism at low T. The paramagnetism is to be expected in a system of localized magnetic moments. By separating out the paramagnetic component, the data can be evaluated to determine S, the spin state of the Mn. Analysis shows a good fit for $S = 5/2$, indicating that much of the Mn is incorporated substitutionally in the GaMnN. The $S = 5/2$ result was also confirmed with independent electron spin resonance studies [154]. The observed second phase Mn_3N_2 is also believed to contribute to the magnetization, as it is a known antiferromagnet. The $S = 5/2$ measurement, corresponding to a moment of 5 μ_B is contrasted by recent theoretical models for Mn in zincblende GaN, indicating a maximum possible moment of 3.3 μ_B [156-157].

3.2.5 Manganese in Group III-Phosphide Materials

InMnP was investigated to a limited extent as a material for magneto-optical applications. InMnP grown by LPE on (100) InP was shown to produce Mn levels as high as $1.3\text{x}10^{20}/\text{cm}^3$ [158]. However, this material was also found to be semi-insulating. By lowering the Mn concentration to $5\text{x}10^{16}/\text{cm}^3$, also using LPE, p-InMnP was produced with a hole concentration of $4.7\text{x}10^{16}/\text{cm}^3$ [159]. However, none of this material was measured magnetically. Using an intermediate Mn level of $8\text{x}10^{18}/\text{cm}^3$, Curie-Weiss behavior was observed with a T_{Curie} of 0.5 K. At the time, this phenomena was explained to be due to the presence of ferromagnetic spin clusters.

Experiments with GaMnP to date have mainly investigated the valence state of Mn within GaP. From positron annihilation experiments, it was found in CZ grown GaMnP that the Mn is in the +2 state [161]. The Mn was incorporated at the solubility limit of $3\text{x}10^{19}/\text{cm}^3$, while the actual concentrations ranged from $1.8\text{x}10^{18}/\text{cm}^3$ to $1.2\text{x}10^{19}/\text{cm}^3$. The material was also found to be p-type between $4.3\text{x}10^{18}/\text{cm}^3$ and $1.6\text{x}10^{19}/\text{cm}^3$. The Mn was also determined to be acting as a deep acceptor in GaP with an energy level of $E_{\text{valence}} + 0.4$ eV. No magnetic measurements were performed. Other studies confirmed the +2 valence state, utilizing liquid encapsulated CZ material [162,163].

3.2.6 Manganese in II-VI Semiconductors

In addition to investigating the possible ferromagnetism in Mn-doped III-V semiconductors, a significant research effort was directed towards II-VI semiconductors. Although DMS theory predicts lower overall Curie Temperatures for II-VI materials, they have several advantages that III-V semiconductors do not. In both cases, the Mn atoms are required to be in the +2 state. For the II-VI materials, when Mn substitutes in the related sublattice, it does not contribute electrically to the semiconductor, as in a III-V. Therefore, the charge and spin dopants can be controlled independently, allowing theoretical predictions to possibly be checked systematically, without one influencing the other. Spin-carrier and spin-spin exchange mechanisms are also well documented in II-VI semiconductors, less so in III-Vs. Finally, as the Mn will substitute with greater ease on the group II sublattice, doping on the order of 5 % while avoiding the formation of Mn-VI second phases is less of an issue.

Since thus far theory predicts $Zn_{1-x}Mn_xO$ to be the only other DMS with a Curie point above room temperature (so far), research with this material is beginning to increase. ZnMnO was produced by pulsed laser deposition (PLD) with up to 35 % Mn on sapphire substrates at a T_{growth} of 600 °C [164,165]. However, electrically doping ZnO with holes is the major setback. By doping with Al, the material was made n-type up to $10^{20}/cm^3$. According to DMS theory, ferromagnetism is still possible, although with a very low T_{Curie}. For material with x = 0.19 Mn, a Curie point was measured to be 13 K, although this material was a spin glass. Positive magnetoresistance was measured at low fields, while negative magnetoresistance was measured at high fields.

The study of DMS ferromagnetism has been more successful with ZnMnTe. ZnMnTe layers have been grown by the Bridgman method and by MBE [166-168]. MBE grown layers with 1.9 % to 5.5 % Mn have been produced. This material was doped p-type using N from an atomic plasma source to produce hole densities between $10^{19}/cm^3$ and $10^{20}/cm^3$. In undoped layers with $x_{Mn} = 0.04$, an antiferromagnetic phase resulted with $T_{AF} = 2$ K. By successfully increasing the hole concentration from

$8x10^{17}/cm^3$ to $1.2x10^{20}/cm^3$, ferromagnetic material was produced with an increasing T_{Curie}. The maximum T_{Curie} measured was 2.4 K. Negative magnetoresistance was also measured. Since the behavior of the undoped versus doped material produces antiferromagnetic versus ferromagnetic behavior, this is seen as being direct evidence that the ferromagnetism is hole induced, as stipulated by theory.

The last II-VI DMS material studied to date is CdMnTe. CdMnTe research provides another opportunity to study another aspect of the current theory [169-172]. Experimentally, it was found that unlike ZnMnTe, CdMnTe cannot be doped p-type, even when using a nitrogen plasma. One of the parameters within equation 3-1 regards the confinement of the magnetic ion/charge carrier system. The larger the degree of confinement, the higher the T_{Curie} should become. Therefore, CdMnTe research has involved the fabrication of quantum well and superlattice structures, specifically CdMnTe layers between CdMgZnTe barriers grown by MBE. The CdMnTe layers have been doped p-type using atomic N to a hole concentration of $3x10^{17}/cm^3$. The higher bandgap of the CdMgZnTe:N clad layers causes the holes to drift into the CdMnTe quantum well, where a 2D hole gas is produced. The exchange interaction between the Mn ions can now be mediated via the holes, producing ferromagnetism. By increasing the N doping level in the clad layers, the density of the hole gas can be increased, increasing the T_{Curie} for a given Mn level. Using this method, Curie temperatures as high as 2.5 K have been observed.

3.2.7 Other DMS Semiconductors

DMS ferromagnetism has also been observed in the III-VI semiconductors GaMnS (T_{Curie} (max) = 10.9 K) and GaMnSe (T_{Curie} (max) = 160 K), and the IV-VI semiconductors GeMnTe, HgMnTe, SnMnTe (T_{Curie} (max) = 15.5 K), and PbSnMnTe (T_{Curie} (max) = 4.1 K) [173-176]. These materials have been grown using the bulk Bridgman technique with ~5 % Mn and hole concentrations ~$10^{20}/cm^3$.

Finally, in terms of using Mn as the preferred magnetic dopant, research with the II-IV-V_2 type chalcopyrite semiconductor $Cd_{1-x}Mn_xGeP_2$ has shown the highest recorded T_{Curie} to date [177]. As with the II-VI materials, Mn^{+2} can be easily substituted into the chalcopyrite structure on the group II site without upsetting electrical neutrality. If Mn occupies a group IV site, it will act as a source of holes to mediate the Mn-Mn exchange interaction. The DMS was prepared by depositing an Mn layer via MBE onto a single crystal of $CdGeP_2$, and then annealing at high temperature under vacuum. In this way, Mn levels as high as x = 0.1 were produced in the material. Magnetic hysteresis in this material was observed at 300 K, indicating that the T_{Curie} is at least that high, although the exact figure has yet to be determined [177].

Other DMS materials have also been produced using other transition metals as the source of the magnetic ions. This includes MBE-derived GaFeN, Bridgman-derived GaFeSb, powder-based CdCoSe and CdFeSe, and PLD-derived $TiCoO_2$ [178-181]. While only paramagnetism was observed in the CdCoSe and CdFeSe powders, ferromagnetic ordering was observed in the GaFeN ($T_{Curie} \leq 100$ K) and in the $TiCoO_2$ ($T_{Curie} \geq 400$ K). However, at this time, due to the large magnetic moments of Fe and Co, it is not known if the observed hysteresis in the M vs. H measurements are due to dilute magnetic behavior or superparamagnetism. These materials continue to be investigated by high resolution transmission electron microscopy (HRTEM) to search for clusters of Fe or Co, so the possibility of superparamagnetism can be either be proved or discounted.

Table 3-1: Summary of theoretical and experimental results for Mn-based DMS materials [97-181].

Host Material	Predicted T_{Curie} (K)	Highest T_{Curie} to date (K)	Range of Mn Reported (x)	Reported p range (cm^{-3})	Eg w/o Mn (eV)
Si	136	38 (MnSi)	-	-	1.12
Ge	74	304 (Mn_5Ge_3)	-	-	0.66
InP	63	0.5	0.0001 - 0.003	$4.7x10^{16}$	1.35
GaP	100	-	< 0.00024	$4.3x10^{18}$-$1.6x10^{19}$	2.26
AlP	233	-	-	-	2.45
InAs	46	35	0.004 – 0.15	$2x10^{19}$-$3.8x10^{19}$	0.36
GaAs	117	110	< 0.08	$4x10^{17}$-$3x10^{20}$	1.42
AlAs	141	-	< 0.45	-	2.16
InN	304	-	-	-	1.89
GaN	414	-	0.001 – 0.02	-	3.36
AlN	-	-	0.00005 - .04	-	6.2
InSb	-	0	< 0.00003	$3x10^{17}$-$3x10^{18}$	0.17
GaSb	43	25	0.000002 - 0.6	$2.45x10^{17}$-$8x10^{20}$	0.72
AlSb	-	-	< 0.0003	$2.7x10^{16}$	1.58
ZnO	341	13 (n-type)	< 0.36	$3.1x10^{19}$-10^{20} (n)	3.35
ZnSe	76	-	-	-	2.71
ZnTe	33	2.4	0.019 – 0.055	$8x10^{17}$-$1.2x10^{20}$	2.39
ZnS	192	-	-	-	3.68
CdS	200	-	-	-	2.42
CdSe	79	-	-	-	1.70
CdTe	29	2.5	0.024 - 0.20	$3.3x10^{19}$	1.56
SnTe	-	15.5	< 0.10	$5x10^{20}$-$2.3x10^{21}$	-
GaSe	-	160 (AF)	0.012	-	-
GaS	-	-	0.066	-	-
PbSnTe	-	4.1	0.03	$1x10^{20}$–$1.4x10^{21}$	-

Table 3-2: T_{Curie} of the metallic second phases found in Mn-based DMS materials.

Phase	T_{Curie} (K)
MnAs	310
Mn_2As	290
MnSb	587
Mn_2Sb	150
MnGa	> 300
Mn_4N	745
Mn_2N_x (0.8 < x < 1.06)	$300 < T_{Curie} < 360$
MnP	291

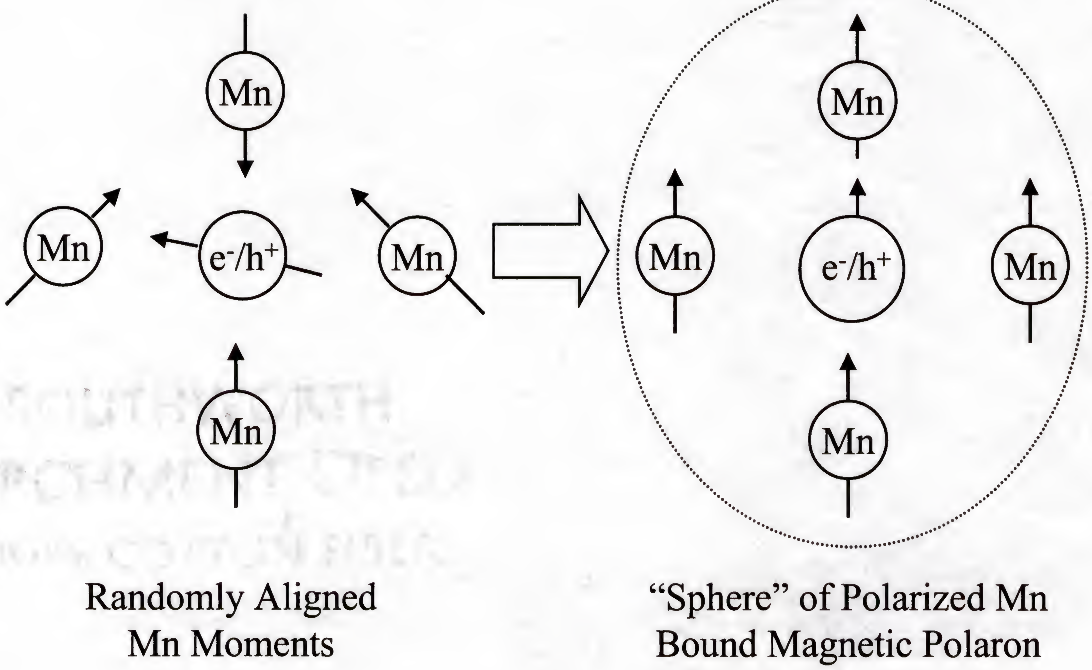
Mn
Mn
e-/h+
Mn
Mn
Randomly Aligned Mn Moments
Mn
Mn
e-/h+
Mn
Mn
"Sphere" of Polarized Mn Bound Magnetic Polaron

Figure 3-1: A Bound Magnetic Polaron (BMP) consisting of four Mn atoms.

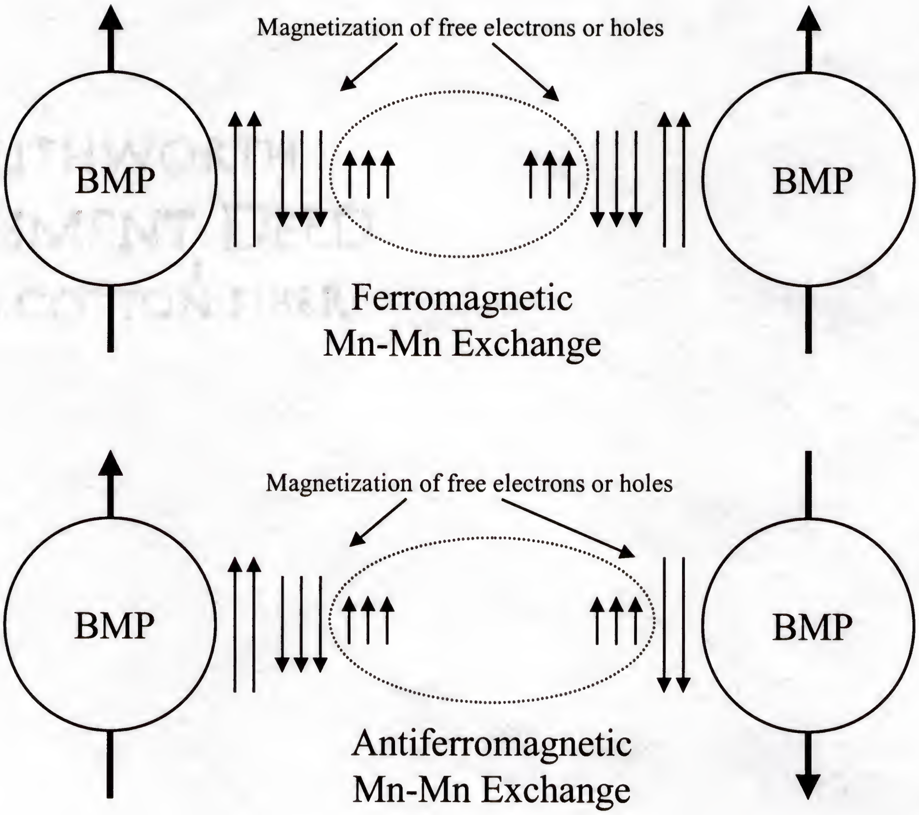
Magnetization of free electrons or holes
BMP
BMP
Ferromagnetic
Mn-Mn Exchange
Magnetization of free electrons or holes
BMP
BMP
Antiferromagnetic
Mn-Mn Exchange

Figure 3-2: Interactions involving the RKKY mechanism to produce either ferromagnetic exchange or antiferromagnetic exchange between two Mn bound magnetic polarons.

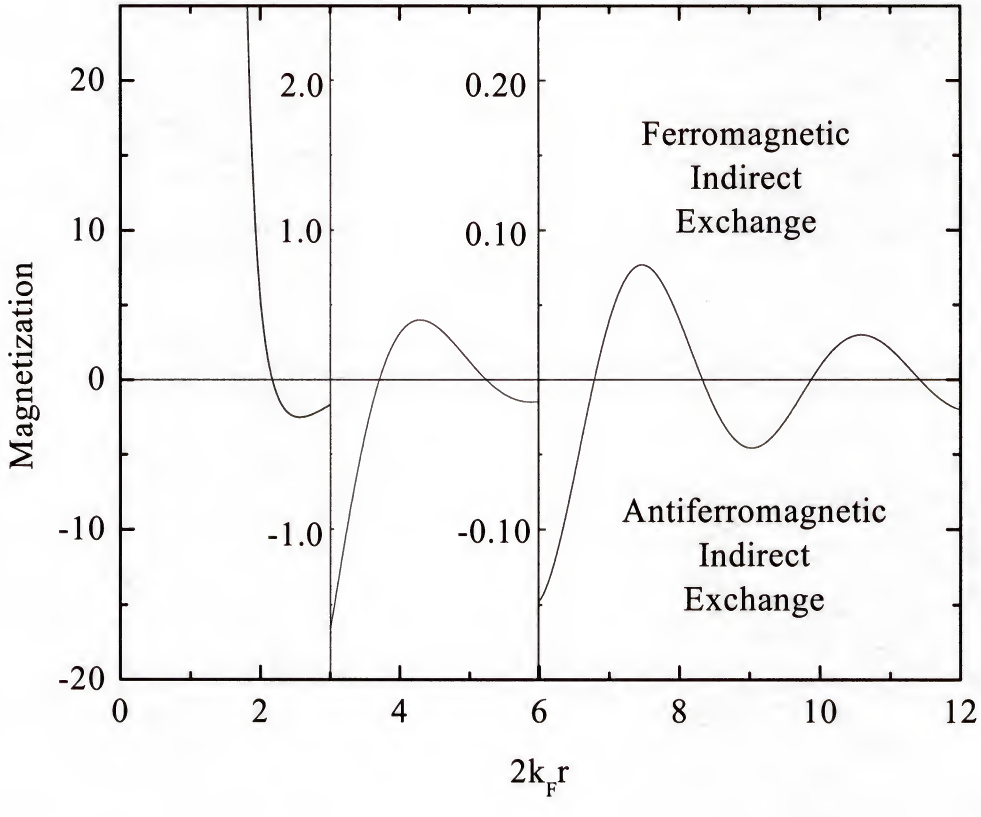

Figure 3-3: The RKKY mechanism indicating carrier magnetization versus distance from the bound magnetic polaron [92].

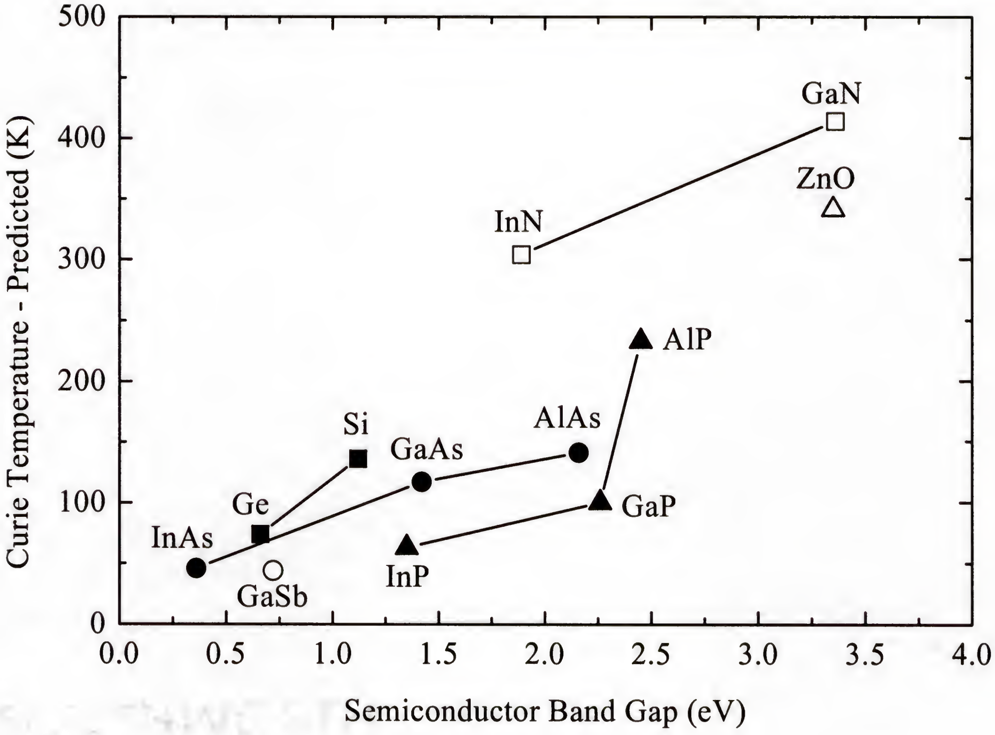

Figure 3-4: Predicted Curie temperatures for the III-V semiconductors with 5 % Mn and a hole concentration of $3.5x10^{20}/cm^3$.

CHAPTER 4
EPITAXIAL GROWTH WITH THE MOMBE TECHNIQUE

Currently, the two main techniques used in the epitaxial growth of compound semiconductor materials are molecular beam epitaxy (MBE) and metalorganic chemical vapor deposition (MOCVD). Both techniques possess unique advantages and disadvantages for film preparation. While MBE is characterized by its thickness control, uniformity, purity, and the crystallinity of the material it produces, it has a disadvantage in its low throughput and the necessity of breaking the system vacuum to replenish its source material. This can be dangerous if highly toxic materials are routinely used. MOCVD is advantageous as its throughput is high and its source materials are external to the growth chamber, enabling quick change-out and low downtime. However, its thickness and purity control can be problematic. The metalorganic molecular beam epitaxy (MOMBE) technique is a hybrid of the two techniques, and can offer good uniformity and thickness control, while having lower downtimes due to its use of external, MOCVD-style source material.

4.1 System Geometry

The MOMBE growth performed in this dissertation was done in a Varian Intevac Modular Gen II system. This system is shown schematically in Figure 4-1. The three separate zones of this system are the main growth chamber (shown in the figure), the loadlock (for sample introduction), and the conjoining buffer chamber. A tracked trolley system is used to shuttle samples back and forth between the buffer and the load lock, while a transfer arm with a three pin locking mechanism is used to transfer samples between the buffer and the growth chamber. Two gate valves separate the three sections. The main chamber is pumped to high vacuum (~ 10^{-8} torr) using a 2200 L/s turbo pump and a CTI-8 cryogenic pump. The buffer chamber is pumped to high vacuum using an ion pump, while the loadlock is pumped to high vacuum using a CTI-100 cryogenic pump. Further pumping of the growth chamber (during a growth run) is provided by an extensive LN_2 cryoshroud within the growth chamber. This cryoshroud also provides cooling for the system effusion ovens. Attached to the main chamber source flange are all of the points of injection for the Group III, Group V, and dopant sources used. These sources are angled to converge at a point at the sample heater, which is calibrated to provide controlled temperature growth to over 1000 °C. The system mass spectrometer and RHEED gun and screen (for in-situ sample characterization) are also attached to the main growth chamber. When the system is being baked before and after venting, all three vacuum zones are enclosed with resistively heated, insulated bake-out panels. These panels reach ~ 150 °C, and enclose the machine like a sarcophagus. A source cabinet separated from the vacuum system contains the metalorganic sources.

4.2 Group III Sources

Since the Varian system is configured for MOMBE operation, a variety of sources are available to provide the Group III species. As with traditional MBE systems, the MOMBE is outfitted with solid source effusion (Knudsen) ovens (Figure 4-2). The K-cells are charged with a suitable Group III element of high purity, and are individually shuttered and controlled. For this work, a K-cell was charged with 99.99999 % (7N) pure gallium (Ga). Through resistive heating, the Ga is made to evaporate out of the cell as an atomic or clustered beam, which is directed toward the substrate. The higher the cell temperature, the higher the Group III flux of atoms.

The MOMBE is also equipped with bubbler-based metalorganic sources that are external to the growth chamber, unlike K-cell sources. The advantage with a bubbler-based source is that system vacuum does not need to be broken in the event of bubbler replacement and/or replenishment. The bubbler-based material delivery system is shown schematically in Figure 4-3. The bubbler itself consists of a steel flask containing the alkyl metalorganic species, which can either be a solid or a liquid, and is placed in a constant temperature bath. The bubbler has manual inlet and outlet valves, with a dip tube extending into the metalorganic. Helium of 6N purity flows from a regulated gas bottle through a chemical purifier and then into the metalorganic module. The MOMBE can operate with up to seven separate bubbler-based sources at one time. The He gas is made to flow through the dip tube, saturating the He with metalorganic, and then out through to the vent. When ready for growth, the gas flow is switched from the vent to the injector, where the He is introduced into the chamber. By controlling the He via a mass flow controller and a pressure controller, and the metalorganic pickup via the bath temperature, the flux can be accurately controlled. The metalorganic species pyrolizes at the substrate surface, breaking into its metallic atom and methane. The metalorganic group III sources used consisted of triethylgallium (TEG – $Ga(C_2H_5)_3$) to provide a Ga flux and dimethylethylamine alane (DMEAA – $(CH_3)_2(C_2H_5)N{:}AlH_3$) to provide an Al flux.

4.3 Group V Sources

The Varian MOMBE system also offers a large degree of flexibility in the types of Group V sources that are available for semiconductor growth. Regardless of the group V source used, III-V epitaxy systems are normally operated with an overpressure of the group V species. The MOMBE is equipped with gas-based sources to provide reactive As, P, and N. The system is outfitted with arsine (AsH_3) and phosphine (PH_3) to provide the As and P fluxes. Due to the toxicity of these hydride gasses, their bottles are contained in a gas cabinet outside of the system facility, and plumbed into the building through an evacuated conduit to contain the gas in the event of a leak. The hydride gas flow is regulated through a dedicated mass flow controller, and introduced into the chamber through a catalytic-based thermal cracker unit (Figure 4-4a). This injector is operated at high temperature to decompose the hydride gas into its monatomic and diatomic species, plus H_2 gas. These species are then free to react at the substrate, while the H_2 is pumped out of the system. A gas source for As and P is an alternative to the dual zone solid effusion cells that can be used to provide the monatomic and diatomic species from solid As_4 and P_4. Through the mass flow controller, it is easier to consistently control the group V flux than through resistive heating and evaporation of a solid. Replenishing the source is also easier, as the bottle simply has to be changed. Reactive nitrogen is provided by an RF plasma unit that operates at 13.56 MHz. The RF power is coupled to mass flow controlled 6N pure N_2, which serves to ionize the gas, producing atomic and molecular species that then flow into the main chamber and are reacted at the substrate (Figure 4-4b). The cracker and plasma units are attached to the system source flange, as shown in Figure 4-1.

4.4 Dopant Sources

Concurrent with the growth of the III-V semiconductor matrix material, dopants are added to produce either optically, magnetically, or electrically active material. This is achieved in a variety of ways in the MOMBE system. The optically active rare earth elements used in this study consisted of solid erbium (Er) and solid europium (Eu). Both elements were obtained in a dendritic form of 99.9 % (3N) purity, and loaded into K-cells for standard evaporative growth. The magnetic dopant, 99.99 % (4N) pure manganese (Mn) was also introduced into the III-V material from a K-cell. The electrical dopants used in the course of this study consisted of carbon tetrabromide (CBr_4) and bis(cyclopentadienyl)magnesium (Cp_2Mg). These materials are introduced into the MOMBE growth system from bubblers, identical in operation to those used for the group III sources.

4.5 System Control

The mass flow controllers and the pressure controllers used on the MOMBE (as in Figure 4-3) are operated through their own related control hardware with front panel operation. The K-cells for the solid dopants are individually controlled using a dedicated AC power supply and an individually activated pneumatic shutter control mechanism. The hydride cracker and the alkyl injector temperatures are controlled with the same kind of power supply. Control of the system gas valves (for all seven alkyl metalorganic modules, the three hydride modules, the RF plasma source module, and the carrier gas main module) is provided by Labview™-based programs that run off of a dedicated system computer. Details of this system can be found in Appendix A. An example of one of these programs is given in Figure 4-5. Note that the program layout resembles

Figure 4-3. The valves are controlled as simple Boolean on/off switches by left-clicking the mouse, and are displayed as open/closed by color (green/red, respectively). Program choices for actions performed frequently (purge, vent, growth) are preprogrammed into the software. Each module is also programmed with an emergency off (red) button. In the event of an emergency, pressing this button will automatically close all the valves related to this particular module.

4.6 System Safety

Due to the hazards involved in working with the source materials installed on the MOMBE, many safety features are incorporated into the system design and operation. In addition to the danger involved with using hydride gasses (lethal in the PPB level) is the fact that many of the metalorganic compounds used for III-V growth are pyrophoric and will combust when in contact with water. The entire gas handling and control system on the MOMBE is routed through an interlock box. In the event that an interlock is tripped, this box will disconnect the power from the power supply that controls all of the system valves. As all the valves are of the normally closed variety, power loss will immediately shut all of these valves. The main interlocks consist of the main system turbo pump and gate valve, the pressure in the system exhaust stack, the system smoke detector, and the system toxic gas monitor. Air is sampled at 8 points on the system and monitored for AsH_3 and PH_3. Levels above a certain point will trip the system and sound a facility alarm. As the system exhuast from all of the MOMBE vacuum pumps may still contain unreacted gas or some other toxic effluent, all exhaust gasses are run through a pellet-based Purofil scrubbing material before being sent to the facility dilution scrubber and exhaust stack.

4.7 Sample Loading and Preparation

The initial step in the epitaxial growth process is sample preparation and loading. Before epitaxial growth, it is often necessary to perform an ex-situ cleaning treatment on the substrates before introduction into the system growth chamber. In this study, (0001) Al_2O_3 sapphire and MOCVD-grown GaN layers on sapphire substrates were used for the GaN growth, while (100) GaP substrates were used for the GaP growth. The sapphire and the GaP substrates were obtained in an epi-ready form, meaning the growth surface needed no ex-situ and a minimal amount of in-situ treatment before sample growth could commence. The GaN substrates consisted of 2 –3 μm of MOCVD-derived n-GaN grown on (0001) sapphire with a 400 Å AlN buffer layer. As the GaN surface is sensitive to contamination by carbon, metals, and the native oxide, an ex-situ cleaning process is used. This process consists of 3 minutes in a 1:1 $HCl:H_20$ solution, a 25 minute UV/O_3 exposure, and finally 5 minutes in a buffered oxide etch solution (HF based).

After cleaning and sectioning, the samples are ready to be mounted on the sample blocks and loaded into the system. In the case of the GaP and some of the sapphire, the samples were In-mounted (via a hot plate) on 2 inch silicon wafers and then attached via wire clips to annular sample blocks unique to Varian style MBE systems. As higher growth temperatures would be used for the remaining sapphire and GaN substrates, solid molybdenum (Mo) block sample holders were employed. The larger thermal mass of these holders allows more accurate, steady control at higher growth temperatures. As before, the samples are In-mounted to the Mo blocks. However, after mounting, the samples were further held down mechanically with either Mo wire or tantalum (Ta) strips. It was found that at the higher temperatures used to perform nitride growth, the cohesive force provided by the In would quickly give way, allowing the sample to fall off if not held in place with a second retention method. The Ta strips serve a second useful purpose, in that they provide a convenient step edge for measuring the film thickness and the film growth rate.

When the mounting procedure for the samples onto the Varian blocks has been finished, they may be introduced into the system. The blocks are twist-locked onto the transfer trolley using the three-pin mechanical system. After the trolley was placed into the loadlock and the door was secured, the loadlock is then pumped to high vacuum ($\sim 5 \times 10^{-8}$ torr) using a succession of roughing, molecular drag, and cryogenic pumps. When this pressure was obtained, a gate valve is opened, allowing the trolley to be rolled (using magnets) into the system buffer chamber. Samples are normally prepared so that the trolley can sit in the buffer chamber overnight prior to growth. When the system is ready for growth (LN_2 cryoshroud panels are full, K-cells are at temperature, the PH_3 cracker is outgassed and at temperature), the gas valve between the growth chamber and the buffer chamber is opened. The sample block is then removed from the trolley onto the sample transfer arm via the pins. The transfer arm is then extended into the growth chamber, the sample block is twist-locked onto the substrate heater, removed from the transfer arm, and the transfer arm is retracted back into the buffer chamber. The gate valve between the main chamber and the buffer chamber is closed. With the sample still facing the buffer chamber, the group V source is turned on. This flux of material, while not starting layer growth, will keep contaminants from absorbing onto the sample surface before growth is started. The sample holder and heater is then rotated into the growth position, which faces the source flange, as shown in Figure 4-1. The sample rotation is then adjusted to a speed of 15 rpm, which was found to produce the optimal level of coverage for the various atomic beams impinging onto the sample surface. The III-V semiconductor growth recipe may now begin!

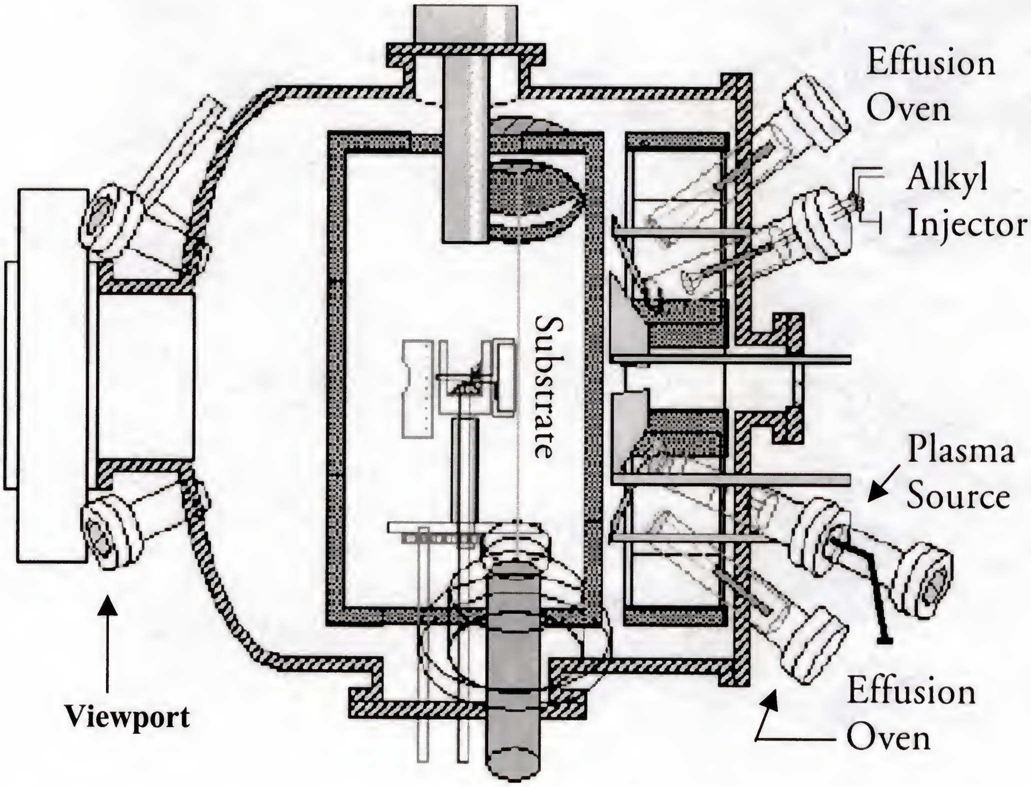

Figure 4-1: A top down view of the Varian MOD Gen II MOMBE growth system [182]. The buffer and load lock chambers (not shown) are to the left side of the figure. Many of the system components are labeled.

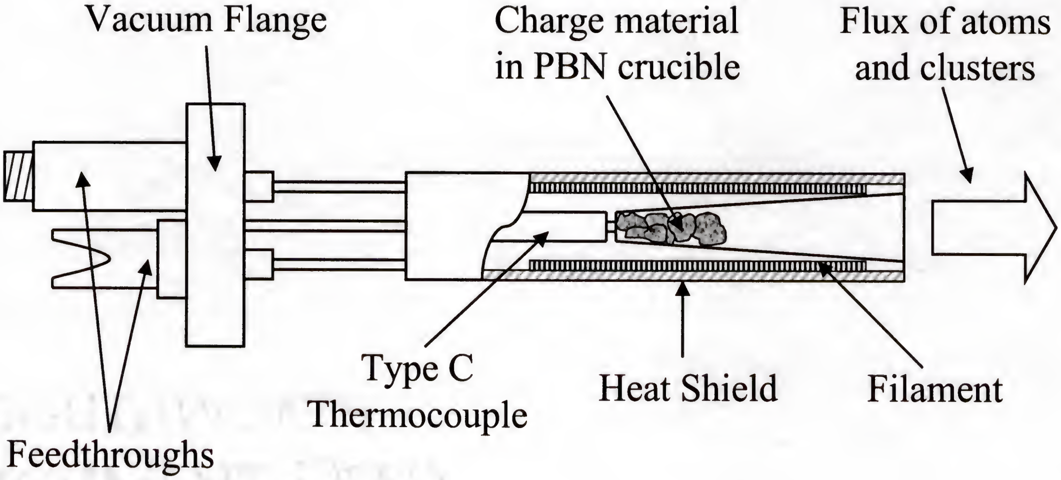

Figure 4-2: A Knudsen Effusion Oven (K-Cell) used on the Varian MOMBE. Resistive heating from the filament evaporates the charge material.

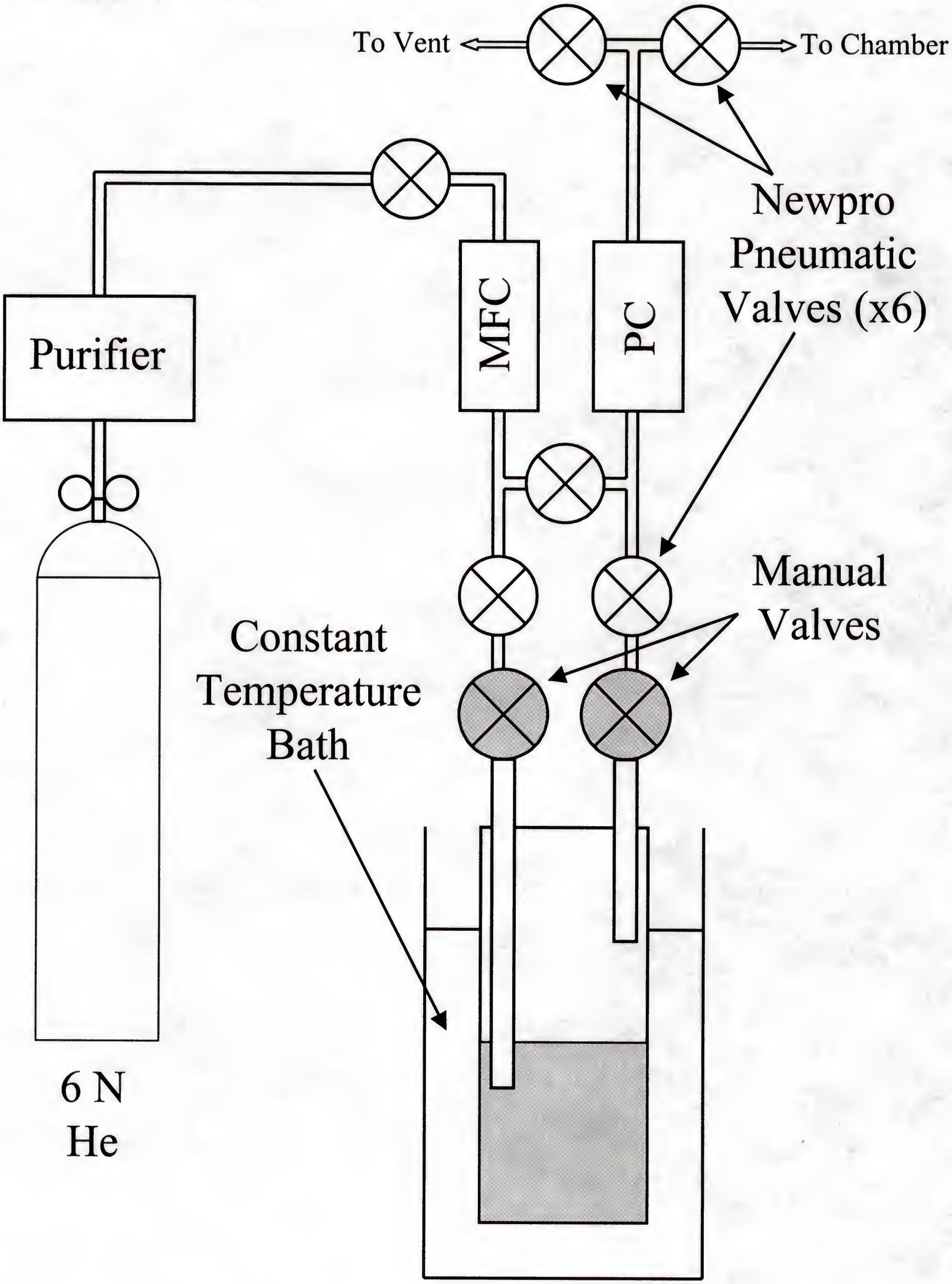

Figure 4-3: An alkyl module used to deliver a metalorganic or other bubbler-based source materials into the Varian MOMBE growth system.

A)

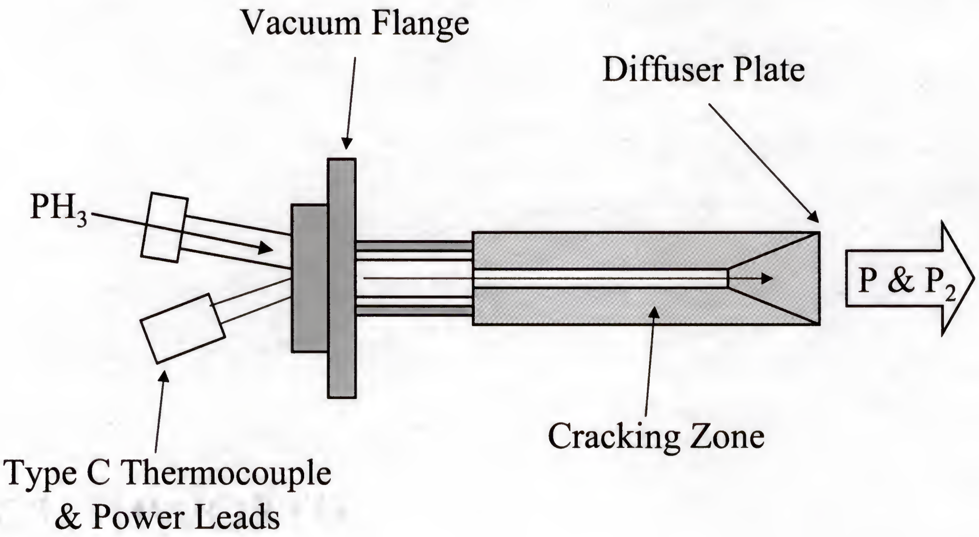

B)

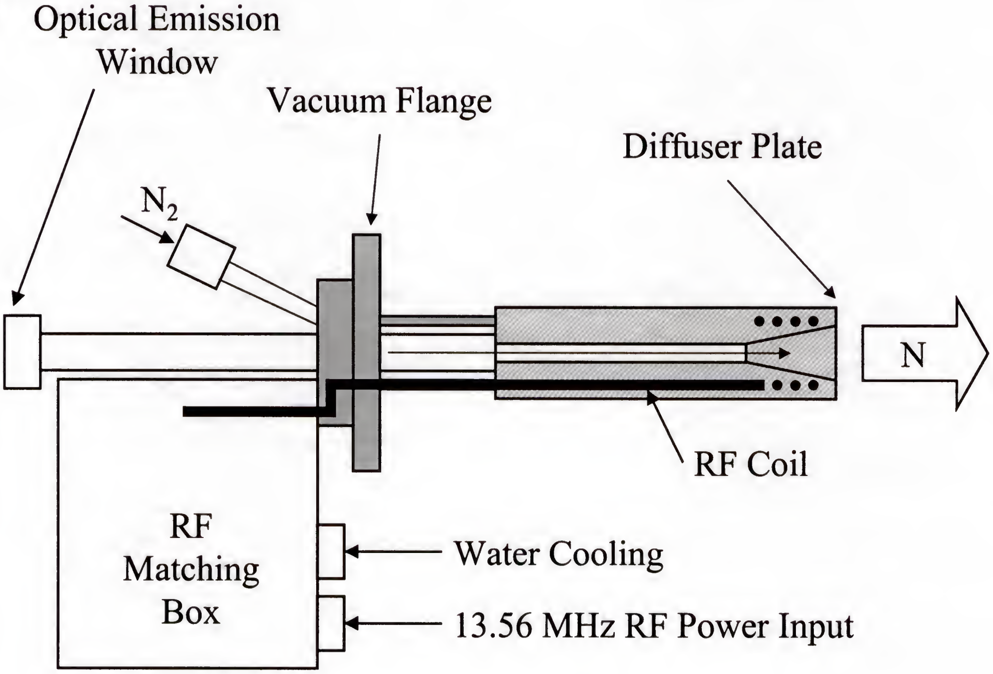

Figure 4-4: Group V sources on the Varian MOMBE A) Hydride Cracker B) RF N_2 Plasma Head

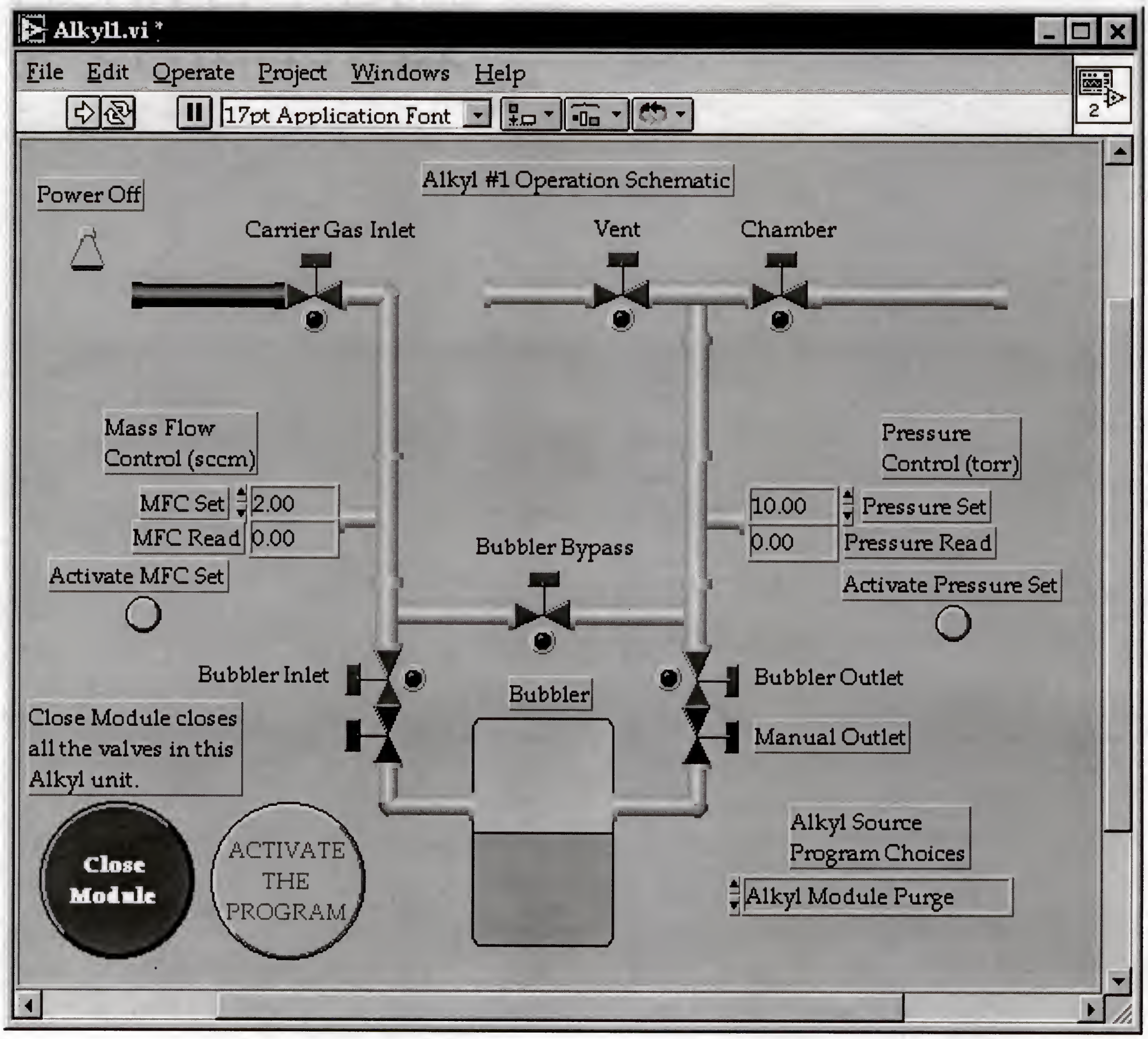

17pt Application Font

MFC Set 2.00

MFC Read 0.00

Pressure Set 10.00

Pressure Read 0.00

Close Module closes all the valves in this Alkyl unit.

Alkyl Source Program Choices: Alkyl Module Purge

Figure 4-5: Labview™ program to control an alkyl module on the Varian MOMBE.

CHAPTER 5
SAMPLE CHARACTERIZATION

After growth, all samples underwent a significant amount of characterization to determine what effect varying the growth parameters had on the final material properties. As the primary interest of the doping study focused on the optical and magnetic properties of the rare earth and transition metal doped films, the majority of the characterization was in this area. However, the morphological, structural, chemical, and electrical properties are also very important. This chapter will briefly review the many different characterization techniques used during the course of this thesis work.

5.1 Atomic Force Microscopy

Film morphology was measured primarily using tapping mode atomic force microscopy (AFM) with a Digital Instruments Nanoscope III. In AFM, an atomically sharp tip of Si_3N_4 with a radius on the order of 50 Å is brought within several Å of the sample surface. The tip is mounted at the end of a flexible cantilever. At this point, repulsive van der Waals forces between the sample surface and the tip cause the cantilever to flex. This deflection is measured by a laser beam that is aligned to reflect off of the mirrored end of the cantilever and into a position-sensitive photodiode. A given cantilever position corresponds to a specific beam position in the photodiode, which is then translated into a sample height. A feedback circuit between the photodiode and the scanner allows a 3D map of the surface to be determined. The map can then be analyzed to quantify parameters such as the average surface roughness. The scans were performed over a 1 μm^2 area. The vertical resolution with AFM can be as high as 0.1 Å.

5.2 Scanning Electron Microscopy

Another technique used to determine surface morphology is scanning electron microscopy (SEM). The SEM technique enables an image to be taken of the sample surface at a very high magnification, from between 5000X to 100,000X. The SEM images in this dissertation were obtained using a JEOL 6400. In this technique, an electron beam of energy between 5 keV to 30 keV is rastered across the sample surface. One requirement of an SEM sample is that it be conducting, in order to prevent surface charging due to the interaction of the beam with the sample. In the case of insulating samples, a thin carbon coating is applied. The interaction of the incident electron beam with the sample produces many species at differing depths from within the sample, including secondary electrons, Auger electrons, backscattered electrons, and characteristic x-rays. Secondary electrons have energies below 50 eV, and due to this low energy, can only escape from the sample if they are produced within a few nm of the surface. As the electron beam is rastered, a detector picks up the secondary electron signal. This signal is fed into a cathode ray tube that is scanned at the same rate as the electron beam, producing an image of the sample surface.

5.3 X-ray Diffraction

Structural information was determined with powder x-ray diffraction (XRD), specifically to determine what phases are present within the epitaxial material. The XRD measurements were performed in a Philips APD 3720 system that uses a copper (Cu) x-ray source. The source predominantly emits Cu $K_{\alpha 1}$ x-rays with a 1.54056 Å wavelength for diffraction, although $K_{\alpha 2}$ and K_{β} x-rays are emitted as well. In XRD, the incident x-rays are subjected to constructive and destructive interference due to their interaction with the repeating planes of the crystalline sample, in accordance with Bragg's Law:

$$n\lambda = 2d\sin\theta \quad (5.1),$$

where d is the atomic plane spacing and θ is the angle between the incident x-ray beam and an atomic plane. This is shown schematically in Figure 5-1. In the Philips diffractometer, the intensity of the diffracted x-rays is measured by a photomultiplier tube as a function of 2θ, the angle between the incident and diffracted x-ray beams. A plot of intensity versus 2θ yields the sample diffraction pattern. The high intensity of the x-ray source allows polycrystalline samples to be measured. In this study, it can therefore be determined if the semiconductor was "overdoped", resulting in extra dopant-induced phases in addition to the main matrix semiconductor phase.

5.4 Reflection High Energy Electron Diffraction

In addition to XRD, structural characterization can be performed in-situ in the MOMBE growth system via reflection high energy electron diffraction (RHEED). RHEED is performed by striking the surface of the sample at a grazing angle (1-2°) with a high energy electron beam. The MOMBE is equipped with a Staib electron gun for this purpose that is operated at 15 kV. Due to the small angle, the incident electrons will only diffract from the first few layers of atoms, allowing RHEED to be useful for determining the surface crystal structure, the surface orientation, and the degree of surface roughness of the sample. The incident electrons diffract off ordered rows of atoms on the sample surface, concentrating the scattered electrons into particular directions. These beams of scattered electrons are made to intersect a phosphor screen opposite to the electron gun. This light produces a pattern on the screen that can be recorded by a camera. In epitaxy, RHEED is predominantly used to determine the surface reconstruction and the surface growth mode. RHEED photographs of the various growth modes are given in Figure 5-2. A surface growing layer-by-layer (2D) will produce a pattern with streaky lines, whereas a surface growing by islanding (3D) will produce a pattern that is spotty. A polycrystalline film produces the familiar ring pattern. As an amorphous film has no long range order for diffraction, no RHEED pattern will result.

5.5 Auger Electron Spectroscopy

Chemical composition information was determined using Auger Electron Spectroscopy (AES). As with SEM, AES involves the detection of electrons emitted from the sample surface due to the interaction of an incident electron beam. As with the secondary electrons in SEM, Auger electrons are also of low energy and are released from the first few atomic layers of the sample. As a result, AES is a very surface-sensitive technique. However, the energy of an Auger electron is characteristic of the atom that released it. An Auger electron is the result of a three electron process. The incident electron beam, through interaction, first knocks an inner shell electron off of the atom in question. To lower the overall atom energy, an outer shell electron will then jump down, filling the inner shell void. The excess energy difference that results from this transition is given off as a photon, which is then reabsorbed by the same atom, ejecting another outer shell electron. It is this second outer shell electron that is detected as the Auger electron. The resulting detected energy spectrum then allows a qualitative compositional analysis to be obtained of the surface, and through peak height analysis using published elemental sensitivity factors, an approximate quantitative analysis can also be calculated. AES can be used for accurate compositional information down to roughly 1 atomic %. The Auger system is also fitted with an Ar sputter gun allowing compositional depth profiling. The Auger system used in this dissertation was a Perkin Elmer 6600.

5.6 Secondary Ion Mass Spectrometry

A second technique that allows compositional determination with depth profiling is secondary ion mass spectrometry (SIMS). In SIMS, an incident beam of either oxygen (O) or cesium (Cs) ions is used to sputter away the sample in the targeted area. The sputtering process causes the ejection of atoms and clusters of atoms from the sample surface. A portion of these atoms and clusters will be ionized. These ions are then accelerated into a mass spectrometer, where a bending magnet or quadrupole analyzer separates the ions based on their charge to mass ratio, and then these ions are counted. The relative number of counts is then translated into an atomic concentration through the use of standards. Trace impurities can also be measured. As the SIMS technique sputters away the sample in a particular spot, depth profile information can also be obtained. SIMS can be used for impurity levels down to $10^{15}/cm^3$, although it is not generally used to determine concentration levels above ~1 %.

5.7 Photoluminescence

Photoluminescence (PL) measurements were performed to evaluate the optical activity of the rare earth doped epitaxial material. To perform the PL measurements, a laser beam that was filtered, bent, and focused is directed onto the sample holder.

Emission from the sample is then gathered by two lenses and passed into an optical spectrometer with an attached photodetector. The spectrometer contains entrance and exit slits through which the resolution of the measurement can be controlled. A diagram of the PL system used is given in Figure 5-3. Samples can be measured at either room temperature with a dedicated sample holder or down to 15 K using a sample holder fitted with a liquid helium coldfinger. The spectrometer is outfitted with a GaAs photomultiplier tube for measuring signals in the visible regime and with a liquid nitrogen cooled InGaAs photodiode detector for measuring signals in the near IR regime. The action of the laser beam on the sample serves to promote ground state electrons to excited states within atoms or molecules, or to promote electrons from the valence band to the conduction band, creating electron/hole pairs. The excited states relax by nonradiative and radiative means, producing an emission spectrum that will provide qualitative information about the sample properties. For the III-V semiconductors studied, an argon ion (Ar^+) laser with $\lambda = 514.5$ nm (2.4 eV) was used to provide below bandgap excitation, while a HeCd laser with $\lambda = 325$ nm (3.8 eV) was used to produce above bandgap electron/hole pairs.

5.8 Hall Effect

To determine the electrical properties of a semiconductor material, specifically the number density and type of the charge carriers within the solid, Hall effect measurements were performed. The Hall effect in a thin film sample is measured in a transverse geometry, with the sample voltage being measured across one pair of opposite corners on the sample while a current is sourced through the other opposite pair. This is in contrast to a longitudinal (Van der Pauw) resistance measurement, where the current is sourced along one side of the sample while the voltage is measured along the other side. In addition to the transverse electrical contacts, a magnetic field is applied perpendicular to the sample plane. The charge carriers (electrons or holes) are deflected in the sample due to the Lorentz force, setting up an electric field in the sample, the sign of which depends on the majority charge carrier involved. Based on the known magnetic field, measured electric field, and known source current, the charge carrier density and type can be calculated via the Hall constant, R_0. Hall effect measurements can also indicate ferromagnetic ordering within the sample. The aligned spins within a ferromagnetic sample will enhance the probability that the charge carriers will undergo additional scattering. This scattering adds a second term to the Hall resistivity, ρ_{Hall}:

$$\rho_{Hall} = R_0 H + R_S M \qquad (5.2)$$

where R_0 is the normal Hall constant, H is the applied magnetic field, M is the sample magnetization, and R_s is the anomalous Hall coefficient. The anomalous Hall effect, measured at low fields, manifests itself as a non-zero ρ_{Hall} intercept in a plot of ρ_{Hall} versus H, and will be observed in materials showing ferromagnetic ordering. Hall effect measurements in this study were performed at room temperature in a home-built system with a 0.8 T electromagnet, and at cryogenic temperatures with a Quantum Design Physical Properties Measurement System (PPMS) with a 7 T superconducting magnet.

5.9 SQUID Magnetometry

All the magnetic measurements in this dissertation were performed in a Quantum Design Magnetic Properties Measurement System (MPMS, hereafter referred to as the SQUID). The heart of the system is a closed loop of a superconducting material containing two Josephson junctions, also known as a SQUID. A system of superconducting detection coils is connected to the SQUID device with superconducting wire. The measurements are made by moving the sample through these detection coils. As the sample moves through the coils, the magnetism of the sample induces an electric current in the coils. The SQUID device can be configured with its related electronics to produce an output voltage that is proportional to current flowing into it, which is also proportional to the magnetic moment of the sample. The system is initially calibrated with a sample of known magnetism. A superconducting solenoidal magnet is used to produce magnetic fields in the range of +/- 7 T, and can be swept for making hysteresis-type measurements. A superconducting shield is placed between the magnet and the SQUID device to shield the SQUID from the field generated in the magnet and to stabilize the field contained by the shield, due to the high sensitivity of the SQUID device. A SQUID can be sensitive to a change of 10^{-15} T in a field of up to 7 T. Due to the superconducting nature of the detection system and the magnet, the MPMS system is cooled to liquid helium temperatures. Figure 5-4 shows the SQUID (pickup coils) in relation to the sample in the bore of the superconducting magnet.

In addition to using the SQUID for making magnetization versus field (M vs. H) measurements, another method to check for ferromagnetism is to make a field cooled/zero field cooled (FC/ZFC) measurement of magnetization versus temperature (M vs. T). This type of measurement consists of first cooling the sample to roughly 10 K with no applied field, turning on the magnet to a predetermined value, and measuring the magnetization as the temperature is increased back to room temperature. This is the ZFC part. With the field still on, the sample is cooled back to 10 K, while again making measurements of the magnetization. This is the FC part. If plotted on the same set of axes, the location where these two curves begin to diverge is a measure of the Curie temperature for a ferromagnetic sample. In a diamagnetic or a paramagnetic sample, where there is no hysteresis to measure, the ZFC and FC curves are identical. In a ferromagnetic sample, although the curves will be different, the non-hysteretic component due to diamagnetism will be the same for each. By subtracting the ZFC curve from the FC curve, the sample diamagnetism can be removed, leaving only the ferromagnetic component. Where the resulting FC-ZFC curve intersects the T axis at M = 0 is a measure of the Curie temperature.

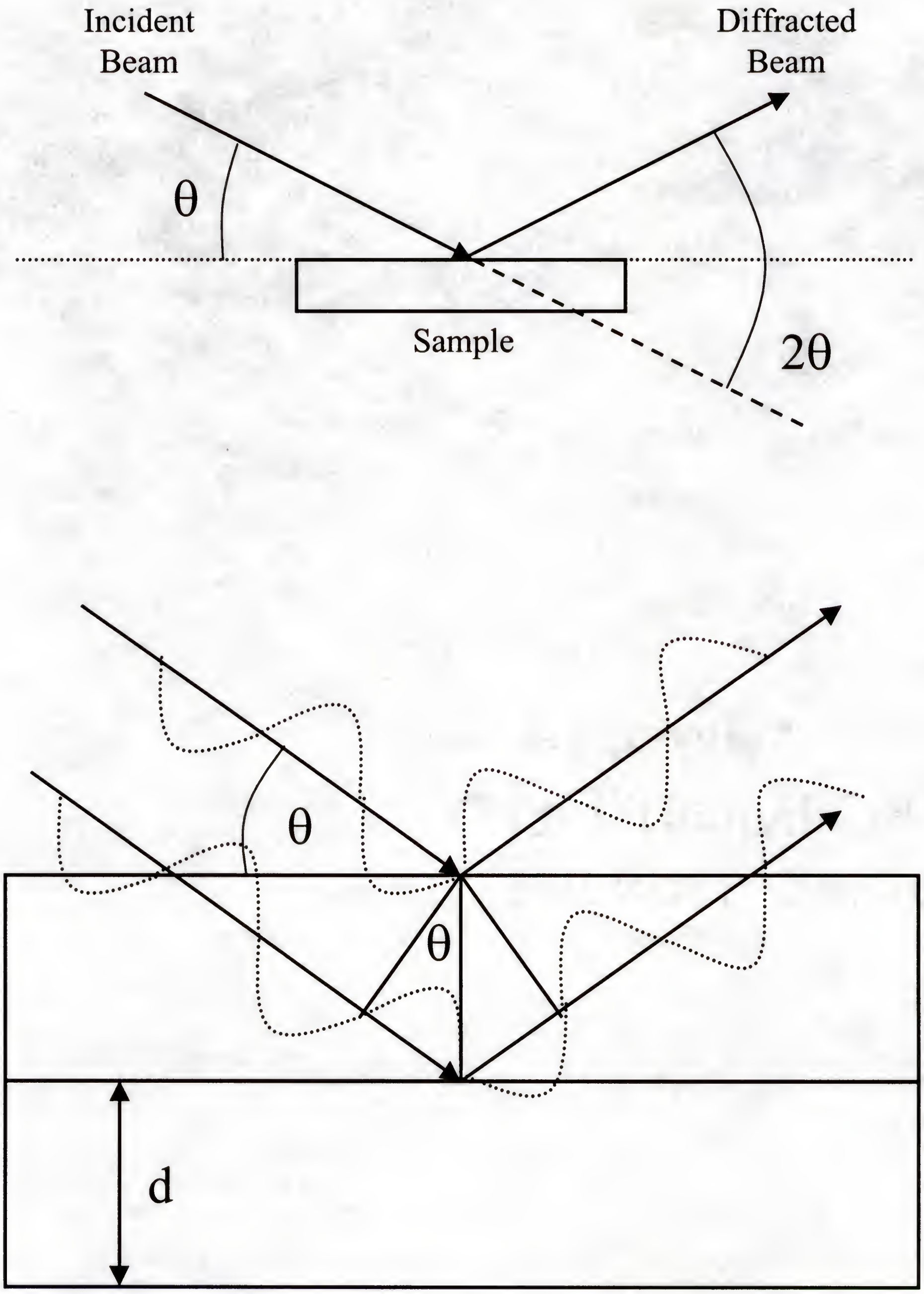

Figure 5-1: X-ray diffraction according to Bragg's Law in a crystalline sample.

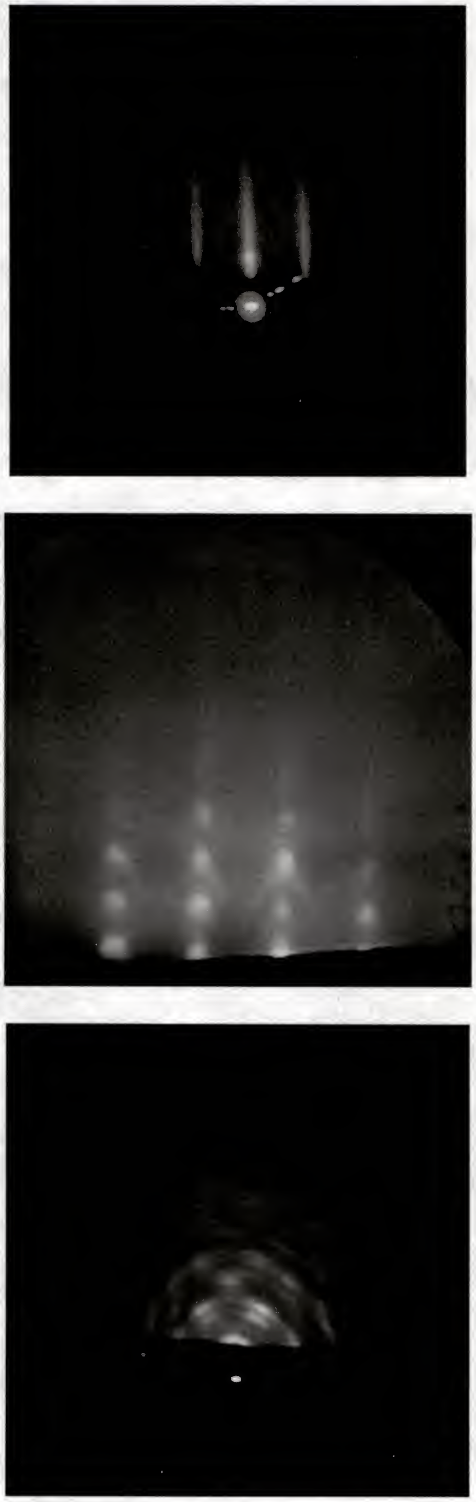

Figure 5-2: RHEED photographs indicating 2D growth (top), 3D growth (middle), and polycrystalline growth (bottom). An amorphous film will produce no pattern.

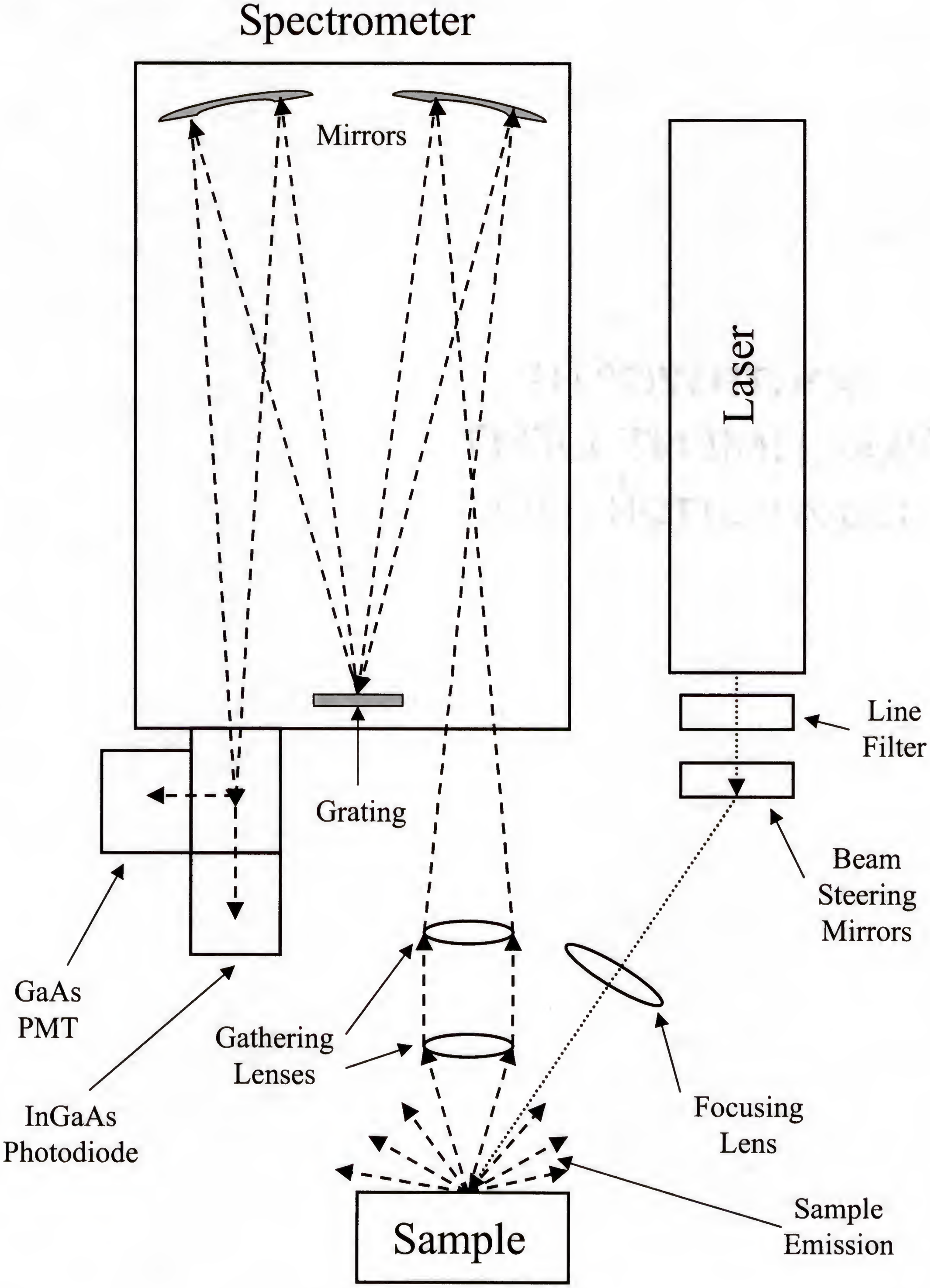

Figure 5-3: Experimental setup for photoluminescence (PL) measurements (not to scale).

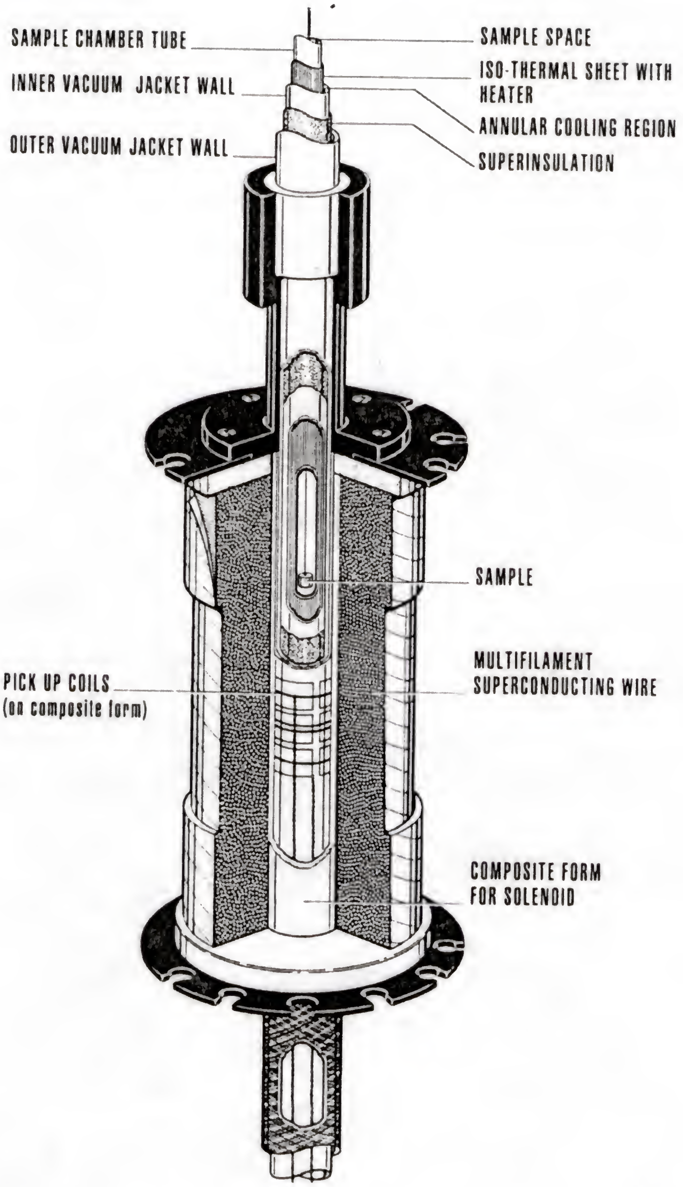

Figure 5-4: The Quantum Design SQUID Magnetic Properties Measurement System [183].

CHAPTER 6
RESULTS AND DISCUSSION: RARE EARTH DOPING OF GaN

In this chapter, the doping of GaN with the rare earth elements Er and Eu will be investigated with the goal of achieving optical activity. While initial results have been promising, a systematic approach towards maximizing the optical activity at 1.54 μm for GaN:Er has yet to be undertaken via epitaxial growth. To date, all intentional codoping experiments in GaN:Er have been performed via ion implantation. In addition, it is not clear whether the same surface degradation observed in heavily doped AlN will occur in GaN as well. Generally speaking, the interplay between rare earth content and surface structure, an important aspect in incorporating these layers in devices, also has not been undertaken. In this portion of the thesis work, the effect of rare earth content on the structural and optical properties of GaN:RE films grown on sapphire via metalorganic molecular beam epitaxy (MOMBE) will be investigated in an attempt to begin to address these issues. MOMBE growth utilizing triethylgallium (TEG) as the Ga source was chosen as the starting point, due to the many advantages a metalorganic source has to offer. These include ease of replacement, lifetime, and the degree of delivery control.

6.1 Gallium Nitride Doped with Er Grown Using Triethylgallium

6.1.1 Material Growth by MOMBE

Films were grown by MOMBE on (0001) Al_2O_3, In-mounted to 2" Si wafers. A 20 nm low temperature AlN buffer layer (T_{growth} = 435 °C) using dimethylethylamine alane (DMEAA) as the Al source was initially deposited for 5 minutes. The DMEAA was introduced into the growth chamber utilizing a 10 sccm flow rate and a 8.5 torr pressure setpoint. The recirculating bath was maintained at 9.1 °C. An ~500 nm GaN layer grown from TEG was then deposited for 40 minutes at $T_{growth} = 750$ °C. The TEG flow rate was 2.3 sccm with an 11.7 torr pressure setpoint. The TEG bath temperature was 9.3 °C. Finally, approximately 1.15 μm of GaN:Er was grown for 100 minutes by switching open the Er K-cell, with cell temperatures varying between 1250 ° and 1450 °C. Reactive nitrogen for the growth of all the layers was provided by an SVT RF plasma source operating at 375 W of forward power, 3 W of reflected power, and 3 sccm of N_2. Previous calibration experiments with this Er K-cell, in addition to results from secondary ion mass spectrometry (SIMS) obtained from Charles Evans and Assoc., indicate an approximate concentration range of 10^{20} to $10^{22}/cm^3$ for this range of cell temperatures.

6.1.2 Sample Morphology

The surface morphologies of the GaN:Er samples are shown in Figure 6-1 as a function of Er cell temperature. From SIMS it was found that the highest Er concentration obtained was ~ 1 x $10^{22}/cm^3$ and the lowest was ~ 1 x $10^{20}/cm^3$. As the Er temperature, and therefore the Er concentration, was increased, the round surface features decreased in size until a smooth morphology was obtained at 1450°C. This trend in surface smoothness is in sharp contrast to the results obtained from similar experiments with AlN [64-67]. In AlN, as the Er concentration was increased, the surface roughness increased due to the formation of surface nodules. SIMS analysis of the AlN did not show any evidence of Er segregation and the nodules appeared to be of the same composition as the underlying matrix. It is possible that the Er, though not segregating, was clustering and thus disturbing the growth front. The fact that this degradation does not occur in GaN may suggest that the Er is more soluble due to the larger Group III site in GaN relative to AlN. It is surprising, however, that the GaN surface morphology actually improves with increasing Er content. From the SEM data it would appear that the surface is smoother due to a reduction in the domain size. GaN grown by MBE often exhibits a columnar structure that is induced by the large lattice mismatch between the GaN and the sapphire. This reduction in column diameter is also supported by AFM measurements of the surface roughness, shown in Figure 6-2. The RMS roughness of the films decreased by an order of magnitude (from 18.1 nm to 2.0 nm) as the Er cell temperature was increased from 1250 °C and 1450 °C. When the AFM scans of the surface are examined in detail, seen in Figure 6-3, it is clear that the surface features are reduced in size. These results suggest that the Er may interfere with the surface migration of the reactant species resulting in a smoother less textured surface. This reduction in surface mobility also results in a slight decrease in the growth rate at high Er fluxes, also shown in Figure 6-2, probably due to enhanced desorption of the ethyl-gallium species.

6.1.3 Photoluminescence Analysis

As hoped, PL analysis, depicted in Figure 6-4, shows that the normalized PL intensity increases steadily with increasing Er content, and shows no evidence of concentration quenching over the range investigated. The Ar^+ laser was used to analyze the GaN:Er samples. For AlN, however, the PL emission did not increase along with the Er concentration [64-67]. It is possible that due to the slightly larger radius of Ga compared to Al, the Er^{+3} is more likely to sit substitutionally on group III sites in the GaN lattice than in the AlN lattice. The greater ease of dopant incorporation in GaN:Er compared to AlN:Er would thus lead to more efficient optical activation and hence much greater PL signal at 1.54 μm. This enhanced substitutionality would also be in agreement with the smoother surface morphologies obtained in GaN relative to AlN. It is also possible that the saturation of the AlN:Er PL may be simply due to the degradation of the AlN crystal quality resulting from the poor incorporation behavior of Er in this material.

6.2 Gallium Nitride Doped with Er Grown Using Elemental Ga and Codoped with C

From the previous Section, it was found that in the GaN:Er grown using TEG, the 1.54 μm Er^{+3} emission could be increased in a linear fashion with an increase in the Er K-cell temperature. However, additional samples grown according to the recipe given in Section 6.1.1, while having the proper Er level, had random C and O levels when analyzed by SIMS. No general consistency was observed, as the C and O levels varied on a day to day basis and on a growth run to growth run basis on the same day. It was shown, in Chapter 2, that codopant impurities (O, C, F) can enhance the luminescence and efficiency of Si:Er and GaN:Er, but only when introduced in the proper Er/Impurity ratio. Also from Chapter 2, Torvik et al. have demonstrated using ion implantation of Er and O that a ratio of ~10:1 O/Er is optimal for room temperature emission. As yet there was no similar investigation of the specific role of the concentration of carbon in the luminescence and surface properties of GaN:Er films. As such, the further use of TEG as a Ga source was abandoned, as the C and O levels could not be controlled accurately. The C and O levels in the TEG-derived films are most likely due to residue left over from the TEG synthesis process. In this portion of the work, the effect of C codoping introduced via CBr_4 on the structural and optical properties of GaN:Er films was investigated in an attempt to address these issues. The effect of post-growth annealing on PL intensity in the carbon-doped material was also explored.

6.2.1 Material Growth by GSMBE

Films for this portion of the research were grown by gas source MBE (GSMBE), again on In-mounted (0001) Al_2O_3. A high temperature surface nitridation preceded all layer growth, and was performed at a temperature of 865 °C. Due to this high temperature step, the samples were mounted on the molybdenum blocks instead of Si. A 20 nm low temperature AlN buffer layer ($T_{growth} = 435°C$) was again grown using dimethylethylamine alane (DMEAA) as the aluminum source. This was followed by a 1.2 μm GaN, GaN:Er or GaN:Er:C, grown at a temperature of 750 °C for 150 minutes. A solid source effusion cell provided the gallium flux, while the carbon was provided by the surface decomposition of CBr_4. The CBr_4 flow rate, pressure, and bath temperature were varied to adjust the amount of C in the GaN:Er:C layers. The shuttered erbium cell was maintained at a temperature of 1250 °C, which corresponds to a dopant level of $8.5 \times 10^{20}/cm^3$ as determined by SIMS analysis. Rapid thermal annealing (RTA) was performed in an AG Associates annealing oven using either nitrogen or forming gas ($90\%N_2/10\%H_2$) ambients.

6.2.2 Effect of Carbon Doping on Film Morphology

The surface morphologies of the GaN:Er samples codoped with different C levels from the CBr_4 source are shown in Figure 6-5. SEM micrograph A shows the undoped GaN surface. In micrographs B through D, as the CBr_4 flow, and therefore the C concentration, is increased, the round surface features decrease in size until a smooth morphology was obtained in the GaN:Er that was codoped with roughly 1.3 x 10^{20}/cm^3 of C. On further codoping, shown in micrograph E, it would appear that the round surface features then increase in size. The highest codopant level, shown in micrograph F, then appears to decrease in size again. The C concentration in micrograph F was approximately 1.3 x 10^{21}/cm^3. From the SEM data, it would again appear that the initial increase in film smoothness is due to a reduction in the GaN domain size.

As with the SEM, AFM measurements of the GaN:Er surface roughness indicate an initial improvement in morphology with increasing C level, as shown in Figure 6-6. The RMS surface roughness of the undoped GaN film was found to be approximately 73.5 Å. Improved morphologies can be obtained using higher growth temperatures. However, previous work has shown the Er emission decreases as the growth temperature increases for the same Er level. On the addition of Er, and with subsequent C addition, the surface roughness initially decreased by a factor of 7. However, with further C addition, the surface roughness increased dramatically. It is possible that at this C concentration (~6x10^{20}/cm^3), the GaN has reached its solubility limit. The increase in surface roughness could then be due to the incorporation of C in the form of defects, clusters, or precipitates. From Chapter 2, high levels of crystal defects were observed in Si:Er when the material system was overdoped with O. With further C addition, the surface roughness drops for a CBr_4 flow of roughly 0.16 sccm. As shown in the AFM in Figure 6-7, rough regions and very smooth regions characterize this sample. The solid line in Figure 6-6 represents the overall surface roughness of the whole sample, while the dotted line represents the surface roughness of the smooth regions only. Note that there is roughly an order of magnitude drop between the two values. This suggests that coarsening effects due to increased C incorporation are opposed by surface etching of the GaN by Br left over from the CBr_4 decomposition.

When the AFM surface scans, given in Figure 6-7, are examined in detail, it appears that the growth mode is altered for samples A through D. These results suggest that first the Er, then the C, may interfere with the surface migration of the reactant species, resulting in a smoother, less textured surface. The obvious roughening in micrograph E gives further credence to the theory that the GaN has reached its solubility limit for C, and that the roughening is due to an enhanced number of defects. Finally, in micrograph F, the defect related roughening is partially compensated by Br assisted surface etching.

Figure 6-8 shows that the growth rate of the GaN: Er at first increases slightly with C incorporation, but then decreases as more C is added. The slight increase is possibly due to the C enhancing the Ga sticking coefficient. The decrease in the growth rate at higher CBr_4 fluxes is almost certainly due to the Br species left over from the thermal decomposition of the CBr_4 at the growth surface which parasitically etches the GaN. Enhanced Br levels (and etch rates) due to the higher C fluxes will produce lower overall growth rates for the same initial GaN growth rate. Similar behavior was observed in GaAs, GaP and AlGaAs.

6.2.3 Effect of Carbon Doping on Film Luminescence

The PL analysis, depicted in Figure 6-9, shows that the PL intensity at first increases sharply with increased C content (over the non C-doped sample), and then decreases. This result indicates that for the Er concentration used ($8.5 \times 10^{20}/cm^3$), the optimum codoping concentration of C is ~7.7 x $10^{20}/cm^3$ as measured by SIMS. The initial increase in PL can be attributed to C affecting the local environment of the Er atoms. Normally, electric dipole radiation from 4f Er^{+3} transitions would be forbidden due to the parity selection rule. It was found that a noncentrosymmetric crystal field leads to parity intermixing, resulting in a finite lifetime for radiative decay; such a crystal field can be produced by the formation of Er-C complexes, allowing efficient Er^{+3} pumping. It has also been suggested that a reduction in deep levels in the GaN, as well as enhanced promotion of Er from the +2 state to the +3 state by Er-C centers will produce a luminescence enhancement. The decrease in the PL luminescence at high CBr_4 flows can be attributed to the further increased number of C atoms surrounding the Er producing nonradiative decay centers in the GaN matrix material. The nonradiative sites could be produced as a result of C-C clustering, precipitates, C related defects, and C atoms not linked to Er atoms. Similar results (optimum codopant level, enhanced nonradiative decay) have been seen previously in work done with Si:Er codoped with O.

The quenching behavior of the carbon-doped material has also been investigated, shown in Figure 6-10. It was found that reducing the measurement temperature for the sample with the optimum carbon level produced a sharp increase in the peak located near 1535 nm, but not for the peak located near 1510. Comparison of the integrated intensity at 20K with that at 300K shows the thermal quenching to be ~40%. This is significantly higher than the degree of quenching observed for material grown with TEG, as shown in Table 6-1, but much lower than is typically seen for low impurity GaN:Er which shows ~75% quenching. The material grown with TEG which contains an O/Er ratio of 0.9 in fact gave a higher integrated intensity at room temperature than at 20K. As shown in

Figure 6-11, this negative quenching was due primarily to an increase in the secondary peak at 1510 as the main peak at 1535 remained virtually unchanged with temperature. While the Er peak at 1510 was identified by other groups, its behavior does not track with the main peak at 1535. It is possible that changes in temperature could influence the peak height by varying the splitting of the initial and final transition states, as well as the transition cross section. Increasing the carbon concentration in the CBr_4 doped material did further suppress the quenching, though at the expense of the absolute emission. The oxygen levels in the samples grown with elemental Ga could not be determined due to a high oxygen background in the SIMS instrument. At the most, the oxygen level is ~3.5 x $10^{20}/cm^3$. However, previous analysis of similarly grown material showed oxygen levels of ~$10^{19}/cm^3$ or less. If similar levels are present in this material then the O/Er ratio would be ~0.01, which is significantly less than that obtained with TEG. Given that the C/Er ratios in the TEG grown material are the same or lower than those doped with CBr_4, it would appear that the reduced quenching in material grown with TEG is due to the presence of oxygen.

Table 6-1: Impurity ratios and thermal quenching for GaN:Er grown using various sources along with an N_2 plasma.

Sources used for growth	[Er] (cm^{-3})	O:Er	C:Er	PL intensity at 20 K	Quenching between 20 and 300 K (%)
TEG	10^{22}	0.175	0.0084	2.6	0
TEG	10^{21}	0.9	2.3	1.7	-62
Ga, CBr_4	8.5 X 10^{20}	<0.4	9.0	1.4	31
Ga, CBr_4	8.5 X 10^{20}	<0.4	0.9	4.0	40
Ga	8.5 X 10^{20}	<0.4	-	0.32	92

TEG is synthesized with ether which can be transported to the growth surface, decompose and lead to high backgrounds of oxygen. It is most likely this oxygen which is responsible for the lack of thermal quenching.

From these results it would appear that oxygen is a better co-dopant for GaN:Er than carbon. Further, carbon produces mid-gap states which cause the material to be highly resistive. This could lead to high series resistance in actual devices. Oxygen, by contrast, behaves as a shallow donor, making the material conductive and possibly easier to fabricate into an efficient device. Unfortunately the use of oxygen in UHV growth chambers can lead to contamination of the system, resulting in oxygen contamination throughout the device structure. In order to take advantage of the benefits of oxygen without compromising system integrity, a low vapor pressure oxygen-containing source which decomposes efficiently at the growth surface is needed.

6.2.4 Annealing of GaN:Er and GaN:Er:C

Annealing of the co-doped material produced no effect on the room temperature PL intensity for temperatures up to 600°C, regardless of ambient, as shown in Figure 6-12. Annealing at higher temperatures appeared to increase the intensity from carbon-doped material but did not increase the intensity from the GaN:Er without carbon. In fact, annealing in the forming gas ambient actually decreased the intensity from the non-carbon-doped material. This suggests that annealing enhances the Er-C interaction, and possibly helps to remove some of the defects generated by the introduction of high amounts of carbon. The variation of the annealing time was not investigated.

6.3 Gallium Nitride Doped with Eu Grown Using Elemental Ga

While the III-Nitrides have proven quite successful for fabrication of blue and green light emitting devices, realization of red devices has not been successful due to the difficulties associated with the synthesis of the high In-content InGaN needed to achieve red emission. An attractive alternative may be the use of Eu-doped GaN, which will possess the same advantages as Er-doped GaN, i.e. a host-material insensitive wavelength and a reduced degree of thermal quenching. This reduction in quenching allows efficient operation of Er-doped material at room temperature, and should offer the same benefit for Eu^{+3}, though thermal quenching measurements of GaN:Eu have not yet been reported. In the past, Eu doping was used to produce emission in organic-based devices [184], phosphor applications [185], and in CaF_2-based devices [186]. The use of red emitting GaN:Eu has also been previously reported[76,187,188]. However, the intensity of GaN:Eu has yet to be compared to materials used for commercially available LED devices, such as AlGaAs.

6.3.1 Material Growth by GSMBE

Films were grown by GSMBE using the same recipe as in Section 6.2.1. In lieu of the GaN:Er or GaN:Er:C layer, a 1.2 μm GaN:Eu layer was grown. The shuttered europium cell was maintained at a temperature of 500°C. The GaN:Eu growth rate was ~92 Å/min.

6.3.2 Photoluminescence Analysis

The results of PL analysis of the GaN:Eu film using above bandgap excitation from the HeCd laser are presented in Figure 6-13. The Eu^{+3} transition at 621 nm is due to the $^5D_0 \rightarrow {}^7F_2$ transition of the 4f shell. Also superimposed with the GaN:Eu spectra are spectra from $Al_{0.35}Ga_{0.65}As$ and $Al_{0.30}Ga_{0.70}As$ using above bandgap excitation from the Ar ion laser. The laser power in both cases was approximately 35 mW. The emission from the GaN:Eu sample was visible with the naked eye. From the figure, the GaN:Eu emission is more intense than both AlGaAs samples and also has a much narrower full width half maximum (FWHM). The FWHM of the GaN:Eu is approximately 2.2 nm, compared to 14 nm for the $Al_{0.35}Ga_{0.65}As$, and 13 nm for the $Al_{0.30}Ga_{0.70}As$. Rapid thermal annealing results for N_2 and forming gas (10% H_2/90% N_2) ambients are presented in Figure 6-14. After annealing at 800 °C, the integrated PL for both cases is virtually identical to the as grown values. The increased emission after annealing at 400°C and 600°C may be due to the enhanced promotion of Eu from the +2 state to the +3 state and also to the removal of nonradiative defect sites. The decrease in emission after annealing at 800°C may be due to the precipitation of separate Eu phases from GaN:Eu solid solution. The role of H_2 in this case is believed to be limited to providing less N_2 per unit volume for annealing, hence the decreased PL intensities that track the N_2 results in Figure 6-14. This is comparable to the results obtained in similar experiments involving annealing studies with GaN:Er from Section 6.2.

Thermal quenching measurements (Figures 6-15 and 6-16) on the as-grown and 800°C N_2 annealed samples were performed with a liquid He cooled coldfinger. The as grown sample was found to quench by approximately 82% as the measurement temperature was increased from 20K to 300K. This is in agreement with the quenching result for GaN:Er from Section 6.2, indicating the similarity in the incorporation for both of the lanthanides, despite the pump source used for the excitation. After annealing in

N_2, the thermal quenching was reduced to 66% over the same measurement range. The improved quenching behavior further verifies the conclusion from Figure 6-14 that the improvement in emission on annealing is due to the removal of nonradiative defects and the enhancement of the Eu from the +2 to the +3 valence state. At low temperatures, additional peaks were visible at 598 nm, 606 nm, 616 nm, and 632 nm as shown in Figure 6-16.

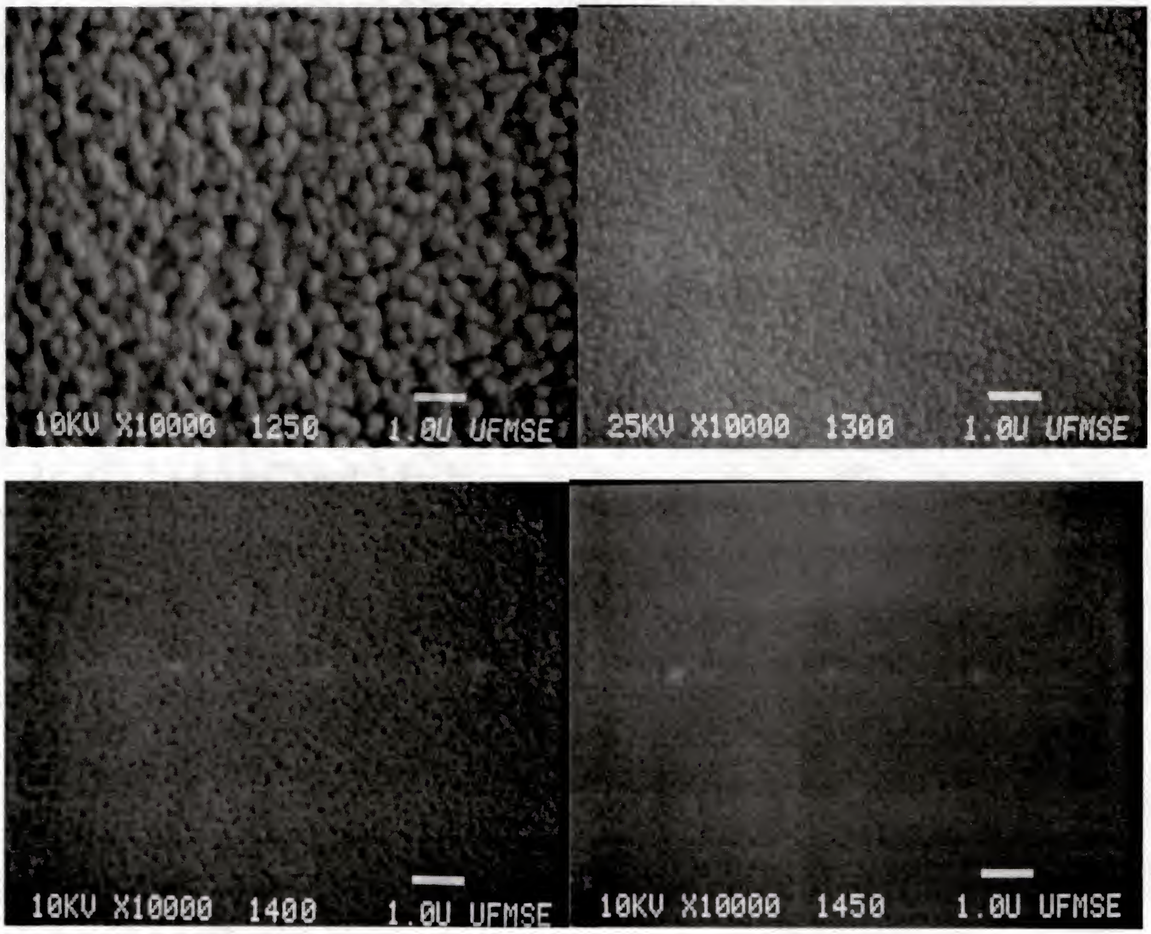
10KV X10000 1250 1.0U UFMSE
25KV X10000 1300 1.0U UFMSE
10KV X10000 1400 1.0U UFMSE
10KV X10000 1450 1.0U UFMSE

Figure 6-1: Scanning electron micrographs (SEMs) of GaN with a progression of Er cell temperatures: 1250°C (upper left), 1300°C (upper right), 1400°C (lower left) and 1450°C (lower right).

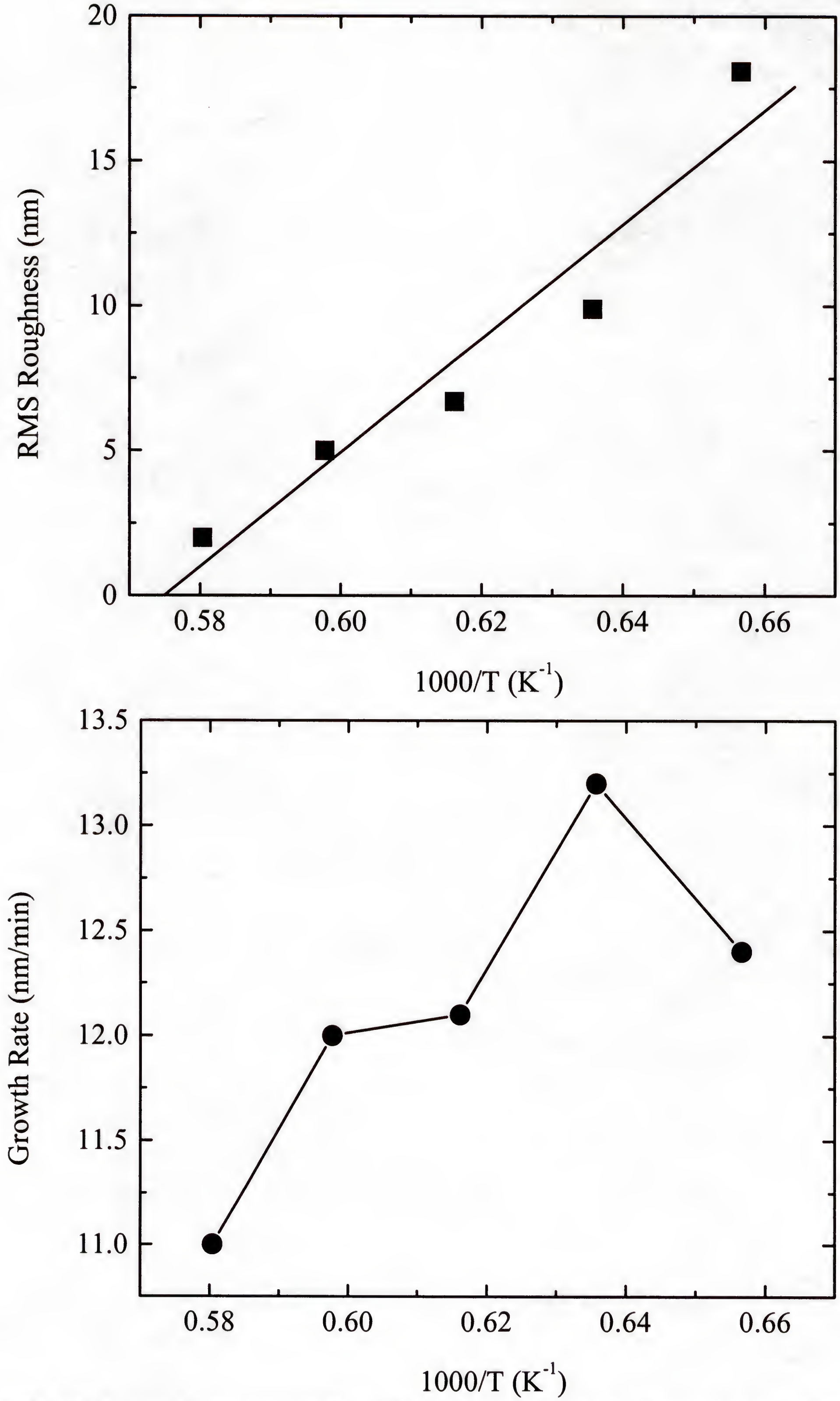

Figure 6-2: RMS roughness versus Er cell temperature (top) and growth rate of GaN:Er versus reciprocal Er cell temperature (bottom).

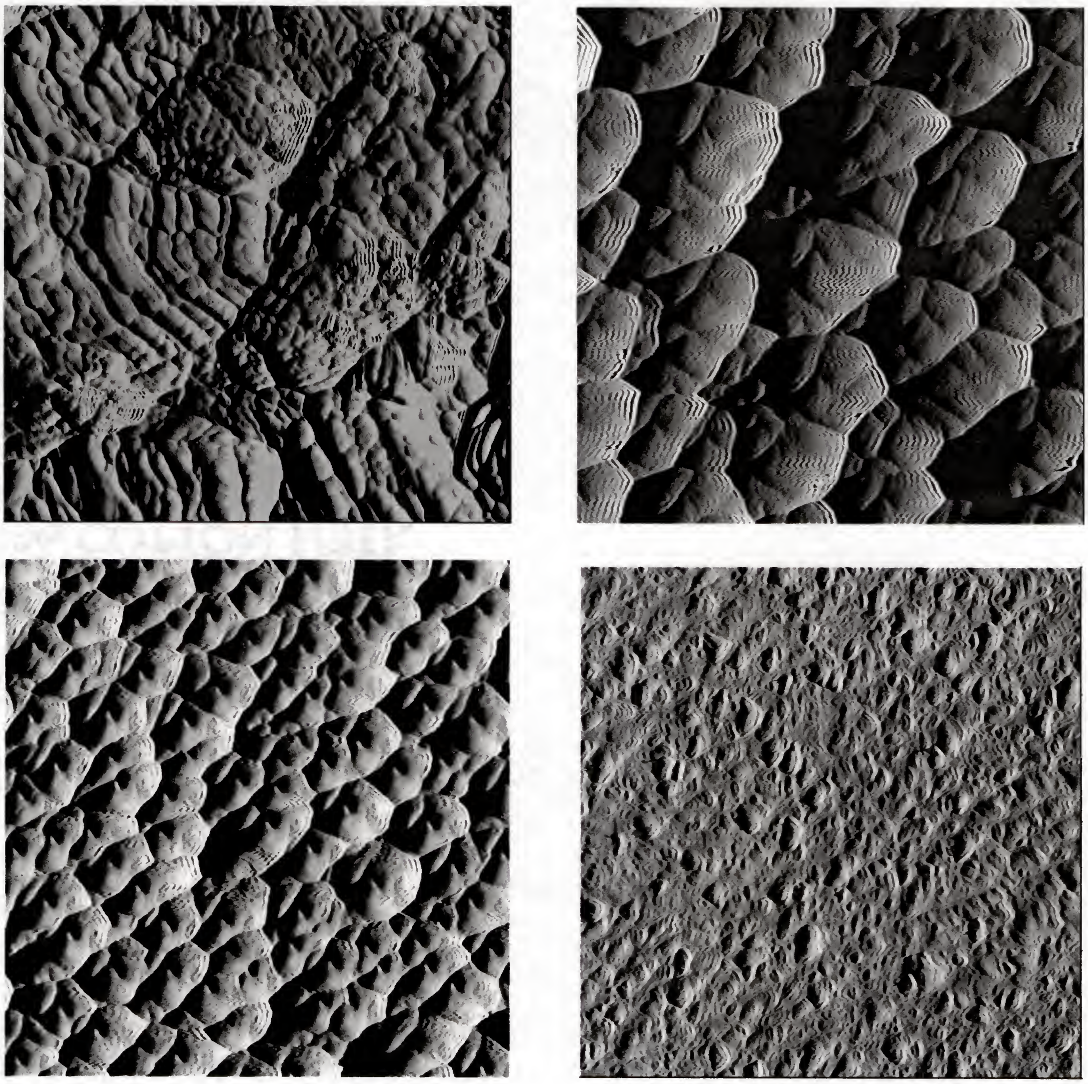

Figure 6-3: AFM surface scans of GaN with a progression of Er cell temperatures from: 1250°C (upper left), 1300°C (upper right), 1400°C (lower left) and 1450°C (lower right). Area represented is 1 μm x 1μm.

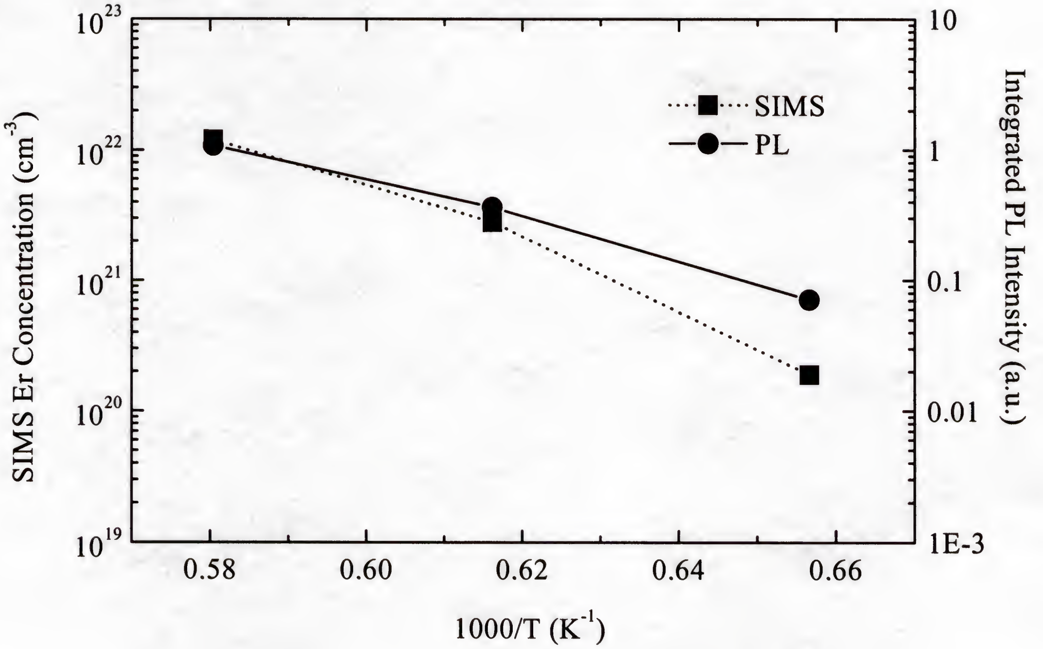

Figure 6-4: Er concentration as determined by SIMS and integrated room temperature 1.54 μm PL for GaN:Er versus reciprocal Er cell temperature.

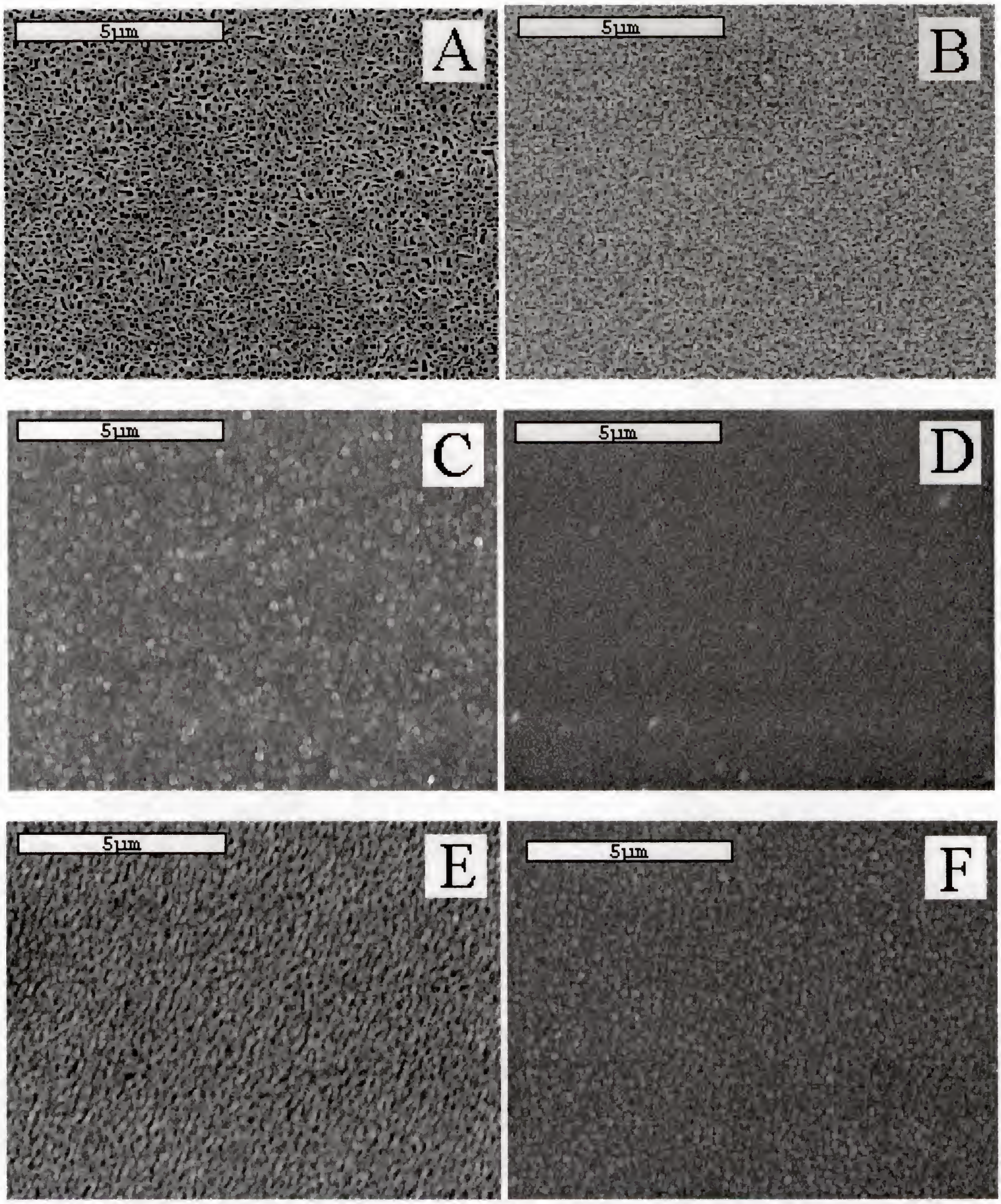

Figure 6-5: SEMs of GaN and GaN:Er with a progression of CBr_4 doping (CBr_4 in sccm), (A) GaN (B) GaN:Er (C) GaN:Er ($CBr_4 = 3.2 \times 10^{-3}$) (D) GaN:Er ($CBr_4 = 1.6 \times 10^{-2}$) (E) GaN:Er ($CBr_4 = 7.9 \times 10^{-2}$) (F) GaN:Er ($CBr_4 = 1.6 \times 10^{-1}$).

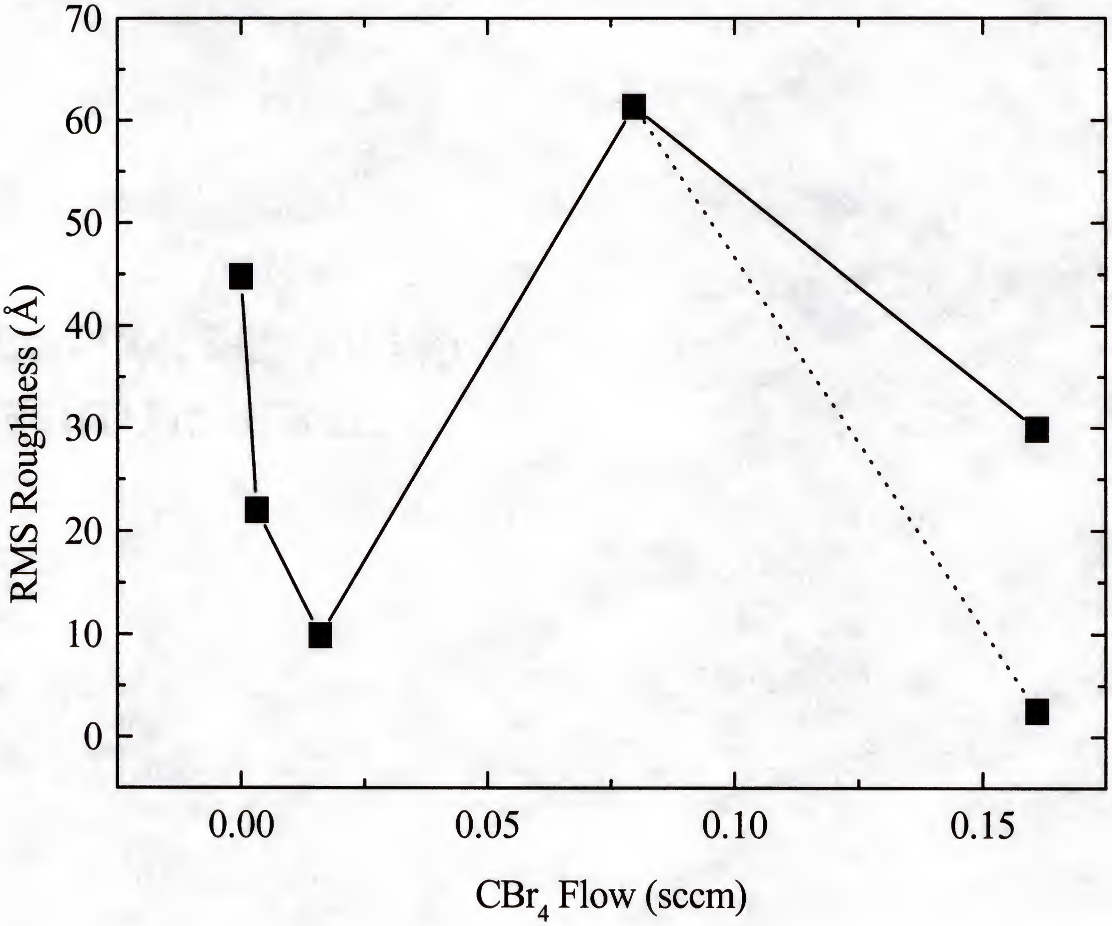

Figure 6-6: GaN:Er RMS roughness vs. CBr$_4$ flux.

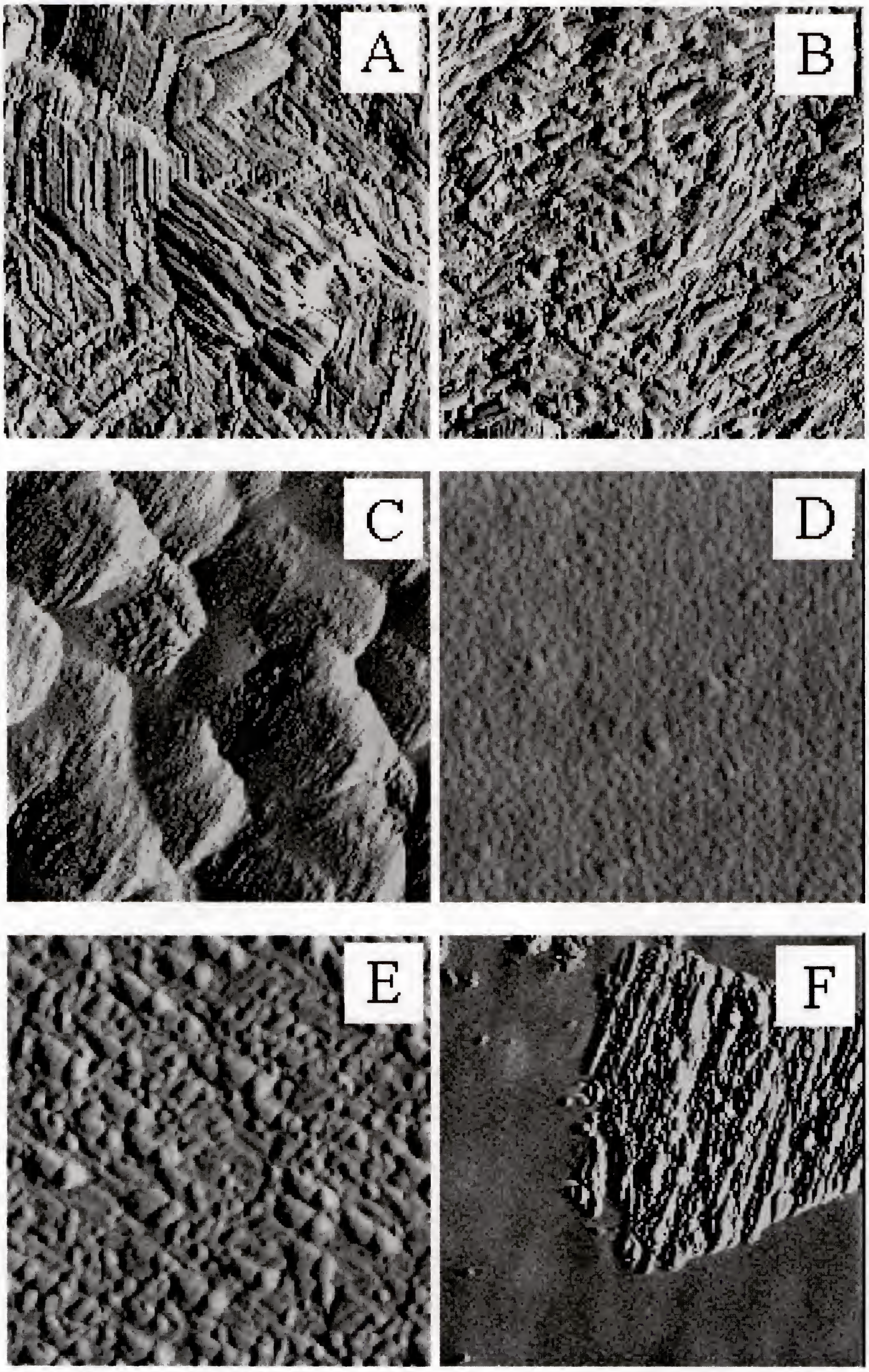

Figure 6-7: AFM surface scans of GaN with a progression of Er and C doping (CBr_4 in sccm), (A) GaN (B) GaN:Er (C) GaN:Er ($CBr_4 = 3.2 \times 10^{-3}$) (D) GaN:Er ($CBr_4 = 1.6 \times 10^{-2}$) (E) GaN:Er ($CBr_4 = 7.9 \times 10^{-2}$) (F) GaN:Er ($CBr_4 = 1.6 \times 10^{-1}$). Scan dimensions were 1 X 1 μm X 5 nm.

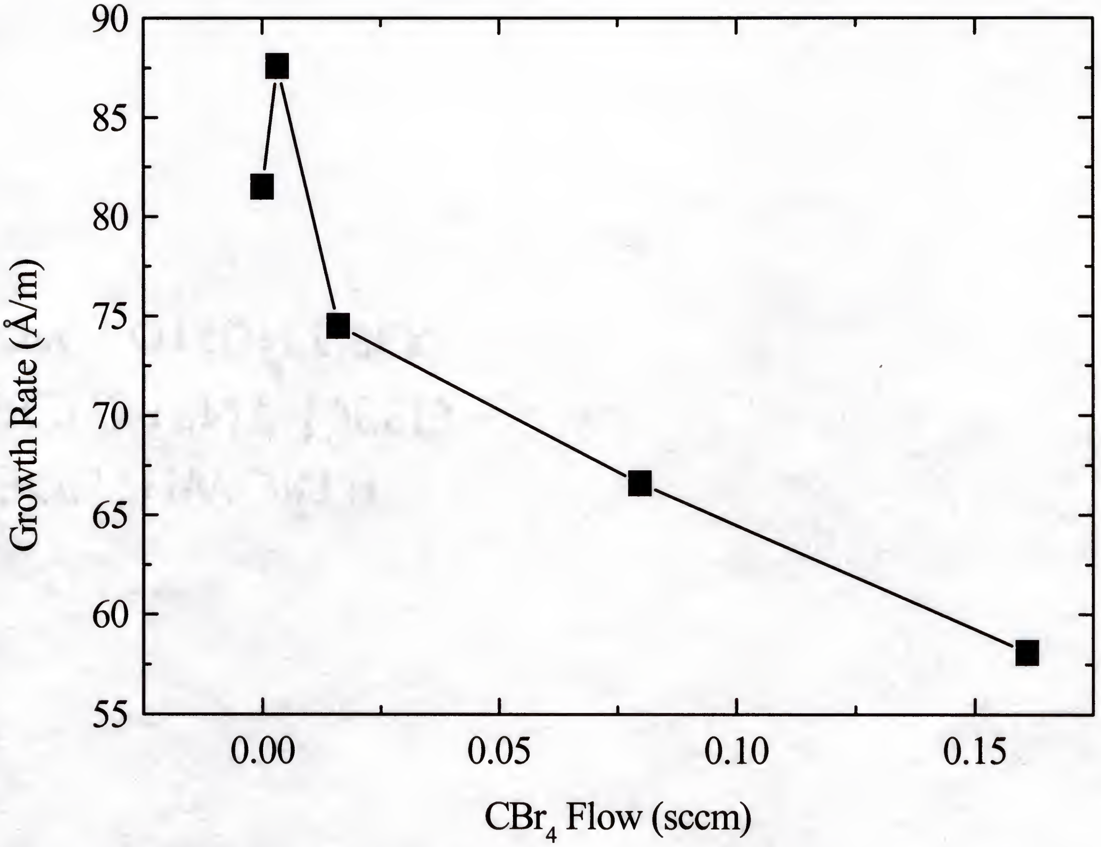

Figure 6-8: GaN:Er growth rate vs. CBr$_4$ flux.

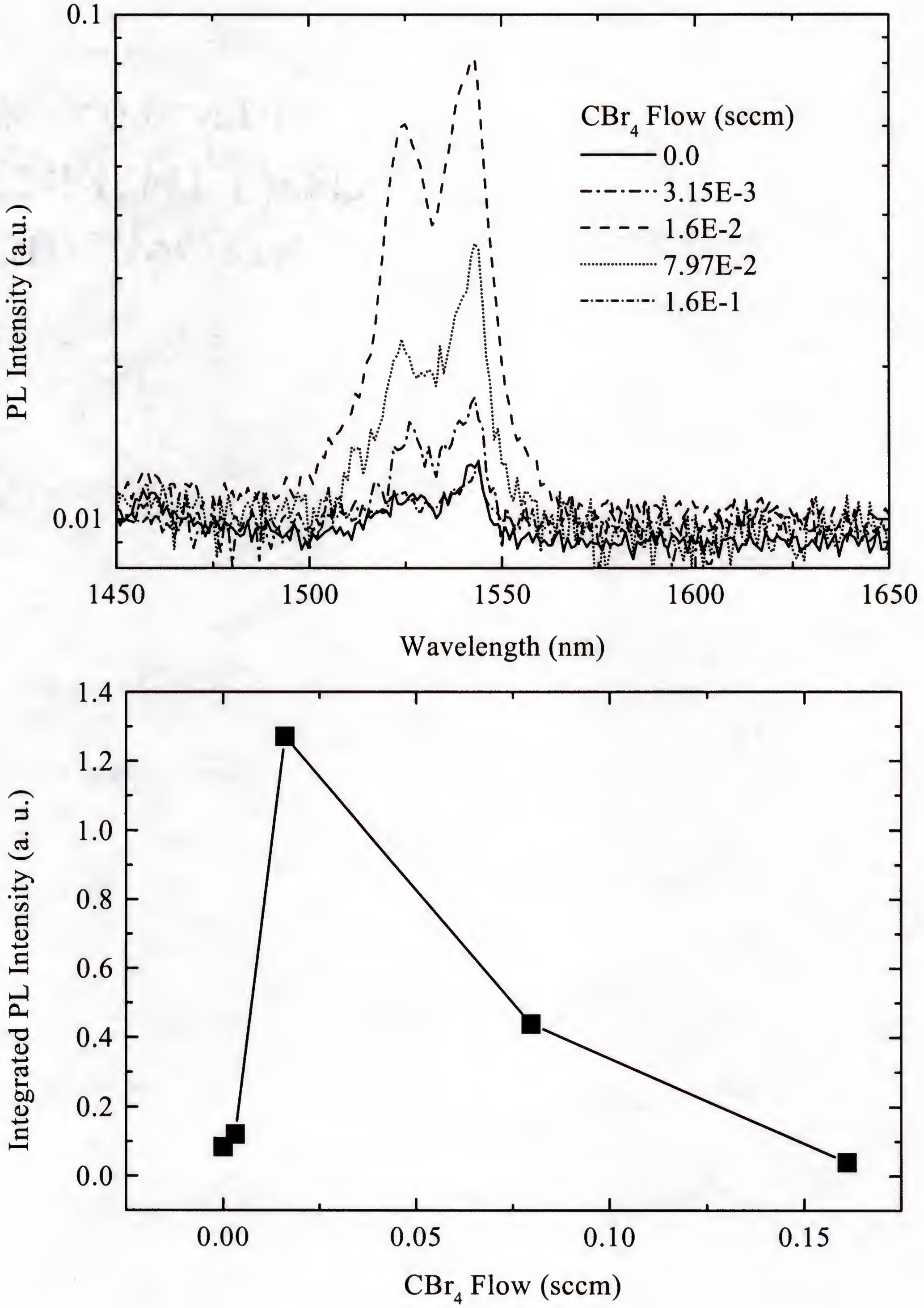

Figure 6-9: Room temperature PL spectra from GaN:Er doped with carbon (top) and integrated PL intensity of the 1.54 μm emission vs. CBr_4 flow (bottom).

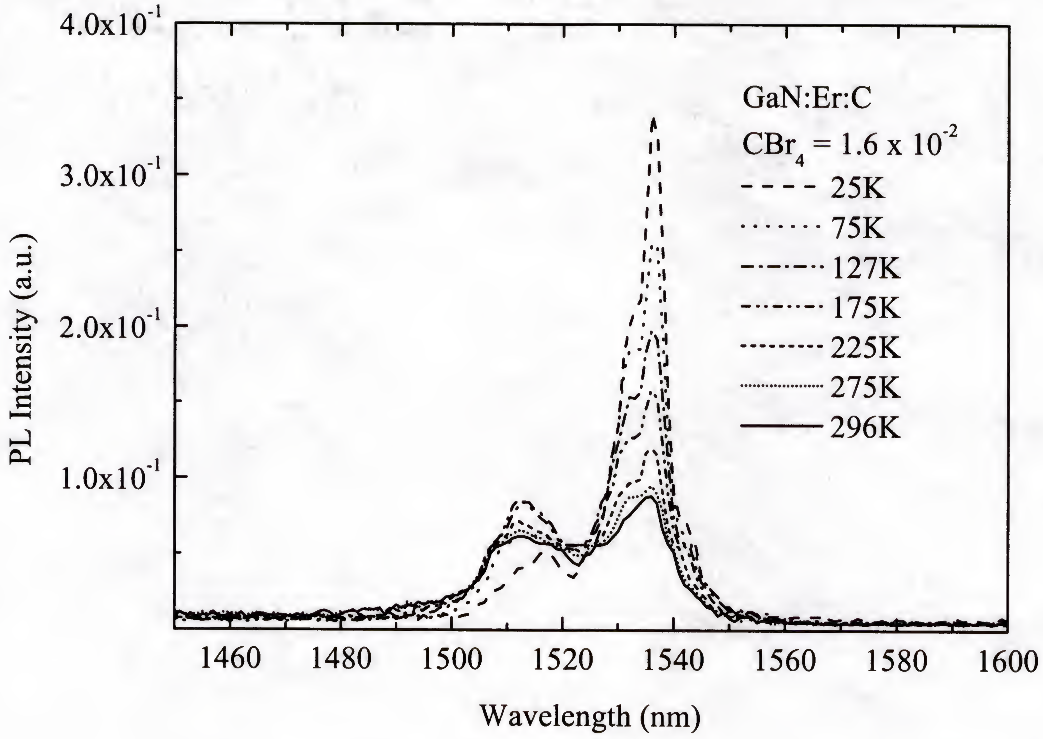

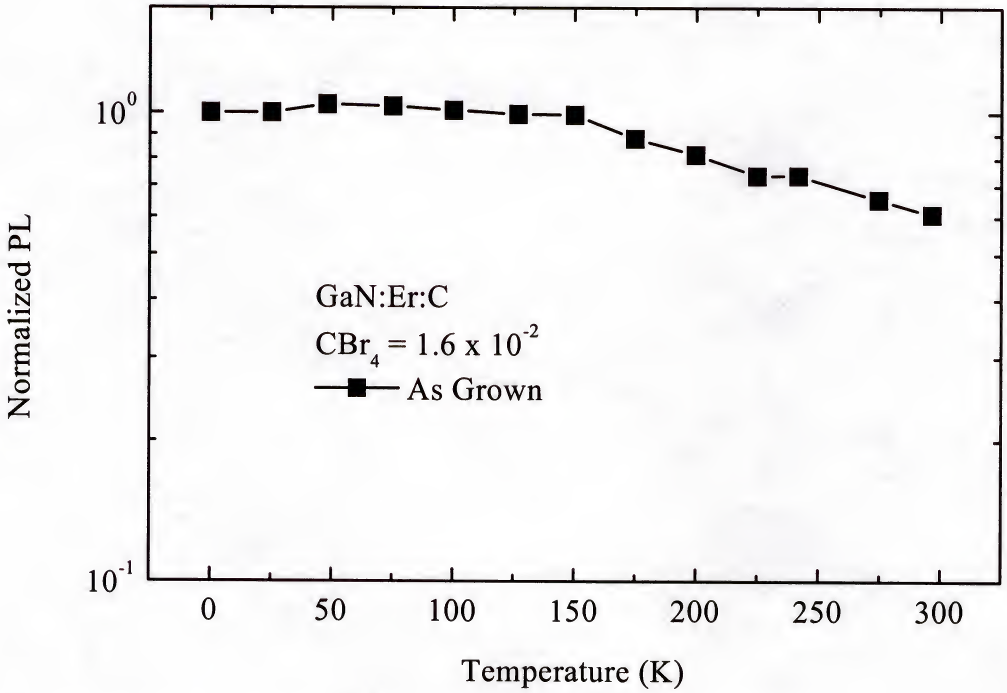

Figure 6-10: PL emission vs. measurement temperature for GaN:Er:C.

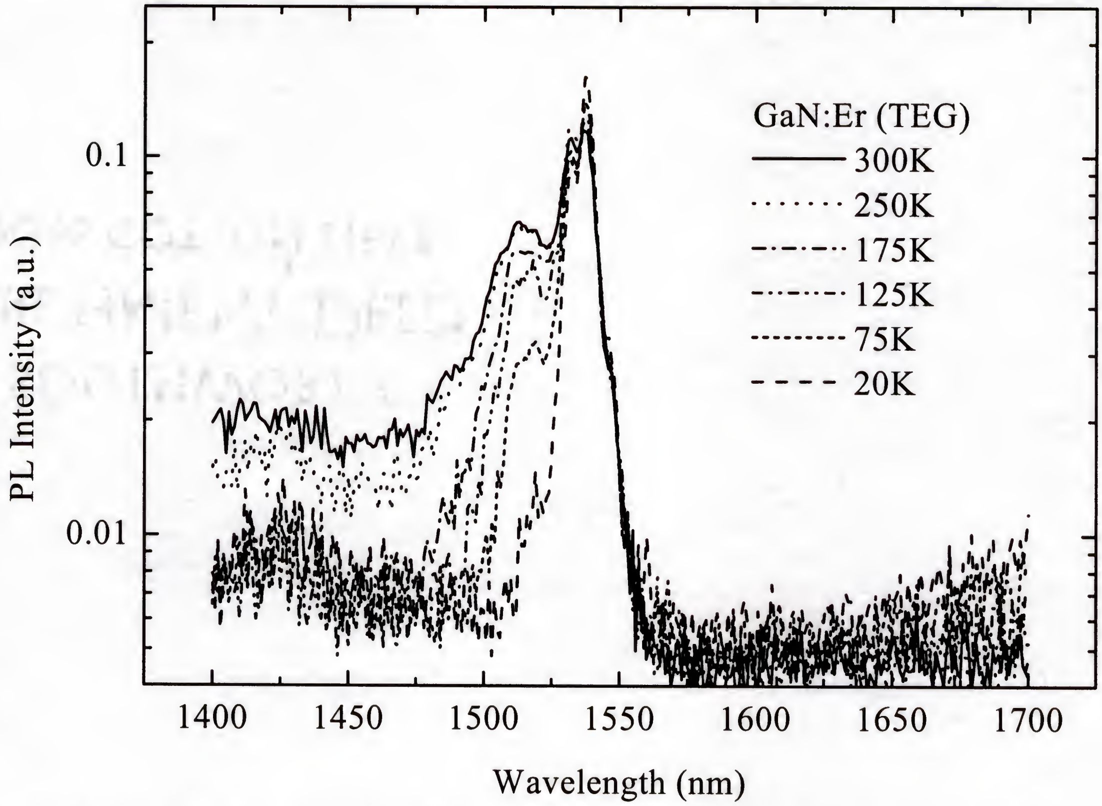

Figure 6-11: PL spectra taken at various temperatures from GaN:Er grown using TEG with [Er] ~ 10^{21}/cm^3.

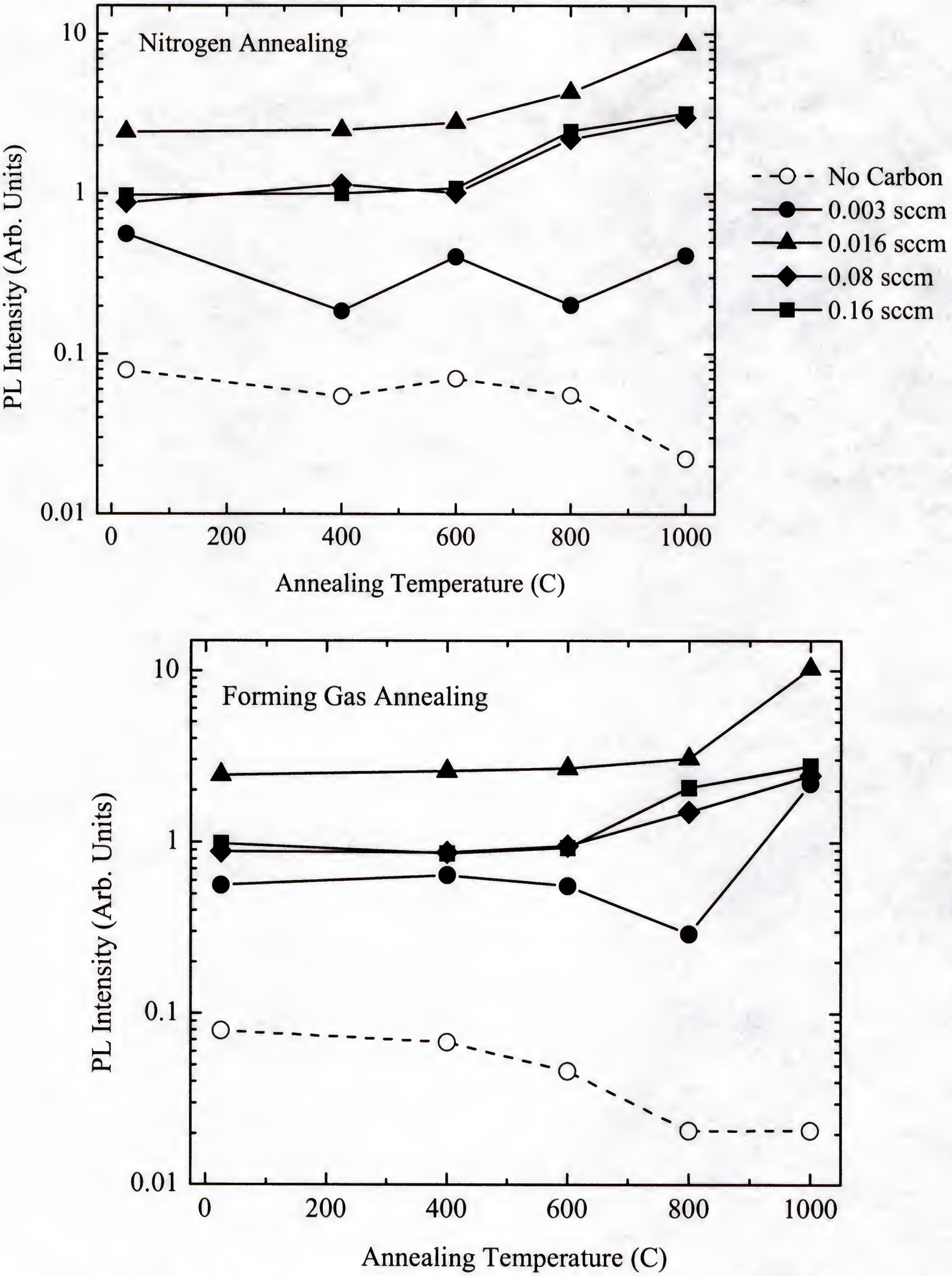

Figure 6-12: Effect of annealing on room temperature 1.54 μm PL intensity from GaN:Er using Ar^+ laser excitation. The annealing ambient was either nitrogen (top) or forming gas (bottom). The CBr_4 flows used during growth of the various layers are listed in the figure.

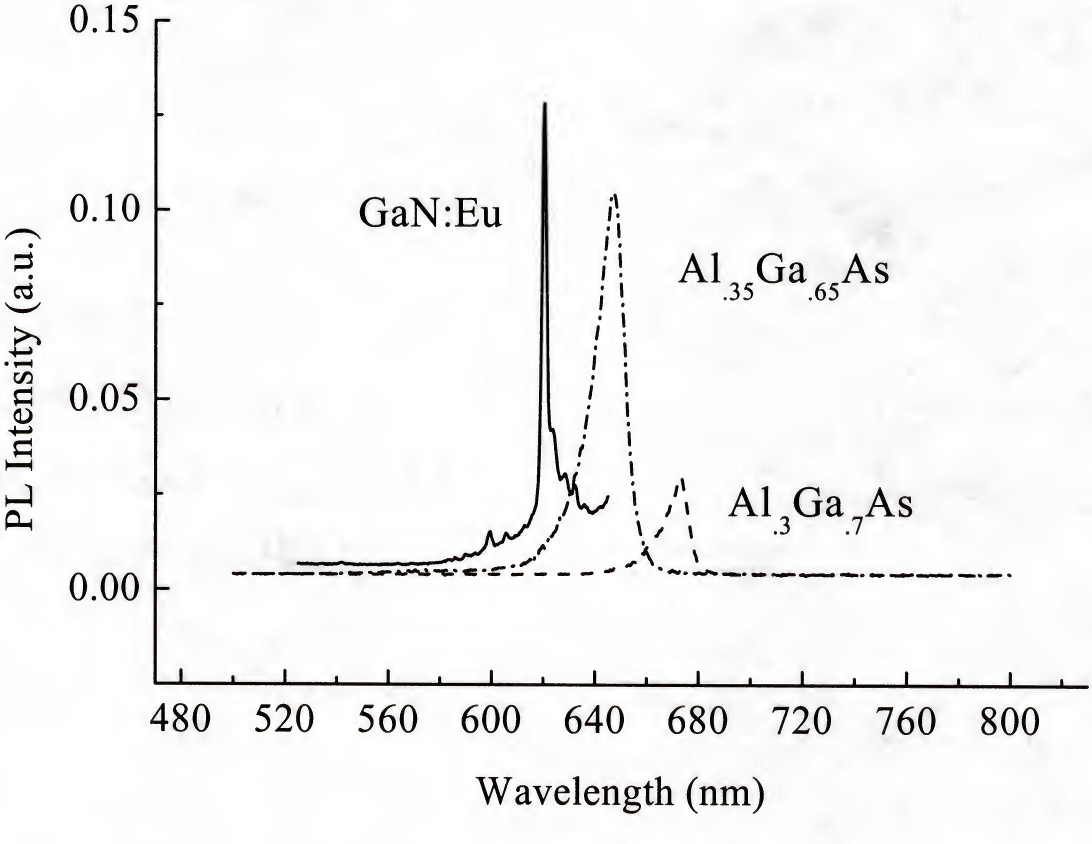

Figure 6-13: PL spectra of GaN:Eu in comparison with MOCVD derived AlGaAs. The GaN:Eu PL was measured with a He-Cd laser, while the AlGaAs was measured with an Ar^+ laser. The laser power in both cases was 35 mW.

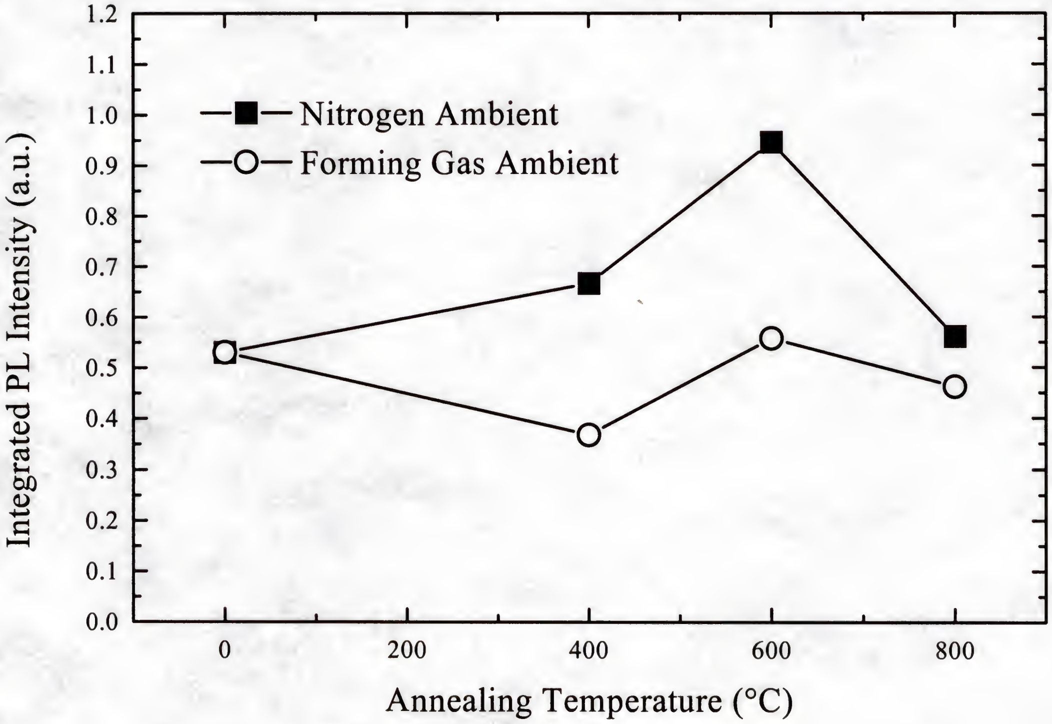

Figure 6-14: Integrated 621 nm PL intensity for GaN:Eu annealed in either N_2 or forming gas ambient.

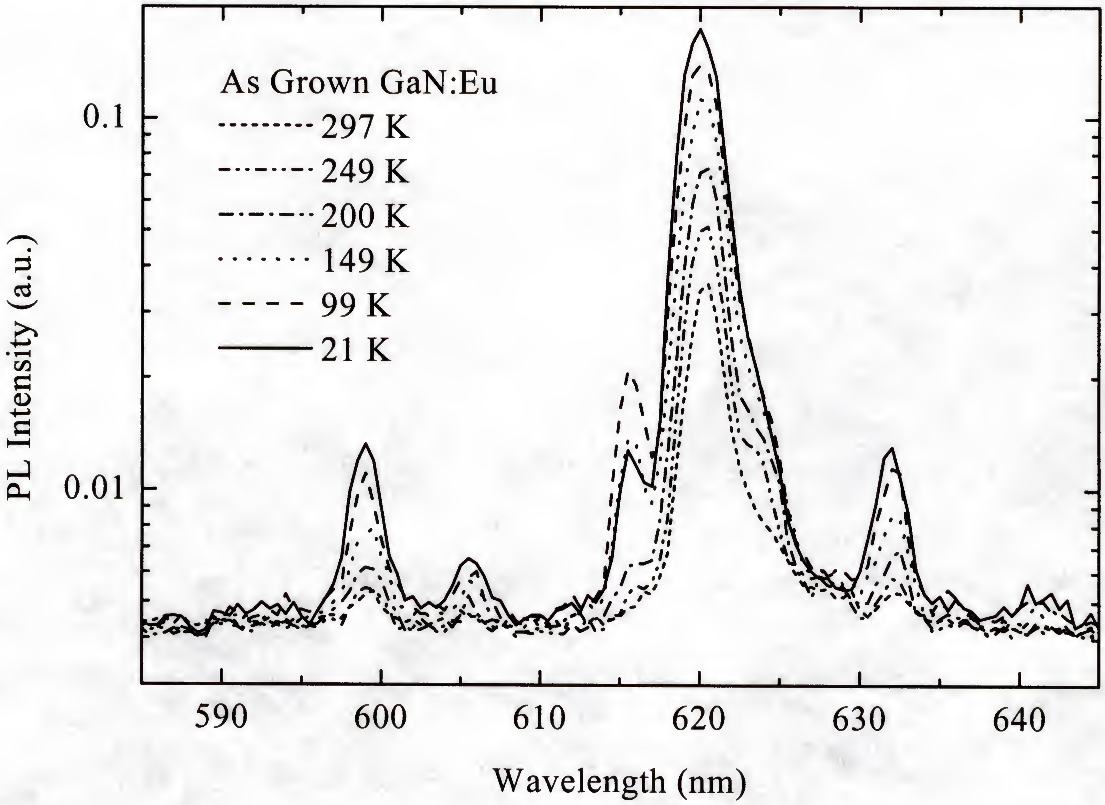

Figure 6-15: PL spectra taken at various measurement temperatures from as-grown GaN:Eu.

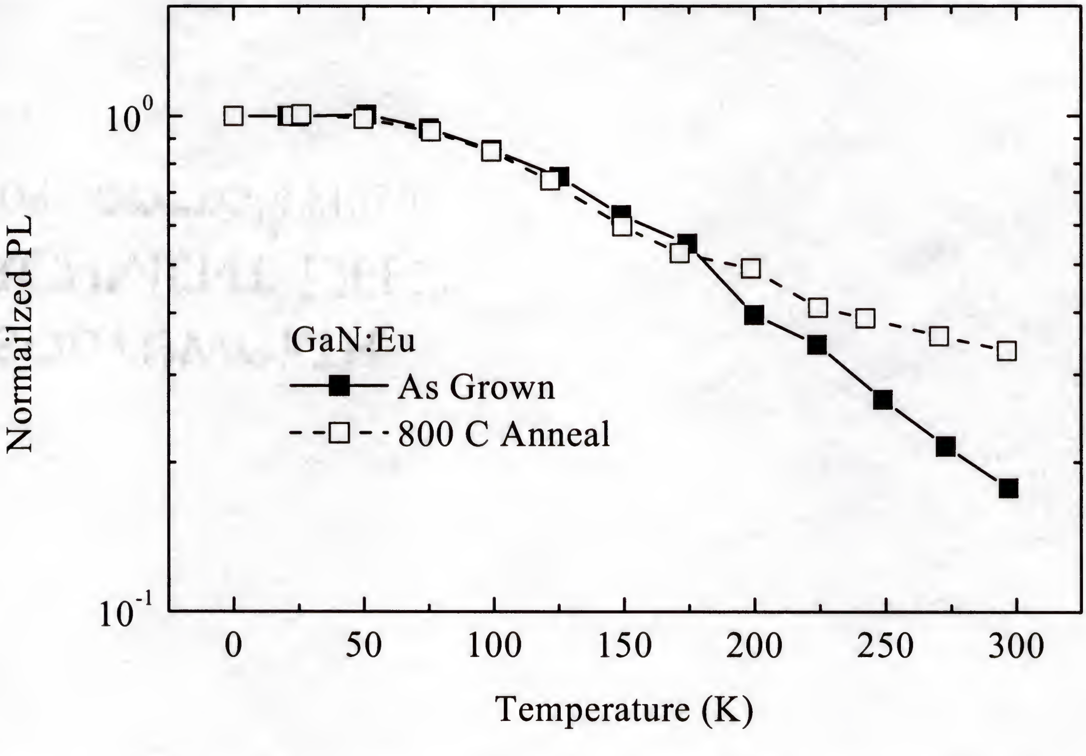

Figure 6-16: Thermal quenching results for both as-grown and N_2 annealed GaN:Eu. The PL was measured with a He-Cd laser.

CHAPTER 7
RESULTS AND DISCUSSION: GaMnN

In the theory based on a bound magnetic polaron (BMP) model from Chapter 3, predicted Curie temperature (T_{Curie}) values are presented for 5% Mn in various III-V and II-VI semiconductors with a concentration of free holes equal to $3.5 \times 10^{20}/cm^3$. To date, the best experimental T_{Curie} values for InMnAs, GaMnSb, and GaMnAs reasonably agree with theory, but are still well below room temperature. However, the III-V DMS material GaMnN is predicted to have a T_{Curie} well above room temperature. In this chapter, the doping of GaN with Mn will be investigated with the goal of realizing ferromagnetism for an approximate Mn level of 5 %. As charge carriers and crystal quality also play a significant role in the overall ferromagnetic exchange effect, the interplay between carrier type, carrier concentration, and sample quality with the sample magnetic properties will also be studied. An attempt to dope the GaN (or any III-V) with 5 % of any element poses unique challenges.

7.1 Incorporation of Mn into GaN

7.1.1 Starting GaN Growth Recipe

As with the growth of the RE-doped GaN in Chapter 6, a growth temperature of 750 °C was used as a starting temperature towards the synthesis of GaMnN. Although the general rule-of-thumb indicates a T_{growth} of 1000 °C should be used for the GaN, again it was felt that due to the high vapor pressure of Mn at this temperature, the Mn incorporation might be prohibitively low making a 5 % level difficult to achieve. In the epitaxy of the III-Mn-As and III-Mn-Sb given in Chapter 3, reduced growth temperatures were used to incorporate the necessary 5 % of Mn and to avoid the formation of precipitates. For example, epitaxial GaAs is normally grown at 600 °C, while the GaMnAs was grown at 250 °C. For the epitaxial growth of GaMnN, the growth temperature cannot be dropped to such an extent. Amorphous GaN will begin to form if T_{growth} is less than approximately 600 °C, so the 750 °C growth temperature was deemed to be the lowest temperature to be used for producing the GaMnN.

The GaMnN films were initially grown using the same GaN recipe that was used in the later parts of Chapter 6. The (0001) Al_2O_3 substrates were exposed to a nitrogen plasma (375 W forward power, 3 sccm N_2) at a temperature of 865 °C for 5 minutes. A 20 nm low temperature (T_{growth} = 435 °C) AlN buffer layer was then applied. A GaN layer was then grown for 40 minutes at a temperature of 750 °C. Finally, a GaMnN layer was grown for 20 minutes, also at 750 °C. The growth rate of GaN under the conditions used was approximately 69 Å/min. Room temperature Hall effect measurements indicate that the GaN is n-type with an electron concentration of 4 X $10^{19}/cm^3$. The high level of donors is believed to be due to a large concentration of N vacancies.

7.1.2 Doping with Mn

For the GaMnN growth, after the 40 minutes of GaN growth, the shutter for the 4N Mn K-cell was opened. No other system parameters were changed. A series of samples was grown using Mn cell temperatures that varied between set points of 675 °C and 937 °C, which corresponds to a change in the Mn vapor pressure of three orders of magnitude. After growth, the Mn level was evaluated using Auger electron spectroscopy

(AES). A representative spectrum of GaMnN is given in Figure 7-1. This sample corresponds to GaMnN with a Mn level of 7.0 %. The peak at 385 eV is the N, the peak at 589 eV is the Mn, and the peak at 1065 eV is the Ga. For the range of cell temperatures used, the AES analysis showed the Mn incorporation to be linear with Mn cell temperature for Mn concentrations in the range of ~1.1 % to 43.1 %, as shown in Figure 7-2. The high concentrations that could be achieved suggest that in spite of the high vapor pressure, the Mn sticking coefficient is adequate even at elevated GaN growth temperatures. The [Mn] vs. $1/T_{Mn}$ behavior was fit with an Arrhenius-type curve (shown in Figure 7-2), and an activation energy for Mn incorporation was determined to be 1.53 eV. This compares to a activation energy of 2.57 eV from the [Mn] vs. $1/T_{Mn}$ vapor pressure curve. The lower activation energy would indicate easy incorporation of Mn into the epitaxially growing GaN. The growth rate of the GaMnN is plotted as a function of $1/T_{Mn}$ in Figure 7-3. For the lower Mn fluxes, Figure 7-3 indicates a slight drop in the growth rate. This can possibly be due to the Mn slightly lowering the Ga sticking coefficient in this range of concentrations. However, as the Mn flux is increased, the GaMnN growth rate increases dramatically. This is most likely due to the Mn flux at this temperature becoming comparable to the Ga flux, producing a Mn_xGa_y alloy rather than GaMnN. This is supported by electrical measurements of the material carrier concentration. As the Mn concentration was increased in the single-phase GaN semiconductor, the GaMnN became increasingly resistive. This is in keeping with the expectation of a deep Mn acceptor (as in GaMnAs) that would serve to compensate the shallow nitrogen vacancy donor. At the very high Mn concentrations, Mn $\approx$ 47%, the films become conductive, presumably due to formation of the MnGa phases. MnGa is a metallic ferromagnet (Table 3-2).

7.1.3 Structural Characteristics of the GaMnN

The GaMnN material from this first series of growth experiments was investigated using x-ray diffraction to determine the presence of second phases within the material. Specifically, it was desired to know at what Mn level, as determined by AES, would second phases begin to appear. For the successful growth of GaMnN at a temperature of 750 °C, the Mn level must therefore be kept below this level. Magnetic measurements of GaMnN with higher concentrations of Mn would tend to measure this second phase, and not the DMS. As with the arsenides and the antimonides, the different Mn-N phases possess some magnetism. A powder x-ray diffraction scan of GaMnN with T_{Mn} = 747 °C is given in Figure 7-4. As can be seen from the figure, the only peaks that appear in the data are the GaN K_α (002) (34.6°), the GaN K_α (004) (72.8°), the sapphire K_α (006) (42.0°), the sapphire K_α (0012) (90.8°), and the sapphire K_β (0012) (80.1°). The remaining weak K_β peaks are lost in the noise of the measurement. This T_{Mn} corresponds to a Mn level of 8.8 % as determined by AES. Further increasing the T_{Mn} to 887 °C produced the diffraction pattern given in Figure 7-5. This produces a Mn level of 43.1 % as determined by AES. In addition to the GaN and sapphire peaks due to the underlying material, peaks of the tetragonal $Mn_{0.6}Ga_{0.4}$ phase become clearly visible. Obviously the solubility limit for Mn in GaN was exceeded and metal rich phases have been formed. This data also serves to verify what was implied from the growth rate and electrical data. RHEED analysis also showed evidence of a 3D or a polycrystalline structure. However, when GaMnN films with Mn concentrations less than 9 % were examined, no evidence of any other Mn-containing phase could be found other than GaMnN.

7.2 Effect of Substrate Type and C Doping on GaMnN Magnetic Properties

From Section 7.1, it was determined from Figure 7-2 that a T_{Mn} of 724 °C should be used to produce a Mn level of approximately 5 % within the GaMnN. Subsequent experiments were carried out using this Mn flux to try to produce material showing DMS-induced ferromagnetism. In addition, the effect of GaMnN film crystallinity and the effect of carrier concentration on the resulting magnetism were also investigated.

7.2.1 Gallium Manganese Nitride Growth Recipe

In this series of experiments, (0001) Al_2O_3 and the MOCVD derived GaN would be used as the starting substrate materials. In order to directly compare the results of using more than one type of substrate, and to remove the possibility of the MOMBE parameters drifting over the course of multiple growth runs, GaMnN was grown on both substrates simultaneously. The MOCVD GaN was n-type to $10^{18}/cm^3$, doped with Si donors. The high quality of the MOCVD GaN can be seen in AFM images of the as-received material in Figure 7-6. Evidence of the step-flow growth of the surface is evident in the two and three dimensional renderings of the surface, indicating the 2D nature of the film. The Root Mean Square (RMS) roughness of this surface is approximately 2.2 Å. Therefore, any GaMnN grown on top of this surface should be of high crystal quality. Because of the exposed GaN surface, no surface nitridation step or AlN buffer growth was performed prior to the growth of the GaMnN. Due to the GaMnN then being directly grown on the sapphire surface, the approximate 14 %

mismatch was assumed to produce a highly polycrystalline film. Again, the films were grown at a temperature of 750 °C with T_{Ga} = 955 °C and T_{Mn} = 724 °C, with the same N_2 plasma conditions, for 90 minutes. In the first case the material was grown without adding C. A second identical experiment was performed, this time adding C from the CBr_4 source. The CBr_4 was operated at a flow of 6.8 sccm and a pressure of 68 torr, while the recirculating bath was held at a temperature of 0.0 °C. These CBr_4 operating parameters have been previously calibrated by SIMS to produce a C concentration of $10^{20}/cm^3$ within the GaN. Before the growth was started, the substrates were held at 750 °C for 10 minutes under no nitrogen plasma. This was done as an in-situ clean to remove any oxide from the MOCVD GaN surface. The GaN surface went from a polycrystalline/amorphous RHEED pattern to the streaky 2D RHEED pattern evident in Figure 7-7. This assures a high-quality starting surface for growth. Chemical analysis of the material by AES indicates a level of 6.1 % Mn in the GaMnN sample and 4.5 % Mn in the GaMnN:C sample. Hall effect measurements on the finished material showed the GaMnN to be highly resistive to $n \approx 5 \times 10^{14}/cm^3$, while the GaMnN:C was conductive to $n \approx 5 \times 10^{18}/cm^3$. The non-carbon-doped sample again indicates that the Mn is probably acting as a deep acceptor in the material. However, the addition of C typically produces highly resistive material. The fact that n-type GaMnN was observed suggests that the C is behaving as an amphoteric dopant in this material (in the presence of the Mn).

7.2.2 Structural Characteristics of the GaMnN and GaMnN:C

The x-ray diffraction scan of the GaMnN grown on the MOCVD GaN is given in Figure 7-8, while the scans of the GaMnN:C grown on the sapphire and MOCVD GaN are given in Figure 7-9. In all three scans, the main peaks correspond to the K_α and K_β

peaks of the GaN and sapphire, as was the case in Section 7.1. However, a close examination of all three scans indicates the presence of other peaks in the material. This is particularly true in the case of the GaMnN:C film on the MOCVD GaN. In this sample, there are seven peaks that are not directly associated with either GaN or sapphire. These peaks are numbered one through seven. They all appear to some extent in Figures 7-8 and 7-9. In order to produce a high quality DMS material, the formation of second phases must be avoided, as is particularly true with the III-Mn-As work in Chapter 3. The MOCVD GaN substrates themselves were surveyed in the diffractometer to see if these peaks were visible in the bare substrate. The results of these scans are shown in Figure 7-10. Due to the difficulties in scanning single crystal samples by powder x-ray, the GaN substrate was scanned, turned 90° in relation to the detector and source, and then scanned a second time. From Figure 7-10, it is clear that six of the seven peaks are also visible, indicating that they originate from either the sapphire or the GaN. Peak number 3, occurring at $2\theta = 57.7°$, while not appearing in Figure 7-10, is closely associated with the (110) plane in GaN. It is also believed to be from the substrate. Having identified and associated all of the peaks in the GaMnN and GaMnN:C data with either GaN or sapphire, it is inferred that no second phases are present in the material.

While no second phases were visible within the material, it becomes important to ascertain what Mn_xN_y phase will appear within the epitaxially grown GaMnN films. In the GaMnN powder material from Chapter 3, it was found that Mn_3N_2 was the stable phase at the pressures and temperatures used for growth. A Mn_xN_y x-ray standard was grown at 750 °C using the 350 W/3 sccm N_2 plasma condition used to date for growth.

In order to assure a sufficient flux of Mn, T_{Mn} was 887 °C for this sample growth run. Subsequent x-ray diffraction of this sample is given in Figure 7-11. Analysis indicates that the thermodynamically stable Mn_xN_y phase at this growth temperature is Mn_4N. The K_α and K_β peaks can be identified within this sample to be from the (111) and (222) planes of Mn_4N. X-ray diffraction of the GaMnN has never indicated the presence of these peaks within the limit of detection of this measurement.

7.2.3 Magnetic Properties of GaMnN and GaMnN:C

Magnetically, higher carrier concentrations appear to be beneficial, as is prescribed by the bound magnetic polaron theory of Chapter 3. The highly resistive films with $n = 5 \times 10^{14}/cm^3$, despite 6.1 % Mn, only show paramagnetic behavior. In the films with $n = 5 \times 10^{18}/cm^3$, clear hysteresis in M versus H was observed at a temperature of 10 K, as shown in Figures 7-12 and 7-13, indicative of a ferromagnetic material. This suggests that the Mn-Mn exchange is indeed mediated by charge carriers. The effect of crystal quality on the ferromagnetism of the single-phase films is also apparent. The GaMnN:C film grown directly on sapphire (Figure 7-12), due to the lack of a buffer and the 14 % mismatch, is assumed to be polycrystalline. This film has a measured saturation magnetization of approximately 0.3 emu/cm^3. The same material grown on the MOCVD GaN buffer has a measured saturation magnetization of approximately 2.4 emu/cm^3 (Figure 7-13). This suggests that crystallinity plays a significant role in the magnetization since the MOCVD GaN is expected to produce superior growth. This is also evident in the moment of the grown films, ~0.008 Bohr magnetons per Mn for the material on sapphire versus ~0.28 Bohr magnetons per Mn for the material on GaN. This suggests also that a more ordered film leads to enhanced incorporation of Mn ions onto the Ga sublattice. Finally, the polycrystalline versus single crystal nature of the films manifests itself in the values of the coercive field for the two GaMnN:C films. The polycrystalline sample has a higher coercivity (~200 Oe) compared to the single crystal sample (~30 Oe). The higher coercive field suggests that the polycrystalline material is broken up into randomly oriented domains of local ferromagnetic order than the single crystal film, where the carrier mediated exchange can exist over larger distances without being interrupted by grain boundaries. This allows an enhanced collective ferromagnetism, resulting in a lower coercive field. For the polycrystalline sample, the application of a field must align the individual grains, producing more of a magnetic history when the field is reversed.

Measurements of magnetization versus temperature in the form of the difference between field cooled and zero field cooled scans of the GaMnN:C on GaN is also given in Figure 7-13, for an applied field of 1000 Oe. An asymptotic fit to this data at low temperature will give an approximate measure of the T_{Curie}, as indicated where the asymptote intersects M = 0. From the figure, the T_{Curie} is roughly estimated to be 100 K. However, a definitive measurement of the anomalous Hall effect and the production of an Arrott plot (M^2 vs. H/M) will be required to precisely determine T_{Curie}.

7.3 Gallium Manganese Nitride Growth at Elevated Temperature

From Section 7.2, the presence of C impurities and their related effect on the carrier concentration of the GaMnN indicates the importance of the carrier concentration on the DMS ferromagnetism. However, as was found in Chapter 6, the influence of C in the possible formation of a Mn-C complex and any possible related effect on the observed magnetic properties leads to the need to deconvolute C from the GaMnN material. In other words, will ferromagnetism be observed if the carrier concentration is increased without using the CBr_4 dopant source? To this end, the GaMnN was grown at an elevated temperature compared to that used in Section 7.2. Normally, as-grown GaN is n-type due to the formation of group V (nitrogen) vacancies during epitaxy and also due to oxygen if present in the film. With an elevated growth temperature, this effect will be enhanced, as more of the atomic nitrogen will tend to desorb from the GaMnN surface.

7.3.1 Material Growth

The material in this case was grown on (0001) Al_2O_3 that had been subjected to the surface nitridation step at 865 °C for 5 minutes. Identical AlN buffer layers were grown, as used in Section 7.1.1. Following the AlN growth, GaN was grown for 20 minutes, and the GaMnN layer was grown for 180 minutes. The GaN and GaMnN layers were grown at a substrate temperature of 865 °C. The total thickness was approximately 1.0 μm, resulting in a GaMnN layer growth rate of 54 Å/min. This lower growth rate, compared to that for GaN at 750 °C is directly due to the higher growth temperature causing enhanced desorption of the high vapor pressure materials. The Mn effusion oven was set to a temperature of 724 °C, resulting in a total Mn concentration of 7.0 at %, as determined by AES depth profiling.

7.3.2 Structural Properties

RHEED measurements of the GaMnN surface on the termination of the layer growth along the <11-20> direction, shown in Figure 7-14, clearly show a combination of well defined streaks with some evident spots. This mixture of 2D/3D growth indicates the acceptable quality of the GaMnN layer despite the large fraction of Mn within the material. Subsequent x-ray diffraction of the GaMnN reveals only the presence of K_α and K_β peaks corresponding to hexagonal GaN and Al_2O_3; no second phase peaks were found. The x-ray diffraction scan of this material is given in Figure 7-15. The slight bump at a 2θ angle of roughly 16° can be calculated to correspond with the (003) plane of sapphire. Due to the inherent difficulties in evaluating single crystal material in a powder diffractometer, this peak in particular often does not appear. This can be seen in the scans in Figure 7-10. This result shows promise for the future investigation of GaMnN, as low-temperature epitaxy of GaN is not required to obtain the necessary concentration of Mn within the material while avoiding the formation of second phases, as was the case with GaMnAs and InMnAs [105-129]. It also indicates that the relatively high growth temperatures needed for the epitaxial growth of the III-nitrides will not prohibit Mn incorporation, despite the high vapor pressure of Mn at these growth temperatures.

7.3.3 Electrical and Magnetic Properties

Magnetization versus magnetic field (M-H) as measured by SQUID magnetometry is shown in Figure 7-16. For this measurement, H was parallel to the sample plane and the measurement temperature was 10 K. From the figure, a clear nonlinearity in M is observed with a small amount of hysteresis. The coercive field is approximately 35 Oe and the saturation magnetization corresponds to 0.3 Bohr magnetons/Mn atom. This corresponds to 12 % of the deposited Mn ions contributing to the resulting magnetism. Again, the nonlinear shape and the observation of hysteresis indicates the presence of ferromagnetic ordering within the material and not simple paramagnetic behavior. The dependence of the magnetization on temperature is also shown in Figure 7-16, evaluated at a constant applied field of 1000 Oe. In this case, although the difference in the field cooled/zero field cooled data is small, a preliminary estimate can be made that the T_{Curie} for this material is below approximately 30 K. A more definitive measurement for the location of the Curie temperature can be made by searching for the appearance of the anomalous component in Hall effect measurements, as discussed in Chapter 5.

Magnetotransport properties of the GaMnN material were investigated in the temperature range between 10 K and 300 K for magnetic field sweeps between –7 T and +7 T. The Hall (transverse) and sheet (longitudinal) resistances were measured after applying In ohmic contacts to the GaMnN. The magnetotransport data are given in Figures 7-17 and 7-18. An AC impedence bridge was used in these measurements to maximize the signal to background noise ratio. The electron carrier density at 300 K was found to be 2.4 X $10^{19}/cm^3$, while the carrier density at 10 K was found to decrease slightly to 1.3 X $10^{19}/cm^3$. The high carrier density at 300 K indicates that the high growth temperature was effective in increasing the number of free electrons via an excess in nitrogen vacancies, despite the presence of the high concentration of Mn. The sheet resistance showed clear negative magnetoresistance below 75 K, with the value of $\Delta R/R$ at 10 K equal to 2.3 %. Also from Figure 7-17, a clear anomalous component to the Hall resistance can be observed in the 10 K measurement. This anomalous nonlinear component is found to vanish by the 25 K measurement. A slight anomalous component exists at a temperature of 20 K. From 25 K to 300 K, the Hall resistance data is found to be linear with a gradually decreasing slope, indicative of an increasing carrier concentration. The disappearance of the the anomalous Hall coefficient between 20 K and 25 K indicates that the ferromagnetic material has a T_{Curie} between these two temperatures. The linear Hall resistance data from 25 K to 300 K is consistent with the absence of magnetic moments due to the thermodynamically stable ferrimagnetic Mn_4N phase, which is reported to have a T_{Curie} as high as 745 K (Table 3-2). Another possibility is the presence of superparamagnetic clusters of MnGa, or some alloy thereof, with a diameter too small to be seen in the diffraction experiments and with a blocking temperature < 25 K. A definitive answer on the possibility of superparamagnetism will necessitate a high resolution transmission electron microscopy investigation of this material showing no clusters within the GaMnN to a resolution of approximately 20 Å.

Finally, the appearance of ferromagnetic ordering within the GaMnN material between 20 and 25 K is also interesting when compared to the theoretical prediction for n-GaMnN. In Chapter 3, it was mentionned that although electron-mediated Mn-Mn exchange was not impossible, the T_{Curie} predicted from theory was too low to be of practical use (< 1 K). When comparing p-GaMnN to n-GaMnN in relation to equation 3.1, few of the parameters are different. Assuming a consistent level of 5 % Mn, a similar spin (S), a similar confinement term, and $T_{AF} \approx 0$, the expected T_{Curie} can be calculated by substituting an electron concentration of 2.4 X $10^{19}/cm^3$, the electron effective mass in GaN ($0.2m_0$), and the exchange interaction constant, $\alpha = 0.2$, for electrons. The constant α substitutes for β in equation 3.1 (= 1.2 for holes). The result of this calculation gives an expected T_{Curie} of 0.67 K for n-GaMnN. This discrepancy of roughly an order of magnitude between experiment and theory may indicate that although there is relative agreement with the lower bandgap III-V materials, the theory breaks down for the wider bandgap III-V materials.

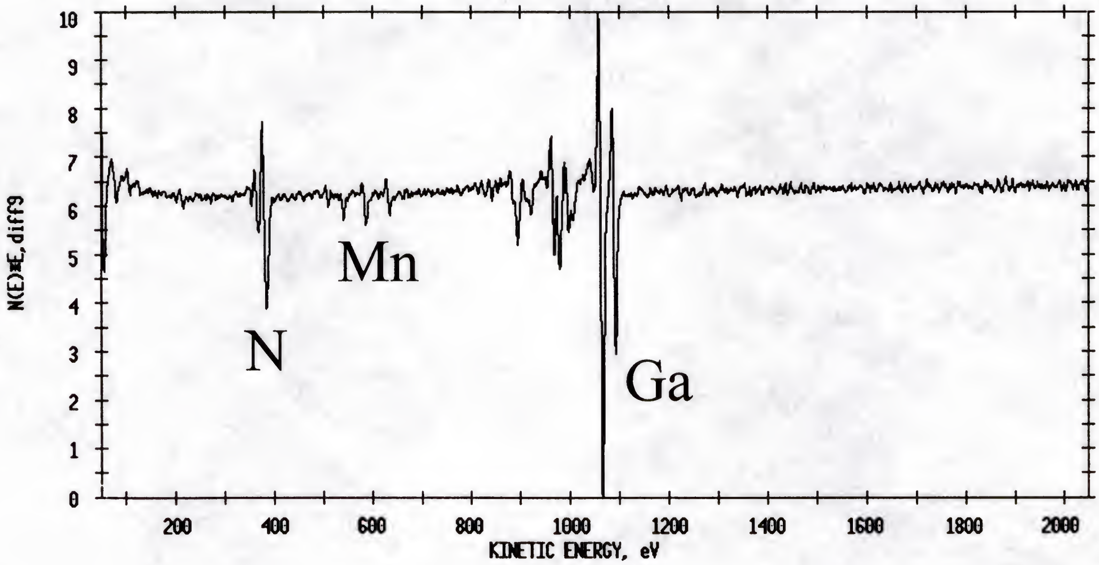

Figure 7-1: Auger electron spectroscopy (AES) survey of GaMnN.

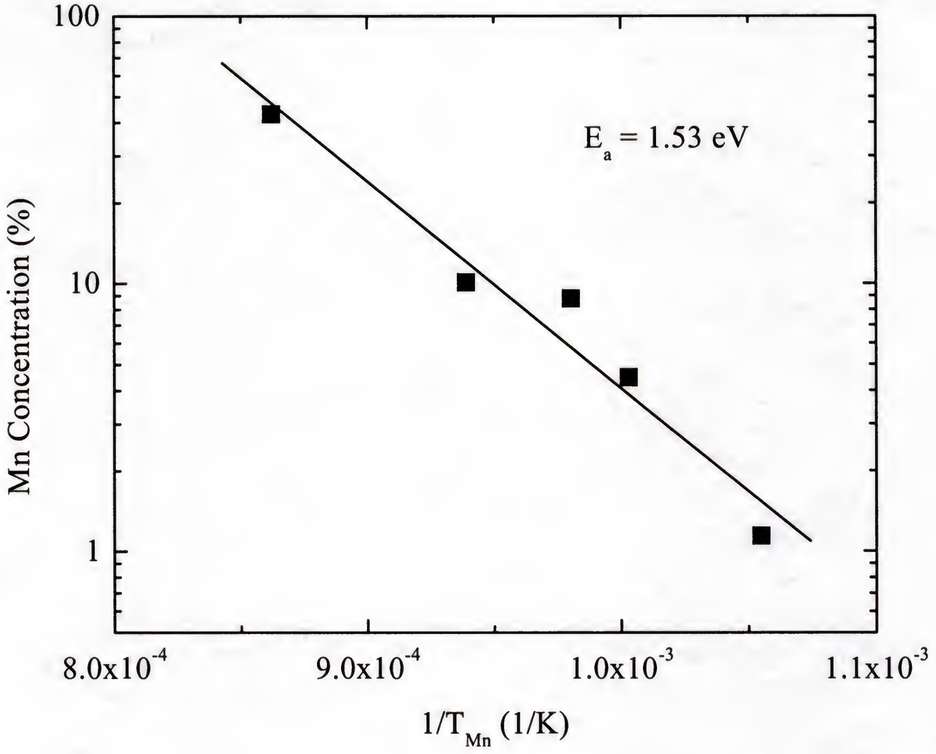

Figure 7-2: Variation of Mn concentration in GaMnN grown at 750 °C as a function of reciprocal Mn K-cell temperature.

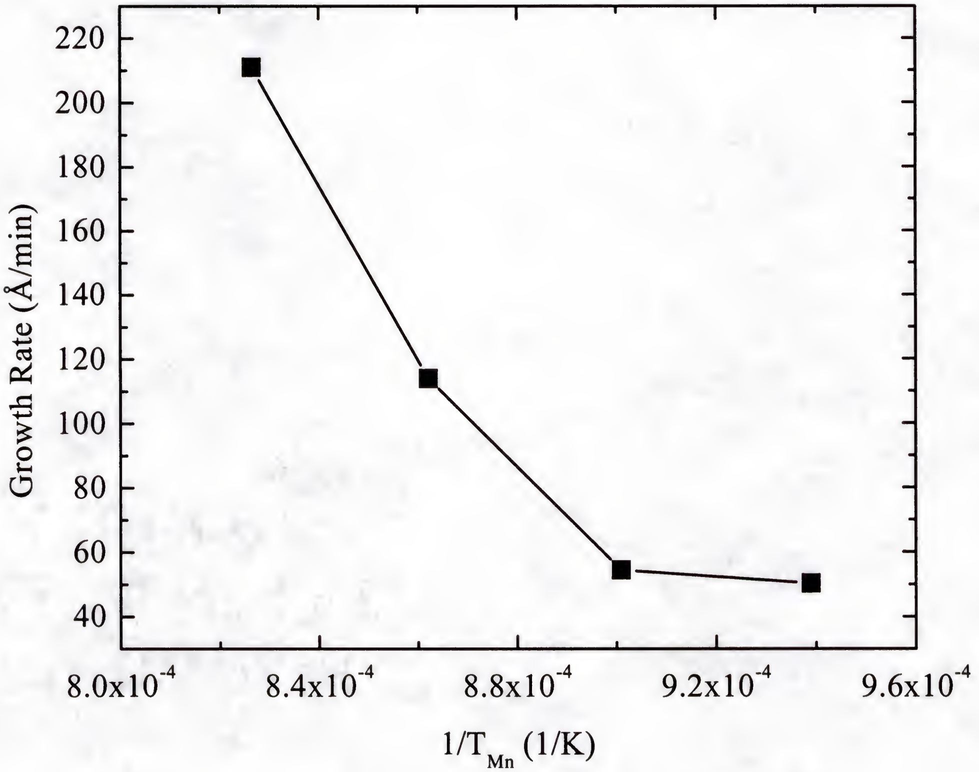

Figure 7-3: Variation of growth rate in GaMnN grown at 750 °C as a function of reciprocal Mn K-cell temperature.

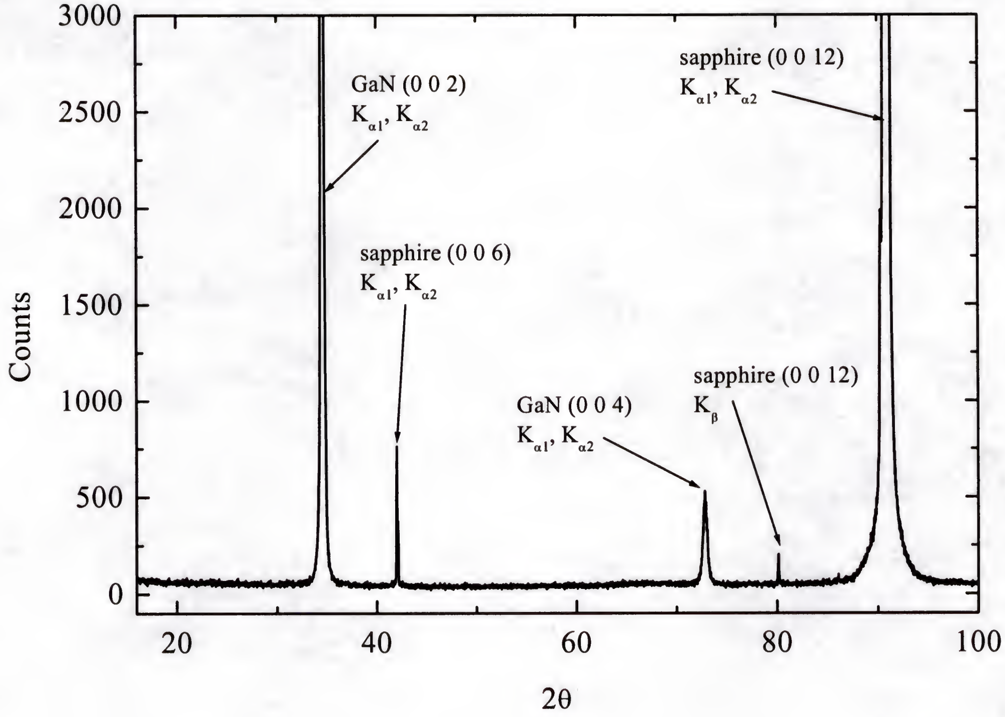

Figure 7-4: X-ray diffraction of GaMnN with the Mn K-cell at a temperature of 747 °C.

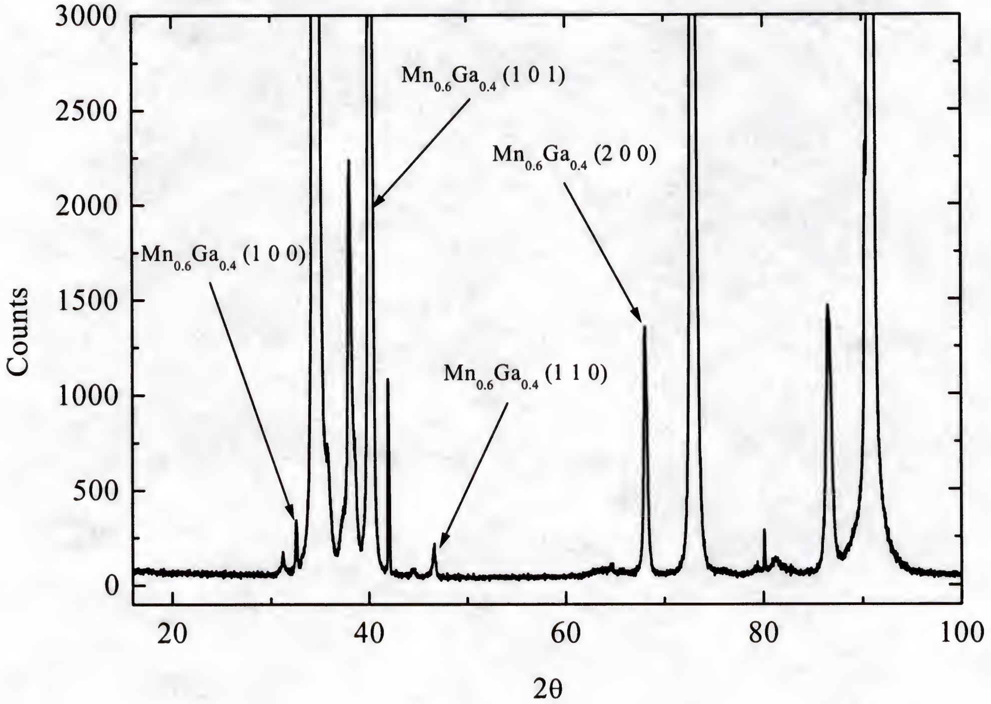

Figure 7-5: X-ray diffraction of GaMnN with the Mn K-cell at a temperature of 887 °C.

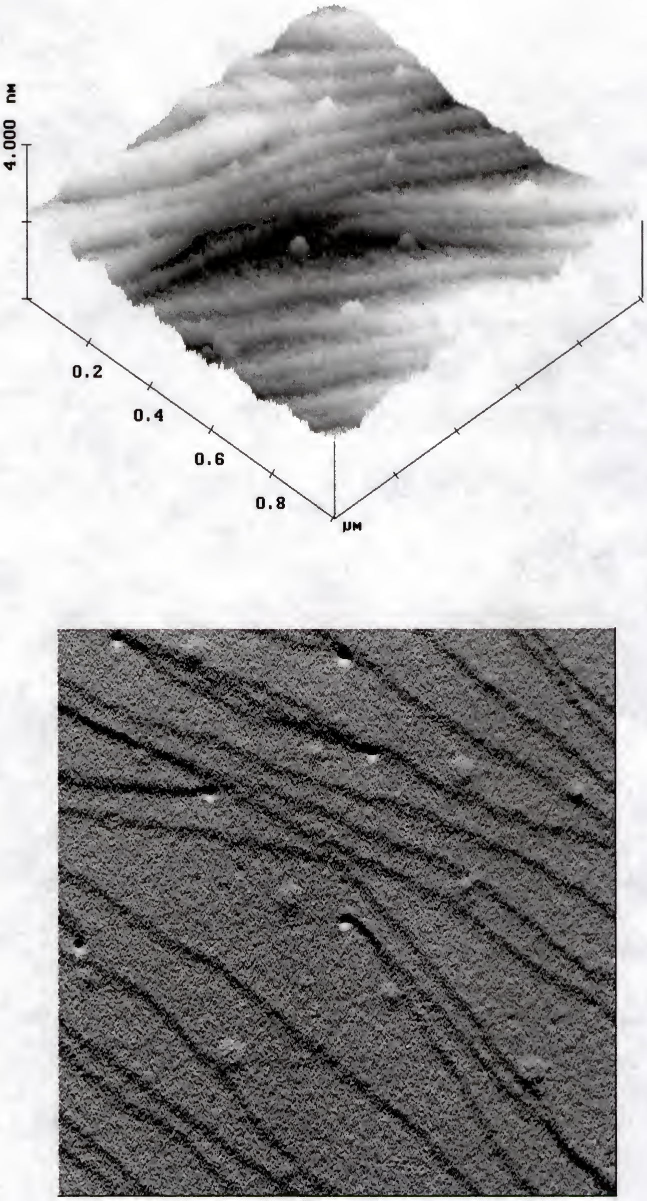

Figure 7-6: Atomic force microscopy (AFM) images of the as-received Epitronics GaN surface grown by MOCVD.

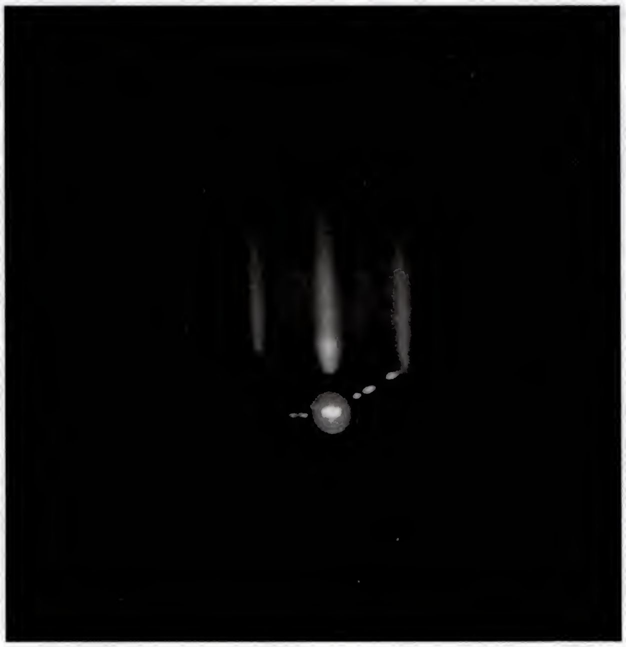

Figure 7-7: Reflection high energy electron diffraction (RHEED) photograph of the Epitronics GaN starting surface after in-situ oxide removal along the <1-100> direction.

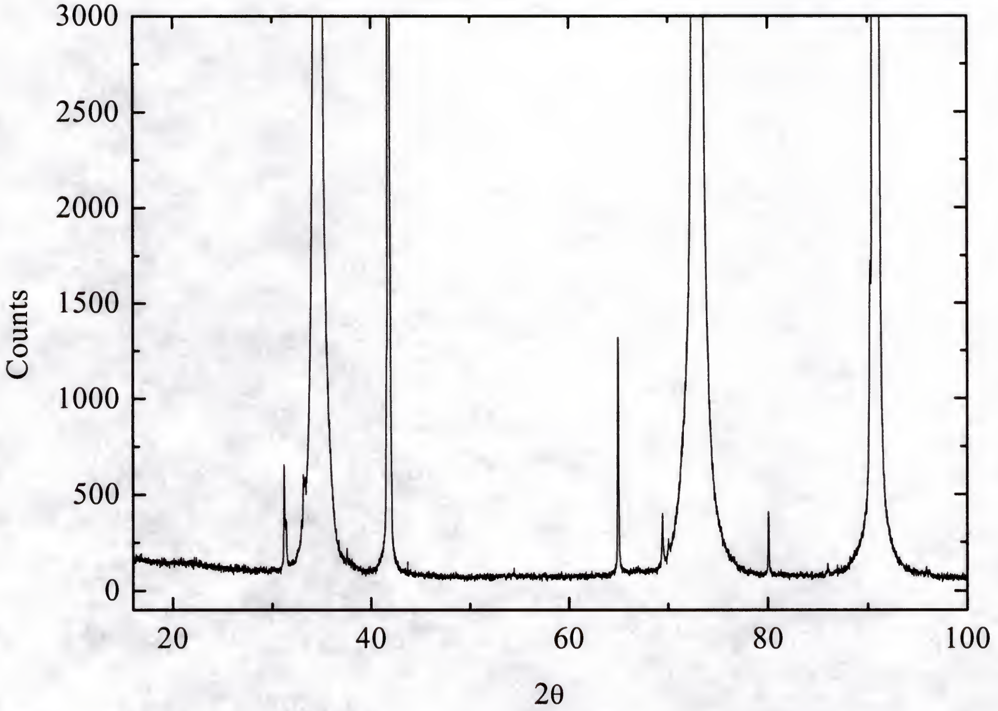

Figure 7-8: X-ray diffraction scan of the GaMnN film grown at 750 °C with the Mn K-cell at a temperature of 724 °C on the Epitronics MOCVD GaN.

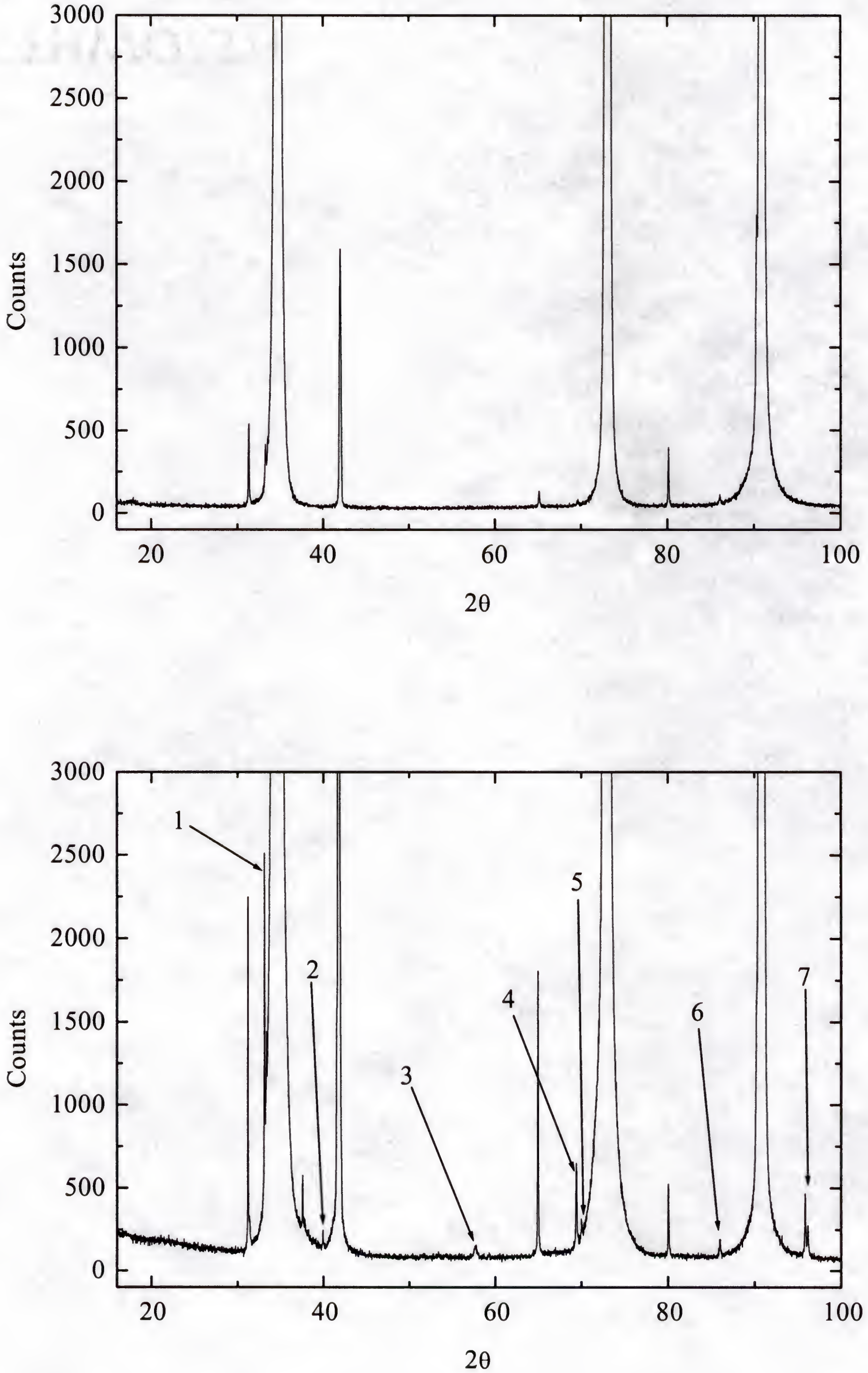

Figure 7-9: X-ray diffraction scan of the GaMnN:C film grown at 750 °C with the Mn K-cell at a temperature of 724 °C on sapphire (top) and on the Epitronics MOCVD GaN (bottom). The seven unidentifiable peaks are labeled.

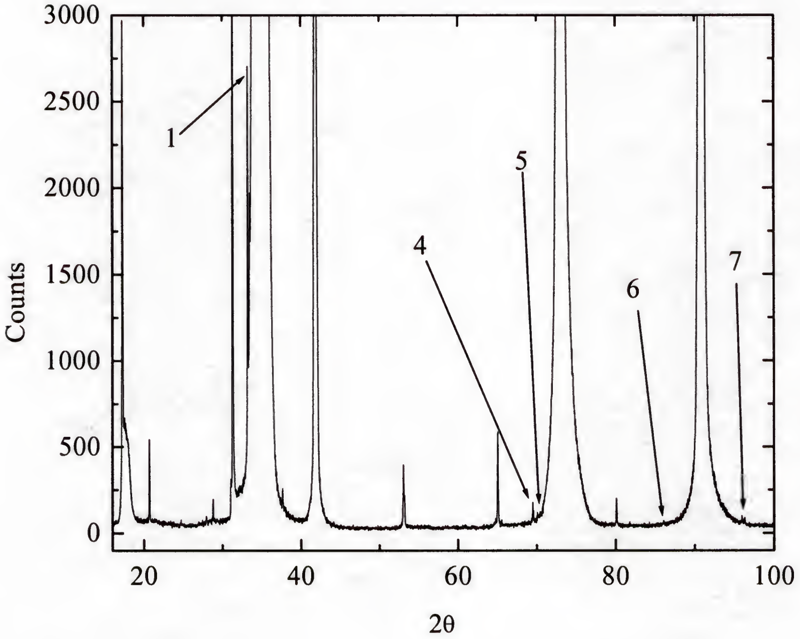

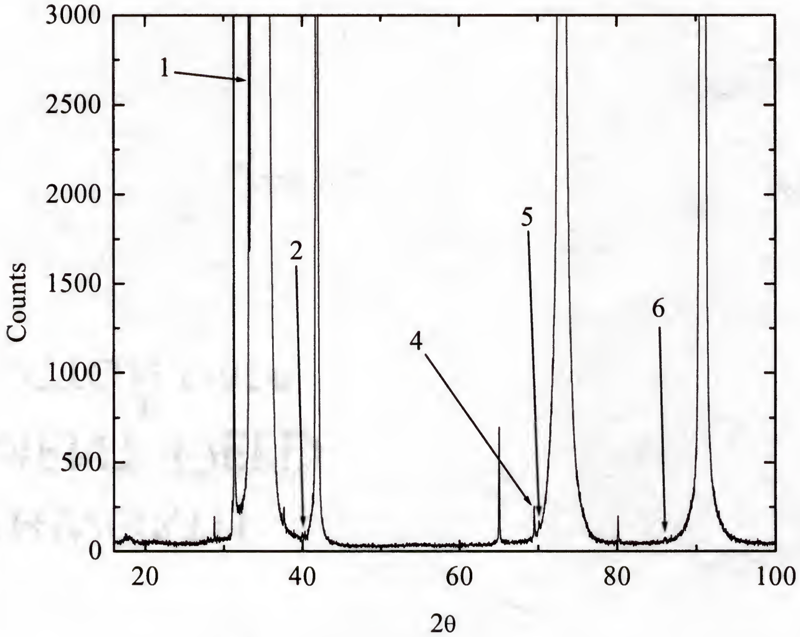

Figure 7-10: X-ray diffraction scans of the as-received Epitronics MOCVD GaN material. The bottom scan is of the same piece as the top scan, turned 90°.

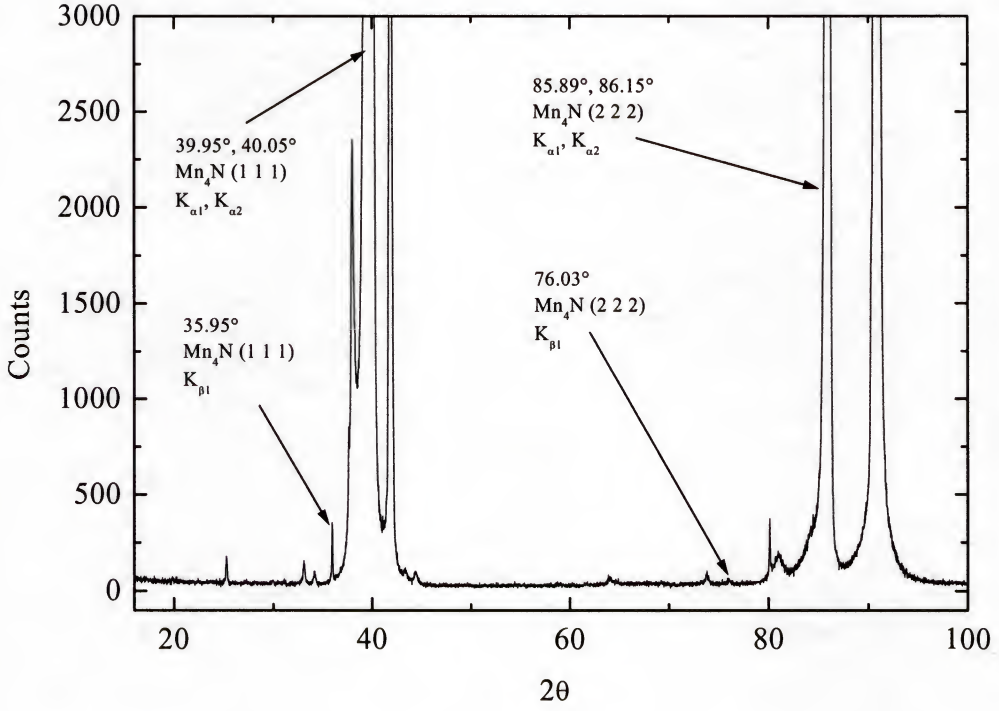

Figure 7-11: X-ray diffraction scan of sample grown at 750 °C with only N plasma and Mn shutters open, identifying the Mn_4N phase. The Mn cell temperature was 887 °C.

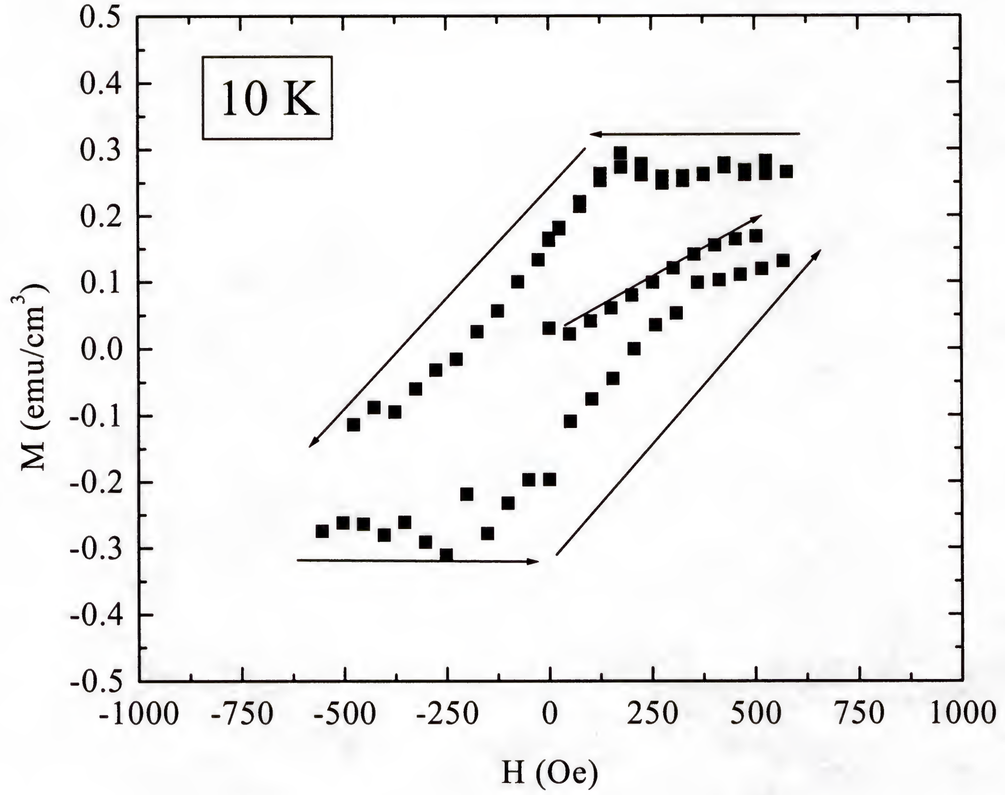

Figure 7-12: Magnetization versus applied field for GaMnN:C grown at 750 °C on sapphire at 10 K.

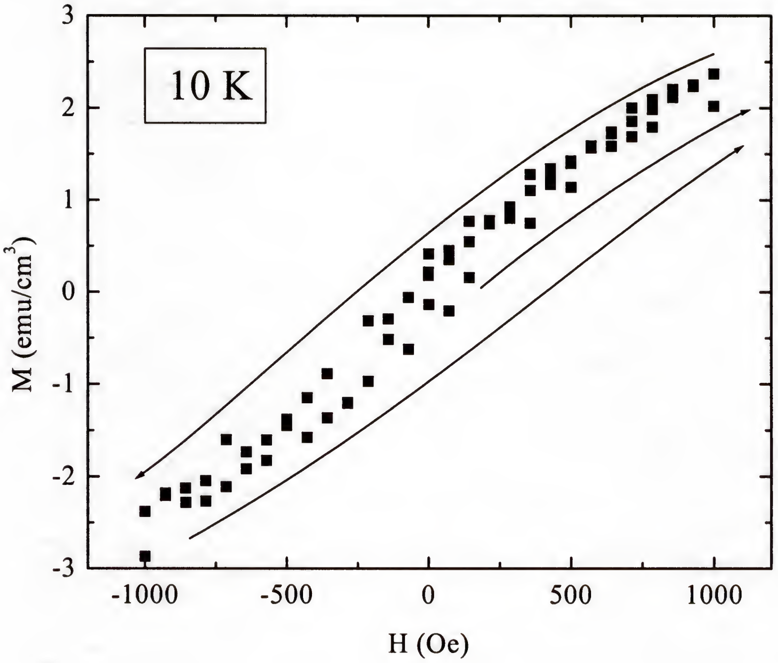

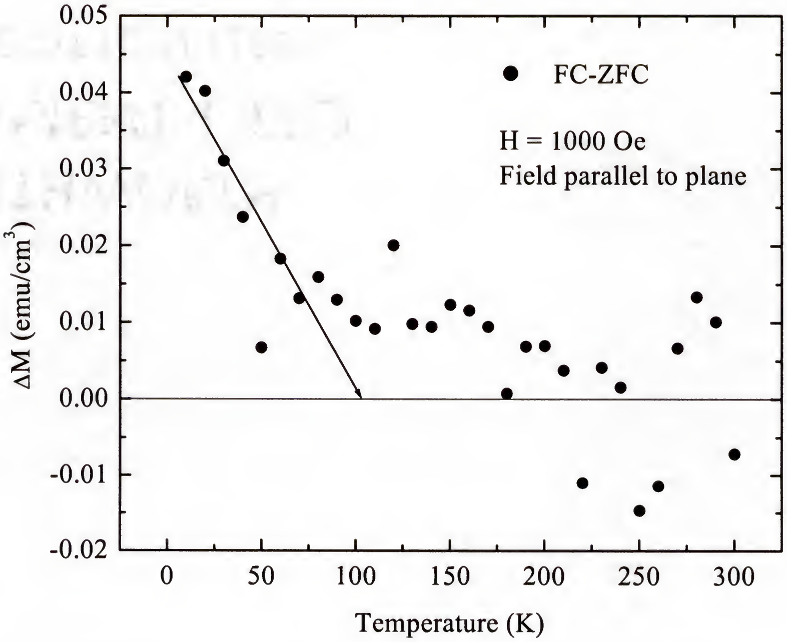

Figure 7-13: Magnetization versus applied field for GaMnN:C grown at 750 °C on Epitronics MOCVD GaN at 10 K (top) and versus temperature (bottom).

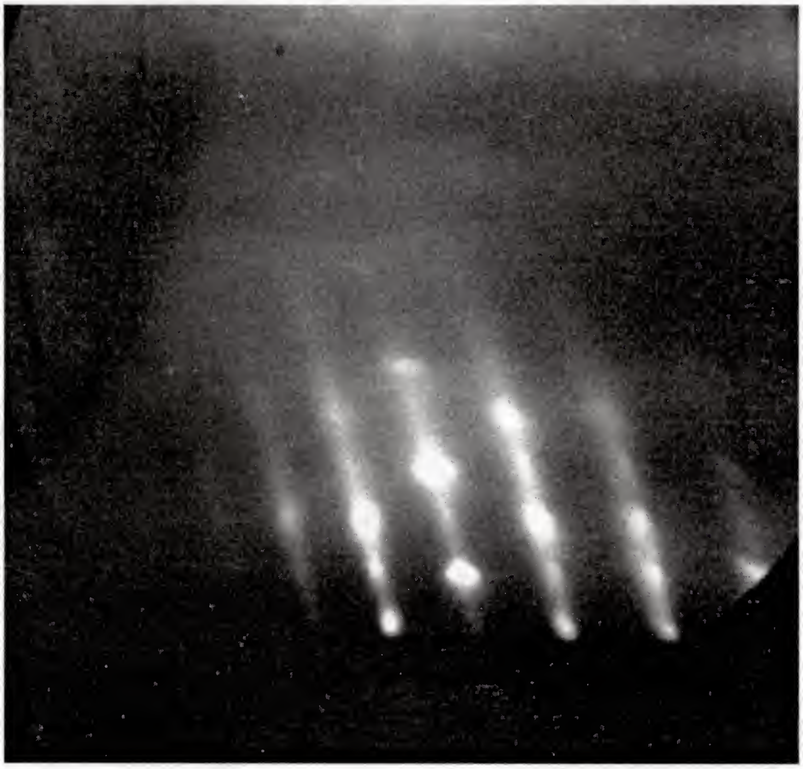

Figure 7-14: RHEED photograph along the <11-20> direction of the GaMnN after growth.

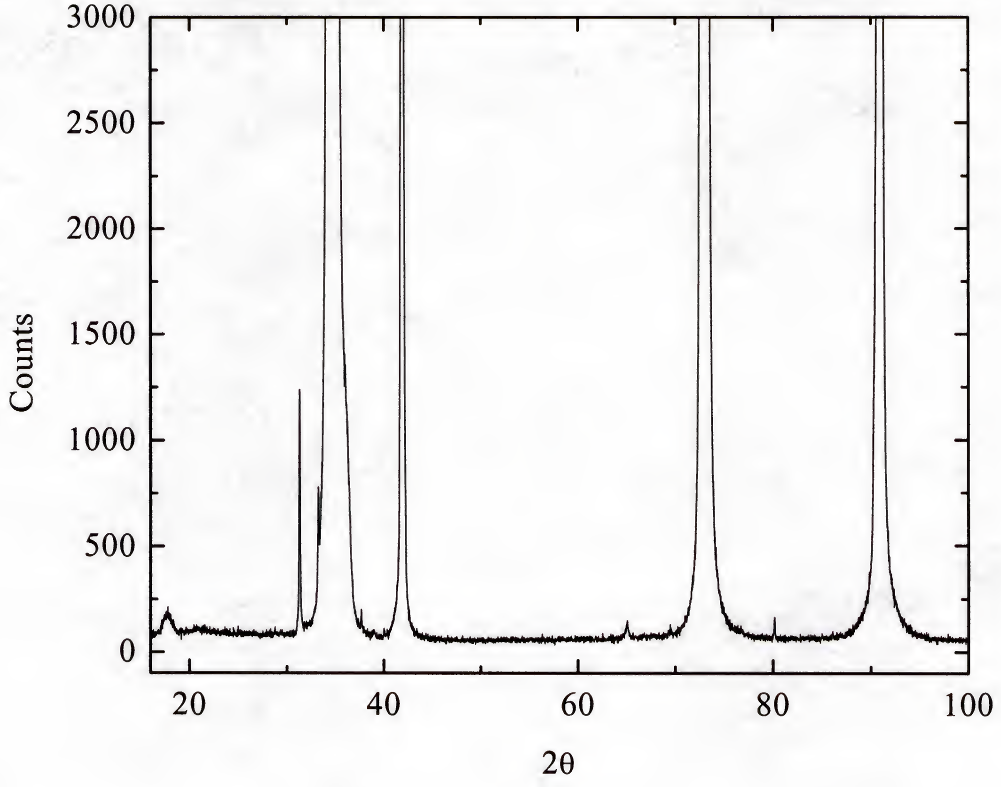

Figure 7-15: X-ray diffraction scan of GaMnN with 7.0 % Mn grown at 865°C.

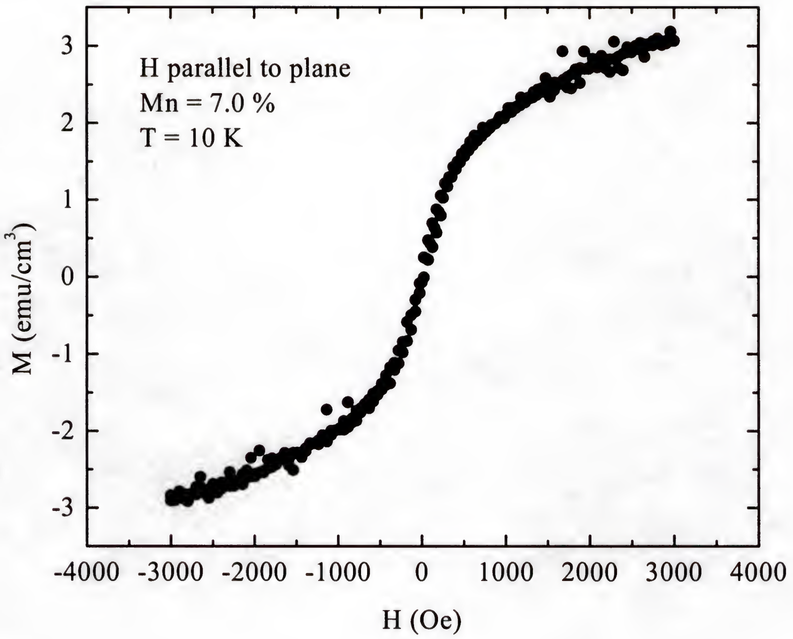

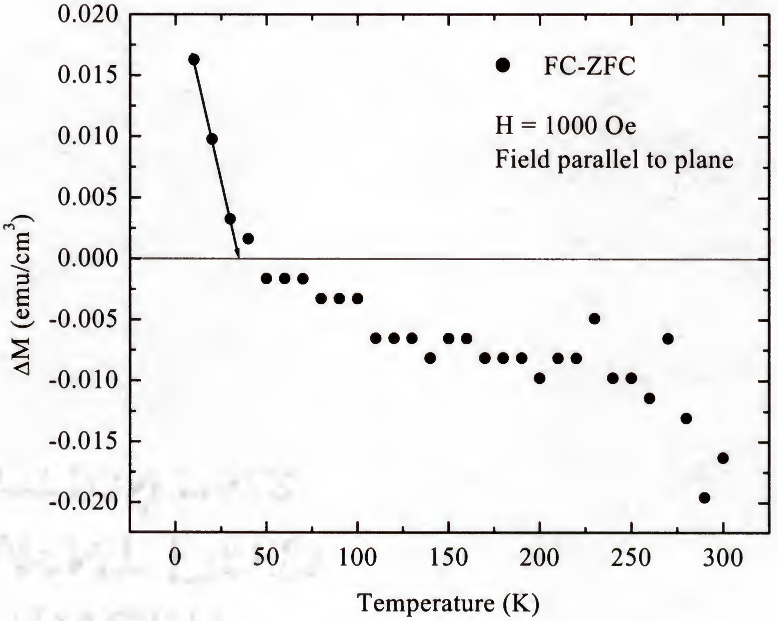

Figure 7-16: Magnetization of GaMnN with 7.0 % Mn versus field at 10 K (top) and versus temperature at constant field (bottom). Magnetic field applied parallel to the sample plane.

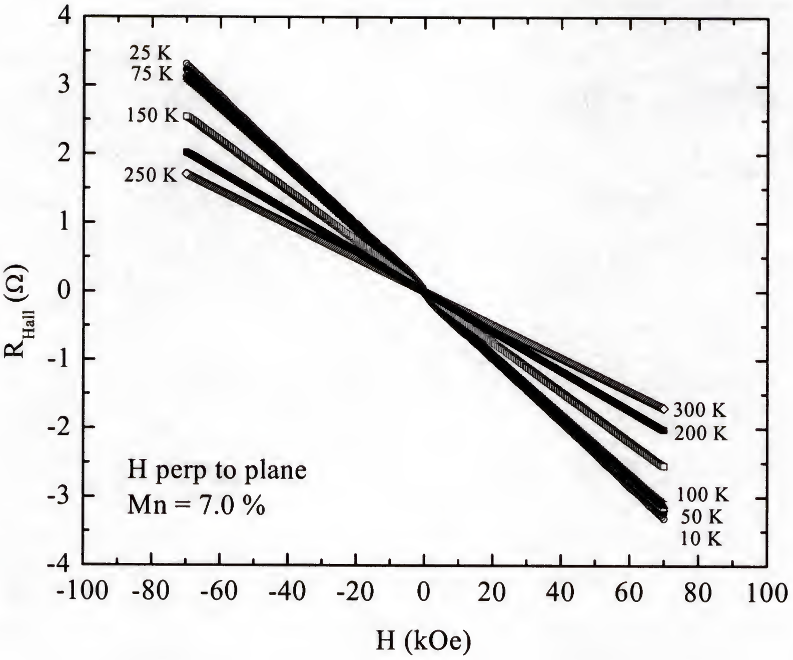

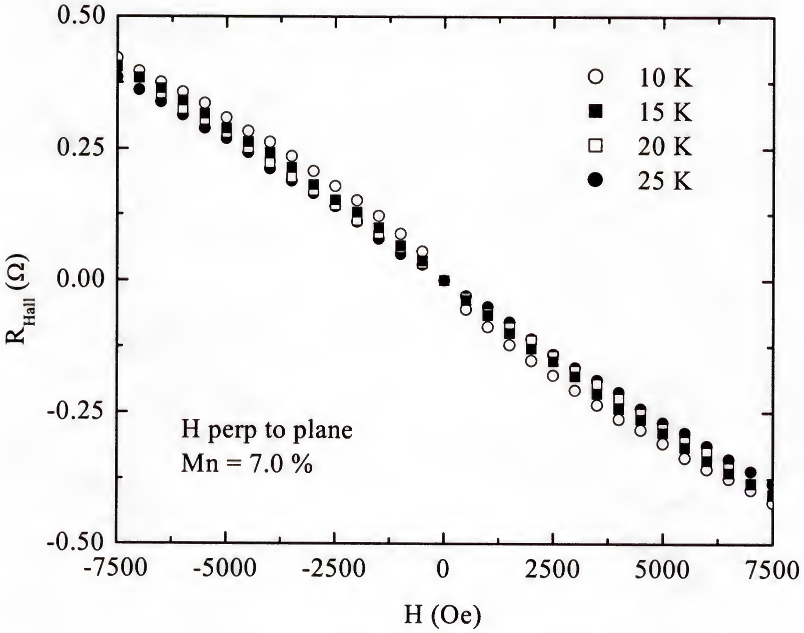

Figure 7-17: Magnetotransport Hall resistance data of GaMnN with 7.0 % Mn. Magnetic field applied perpendicular to the sample plane.

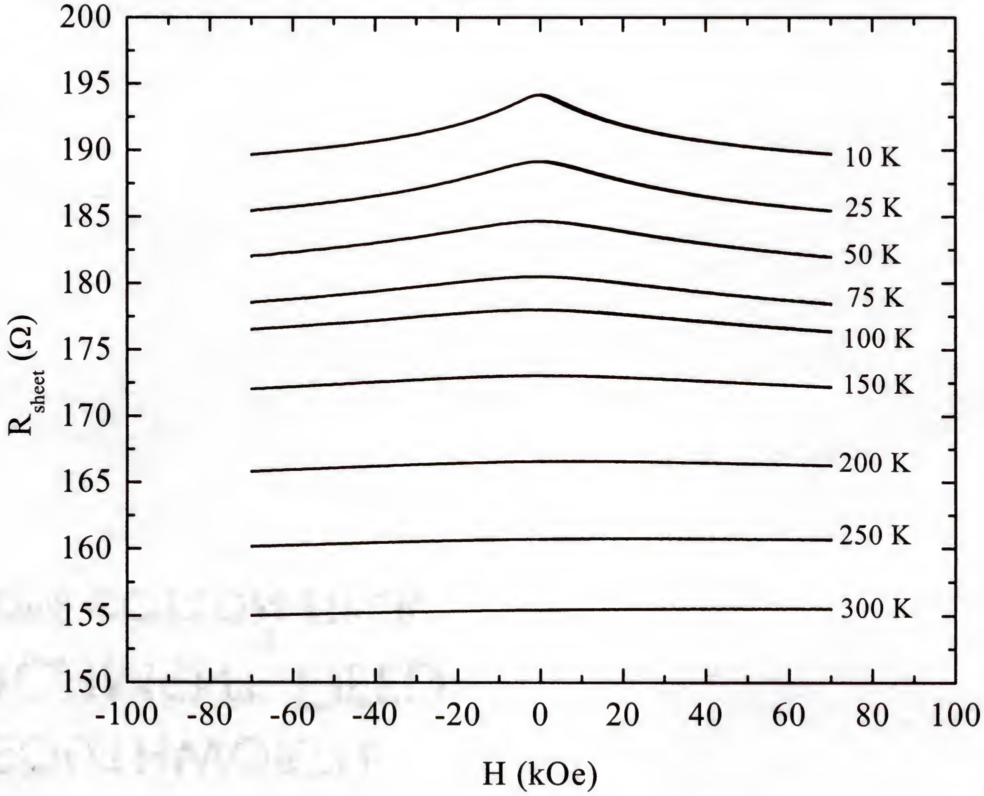

Figure 7-18: Magnetotransport sheet resistance data of GaMnN with 7.0 % Mn. Magnetic field applied perpendicular to the sample plane.

CHAPTER 8
RESULTS AND DISCUSSION: GaMnP

In Chapter 7, ferromagnetic order was observed in MBE-derived GaMnN. The observed T_{Curie} for that material, to the limit of the measurements made to date, indicates that the ferromagnetic to paramagnetic transition temperature is higher than what was theoretically predicted for n-type GaMnN. It is possible that the T_{Curie} that would be observed in the p-type material would also exceed the predicted value of ~400 K. However, growing p-type III-N materials is generally difficult, due to the presence of group V vacancies. By contrast, the n-type background tends to be lower in the arsenides and phosphides. In some III-Vs, such as GaAs and GaP, C can serve as a p-dopant, as it preferentially sits on the group V site. From Chapters 1 and 3, it was indicated that the DMS GaMnP is technologically interesting, as it is closely lattice matched to Si. Through C doping, achieving the necessary concentration of holes may be possible. Although the predicted T_{Curie} is only ~100 K, from the observations in Chapter 7 it seems possible that this figure may be even higher. In this Chapter, a comparable study will be performed on the DMS GaMnP.

8.1 Growth of P-Type GaP:C

8.1.1 Starting Recipe

For the growth of the GaP epitaxial layers, (100) GaP substrates were used, eliminating the need for any buffer layer or strain relief layer, as was done with the

GaMnN. These substrates were In-mounted to 2" Si wafers prior to loading into the MOMBE. The substrates were acquired with an epi-ready surface, indicating that no ex-situ cleaning process would be required. To remove the native oxide, the samples were heated to 600 °C under 5 sccm of the cracked PH_3 gas. The cracker, held at a temperature of 1050 °C, produces a beam of P and P_2, as observed by the mass spectrometer in the growth chamber. After being rotated under this beam for 5 minutes, the RHEED pattern given in Figure 8-1 consistently appeared. This 2D pattern indicates that the surface is ready for the GaP:C growth. The substrate temperature was then ramped to the growth temperature, and the PH_3 flow rate was lowered to 1 sccm. The pattern from Figure 8-1 remained after ramping to the growth temperature. To initiate growth, the Ga shutter and the CBr_4 injector would then be opened. As was described in Chapters 6 and 7, the CBr_4 provided the C. The Ga K-cell was held at a temperature of 955 °C, while the carrier gas was set to produce a CBr_4 flow of 1 sccm at a pressure of 10 torr. The recirculating bath was held at 3.3 °C. On the completion of the GaP:C growth, a good 2D RHEED pattern would result, given in Figure 8-2. Note that this pattern is a 2-by reconstruction; the epitaxial surface was (1 X 2). The growth rate of this material was 71.9 Å/min. The same growth rate and RHEED pattern would result for growth temperatures ranging from 225 °C to 600 °C. Evidence from Chapter 6 indicates that the production of Br radicals from the CBr_4 decomposition serve to planarize the film, possibly enhancing the crystal quality as determined by RHEED. To test this hypothesis, the same film was grown without the C at 350 °C. A RHEED of this surface after 15 minutes of growth is also given in Figure 8-2, showing a distinct 3D (spotty) pattern. This indicates that the Br radicals planarize the islands that form, producing a smooth surface. The growth rate of this material was 94.2 Å/min, indicating that the Br is also etching the surface. This same effect was also observed in Chapter 6.

8.1.2 Structural and Electrical Characterization

A powder x-ray diffraction scan of the starting (100) GaP substrate is given in Figure 8-3. The K_α peaks of the (200) and (400) planes are at 33.0° and 68.99°, respectively. The peak at 29.8° corresponds to the (200) K_β. The short peak at 16.9° can be calculated to correspond with the (100) plane. As with the low 2θ peak from the sapphire substrates in Chapter 7, this peak does not always appear in the diffraction data. The very small peaks at 31.5° and 65.7°, while not corresponding to any common plane in the cubic GaP phase, most likely are (200) and (400) peaks as a result of a slightly miscut GaP surface. An x-ray scan of GaP:C on GaP is also given in Figure 8-3. Again, all of the peaks that were visible in the scan of the substrate are present. A hump at low 2θ, centered at approximately 20° is also observed. This slight peak is probably due to x-ray scattering from regions with only short range order, possibly near the film-substrate interface.

Hall effect measurements were made on the GaP:C films to determine the ability of the C doping to provide an excess of holes. Squares of semi-insulating GaAs were also In-mounted on the Si wafers in addition to the (100) GaP, for the GaP:C and later the GaMnP:C growth. The (100) GaP substrates are nominally n-type, with an electron concentration of $< 10^{16}/\text{cm}^3$. When the ohmic contacts are annealed on the GaP:C on GaP, it is common for the diffusing In from the contact to "punch" through the film and also be in contact with the substrate. The films are approximately 4000 Å thick. When a Hall measurement is made, due to the conducting substrate, the source current will "short" through the substrate, giving a skewed measurement of the film's carrier concentration. For the measurements made in Chapter 7, this was not a problem as the samples were grown on insulating sapphire substrates. By using the semi-insulating GaAs chips, the Hall measurement will only measure the GaP:C film. Due to the lattice mismatch, the GaP:C on GaAs films are expected to be polycrystalline, giving an inaccurate measurement of the carrier mobility. The measurement of the carrier type and carrier concentration, however, should be reasonably accurate. Through the course of this dissertation work, four GaP:C films were grown using the same recipe. The samples were characterized consistently as p-type with a carrier concentration of 2.2 X $10^{20}/cm^3$. This result indicates the effectiveness of the C acceptor dopant. The GaP on GaP sample that produced the 3D RHEED image in Figure 8-2 was measured to be highly resistive.

8.2 Production of GaMnP:C by Ion Implantation

As a "proof of principle" demonstration of the feasibility of the DMS GaMnP, the p-type GaP:C layers were implanted with Mn^+ ions to produce GaMnP:C. Initially using ion implantation over MBE to develop GaMnP has several advantages. First, it is known that the starting material is already highly p-type, so the incorporation of Mn will not be required to produce the high hole concentrations required by the Bound Magnetic Polaron theory. Secondly, the amount of Mn incorporated into the material can be accurately controlled, insuring that the required percentage of the magnetic ions are in the material. Finally, it is relatively quick, as a successful epitaxial growth recipe does not have to be developed. In the following Sections, the magnetism of the GaMnP:C implanted samples will be evaluated in regard to Mn level and carrier type.

8.2.1 Implantation Procedure

The Mn^+ ions were implanted into the p-GaP:C layers with the hole concentration given in Section 8.1.2. The energy of the Mn^+ was 250 keV, while a dose of either 3 X $10^{16}/cm^2$ or 5 X $10^{16}/cm^2$ was used to produce either 3 % or 5 % Mn within the material. The p-GaP:C epilayers were approximately 4400 Å thick. To avoid amorphization during the implantation, the samples were held at a temperature of 350 °C during the implant. Following the implantation, the samples were annealed at 700 °C for 5 minutes under an N_2 ambient. The samples were placed face down during the annealing step.

8.2.2 Magnetic Characterization

The implanted GaMnP:C samples were characterized via SQUID magnetometry following the implantation. Magnetic results for GaMnP:C with 3 % Mn are given in Figure 8-4. From the curve of magnetization versus applied field, nonlinear hysteretic behavior is observed indicating a ferromagnetic sample. Note that the measurement temperature in this case is 250 K. The coercive field at this temperature is 105 Oe, while the saturation magnetization corresponds to a moment of 0.023 Bohr magnetons per Mn atom. The experimental observation of ferromagnetism at 250 K far surpasses the theoretical prediction given in Table 3-1 for GaMnP (~100 K). A more dramatic result is given by the measurement of magnetization versus temperature, also given in Figure 8-4. As with the GaMnN, this curve is the result of the difference between the field-cooled and zero field-cooled measurements. The applied field was 500 Oe. From where the M vs. T curve intersects the line M = 0, a T_{Curie} for this sample is implied to be approximately 275 K. Also, the shape of this curve is similar to that which is predicted theoretically according to the classical Weiss theory of ferromagnetism. On examining

Table 3-2, it may be implied that the observation of ferromagnetism is due to the Mn incorporating preferentially as the ferromagnetic MnP phase, which has a transition temperature of 291 K. As with the arsenides, antimonides, and nitrides, the formation of this second phase is primarily due to the high concentration of Mn in the GaMnP material. The possibility of the ferromagnetism being due to MnP can be discounted by observing Figure 8-5. This figure shows M vs. T behavior for the same p-GaP:C implanted with 5 % Mn, also at an applied field of 500 Oe. This measurement shows a significantly reduced degree of ferromagnetism, with a transition temperature indicated by the arrow of roughly 50 K. If the ferromagnetism shown in Figure 8-4 were due to the formation of MnP as the result of the heavy implantation of Mn, then Figure 8-5 should show a similar or even stronger effect. As this is not the case, this indicates that the ferromagnetism in Figure 8-4 is due to the formation of the DMS material GaMnP. The result given in Figure 8-5 also verifies part of the Bound Magnetic Polaron theory given in Chapter 3. The theory indicates that if the concentration of Mn is more than the optimum concentration, antiferromagnetic ordering of the Mn ions will commence, as was detailed in Figure 3-3. The onset of antiferromagnetism can explain the dramatic drop in the M vs. T behavior. The importance of holes over electrons (or more properly, the carrier concentration) for mediating the Mn-Mn exchange interaction, another requirement of the BMP theory, has also been explored. Figure 8-6 shows M vs. T behavior at an applied field of 1000 Oe for 3 % Mn implanted directly into the (100) GaP substrate. As detailed in Section 8.1.2, the as-received substrates were nominally n-type with an electron concentration $< 10^{16}/\text{cm}^3$. Figure 8-6 also shows a dramatic drop in the degree of ferromagnetic ordering when compared to Figure 8-4 for the samples with 3 %

Mn. The result given by Figure 8-6 indicates the importance of holes over electrons and/or a high carrier concentration in the DMS GaMnP. It also indicates that the strong ferromagnetism given in Figure 8-4 is not due to the formation of MnP precipitates, as the likelihood of formation is the same in both cases.

8.3 Epitaxial Growth of GaMnP:C by MBE

The successful production of GaMnP films via ion implantation indicates that an attempt to produce GaMnP via epitaxy can proceed with confidence. As with the epitaxially grown GaMnN, the challenge to grow GaMnP entails producing the required Mn concentration in the film, while maintaining a high concentration of free holes and avoiding the formation of microscopic precipitates. As the growth temperatures used for GaP are several hundred degrees lower than the temperatures used to grow GaN, care must be taken in controlling the flux of dopant from the Mn K-cell. The general approach used will be similar to that used to produce the GaMnN.

8.3.1 Doping with Mn

The recipe used to grow the epitaxial GaMnP is similar to that used in Section 8.1.1. After producing the 2D RHEED pattern due to desorption of the surface oxide, the substrate was ramped to the intended growth temperature. The epitaxial layers were grown under a flow of 1 sccm of PH_3, although 2 sccm was used if the growth temperature was 600 °C. This was done to insure an adequate P overpressure existed at the substrate. A GaP:C buffer layer was then initially grown for 2 minutes, using the same system parameters as in Section 8.1.1. The RHEED diffraction pattern was measured after the GaP:C step to insure a 2D surface reconstruction was maintained.

The GaMnP:C growth then started, the typical growth time being 30 minutes. The RHEED was again checked at the end of the growth step to see the final surface properties. As with the GaP:C layers, a semi-insulating GaAs chip was also mounted on the Si wafer to allow an accurate Hall measurement of the GaMnP:C film electrical properties.

The relative proportion of Mn in the film was again determined using Auger electron spectroscopy (AES). A typical AES survey spectrum for GaMnP:C is given in Figure 8-7. The spectrum in the Figure corresponds to a GaMnP:C film with 9.4 % Mn. The peaks at 120 eV and 1869 eV correspond to the P, the peak at 589 eV corresponds to the Mn, and the peak at 1075 eV corresponds to the Ga. The Auger analysis supports the conclusion, as with the GaMnN, that high concentrations of Mn can be incorporated successfully. Due to the lower growth temperatures involved, in line with those used for GaMnAs and GaMnSb, this was not considered to be a significant obstacle. The Mn concentration as a function of reciprocal cell temperature is given in Figure 8-8, for a variety of substrate temperatures. A linear relationship is observed for the GaMnP:C grown at 350 °C. This behavior was fit with an Arrhenius-type curve (shown in the Figure), and an activation energy of 2.29 eV was determined for the Mn incorporation. This is in reasonable agreement with the value of 2.57 eV determined from the Mn vapor pressure curve. This is indicative of good incorporation of Mn into the GaP. Samples were also grown at 400 °C and 225 °C, however the exact Mn concentration in some of these is not known, as the Mn level was at or below the Auger detection limit. SIMS analysis will be required to determine if this data fits on the line corresponding to the

2.29 eV activation energy (shown in Figure 8-8) for the 400 °C and 225 °C growth temperatures.

8.3.2 Electrical Properties and Phase Diagram of GaMnP:C

The electrical characteristics of the GaMnP:C films grown at a temperature of 400 °C are given in Figure 8-9. The hole concentration and the film resistivity are plotted vs. $1/T_{Mn}$. The film parameters for no added Mn are the same as those observed in Section 8.1.2 for GaP:C. The GaP:C films were p-type with a hole concentration of $2.2 \times 10^{20}/\text{cm}^3$, and a resistivity of 4.3×10^{-3} Ω-cm. As the amount of Mn is increased, the concentration of holes falls by roughly an order of magnitude for [Mn] = 1.0 %, and by another order of magnitude for [Mn] = 2.1 %. The decrease in free hole concentration with increasing Mn content appears to oppose the observation that Mn acts as a deep acceptor in GaP [163]. The behavior in Figure 8-9 appears instead to indicate that the Mn is acting as a donor within the GaP:C, lowering the overall concentration of the majority carriers. It is also possible that the decrease in the hole concentration is due to the Mn interacting with the C, preventing it from acting as an acceptor. For example, the Mn could interfere with the ability of the C to substitute on the Group V sublattice, or it could induce the C to start acting as an amphoteric dopant atom. The decrease in hole concentration is mirrored by a corresponding increase in the resistivity of the GaMnP:C material compared to the starting GaP:C. The resistivity increases by approximately three orders of magnitude between the Mn-free material and the GaMnP:C with [Mn] = 6.9 %. Again, the increase in the film resistivity may be due to the interaction of the Mn with the C, or the Mn acting as a donor in the GaMnP:C. The degradation of the structural quality of the films, as evidenced by RHEED, may also be a contributing factor. For the GaP:C, as mentioned in Section 8.1.1, a high quality (1 X 2) reconstruction pattern was observed (Figure 8-2). With T_{Mn} = 650 °C, corresponding to a hole concentration of 2.3 X $10^{19}/cm^3$, a single crystal RHEED pattern was still observed, although it shifted from purely 2D to a 2D/3D pattern, which includes streaky lines and highlighted spots. For the final two data points, corresponding to a hole concentration of 3-4.5 X $10^{18}/cm^3$, the RHEED pattern had become fully polycrystalline. This decrease in film quality would further increase the film resistivity, due to the scattering of the holes against the film grain boundaries. No second phases were observed in these films by x-ray diffraction.

The characterization of the GaMnP:C films in regard to chemical and electrical properties enables the creation of a phase diagram for this DMS system. This diagram, using the film growth temperature and Mn concentration as the axes, allows the separate film regions to be mapped, indicating the necessary growth conditions to possibly achieve ferromagnetism. This phase diagram is given in Figure 8-10. It should be noted that this diagram is only valid for a Ga K-cell temperature of 955 °C. Similar diagrams have been created for InMnAs and GaMnAs in the literature. On such a diagram, a lower boundary exists. This boundary indicates the lowest temperature at which single crystal GaP:C may still be grown, regardless of Mn level. In Figure 8-10, this line was placed at 200 °C. Experiments have produced single crystal GaP:C at a growth temperature of 225 °C. As the growth temperature is increased above this lower limit, all the films grown between 225 °C and 375 °C were determined by Hall measurements to be n-type, for all Mn concentrations. GaP:C grown at 350 °C was shown from other experiments to be highly p-type, so a possible explanation for this observation is that as the growth temperature decreases, the presence of Mn disables the C to act as an effective acceptor impurity. For growth temperatures above 375 °C, the GaMnP:C films were p-type, regardless of the Mn concentration. This result, in accordance with the BMP theory of Chapter 3, indicates a growth temperature of at least 400 °C should be used for the successful growth of ferromagnetic GaMnP:C. This demarcation of separate n-type and p-type regions was also observed in the InMnAs system. The phase diagram of Figure 8-10 also has the GaMnP:C system mapped out in regard to film structure, as observed via RHEED at the completion of each film growth run. Measurements by RHEED allowed the determination of structural boundaries for single crystal material and polycrystalline material for n-type and p-type films. The successful growth of the DMS GaMnP should also be performed in such a way that it is p-type in the single crystal region. Further experimentation will allow further refinements to the phase field lines in this diagram.

8.3.3 Growth Dynamics and Structural Characterization of GaMnP:C

An x-ray diffraction scan of GaMnP:C grown at a temperature of 600 °C with $T_{Mn} = 724$ °C is given in Figure 8-11. Analysis by AES indicated a Mn level of approximately 9.4 %. The film has a 3D surface pattern as evidenced by RHEED, and the measured growth rate was approximately 93.0 Å/min. The increase in growth rate and the RHEED pattern over those observed for GaP:C is not surprising, considering the high amount of Mn present. From Figure 8-11, the K_α and K_β peaks for the (200) and (400) GaP planes are clearly visible. The small additional peaks at $2\theta \sim 16°$, 31°, and 65° are from the GaP substrate, as detailed in Section 8.1.2. The small hump at $2\theta \sim 20°$, in addition to the lack of any other peaks indicates that second phases are not present within this material, to the limit of the powder diffraction measurement. The growth rate versus reciprocal Mn K-cell temperature is given in Figure 8-12 for a variety of film growth temperatures. The horizontal line in the figure represents the growth rate of GaP:C, which is 73.4 Å/min. For the lower Mn fluxes at 350 °C and 400 °C, the GaMnP:C growth rate is only slightly higher than the undoped material. As the Mn level is increased at a growth temperature of 400 °C, the growth rate increases initially, but then levels off with a further increase in the Mn flux. This increase in the growth rate is mostly due to the high added flux of Mn at this growth temperature in conjunction with an acceptable value of the Mn sticking coefficient. This supports the data from Figure 8-8, that suggests an excellent incorporation of Mn due to the similarity of the activation energy for incorporation with that of the Mn vapor pressure curve. The only slight increase in the growth rate for the material with T_{growth} = 500 °C and T_{growth} = 600 °C, when compared to the T_{growth} = 400 °C data may be due to the relative decreases in the Ga and Mn sticking coefficients at the higher growth temperatures. The growth rate data for the material grown at 225 °C suggests that the low Mn incorporation for the Mn cell temperatures used is not high enough to significantly change the growth rate. However, this does not appear to make sense when compared to the 400 °C data, as one would intuitively expect the 225 °C data to have higher growth rates. Fortunately, in regard to the formation of ferromagnetic p-GaMnP:C, this discrepancy at 225 °C is irrelevant in light of Figure 8-10, as this material is n-type and therefore expected to have a minimal T_{Curie}. The most interesting growth rate data is in regard to the material grown at 350 °C. From Figure 8-12, as the Mn flux is increased, the growth rate increases dramatically if the Mn K-cell is at a temperature of 724 °C or higher. The growth rate increases by more than a factor of five compared to the material with T_{Mn} = 650 °C. This large growth rate was found to exist in single layer and superlattice (SL – alternating GaP/GaMnP layers) materials. This increase was not observed for growth temperatures higher than 400 °C. The increase in the growth rate at 350 °C can be explained with Figure 8-13, which shows the Mn concentration and growth rate as a function of growth temperature for a Mn K-cell temperature of 724 °C. This cell setpoint was used the most often during the course of this part of the dissertation work, and therefore provides the most amount of data points. As the growth temperature is decreased from 600 °C to 500 °C, the Mn concentration increases. This is to be expected, as the Mn sticking coefficient in this temperature range will increase slightly, while the Ga sticking coefficient will remain relatively constant. As the growth temperature is decreased further, the Mn concentration appears to decrease. It would seem to appear that as the growth temperature decreases, the Mn sticking coefficient decreases and/or the Mn is becoming preferentially etched by the Br radicals that result form the decomposition of the CBr_4. However, the good preliminary agreement of the data in Figure 8-8 with the activation energy of the Mn vapor pressure curve at more than one growth temperature indicates that the Mn etch rate does not change significantly with growth temperature. This conclusion is further supported by the relative Mn incorporation rate as a function of growth temperature in Figure 8-13. Only a slight increase is observed between 600 °C and 350 °C for a constant Mn cell temperature, indicating that the etch rate is not changing significantly. From Figure 8-13, the relative Ga growth rate increases significantly between the 600 °C ad 350 °C growth temperatures (roughly a factor of 4). This large increase in the relative Ga growth rate at 350 °C explains the large growth rates observed in Figure 8-12. It also served to explain why the Mn concentration decreases. While the Mn flux remains relatively constant, the large increase in the relative Ga growth rate “dilutes” the Mn in the film, resulting in a lower observed overall Mn level. The large increase may be due to a decrease in the etching efficiency of Ga by Br at these low growth temperatures. This seems unlikely, as the etching of the Mn did not change appreciably. A second explanation is that at these lower growth temperatures, as the Mn concentration increases, the Ga sticking coefficient increases dramatically when in the presence of the Mn. An early explanation for the rapid increase in the overall growth rate at a growth temperature of 350 °C was that a second phase was forming within the material that had a larger lattice parameter in comparison to the GaP:C. If this were true, then for such a large increase, this second phase would obviously appear in a x-ray diffraction scan of the sample. A scan of the GaMnP:C grown at 350 °C with a Mn K-cell temperature of 747 °C is given in Figure 8-14. This sample had a measured growth rate of 504 Å/min. From this scan, no obvious peak due to a large amount of a second phase jumps out. The K_α and K_β peaks due to the (200) and (400) GaP planes appear as normal. As seen previously, the peaks at 16.8°, 31.5°, and 65.7° were observed in scans of the (100) GaP substrate. The small peaks at 30.9°, 39.0°, 47.4°, 56.3°, 75.9°, and 76.1° have all been previously seen in powder diffraction scans of GaP:C on GaP films grown for implantation, as in Sections 8.1.2 and 8.2.1. The peak at 28.4° corresponds to the K_α of the GaP (111) plane. Although this peak is not normally seen in the epitaxial GaP on GaP films, the large growth rate of this material, in conjunction with the observed polycrystalline RHEED pattern does not make its appearance surprising. Such a large growth rate could potentially make the growth of GaMnP:C at this temperature problematic. However, in light of Figure 8-10, the issue of such a large growth rate can be avoided due to the n-type character of all the films grown at 350 °C.

8.3.4 Microstructural Properties

From Figure 8-10, it would appear that the most promising set of growth parameters to obtain DMS ferromagnetism in GaMnP:C will involve a growth temperature of 600 °C. This material is single crystal (as determined by RHEED) and single phase (as determined by x-ray diffraction in Figure 8-11). The selection of 600 °C as the growth temperature of choice also introduces another apparently unique facet of the GaMnP system, in addition to the higher than expected T_{Curie}. In the growth of InMnAs and GaMnAs, it was found that just as there existed a lower limit on the growth temperature (for single crystal material), a high limit existed as well. Above this temperature, it was found that all the Mn incorporated as a second MnAs phase. It was to avoid this second phase that the lower, less desirable growth temperatures were used. Since no second phases in the GaMnP:C grown at 600 °C were found, it would appear that the upper limit (if it exists) for this system is greater than 600 °C. As epitaxial GaP is normally grown at 600 °C, low temperature growth is not necessary for GaMnP:C.

The lack of second phases or precipitates is also evident in XTEM selected area diffraction (SAD) patterns of the GaMnP:C grown at 600 °C, as shown in Figure 8-15. In both patterns, the primary transmitted spot is clearly visible. In the SAD of the GaMnP:C with 6.8 % Mn, the spots shown coincide with what is observed for the GaP substrate. No additional spots are observed, indicating the single crystal nature of this film. An additional set of spots is observed in the SAD photograph of GaMnP:C with 9.4 % Mn. However, these spots are found to be in line with a shift of the GaP pattern, indicating a slight tilt to the GaMnP:C grains. The single crystal nature of the GaMnP:C with 9.4 % Mn is also observed in the cross sectional transmission electron microscopy (XTEM) image given in Figure 8-16. Although the XTEM photograph shows the film has a rough surface, no evidence of microstructural second phase precipitates or Mn clusters is observed, to the 50 Å resolution of this measurement. This will be important when investigating the magnetic properties of these materials, as it serves to partially discount the possibility of ferromagnetic particles or superparamagnetic Mn clusters, as was discussed in Chapter 7.

8.3.5 Magnetic Characterization

The epitaxially derived GaMnP:C films grown at 600 °C were evaluated by SQUID magnetometry to assess their magnetic properties. Magnetization data for GaMnP:C with 6.8 % Mn is given in Figure 8-17. As with the implanted material, nonlinear, hysteretic behavior is observed at a measurement temperature of 10 K. The coercive field for this material is approximately 195 Oe. Magnetization versus temperature measurements at a constant applied field of 500 Oe (FC-ZFC) indicates that ferromagnetism persists up to approximately 250 K. This places the T_{Curie} for this material in line with the implanted sample of roughly the same Mn concentration. Comparable magnetic results were determined for the GaMnP:C sample with 9.4 % Mn, given in Figure 8-18. Again, hysteresis was observed at a temperature of 10 K, indicating the ferromagnetic nature of the material. The coercive field in this case is 347 Oe, and is possibly reflective of the higher Mn level contributing to an enlarged domain structure within the film. Similar behavior in M vs. T resulted as well, with the T_{Curie} at first approximation being roughly 250 K. For both films, the calculated moment per Mn atom is low: 0.0011 μ_B/Mn for the 6.8 % film and 0.00098 μ_B/Mn for the 9.4 % film. This is directly apparent when one compares the decrease in magnetization at saturation for the epitaxial films versus the implanted films (Figure 8-4). The lower moment is reflective of a low degree of substitutionality in the GaP:C. A second possibility to explain the lower moment is that the AES technique used to determine the Mn concentration in the films is overestimating the actual value. Finally, magnetotransport data for the GaMnP:C with 9.4 % Mn is presented in Figure 8-19. Negative magnetoresistance is observed from measurement temperatures of 200 K to 20 K, with a $\Delta R/R$ of 0.375 % at 20 K. While the effect is smaller than what was observed in GaMnN, again it indicates that the sample possesses collective spin behavior, in agreement with Figure 8-18.

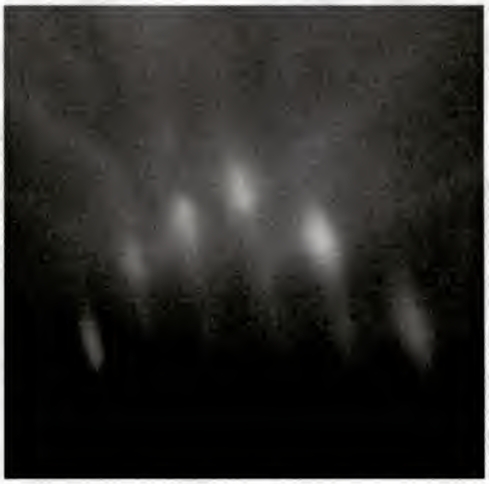

Figure 8-1: RHEED of the starting (100) GaP substrate surface after heat-up under P/P_2 from cracked PH_3 at a substrate temperature of 600 °C for 5 minutes.

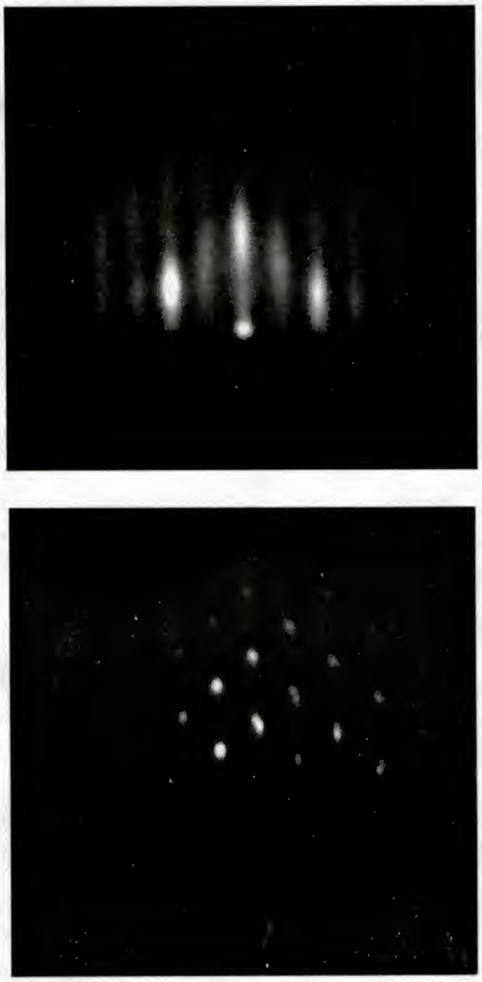

Figure 8-2: RHEED of epitaxially grown GaP:C (top) and GaP (bottom) on (100) GaP after growth at a substrate temperature of 350 °C.

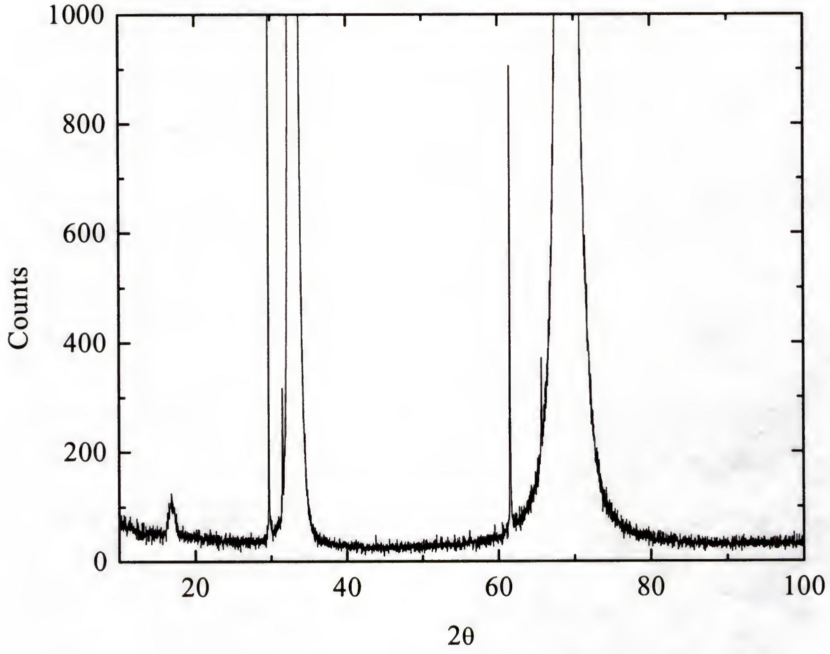

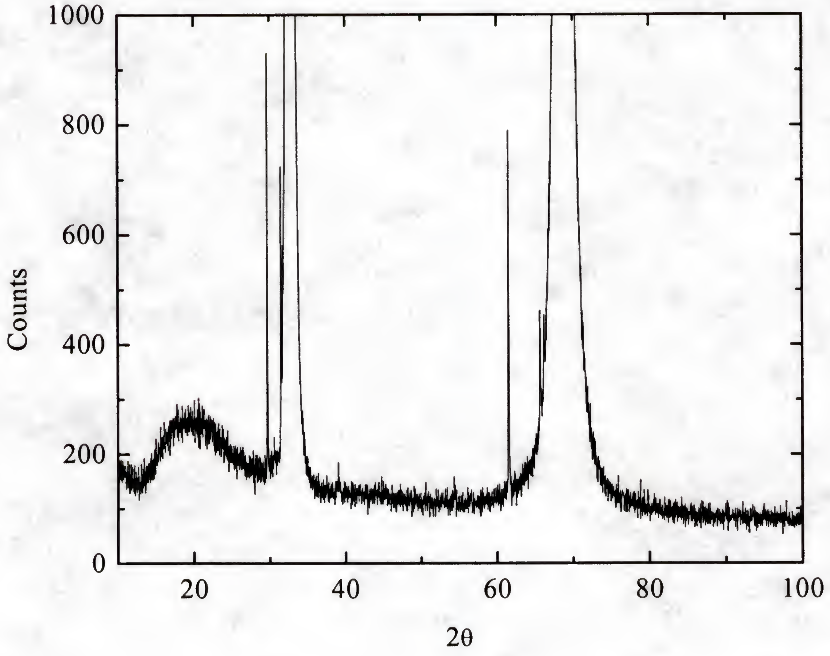

Figure 8-3: X-ray diffraction scans of the (100) GaP substrate (top) and the epitaxially grown GaP:C film on the (100) GaP substrate (bottom).

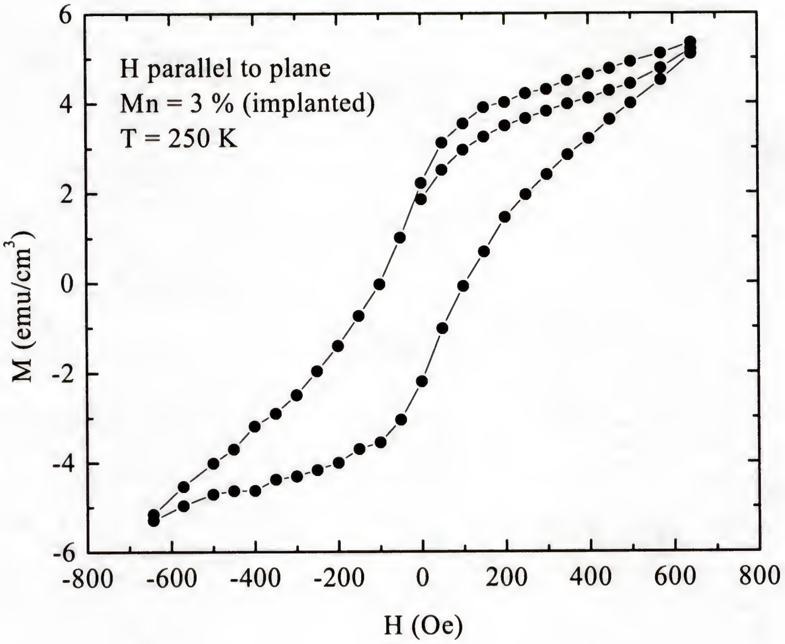

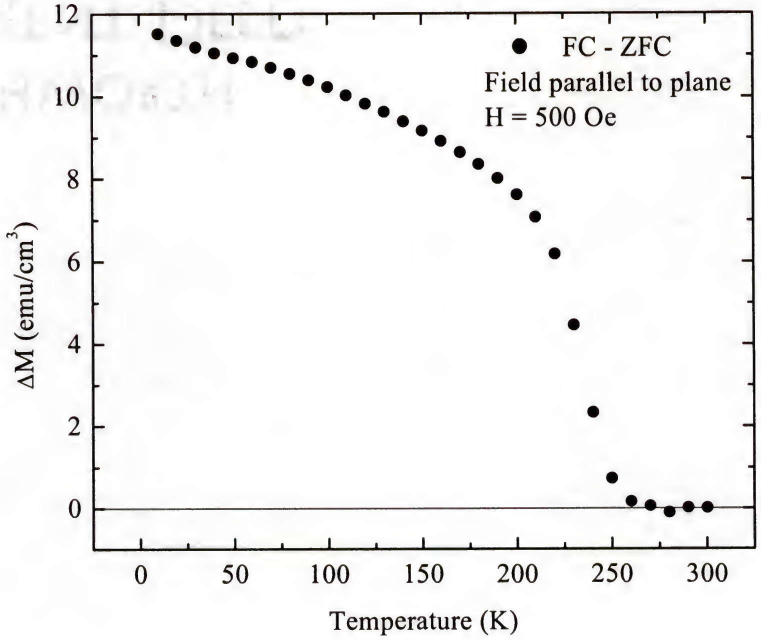

Figure 8-4: Magnetization for GaMnP:C with 3 % Mn (implanted) versus applied field (top) and versus temperature (bottom).

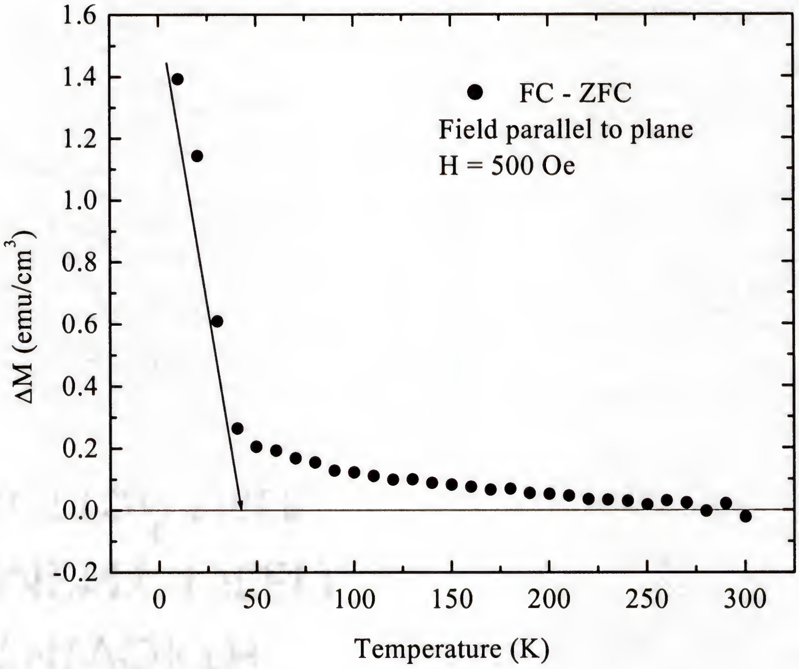

Figure 8-5: Magnetization for GaMnP:C with 5 % Mn (implanted) versus temperature.

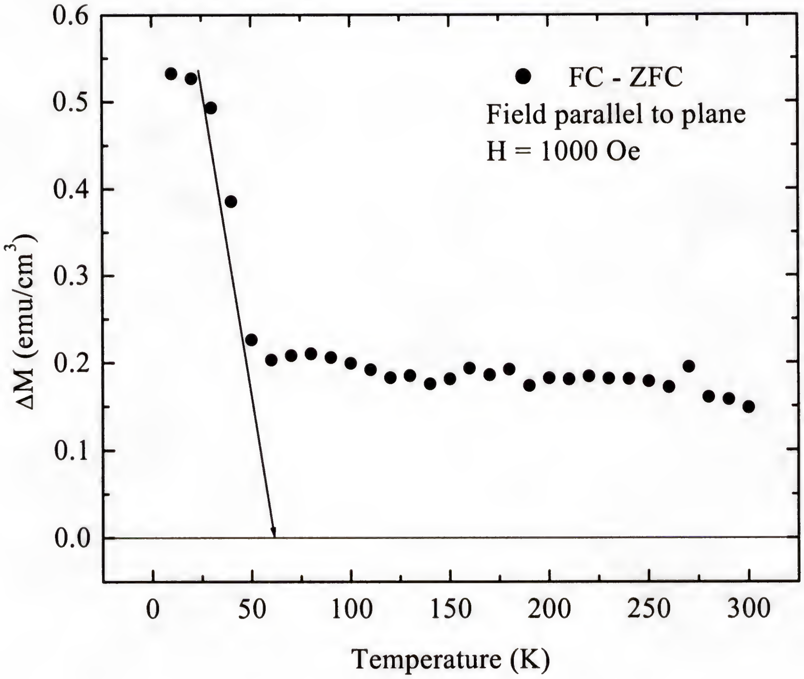

Figure 8-6: Magnetization for GaMnP with 3 % Mn (implanted) versus temperature.

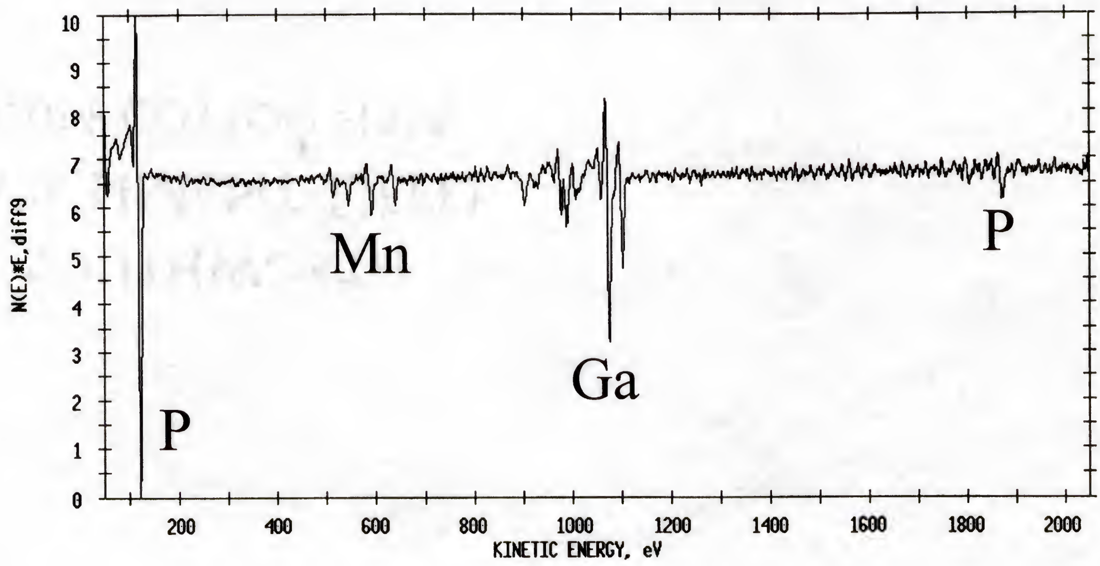

Figure 8-7: Auger electron spectroscopy (AES) survey of GaMnP.

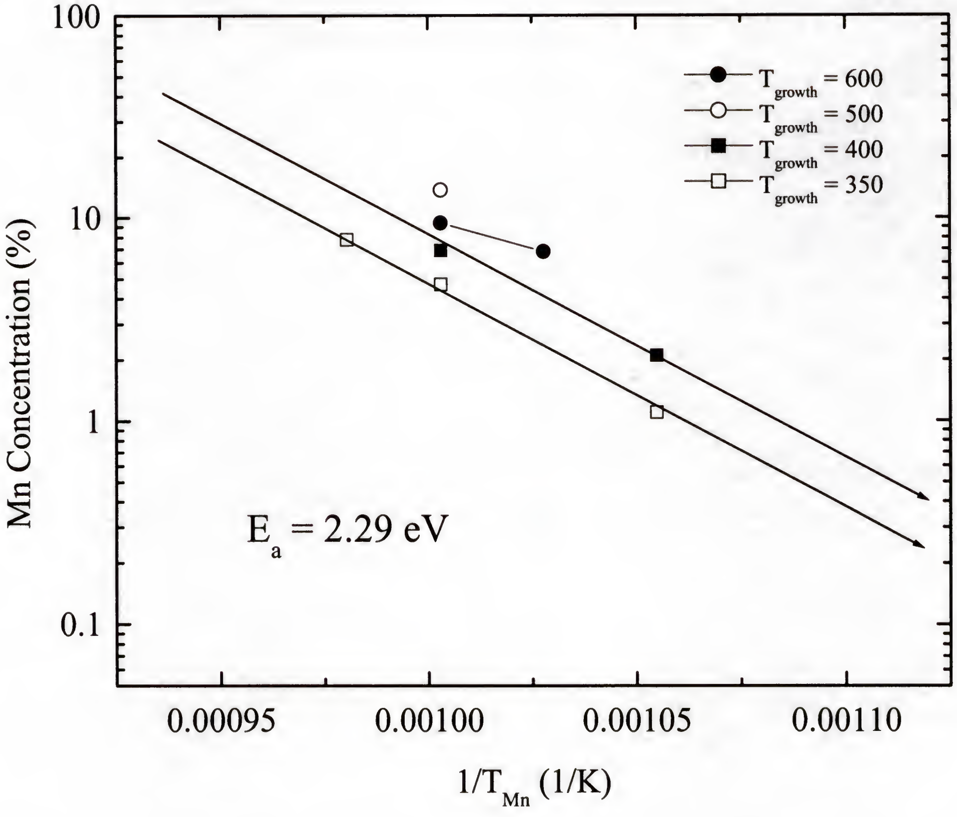

Figure 8-8: Variation of Mn concentration in GaMnP:C as a function of reciprocal Mn K-cell temperature.

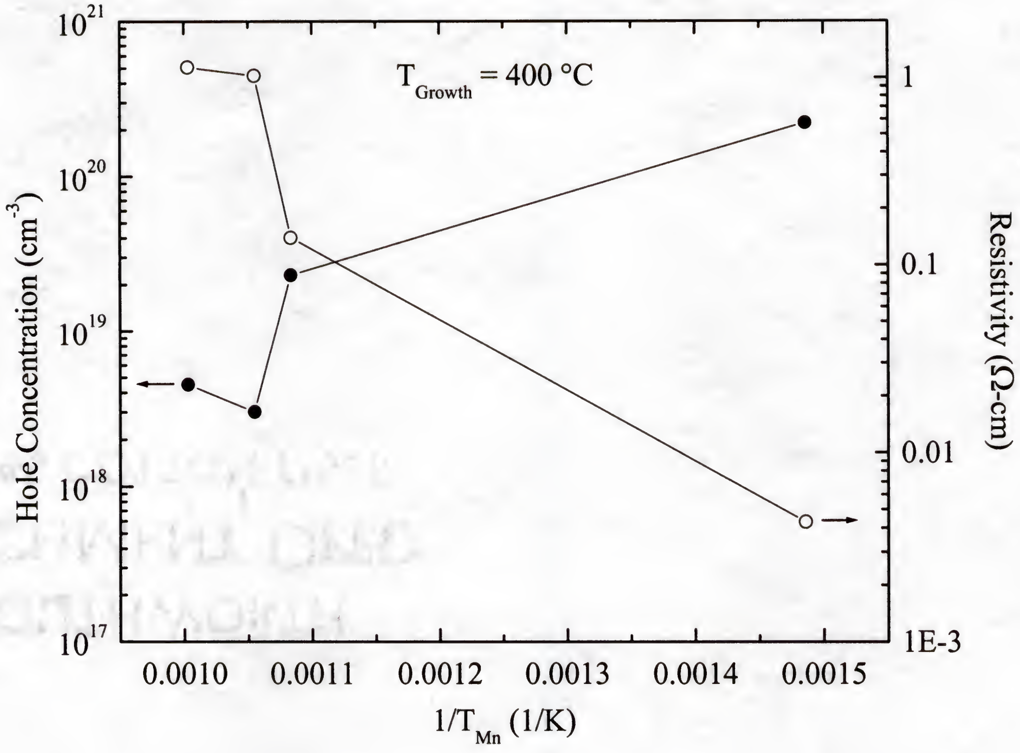

Figure 8-9: Free hole concentration and film resistivity as a function of reciprocal Mn K-cell temperature.

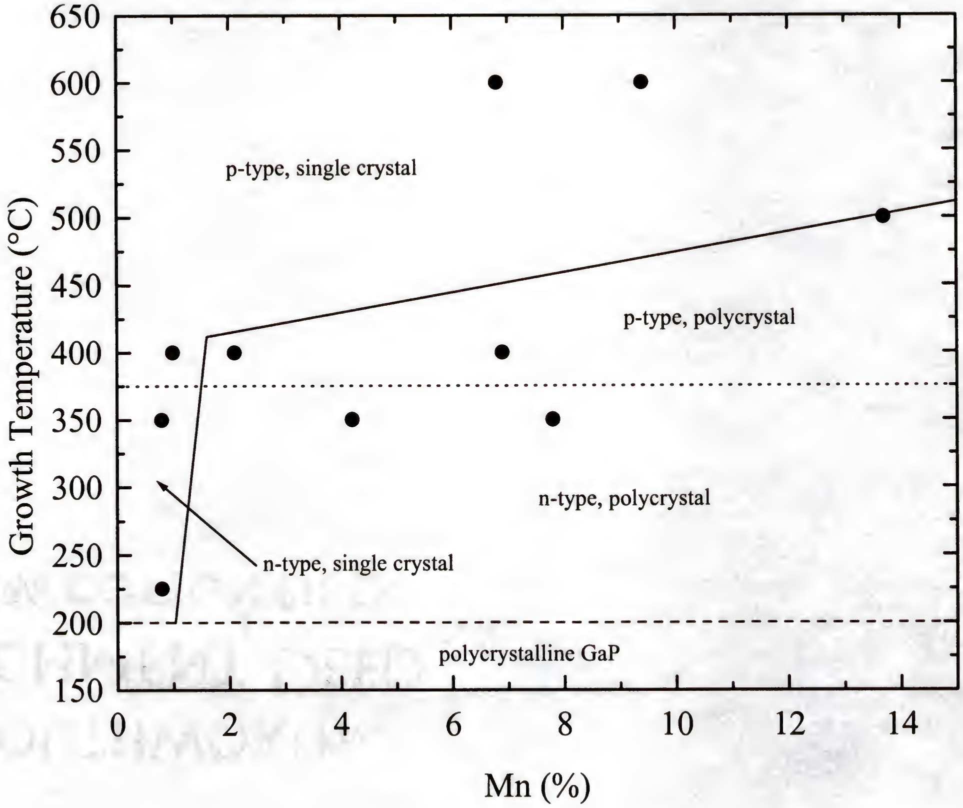

Figure 8-10: Phase diagram of the GaMnP:C system.

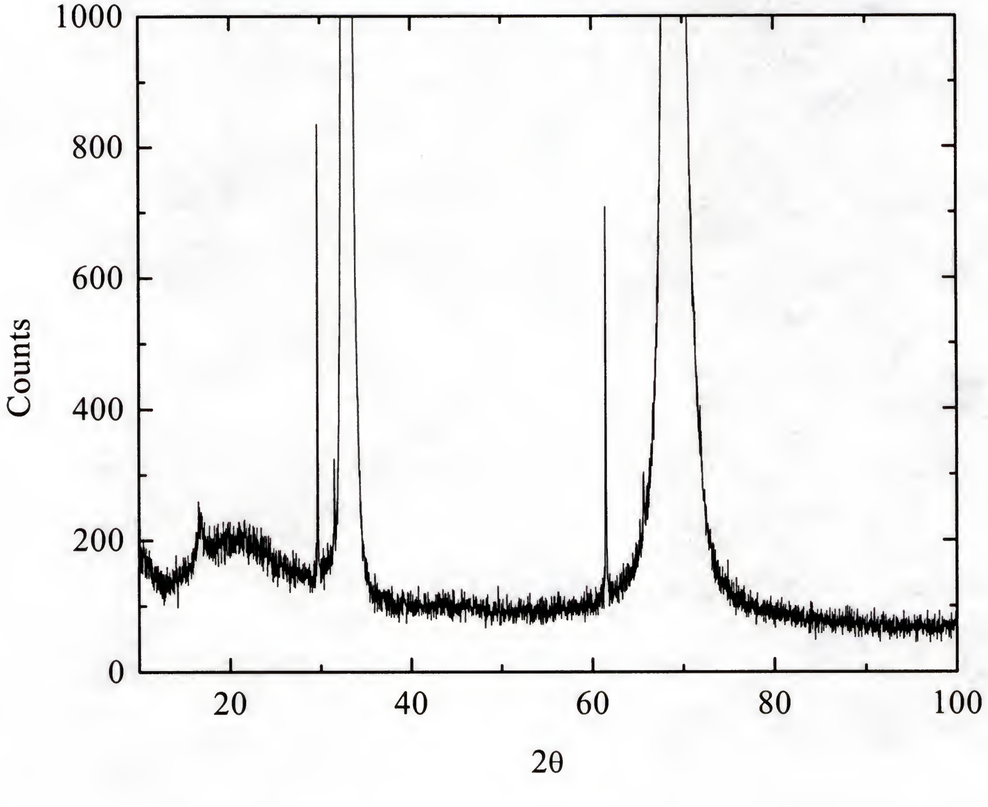

Figure 8-11: X-ray diffraction of GaMnP:C with T_{growth} = 600 °C and T_{Mn} = 724 °C.

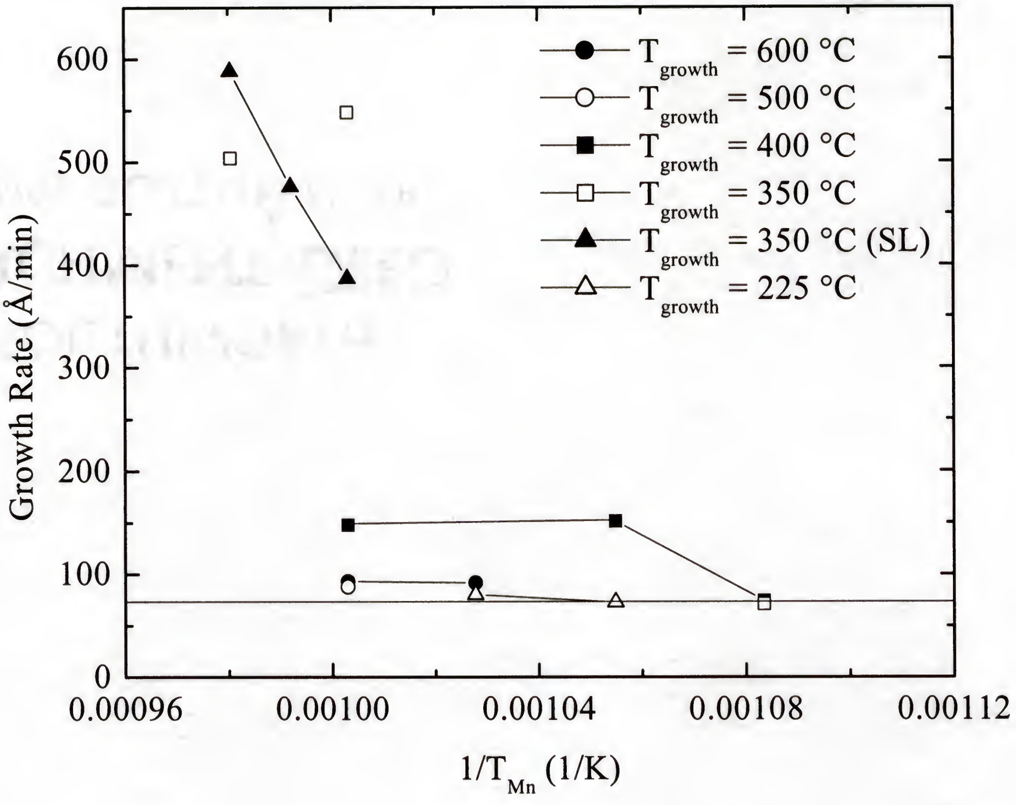

Figure 8-12: Growth rate vs. $1/T_{Mn}$ for GaMnP:C at various growth temperatures.

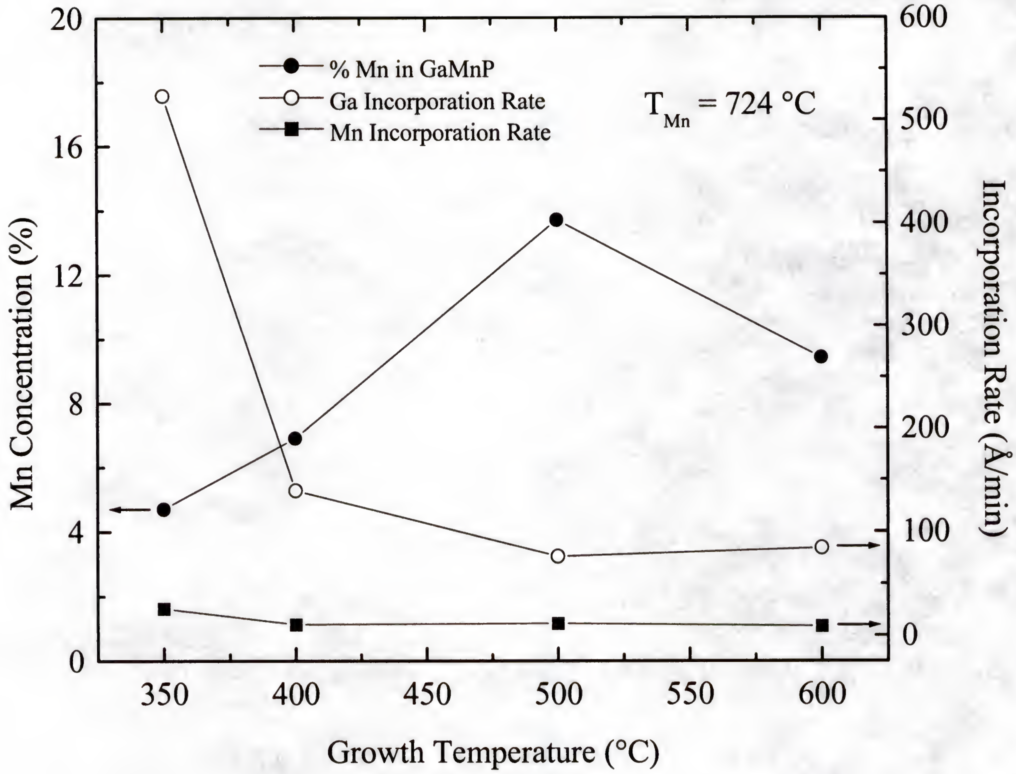

Figure 8-13: Mn concentration vs. growth temperature for T_{Mn} = 724 °C.

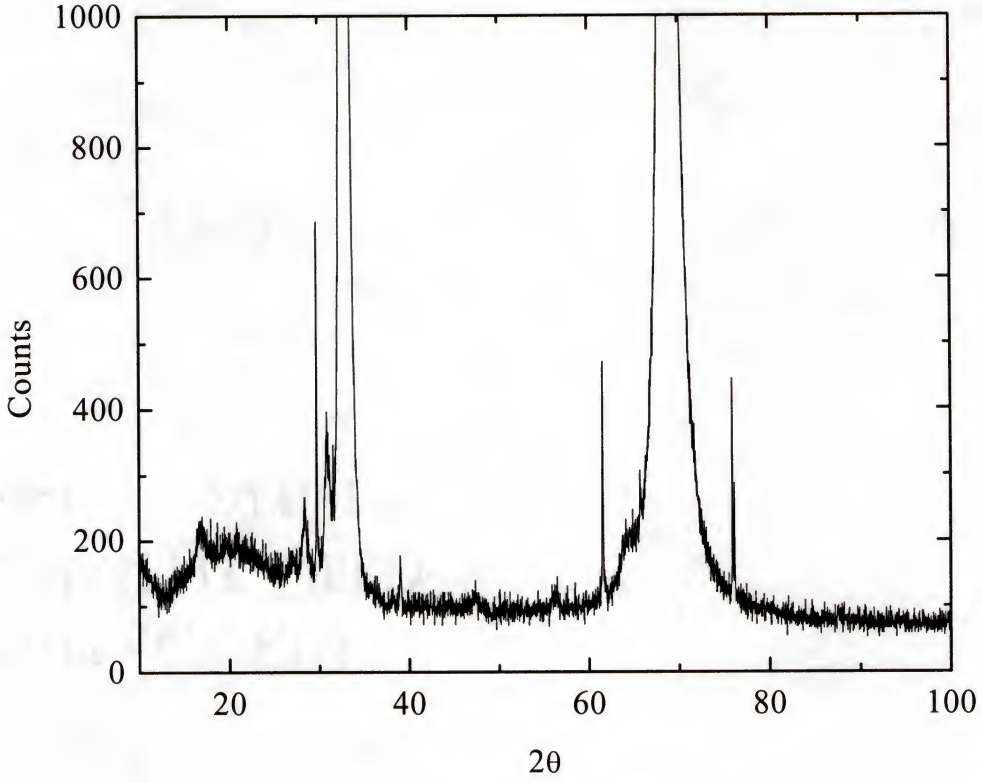

Figure 8-14: X-ray diffraction of GaMnP:C with T_{growth} = 350 °C and T_{Mn} = 747 °C.

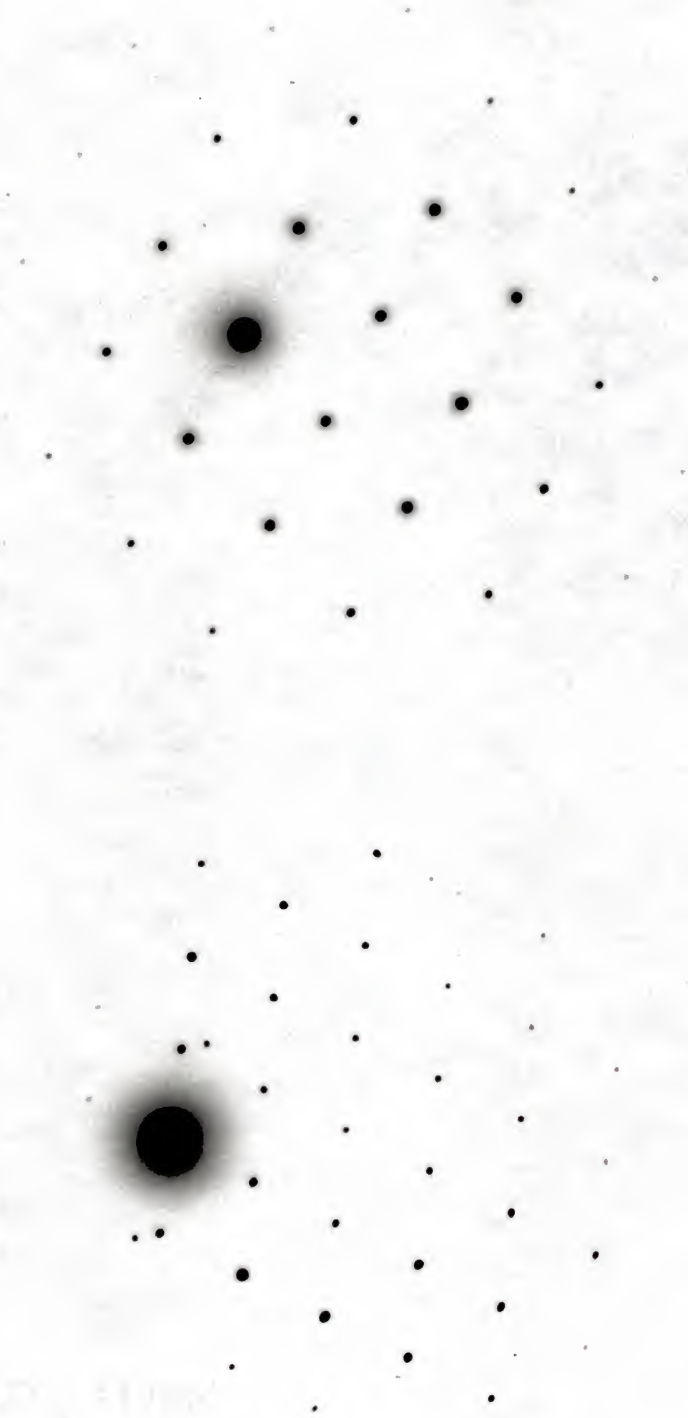

Figure 8-15: Selected area diffraction (SAD) patterns of GaMnP:C grown at 600 °C with 6.8 % Mn (top) and 9.4 % Mn (bottom).

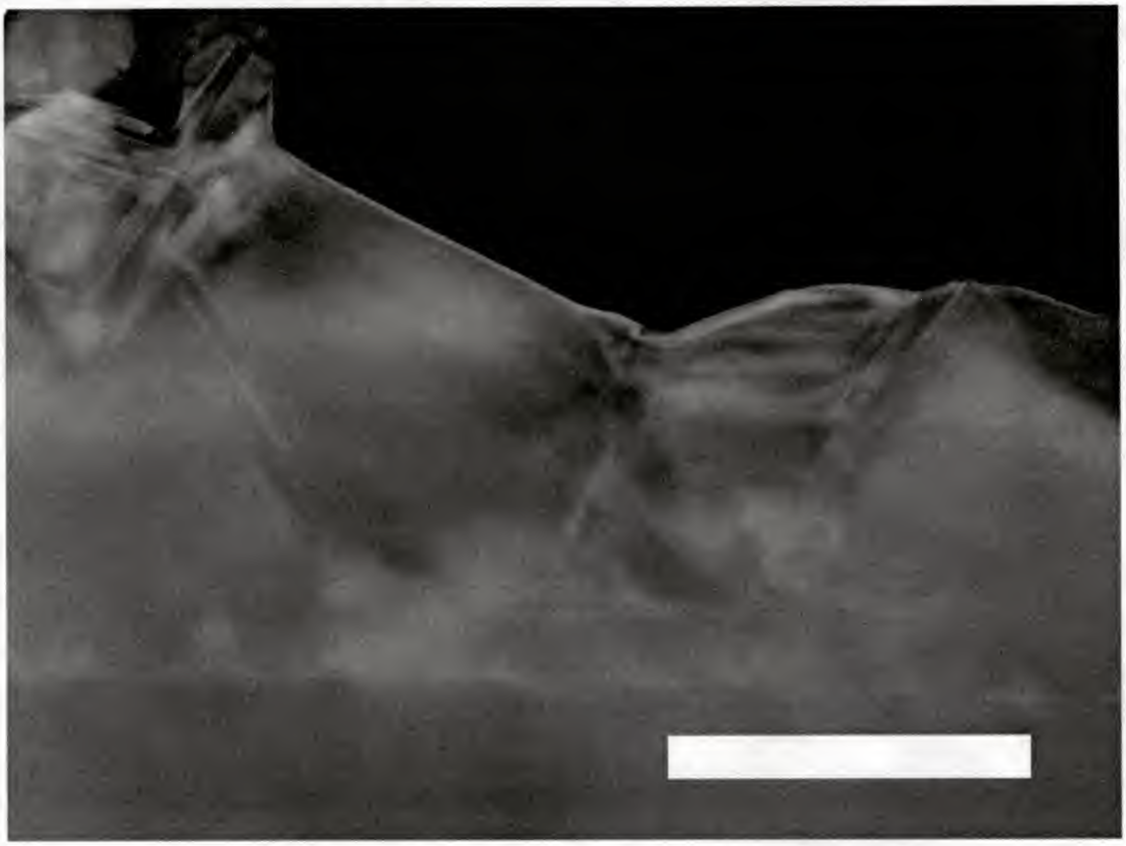

Figure 8-16: Cross sectional TEM (XTEM) photograph of GaMnP:C with 9.4 % Mn. Scale length is 4000 Å.

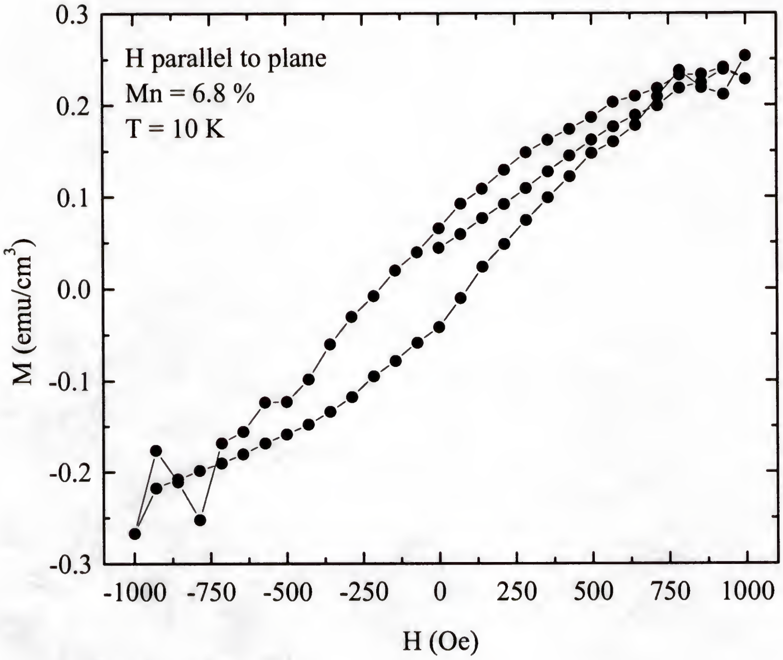

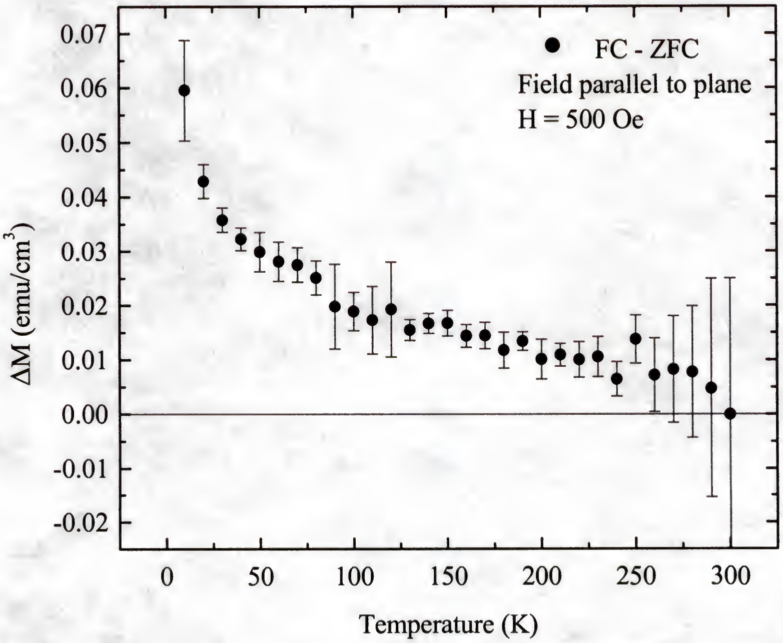

Figure 8-17: Magnetization behavior of GaMnP:C with 6.8 % Mn versus applied field (top) and versus temperature (bottom).

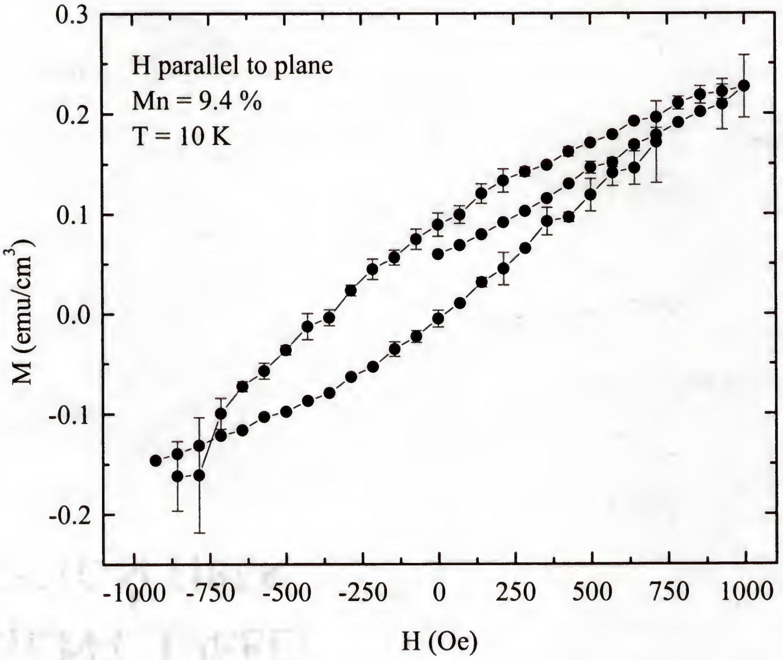

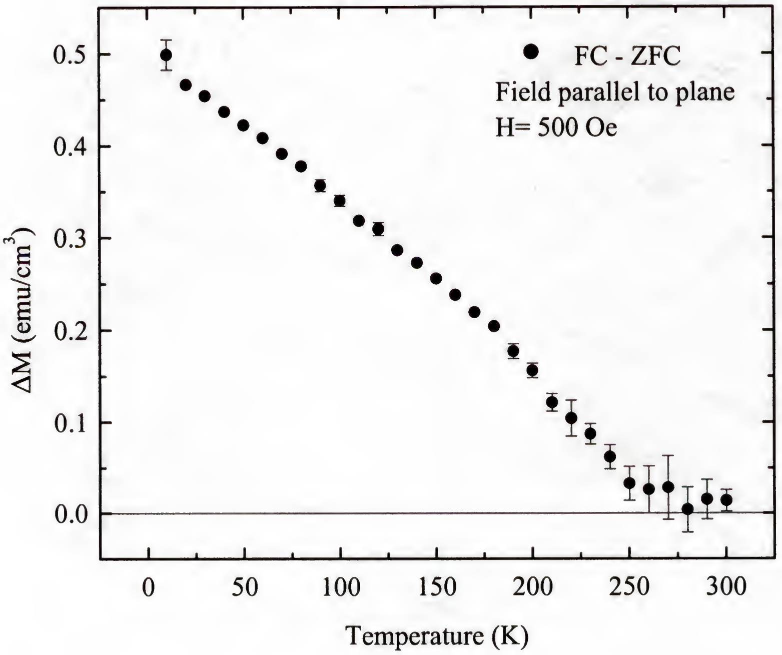

Figure 8-18: Magnetization behavior of GaMnP:C with 9.4 % Mn versus applied field (top) and versus temperature (bottom).

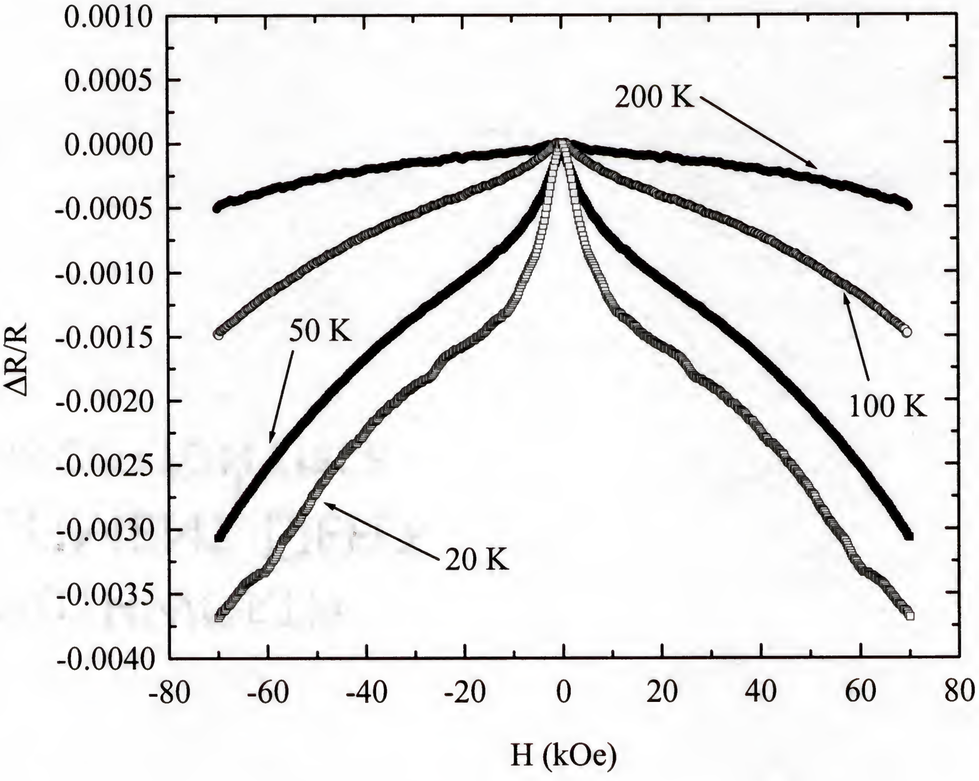

Figure 8-19: Magnetoresistance of GaMnP:C with 9.4 % Mn.

CHAPTER 9

SUMMARY AND CONCLUSIONS

In this dissertation, the compound semiconductors GaN and GaP were doped to produce either optical or magnetic behavior. In general, it was found that not only was control of the dopant level important in determining the macroscopically observed properties, but the growth conditions and the presence of additional elemental species as well. Four different semiconductor/dopant combinations were investigated.

Initial results in doping TEG-derived GaN with Er showed that the 1.54 μm IR emission increased as the Er level increased. However, it was soon determined that the varying C and O levels within the films could not be accurately controlled. It was previously shown in the literature that the presence of both species enhances the emission. The TEG was abandoned in favor of elemental Ga. By codoping the new GaN:Er films with C from a pyrolized CBr_4 source, repeatable C levels could be produced. By increasing the C level, the integrated 1.54 μm room temperature PL was found to go through a maximum, comparable to results with O found in the literature. The quenching of the PL with temperature and the effects of annealing were also investigated. While it was found that the quenching from 10 K to 300 K improved from 92 % for GaN:Er to 31 % for GaN:Er:C, quenching of –62 % was observed in TEG samples where the O:Er ratio was 0.9. It is clear that overall, O is the more beneficial codopant when compared to C. Results from annealing studies showed that while the

GaN:Er PL decreased, the GaN:Er:C PL increased, probably due to the activation of additional C and Er within the films.

Photoluminescence results in GaN doped with Eu showed that under above bandgap excitation, the red emission at 621 nm was of a higher intensity than that of MOCVD-derived AlGaAs used for commercial emitters. Annealing of the GaN:Eu material showed an improvement in the luminescence, in line with what was observed in the GaN:Er system. Quenching experiments on the 621 nm emission indicated that the emission decreases by 82 % from 10 K to 300 K, while after annealing, the quenching is reduced to 66 %. This is also in agreement with the results from the GaN:Er work. As O was found to be the better overall codopant, future work should involve incorporating O during the GaN:Er or GaN:Eu growth. This may be possible through a bubbler-based low vapor pressure O source, to minimize the contamination of the UHV chamber.

Gallium nitride was again investigated, in order to produce ferromagnetic behavior when doped with Mn, a so-called dilute magnetic semiconductor (DMS). It was found that the GaN could be successfully doped with up to 9 % of Mn without producing second phases. In agreement with theory, it was found that the GaMnN doped with 6.1 % Mn grown at 750 °C that was semi-insulating only displayed paramagnetism, while the GaMnN doped with C with 4.5 % Mn showed ferromagnetism. The GaMnN:C was n-type with 5×10^{18} electrons/cm^3. Enhanced ferromagnetic behavior was observed for single crystal GaMnN grown on MOCVD GaN, compared to polycrystalline GaMnN grown directly on sapphire. This also indicates the importance of the crystal quality on the ferromagnetism. Further improvements in the ferromagnetism were made when the GaMnN was grown at higher substrate temperatures (865 °C). Stronger M vs. H behavior was observed, as well as negative magnetoresistance and the anomalous Hall effect. The T_{Curie} was determined to be between 10 K and 25 K, much higher than the theoretically predicted value of 0.6 K. Future work with this material should center on epitaxially growing p-GaMnN, rather than the n-GaMnN that was produced in this work. With the experimentally observed T_{Curie} for n-GaMnN roughly an order of magnitude higher than the predicted value, the T_{Curie} for p-GaMnN may also be higher than the 400 K theoretical prediction.

Gallium phosphide doped with Mn to produce DMS ferromagnetism was the final material system investigated. The GaMnP was produced by direct implantation of Mn^+ into p-GaP:C layers and by MBE growth. The GaP:C implanted with 3 atomic % Mn showed strong ferromagnetism in M vs. H at a measurement temperature of 250 K. Subsequent measurements of M vs. T at a constant field of 500 Oe showed a functional form similar to that predicted by the Weiss theory of ferromagnetism. Subsequent implanted samples showed behavior consistent with the recently advanced theory based on a Bound Magnetic Polaron/hole mediated exchange model in terms of changing the Mn level and changing the carrier concentration within the semiconductor. As with the epitaxial growth of GaMnN, it was found that the required levels of Mn could be incorporated without forming additional phases within the material, despite observed growth rates of over 500 Å/min. A phase diagram for the GaMnP:C system was determined, highlighting the relevant regions in terms of carrier type and crystal quality. It was found that to produce ferromagnetic GaMnP:C, a growth temperature above 375 °C should be used to produce p-type material. Material grown at a temperature of 600 °C for Mn levels of 6.8 % and 9.4 % were found to be ferromagnetic at 10 K, with M vs. T behavior that suggests a T_{Curie} of approximately 250 K. This is comparable to the sample implanted with 3 % Mn. Negative magnetoresistance of 0.375 % was observed for the 9.4 % sample. Analysis of the samples by TEM does not show the presence of microscopic or superparamagnetic particles to a resolution of 50 Å, indicating the observed ferromagnetism in the epitaxial GaMnP:C is most likely due to dilute magnetic ferromagnetism. Future work with the GaMnP system can proceed in many directions. With the implanted and epitaxial material, the effect of varying carrier type and concentration (using CBr_4 for p-doping and $SiBr_4$ for n-doping) can be investigated to determine an optimum level. According to Figure 3-4, it may be possible to increase the T_{Curie} to room temperature or above by creating the ternary $Al_xGa_{1-x}P$, for either implantation or epitaxial incorporation of Mn, using the DMEAA metalorganic source. Lattice matching the DMS material directly to GaAs or Si may then also be possible by creating the ternaries $In_xGa_{1-x}P$ or $Al_xGa_{1-x}P$ respectively. Finally, now knowing the general area of the GaMnP:C phase diagram that will produce a ferromagnetic material, work should involve refining the growth to produce a higher quality material that would be more conducive for integration into spintronic device structures.

APPENDIX
LABVIEW™ CONTROL OF THE VARIAN INTEVAC MOD GEN II MBE

As described in Chapter 4, the Varian Mod Gen II MBE system is designed to deliver metalorganic, hydride, and N_2 gas materials into the growth chamber in addition to the traditional solid sources. As such, gas delivery and control constitutes the bulk of the hardware attached to the growth chamber. To control the seven separate alkyl modules, the three hydride modules, the RF N_2 plasma, and the main He and H_2 supply module, there are 77 separate gas valves within the system. These gas valves (referred to as Nupro™ valves) are all pneumatic; the valves are opened and closed by supplying compressed air to the head of the valve. To actuate each valve, the head is attached by tubing to a solenoid valve on a Nupro™ card. An example of one of these cards is given in Figure A-1. Each card consists of 6 separate solenoids, so up to 6 separate valves can be controlled by one card. A main supply of compressed air at roughly 35 psig is connected to the card. When the solenoid is energized, the compressed air is sent through tubing to the Nupro™ valve, and the valve is opened. If the solenoid is de-energized, no air is sent through the tubing, and spring in the valve head shuts the valve. Individual single pole/single throw (SPST) switches on the card can activate each solenoid. Remote control can also be provided via the serial cable connection, which also supplies the +24 VDC needed to run the card.

Due to the inadequacies of the previous remote control system, the entire Intevac computer control system was discarded and replaced with a new computer control system incorporating the Labview™ graphical programming and control platform. The Labview™ software and all of its supporting software is run from a personal computer. In the event several modules are run simultaneously, the PC motherboard contains 128 MB of RAM. The individual Labview™ programs are run on the computer, and are interfaced with the 13 separate Nupro™ cards using hardware manufactured by National Instruments™ and designed to run in conjunction with Labview™. Installed into a spare expansion slot within the PC is a PCI-MIO-16E-1 I/O board that communicates via a bus cable to two SCXI-1001 12 bay chassises. Each bay in the chassis is designed to accept removable modules for a variety of electronic control and manipulation applications, comparable in nature and scope to CAMAC and NIM protocols.

In one of the SCXI-1001 chassises are three SCXI-1162 32 channel digital input modules, three SCXI-1124 6 channel D/A converters, and one SCXI-1100 32 channel multiplex amplifier. The SCXI-1162 units are intended to read the positions of spring activated switches on each Nupro™ valve to confirm its state. The SCXI-1124 and SCXI-1100 units are intended to interface with the mass flow controllers and pressure controllers in the Gen II to allow for remote operation. Although the software written for the Gen II's operation includes sections for these components, they are not currently used. The SCXI-1162 modules are not used at present due to problems that were found to exist with the positions of state switches on many of the Nupro™ valves. The SCXI-1124 and SCXI-1100 units are not used, as it was found that front panel operation of the MFCs and PCs through local control was still the best option.

In the second SCXI-1001 chassis, there are ten SCXI-1161 power relay modules. Each individual relay module contains 8 optically isolated NO/NC relays. Optically isolated relays in this application are advantageous due to the possibility of highly inductive switching currents when energizing the solenoids. One of these relays is connected to an individual solenoid in the manner of Figure A-2 through the serial cable. The remote strand from the cable for that solenoid is connected to the NO position of the relay. The COM portion of the relay is connected to the ground for the card. So when the relay is activated from the Labview™ program through the NI-DAQ communication software, the solenoid is switched to ground remotely through the relay instead of locally via the SPST toggle switch. All 77 necessary solenoids are wired in the same fashion.

Each individual Labview™ program for the 12 modules is designed with the same structure. The close window button in the upper right corner of each window has been deactivated so the window cannot be accidentally closed during operation. The graphical layout of each program is given in Figure A-3. The main Labview™ program consists of a Main Sequence and a Termination. The Termination involves the Power Off toggle control given in the example in Chapter 4. When this control is activated, every valve related to this particular program is closed in turn, and then the program is stopped. This is the only way to stop the program and then be able to close the window. A breakdown of the Main Sequence is given in Figure A-4. The Main sequence consists of an infinite loop that can only be stopped when the Power Off toggle is activated and consists of six parts. Part 0 is an EMO feature that closes all the related valves for that module but allows the program to continue to run. Part 1 checks the individual state switches, and has been disconnected externally to the software. Part 2 consists of preprogrammed choices for module operation (Module Purge, Switch to Vent, Switch to Run, etc.) that is activated when a separate front panel button is depressed. Part 3 consists of the controls for the MFCs and PCs, and has been disabled in the software. Part 4 checks the individual Boolean controls for the individual valves on the front panel and switches the valves if necessary. Finally, Part 5 controls the Boolean logic of the plumbing indicators on the front panel, indicating the direction of the gas flow, depending upon the positions of the valves related to the particular module in question

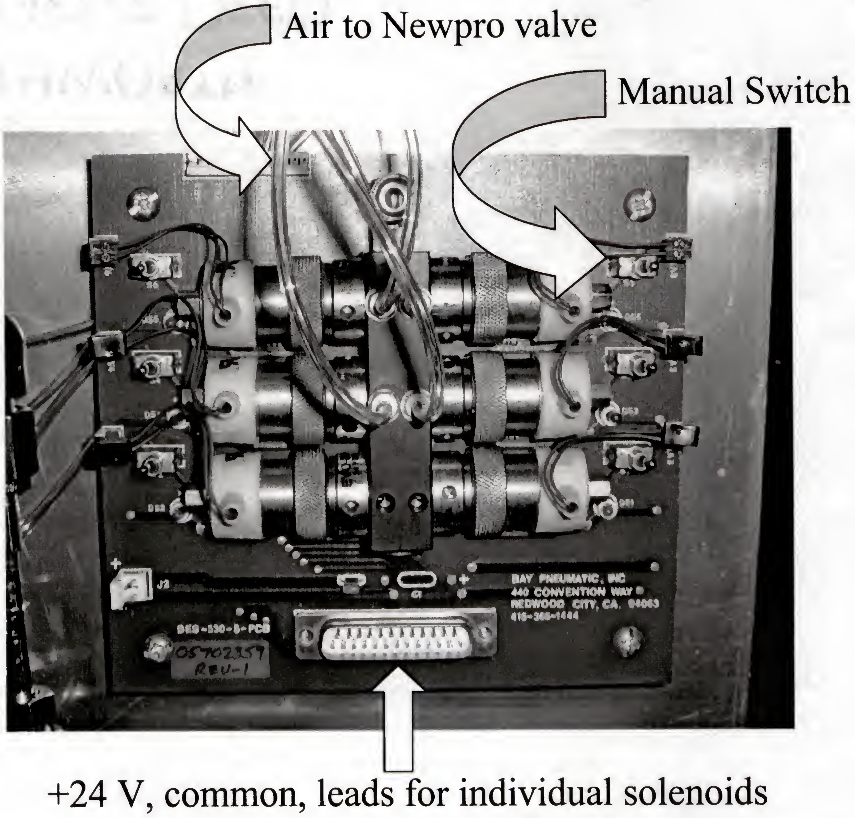

Figure A-1: Nupro™ card used to control pneumatic gas valves on the Varian MOD Gen II MBE system.

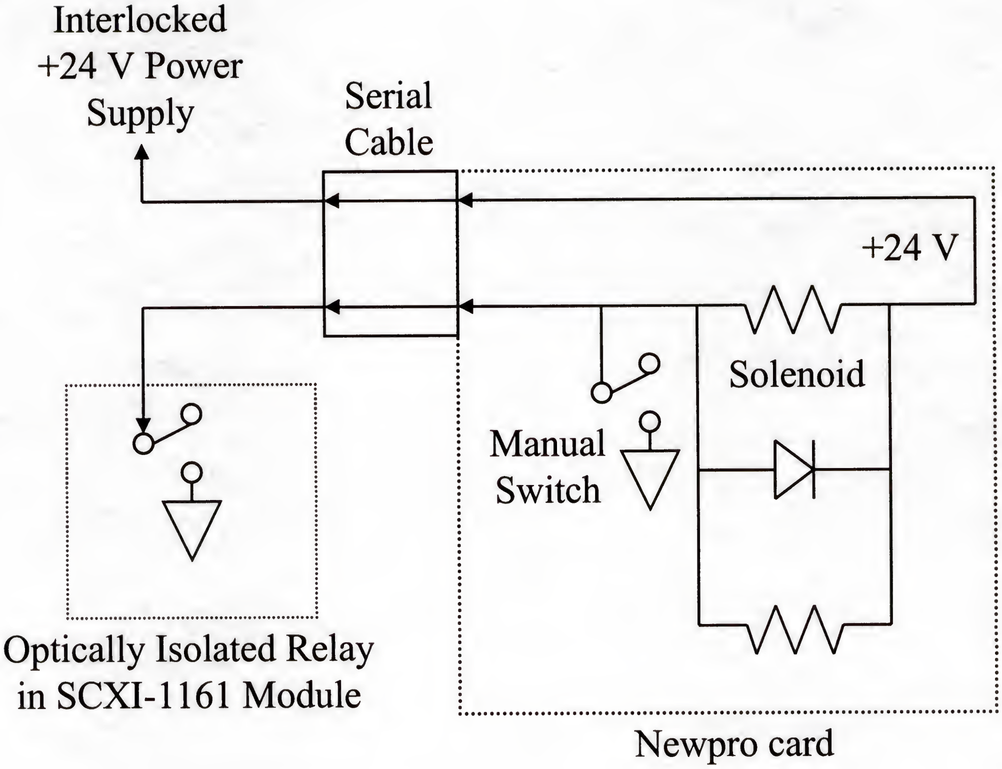

Figure A-2: Schematic of the Nupro™ card attached to the SCXI-1161 Relay Module via a serial cable. The Labview™ software actuates the SCXI-1161 relay.

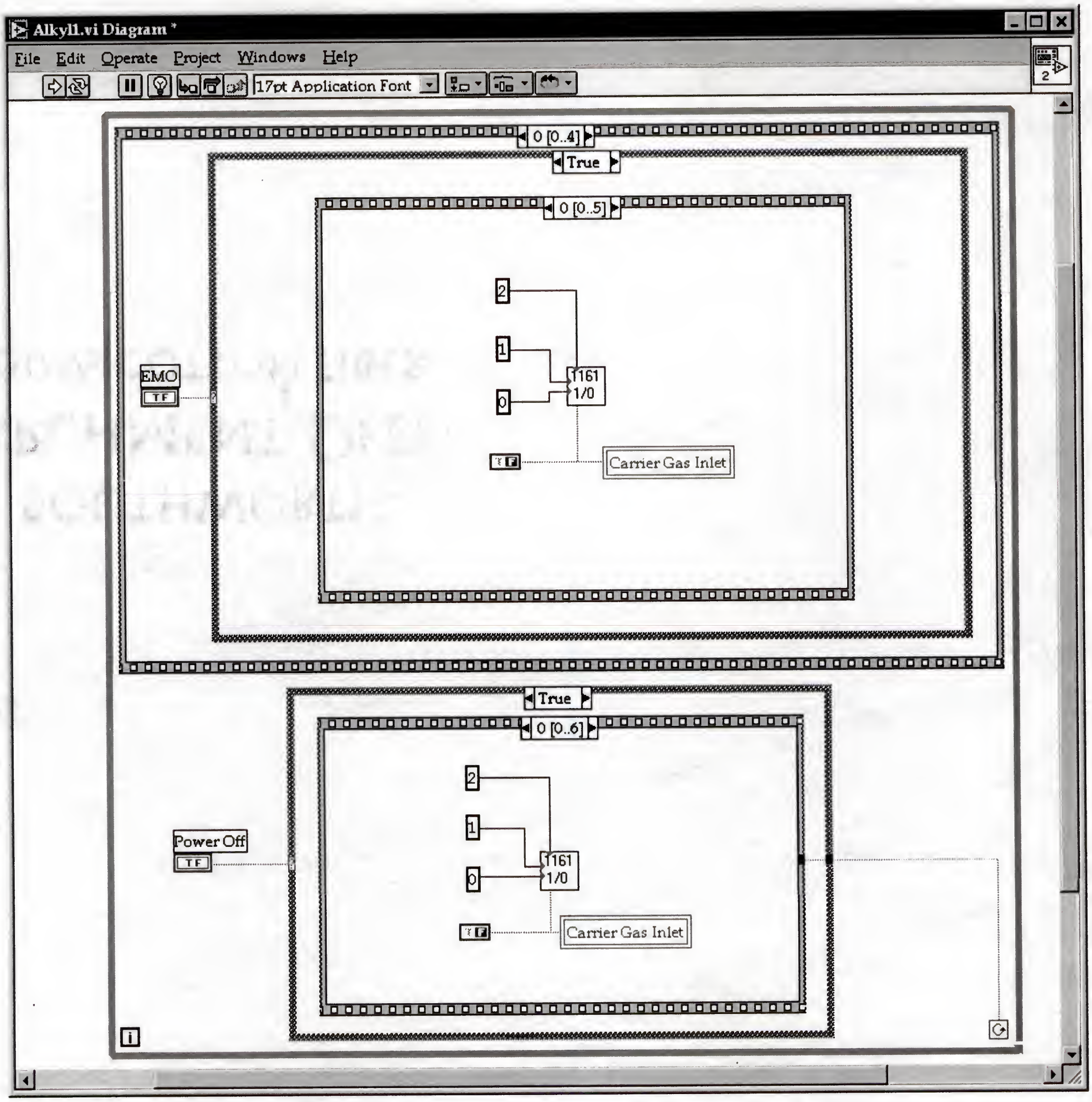

Figure A-3: The graphical layout of each Labview™ Gen II program. The main box represents a while loop that will run as long as the Power Off toggle is in the On position.

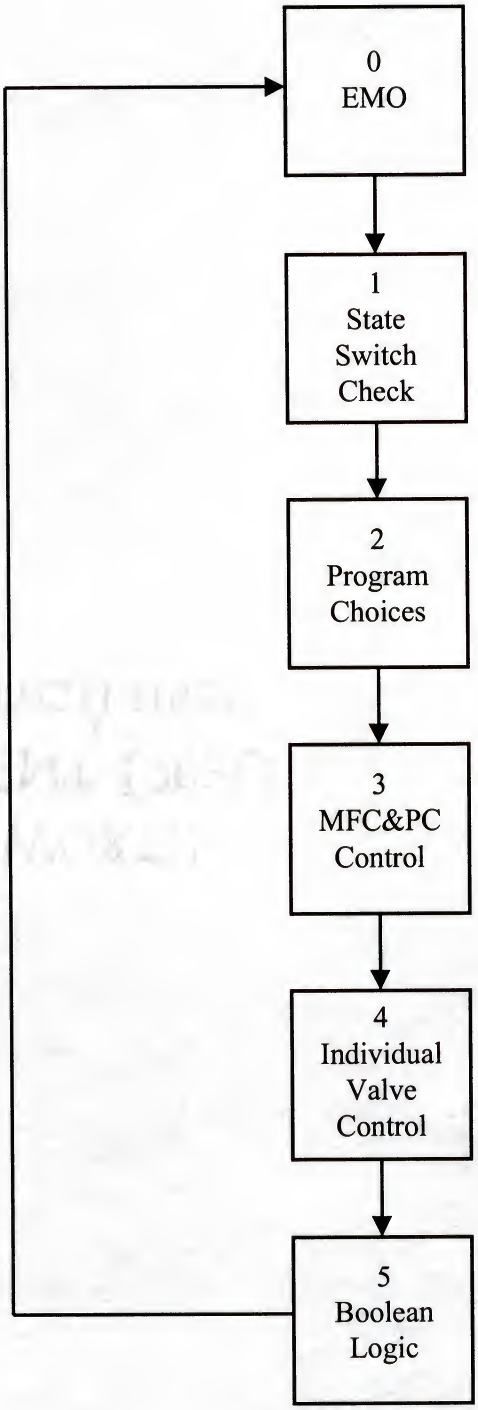

Figure A-4: The Main Sequence of each Labview™ program, set up as an infinite loop.

REFERENCES

[1] E. S. Grosvenor and M. Wesson, *Alexander Graham Bell: the life and times of the man who invented the telephone*. Harry N. Abrams, New York, 1997.

[2] R. G. Wilson, R. N. Schwartz, C. R. Abernathy, S. J. Pearton, N. Newman, M. Rubin, T. Fu, and J. M. Zavada, *Appl. Phys. Lett.*, **65** (8), p. 992 (1994).

[3] Stanley R. Rotman, *Wide-Gap Luminescent Materials*. Kluwer Academic Publishers, New York, 1997.

[4] S. Hüfner, *Optical Spectra of Transparent Rare Earth Compounds*. Academic Press, New York, 1978.

[5] E. Neufeld, M. Markmann, A. Vörckel, K. Brunner, and G. Abstreiter, *Appl. Phys. Lett.*, **75** (5), p. 647 (1999).

[6] A. J. Steckl and J. M. Zavada, *MRS Bulletin*, **24** (9), p. 33, (1999).

[7] H.-K. Lo, S. Popescu, and T. Spiller, *Introduction to Quantum Computation and Information*. World Scientific, London, 1998.

[8] C. P. Williams and S. H. Clearwater, *Ultimate Zero and One*. Copernicus Publishers, New York, 2000.

[9] E. Yablonovich, *MRS Symp. Proc. T/U/V Spring 2001*. Materials Research Society, Warrendale, PA (under review).

[10] J. L. Simonds, *Physics Today*, **48**, p. 26 (1995).

[11] H. Ohno, *Science*, **281**, p. 951 (1998).

[12] S. Datta and B. Das, *Appl. Phys. Lett.*, **56** (7), p. 665 (1990).

[13] S. Gardelis, C. G. Smith, C. H. W. Barnes, E. H. Linfield, and D. A. Ritchie, *Physical Review B*, **60** (11), p. 7764 (1999).

[14] P. R. Hammar, B. R. Bennet, M. J. Yang, and M. Johnson, *Phys. Rev. Lett.*, **83** (1), p. 203 (1999).

[15] M. Tanaka, *J. Crystal Growth*, **201/202**, p. 660 (1999).

[16] M. Oestreich, J. Hubner, D. Hagele, P. J. Klar, W. Heimbrodt, W. W. Ruhle, D. E. Ashenford, and B. Lunn, *Appl. Phys. Lett.*, **74** (9), p. 1251 (1999).

[17] Y. D. Park, B. T. Jonker, B. R. Bennett, G. Itskos, M. Furis, G. Kioseoglou, and A. Petrou, *Appl. Phys. Lett.*, **77** (24), p. 3989 (2000).

[18] B. T. Jonker, Y. D. Park, B. R. Bennett, H. D. Cheong, G. Kioseoglou, and A. Petrou, *Physical Review B*, **62** (12), p. 8180 (2000).

[19} R. Fiederling, M. Keim, G. Reuscher, W. Ossau, G. Schmidt, A. Wang, and L. W. Molenkamp, *Nature*, **402,** p. 787 (1999).

[20] Y. Ohno, D. K. Young, B. Beschoten, F. Matsukura, H. Ohno, and D. D. Awschalom, *Nature*, **402,** p. 790 (1999).

[21] T. Gruber, M. Keim, R. Fiederling, G. Reuscher, W. Ossau, G. Scmidt, L. W. Molenkamp, and A. Wang, *Appl. Phys. Lett.*, **78** (8), p. 1101 (2001).

[22] M. E. Flatte and G. Vignate, *Appl. Phys. Lett.*, **78** (9), p. 1273 (2001).

[23] J. Dean, editor, *Lange's Handbook of Chemsitry*, 13th Ed., McGraw-Hill, New York, 1985.

[24] M. E. Levinshtein, S. L. Rumyantsev, and M. S. Shur, *Properties of Advanced Semiconductor Materials: GaN, AlN, InN, BN, SiC, SiGe*. Wiley, New York, 2001.

[25] J. W. Mayer and S. S. Lau, *Electronic Materials Science: For Integrated Circuits in Si and GaAs*. Macmillan, New York, 1990.

[26] J. M. Zavada and D. Zhang, *Sol. State Elec.*, **38**, p. 1285 (1995).

[27] J. Michel, J. Benton, R. Ferrante, D. Jacobsen, D. Eaglesham, E. Fitzgerald, Y. Xie, J. Poate, and L. Kimerling, *J. Appl. Phys.*, **70** (5), p. 2672, (1991).

[28] J. L. Benton, J. Michel, L. C. Kimerling, D. C. Jacobson, Y.-H. Xie, D. J. Eaglesham, E. A. Fitzgerald, and J. M. Poate, *J. Appl. Phys.*, **70** (5), p. 2667, (1991).

[29] G. Franzó, F. Priolo, S. Coffa, A. Polman, and A. Carnera, *Nucl. Intr. and Meth. in Phys. Res. B*, **96**, p. 374, (1995).

[30] S. Coffa, G. Franzó, F. Priolo, A. Polman, and R. Serna, *Physical Review B*, **49** (23), p. 16313, (1994).

[31] B. Zheng, J. Michel, F. Y. G. Ren, L. C. Kimerling, D. C. Jacobsen, and J. M. Poate, *Appl. Phys. Lett.*, **64** (21), p. 2842, (1994).

[32] P. S. Andry, W. J. Varhue, F. Ladipo, K. Ahmed, E. Adams, M. Lavoie, P. B. Klein, R. Hengehold, and J. Hunter, *J. Appl. Phys.*, **80** (1), p. 551, (1996).

[33] S. Coffa, F. Priolo, G. Franzó, V. Bellani, A. Carnera, and C. Spinella, *Physical Review B*, **48** (16), p. 11782, (1993).

[34] A. Polman, *J. Appl. Phys.*, **82** (1), p. 1, (1997).

[35] H. Ennen, G. Pomrenke, A. Axmann, K. Eisele, W. Haydl, and J. Schneider, *Appl. Phys. Lett.*, **46** (4), p. 381, (1985).

[36] S. Lombardo, S. U. Campisano, G. N. van den Hoven, and A. Polman, *J. Appl. Phys.*, **77** (12), p. 6504, (1995).

[37] J. L. Rogers, P. S. Andry, W. J. Varhue, E. Adams, M. Lavoie, and P. B. Klein, *J. Appl. Phys.*, **78** (10), p. 6241, (1995).

[38] D. Wortman, C. Morrison, and J. Bradshaw, *J. Appl. Phys.*, **82** (5), p. 2580, (1997).

[39] A. Reittinger, J. Stimmer, and G. Abstreiter, *Appl. Phys. Lett.*, **70** (18), p. 2431, (1997).

[40] A. Terrasi, G. Franzó, S. Coffa, F. Priolo, F. D'Acapito, and S. Mobilio, *Appl. Phys. Lett.*, **70** (13), p. 1712, (1997).

[41] L. G. Gerchikov and V. F. Masterov, *Appl. Phys. Lett.*, **73** (4), p. 532, (1998).

[42] J. Wan, Y. Ling, Q. Sun, and X. Wang, *Physical Review B*, **58** (16), p. 10415, (1998).

[43] F. Priolo, G. Franzó, S. Coffa, and A. Carnera, *Physical Review B*, **57** (8), p. 4443, (1998).

[44] G. Franzò, F. Priolo, S. Coffa, A. Polman, and A. Carnera, *Appl. Phys. Lett.*, **64** (17), p. 2235, (1994).

[45] J. S. Custer, A. Polman, and H. M. van Pinxteren, *J. Appl. Phys.*, **75** (6), p. 2809, (1994).

[46] D. L. Adler, D. C. Jacobson, D. J. Eaglesham, M. A. Marcus, J. L. Benton, J. M. Poate, and P. H. Citrin, *Appl. Phys. Lett.*, **61** (18), p. 2181, (1992).

[47] J. D. Carey, J. F. Donegan, R. C. Barklie, F. Priolo, G. Franzó, and S. Coffa, *Appl. Phys. Lett.*, **69** (25), p. 3854, (1996).

[48] J. M. Redwing, T. F. Keuch, D. C. Gordon, B. A. Vaartstra, and S. S. Lau, *J. Appl. Phys.*, **76** (3), p. 1585, (1994).

[49] A. Kozanecki, M. Chan, C. Jeynes, B. Sealy, and K. Homewood, *Solid State Communications*, **78** (8), p. 763, (1991).

[50] P. S. Whitney, K. Uwai, H. Nakagome, and K. Takahei, *Electronics Letters*, **24** (12), p. 740, (1988).

[51] R. S. Smith, H. D. Müller, H. Ennen, P. Wennekers, and M. Maier, *Appl. Phys. Lett.*, **50** (1), p. 50, (1987).

[52] J. Nakata, M. Taniguchi, and K. Takahei, *Appl. Phys. Lett.*, **61** (22), p. 2665, (1992).

[53] A. Rolland, A. LeCorre, P. N. Favennec, M. Gauneau, B. Lambert, D. Lecrosnier, H. L'Haridon, D. Moutonnet, and C. Rochaix, *Electronics Letters*, **24** (15), p. 956, (1988).

[54] K. Takahei, A. Taguchi, and R. A. Hogg, *J. Appl. Phys.*, **82** (8), p. 3997, (1997).

[55] X. Z. Wang and B. W. Wessels, *Appl. Phys. Lett.*, **64** (12), p. 1537, (1994).

[56] X. Z. Wang and B. W. Wessels, *Appl. Phys. Lett.*, **67** (4), p. 518, (1995).

[57] G. M. Ford and B. W. Wessels, *Appl. Phys. Lett.*, **68** (8), p. 1126, (1996).

[58] X. Z. Wang and B. W. Wessels, *Appl. Phys. Lett.*, **65** (5), p. 584, (1994).

[59] H. Nakagome, K. Takahei, and Y. Homma, *J. Crystal Growth*, **85**, p. 345, (1987).

[60] I. A. Buyanova, A. J. Neuhalfen, and B. W. Wessels, *Appl. Phys. Lett.*, **61** (20), p. 2461, (1992).

[61] A. J. Neuhalfen and B. W. Wessels, *Appl. Phys. Lett.*, **59** (18), p. 2317, (1991).

[62] A. J. Neuhalfen and B. W. Wessels, *Appl. Phys. Lett.*, **60** (21), p. 2657, (1992).

[63] L. Kou, D. C. Hall, and H. Wu, *Appl. Phys. Lett.*, **72** (26), p. 3411, (1998).

[64] J. D. MacKenzie, C. R. Abernathy, S. J. Pearton, U. Hömmerich, X. Wu, R. N. Schwartz, R. G. Wilson, and J. M. Zavada, *J. Crystal Growth*, **175/176**, p. 84, (1997).

[65] J. D. MacKenzie, C. R. Abernathy, S. J. Pearton, U. Hömmerich, X. Wu, R. N. Schwartz, R. G. Wilson, and J. M. Zavada, *Appl. Phys. Lett.*, **69** (14), p. 2083, (1996).

[66] C. R. Abernathy, J. D. MacKenzie, and S. M. Donovan, *J. Crystal Growth*, **178**, p. 74, (1997).

[67] J. D. MacKenzie, C. R. Abernathy, S. J. Pearton, U. Hömmerich, J. T. Seo, R. G. Wilson, and J. M. Zavada, *Appl. Phys. Lett.*, **72** (21), p. 2710, (1998).

[68] A. J. Steckl and R. Birkhahn, *Appl. Phys. Lett.*, **73** (12), p. 1700, (1998).

[69] R. Birkhahn and A. J. Steckl, *Appl. Phys. Lett.*, **73** (15), p. 2143, (1998).

[70] R. Birkhahn, R. Hudgins, D. Lee, A. J. Steckl, R. J. Molnar, A. Saleh, and J. M. Zavada, *J. Vac. Sci. Technol. B*, **17** (3), p. 1195, (1999).

[71] A. J. Steckl, M. Garter, R. Birkhahn, and J. Scofield, *Appl. Phys. Lett.*, **73** (17), p. 2450, (1998).

[72] M. Garter, J. Scofield, R. Birkhahn, and A. J. Steckl, *Appl. Phys. Lett.*, **74** (2), p. 182, (1998).

[73] M. Garter, R. Birkhahn, A. J. Steckl, and J. Scofield, *MRS Internet J. Nitride Semicond. Res.*, **4S1**, G11.3, (1999).

[74] R. Birkhahn, M. Garter, and A. J. Steckl, *Appl. Phys. Lett.*, **74** (15), p. 2161, (1999).

[75] L. C. Chao and A. J. Steckl, *Appl. Phys. Lett.*, **74** (16), p. 2364, (1999).

[76] J. Heikenfeld, M. Garter, D. S. Lee, R. Birkhahn, and A. J. Steckl, *Appl. Phys. Lett.*, **75** (9), p. 1189, (1999).

[77] A. J. Steckl, M. Garter, D. S. Lee, J. Heikenfeld, and R. Birkhahn, *Appl. Phys. Lett.*, **75** (15), p. 2184, (1999).

[78] M. Markmann, E. Neufeld, A. Sticht, K. Brunner, G. Abstreiter, and C. Berchal, *Appl. Phys. Lett.*, **75** (17), p. 2584, (1999).

[79] J. D. Carey, R. C. Barklie, J. F. Donegan, F. Priolo, G. Franzó, and S. Coffa, *Physical Review B*, **59** (4), p. 2773, (1999).

[80] G. Franzó, S. Coffa, F. Priolo, and C. Spinella, *J. Appl. Phys.*, **81** (6), p. 2784, (1997).

[81] F. Priolo, S. Coffa, G. Franzó, C. Spinella, A. Carnera, and V. Bellani, *J. Appl. Phys.*, **74** (8), p. 4936, (1993).

[82] F. Priolo, G. Franzó, S. Coffa, A. Polman, S. Libertino, R. Barklie, and D. Carey, *J. Appl. Phys.*, **78** (6), p. 3874, (1995).

[83] S. Coffa, F. Priolo, G. Franzó, A. Polman, S. Libertino, M. Saggio, and A. Carnera, *Nucl. Intr. and Meth. in Phys. Res. B*, **106**, p. 386, (1995).

[84] P. N. Favennec, H. L'Haridon, D. Moutonnet, M. Salvi, and M. Gauneau, *Jpn. J. Appl. Phys.*, **29** (2), p. L524, (1990).

[85] P. Rutter, K. E. Singer, and A. R. Peaker, *J. Crystal Growth*, **182**, p. 247, (1997).

[86] J. Torvik, R. Feuerstein, J. Pankove, C. Qui, and F. Namavar, *Appl. Phys. Lett.*, **69** (14), p. 2098, (1996).

[87] C. Qui, M. Leksono, J. Pankove, J. Torvik, R. Feuerstein, and F. Namavar, *Appl. Phys. Lett.*, **66** (5), p. 562, (1995).

[88] J. T. Torvik, C. H. Qiu, R. J. Feurstein, J. I. Pankove, and F. Namavar, *J. Appl. Phys.*, **81** (9), p. 6343, (1997).

[89] T. Dietl, H. Ohno, F. Matsukura, J. Cibert, and D. Ferrand, *Science*, **287**, p. 1019, (2000).

[90] T. Dietl and H. Ohno, *Physica E*, **9**, p. 185, (2001).

[91] T. Dietl, A. Haury, and Y. Merle d'Aubigne, *Physical Review B*, **55** (6), p. R3317, (1997).

[92] C. Kittel, *Introduction to Solid State Physics, 6th Ed.*, Wiley, New York, 1986.

[93] F. Matsukura, H. Ohno, A. Shen, and Y. Sugawara, *Physical Review B*, **57** (4), p. R2037, (1998).

[94] A. Twardowski, *Mat. Sci, & Eng. B*, **63**, p. 96, (1999).

[95] B. Lee, T. Jungwirth, and A. H. MacDonald, *Physical Review B*, **61** (23), p. 15606, (2000).

[96] K. Sato and H. Katayama-Yoshida, *MRS Symp. Proc. T/U/V Spring 2001.* Materials Research Society, Warrendale, PA (under review).

[97] T. Miyoshi, T. Matsui, H. Tsuda, H. Mabuchi, and K. Morii, *J. Appl. Phys.*, **85** (8), p. 5372, (1999).

[98] M. Gajdzik, C. Sürgers, M. T. Kelemen, and H. v. Löhneysen, *J. Mag. and Mag. Mat.*, **221**, p. 248, (2000).

[99] J. J. Hauser, *Physical Review B*, **22** (5), p. 2554, (1980).

[100] Y. D. Park, A. Wilson, A. T. Hanbicki, J. E. Mattson, T. Ambrose, G. Spanos, and B. T. Jonker, *Appl. Phys. Lett.*, **78** (18), p. 2739, (2001).

[101] T. Takeuchi, Y. Hirayama, and M. Futamoto, *IEEE Trans. Mag.*, **29** (6), p. 3090, (1993).

[102] S. Abe, Y. Nakasima, S. Okubo, H. Nakayama, T. Nishino, H. Yanagi, H. Ohta, and S. Iida, *Appl. Surf. Sci.*, **142**, p. 537, (1999).

[103] Y. Yan, M. M. Al-Jassim, K. Matsuda, H. Tatsuoka, H. Kuwabara, and S. J. Pennycock, *Appl. Phys. Lett.*, **75** (19), p. 2894, (1999).

[104] M. Gajdzik, C. Sürgers, M. Kelemen, and H. v. Löhneysen, *J. Appl. Phys.*, **87** (9), p. 6013, (2000).

[105] H. Ohno, H. Munekata, T. Penney, S. von Molnár, and L. L. Chang, *Phys. Rev. Lett.*, **68** (17), p. 2664, (1992).

[106] S. Koshihara, A. Oiwa, M. Hirasawa, S. Katsumoto, Y. Iye, C. Urano, H. Takagi, and H. Munekata, *Phys. Rev. Lett.*, **78** (24), p. 4617, (1997).

[107] S. Koshihara, H. Munekata, A. Oiwa, M. Hirasawa, S. Katsumoto, Y. Iye, C. Urano, and H. Takagi, *Physica E*, **2**, p. 417, (1998).

[108] H. Ohno, H. Munekata, S. von Molnár, and L. L. Chang, *J. Appl. Phys.*, **69** (8), p. 6103, (1991).

[109] A. Oiwa, A. Endo, S. Katsumoto, Y. Iye, and H. Munekata, *Physica B*, **284-288**, p. 1173, (2000).

[110] S. P. Guo, A. Shen, H. Yasuda, F. Matsukura, Y. Ohno, and H. Ohno, *J. Crystal Growth*, **208**, p. 799, (2000).

[111] H. Munekata, A. Zaslavsky, P. Fumagalli, and R. J. Gambino, *Appl. Phys. Lett.*, **63** (21), p. 2929, (1993).

[112] H. Ofuci, T. Kubo, M. Tabuchi, Y. Takeda, F. Matsukura, S. P. Guo, A. Shen, and H. Ohno, *J. Appl. Phys.*, **89** (1), p. 66, (2001).

[113] Y. K. Zhou, H. Asahi, J. Asakura, S. Okumura, T. Tashima, J. Sato, K. Asami, S. Gonda, *Physica E*, **7**, p. 1001, (2000).

[114] S. P. Guo, A. Shen, F. Matsukura, Y. Ohno, and H. Ohno, *Appl. Surf. Sci.*, **130-132**, p. 797, (1998).

[115] H. Munekata, H. Ohno, S. von Molnar, A. Segmüller, L. L. Chang, and L. Esaki, *Phys. Rev. Lett.*, **63** (17), p. 1849, (1989).

[116] Y. L. Soo, S. W. Huang, Z. H. Ming, Y. H. Kao, H. Munekata, and L. L. Chang, *Physical Review B*, **53** (8), p. 4905, (1996).

[117] Y. Iye, A. Oiwa, A. Endo, S. Katsumoto, F. Matsukura, A. Shen, H. Ohno, and H. Munekata, *Mat. Sci. Eng. B*, **63**, p. 88, (1999).

[118] T. Hayashi, H. Shimida, H. Shimizu, and M. Tanaka, *J. Crystal Growth*, **201/202**, p. 689, (1999).

[119] M. Tanaka, *J. Crystal Growth*, **201/202**, p. 660, (1999).

[120] J. Sadowski, J. Z. Domagala, J. Bak-Misiuk, S. Kolesnik, K. Swiatek, J. Kanski, L. Ilver, *Thin Solid Films*, **367**, p. 165, (2000).

[121] J. DeBoeck, R. Oesterholt, A. Van Esch, H. Bender, C. Bruynseraede, C. Van Hoof, and G. Borghs, *Appl. Phys. Lett.*, **68** (19), p. 2744, (1996).

[122] T. Hayashi, M. Tanaka, K. Seto, T. Nishinaga, H. Shimida, H. Hayashi, and K. Niihara, *Physica E*, **2**, p. 404, (1998).

[123] M. Tanaka, *Physica E*, **2**, p. 372, (1998).

[124] T. Hayashi, M. Tanaka, T. Nishinaga, H. Shimada, H. Tsuchiya, and Y. Otuka, *J. Crystal Growth*, **175/176**, p. 1063, (1997).

[125] H. Ohno, F. Matsukura, T. Omiya, and N. Akiba, *J. Appl. Phys.*, **85** (8), p. 4277, (1999).

[126] B. Beschoten, P. A. Crowell, I. Malajovich, D. D. Awschalom, F. Matsukura, A. Shen, and H. Ohno, *Phys. Rev. Lett.*, **83** (15), p. 3073, (1999).

[127] M. A. Boselli, I. C. da Cunha Lima, and A. Ghazali, *J. Appl. Phys.*, **87** (9), p. 6439, (2000).

[128] M. A. Boselli, A. Ghazali, and I. C. da Cunha Lima, *Physical Review B*, **62** (13), p. 8895, (2000).

[129] H. Ohno, *J. Mag. & Mag. Mat.*, **200**, p. 110, (1999).

[130] W. D. Johnston and W. M. Callahan, *J. Electrochem. Soc.*, **123** (10), p. 1524, (1976).

[131] F. Bantien and J. Weber, *Solid State Communications*, **61** (7), p. 423, (1987).

[132] S. A. Obukhov, B. S. Neganov, Y. F. Kiselev, A. N. Chernikov, V. S. Vekshina, N. I. Pepik, and A. N. Popkov, *Cryogenics*, **31** (10), p. 874, (1991).

[133] S. A. Obukhov, *Solid State Communications*, **88** (3), p. 255, (1993).

[134] D. G. Andrianov, G. V. Lazareva, A. S. Savel'ev, V. I. Selyanina, and V. I. Fistul', *Sov. Phys. Semicond.*, **9** (8), p. 1026, (1976).

[135] D. G. Andrianov, V. V. Karataev, G. V. Lazareva, Y. B. Muravlev, A. S. Savel'ev, *Sov. Phys. Semicond.*, **11** (7), p. 738, (1977).

[136] M. Y. Dashevskii, V. S. Ivleva, L. Y. Krol, I. Kurilenko, L. B. Litvak-Gorskaya, R. S. Mitrofanova, and E. Y. Fridlyand, *Sov. Phys. Semicond.*, **5** (5), p. 757, (1971).

[137] D. G. Andrianov, G. V. Lazareva, A. S. Savel'ev, and V. I. Fistul', *Sov. Phys. Semicond.*, **10** (3), p. 339, (1976).

[138] S. A. Obukhov and N. I. Pepic, *Solid State Communications*, **70** (1), p. 103, (1989).

[139] A. B. Henriques, N. F. Oliveira, S. A. Obukhov, and V. A. Sanina, *JETP Lett.*, **69** (5), p. 386, (1999).

[140] I. S. Dadashev and G. I. Safaraliyev, *Phys. Met. Metallogr.*, **39** (6), p. 185, (1975).

[141] T. Adhikari and S. Basu, *Mat. Sci. & Eng. B*, **27** (1), p. 47, (1994).

[142] S. Basu and T. Adhikari, *Solid State Communications*, **95** (1), p. 53, (1995).

[143] J. J. Mares, P. Hubik, J. Kristofik, B. Stepanek, V. Sestakova, and L. Pekarek, *Mat. Sci. & Eng. B*, **28** (1-3), p. 134, (1994).

[144] B. Stepanek, P. Hubik, J. J. Mares, J. Kristofik, V. Sestakova, L. Pekarek, and J. Sestak, *Semicond. Sci, & Tech.*, **9** (5), p. 1138, (1994).

[145] V. Sestakova, P. Hubik, B. Stepanek, and J. Kristofik, *J. Crystal Growth*, **132**, p. 345, (1993).

[146] V. Sestakova and B. Stepanek, *J. Crystal Growth*, **146**, p. 87, (1995).

[147] F. Matsukura, E. Abe, and H. Ohno, *J. Appl. Phys.*, **87** (9), p. 6442, (2000).

[148] E. Abe, F. Matsukura, H. Yasuda, Y. Ohno, and H. Ohno, *Physica E*, **7**, p. 981, (2000).

[149] F. Matsukura, E. Abe, Y. Ohno, and H. Ohno, *Appl. Surf. Sci.*, **159-160**, p. 265, (2000).

[150] C. T. Lin, E. Schoenherr, and H. Bender, *J. Crystal Growth*, **104** (3), p. 653, (1990).

[151] G. E. Archangelskii, F. Karel, J. Mares, S. Pacesova, and J. Pastrnak, *Phys. Stat. Solidi A*, **69** (1), p. 173, (1982).

[152] F. Karel, J. Pastrnak, J. Hejduk, and V. Losik, *Phys. Stat. Solidi*, **15**, p. 693, (1966).

[153] M. L. Caldwell, H. H. Richardson, and M. E. Kordesch, *Mat. Res. Soc. Proc.*, **595**, p. W3.26.1, (2000).

[154] M. Zajac, R. Doradzinski, J. Gosk, J. Szczytko, M. Lefeld-Sosnowska, M. Kaminska, A. Twardowski, M. Palczewska, E. Grzanka, and W. Gebicki, *Appl. Phys. Lett.*, **78** (9), p. 1276, (2001).

[155] W. Gebicki, J. Strzeszewski, G. Kamler, T. Szyszko, and S. Podsiadlo, *Appl. Phys. Lett.*, **76** (26), p. 3870, (2000).

[156] P. G. Baranov, I. V. Ilyin, and E. N. Mokhov, *Solid State Communications*, **101** (8), p. 611, (1997).

[157] C. Y. Fong, V. A. Gubanov, and C. Bokema, *J. Elec. Mat.*, **29** (9), p. 1067, (2000).

[158] B. J. Stadler, A. Davis, E. A. Martin, K. Vaccaro, H. M. Dauplaise, L. O. Bouthillette, S. M. Spaziani, J. P. Lorenzo, and G. Ramseyer, *IEEE Conf. InP & Rel. Mat.*, IEEE, p. 616, (1995).

[159] L. Eaves, A. W. Smith, M. S. Skolnick, and B. Cockayne, *J. Appl. Phys.*, **53** (7), p. 4955, (1982).

[160] R. Laiho, E. Lahderanta, E. Supponen, and L. Vlasenko, *Physical Review B*, **41** (11), p. 7674, (1990).

[161] S. A. Abagyan, P. U. Arifov, N. Y. Arutyunov, V. Y. Trashchakov, G. A. Ivanov, and E. P. Prokop'ev, *Sov. Phys. Semicond.*, **15** (4), p. 402, (1981).

[162] G. Hofmann, F. G. Anderson, and J. Weber, *Physical Review B*, **43** (12), p. 9711, (1991).

[163] J. Kreissl, W. Ulrici, M. El-Metoui, A.-M. Vasson, and A. Gavaix, *Physical Review B*, **54** (15), p. 10508, (1996).

[164] T. Fukumura, Z. Jin, M. Kawasaki, T. Shono, T. Hasegawa, S. Koshihara, and H. Koinuma, *Appl. Phys. Lett.*, **78** (7), p. 958, (2001).

[165] T. Fukumura, Z. Jin, A. Ohtomo, H. Koinuma, and M. Kawasaki, *Appl. Phys. Lett.*, **75** (21), p. 3366, (1999).

[166] D. Ferrand, J. Cibert, C. Bourgognon, S. Tatarenko, A. Wasiela, G. Fishman, A. Bonnani, H. Sitter, S. Kolesnik, J. Jaroszynski, A. Barcz, and T. Dietl, *J. Crystal Growth*, **214/215**, p. 387, (2000).

[167] D. Ferrand, C. Bourgognon, J. Cibert, A. Wasiela, S. Tatarenko, Y. Merle d'Aubigne, A. Bonnani, D. Stifter, H. Sitter, L. V. Khoi, S. Kolesnik, J. Jaroszynski, M. Sawicki, T. Andrearczyk, and T. Dietl, *Physica B*, **284-288**, p. 1177, (2000).

[168] T. Yasuda, M. D. Duc, and Y. Segawa, *J. Crystal Growth*, **214/215**, p. 159, (2000).

[169] Y. Merle d'Aubigne, A. Arnoult, J. Cibert, T. Dietl, A. Haury, P. Kossacki, S. Tatarenko, and A. Wasiela, *Physica E*, **3**, p. 169, (1998).

[170] J. Cibert, P. Kossacki, A. Haury, D. Ferrand, A. Wasiela, Y. Merle d'Aubigne, A. Arnoult, S. Tatarenko, and T. Dietl, *J. Crystal Growth*, **201/202**, p. 670, (1999).

[171] P. Kossacki, D. Ferrand, A. Arnoult, J. Cibert, S. Tatarenko, A. Wasiela, Y. Merle d'Aubigne, J.-L. Staehli, J.-D. Ganiere, W. Bardyszewski, K. Swiatek, M. Sawicki, J. Wrobel, and T. Dietl, *Physica E*, **6**, p. 709, (2000).

[172] A. Haury, A. Wasiela, A. Arnoult, J. Cibert, S. Tatarenko, T. Dietl, and Y. Merle d'Aubigne, *Phys. Rev. Lett.*, **79** (3), p. 511, (2000).

[173] T. M. Pekarek, M. Duffy, J. Garner, B. C. Crooker, I. Miotkowski, and A. K. Ramdas, *J. Appl. Phys.*, **87** (9), p. 6448, (1998).

[174] T. M. Pekarek, B. C. Crooker, I. Miotkowski, and A. K. Ramdas, *J. Appl. Phys.*, **83** (11), p. 6557, (1998).

[175] P. J. T. Eggenkamp, C. W. H. M. Vennix, T. Story, H. J. M. Swagten, C. H. W. Swuste, and W. J. M. de Jonge, *J. Appl. Phys.*, **75** (10), p. 5728, (1994).

[176] T. Story, R. R. Galazka, R. B. Frankel, and P. A. Wolff, *Phys. Rev. Lett.*, **56** (7), p. 777, (1986).

[177] G. A. Medvedkin, T. Ishibashi, T. Nishi, K. Hayata, Y. Hasegawa, and K. Sato, *Jpn. J. Appl. Phys.*, **39**, p. L949, (2000).

[178] H. Akinaga, S. Nemeth, J. De Boeck, L. Nistor, H. Bender, G. Borghs, H. Ofuchi, and M. Oshima, *Appl. Phys. Lett.*, **77** (26), p. 4377, (2000).

[179] N. Karar and S. Basu, *Mat. Sci, & Eng. B*, **56**, p. 21, (1999).

[180] V. Ladizhansky, A. Faraggi, V. Lyahovitskaya, and S. Vega, *Physical Review B*, **56** (11), p. 6712, (1997).

[181] Y. Matsumoto, M. Murakami, T. Shono, T. Hasegawa, T. Fukumura, M. Kawasaki, P. Ahmet, T. Chikyow, S. Koshihara, and H. Koinuma, *Science*, **291**, p. 854, (2001).

[182] P. van der Wagt, http://snowmass.stanford.edu, Harris Group Webpage, 1996.

[183] M. McElfresh, *Fundamentals of Magnetism and Magnetic Materials*, Quantum Design, 1994.

[184] K. Okada, Y.-F. Wang, and T. Nakaya, *Synthetic Metals*, **97**, 113 (1998).

[185] D. Rüter and W. Bauhofer, *Appl. Phys. Lett.*, **69**, 892 (1996).

[186] T. Chatterjee, P. J. McCann, X. M. Fang, and M. B. Johnson, *J. Vac. Sci. Technol. B*, **16**, 1463 (1998).

[187] D. S. Lee, J. Heikenfeld, R. Birkhahn, M. Garter, B. K. Lee, and A. J. Steckl, *Appl. Phys. Lett.*, **76**, 1525 (2000).

[188] S. Morishima, T. Maruyama, M. Tanaka, Y. Masumoto, and K. Akimoto, *Phys. Stat. Sol. (A)*, **176**, 113 (1999).

BIOGRAPHICAL SKETCH

Mark Eddy Overberg was born on July 18, 1973 in the seaside town of Beverly, Massachusetts, one of the oldest cities in the United States (founded in 1626), and the birthplace of the United States Navy. He graduated from the St. John's Preparatory School in neighboring Danvers, Massachusetts in 1991. In the fall of 1991, he started college at Rensselaer Polytechnic Institute (RPI) in Troy, New York. While working towards his bachelor's degree in the Department of Nuclear Engineering and Engineering Physics, he participated in research projects in the Physics Department and in his own department. These projects were in the separate areas of thin film deposition and remediating contaminated waste with radiation fields. Upon graduating Magna Cum Laude in 1995, he entered graduate school at Rensselaer, also in the Nuclear Engineering Department. For the next two years, he conducted research at RPI's Gaerttner Linear Accelerator (LINAC), sponsored by the Knolls Atomic Power Laboratory (NY) in support of the U. S. Naval Reactors program under the auspices of the U. S. Department of Energy and the U. S. Department of Defense. Wanting to change fields after graduating with his master's degree, he enrolled in the Department of Materials Science at the University of Florida in the fall of 1997 as the first Stephen C. O'Connell Presidential Fellow. He joined Dr. Cammy Abernathy's research group in the spring of 1998, and began research on optical and magnetic properties of doped III-V semiconductors. Post-graduation plans include continuing research on the magnetic doped materials and working as a post-doc under Dr. Abernathy's supervision on the MOCVD growth of III-V semiconducting UV devices.

I certify that I have read this study and that in my opinion it conforms to acceptable standards of scholarly presentation and is fully adequate, in scope and quality, as a dissertation for the degree of Doctor of Philosophy.

Cammy R. Abernathy, Chairperson
Professor of Materials Science and
Engineering

I certify that I have read this study and that in my opinion it conforms to acceptable standards of scholarly presentation and is fully adequate, in scope and quality, as a dissertation for the degree of Doctor of Philosophy.

Stephen J. Pearton
Professor of Materials Science and
Engineering

I certify that I have read this study and that in my opinion it conforms to acceptable standards of scholarly presentation and is fully adequate, in scope and quality, as a dissertation for the degree of Doctor of Philosophy.

Paul H Holloway

Paul H. Holloway
Professor of Materials Science and
Engineering

I certify that I have read this study and that in my opinion it conforms to acceptable standards of scholarly presentation and is fully adequate, in scope and quality, as a dissertation for the degree of Doctor of Philosophy.

Rajiv K. Singh
Professor of Materials Science and
Engineering

I certify that I have read this study and that in my opinion it conforms to acceptable standards of scholarly presentation and is fully adequate, in scope and quality, as a dissertation for the degree of Doctor of Philosophy.

Arthur F. Hebard

Arthur F. Hebard
Professor of Physics

This dissertation was submitted to the Graduate Faculty of the College of Engineering and to the Graduate School and was accepted as partial fulfillment of the requirements for the degree of Doctor of Philosophy.

August 2001

Pramod P. Khargonekar
Dean, College of Engineering

Winfred M. Phillips
Dean, Graduate School